

UNITED STATES AIR FORCE
SUMMER RESEARCH PROGRAM -- 1997
SUMMER RESEARCH EXTENSION PROGRAM FINAL REPORTS

VOLUME 4B

WRIGHT LABORATORY

RESEARCH & DEVELOPMENT LABORATORIES
5800 Uplander Way
Culver City, CA 90230-6608

Program Director, RDL
Gary Moore

Program Manager, AFOSR
Major Linda Steel-Goodwin

Program Manager, RDL
Scott Licoscos

Program Administrator, RDL
Johnetta Thompson

Program Administrator, RDL
Rebecca Kelly-Clemons

Submitted to:

AIR FORCE OFFICE OF SCIENTIFIC RESEARCH
Bolling Air Force Base
Washington, D.C.
December 1997

20010319 034

AQM01-06-1191

REPORT DOCUMENTATION PAGE

AFRL-SR-BL-TR-00-

reviewing
formation

Public reporting burden for this collection of information is estimated to average 1 hour per response, including the time for reviewing instructions, see the collection of information. Send comments regarding this burden estimate or any other aspect of this collection of information, including suggested operations and reports, 1215 Jefferson Davis Highway, Suite 1204, Arlington, VA 22202-4302, and to the Office of Management and Budget, Paper

1. AGENCY USE ONLY (Leave blank)	2. REPORT DATE	3. REPO.
	December, 1997	

0712
5. FUNDING NUMBERS
F49620-93-C-0063

4. TITLE AND SUBTITLE	1997 Summer Research Program (SRP), Summer Research Extension Program (SREP), Final Report, Volume 4B, Wright Laboratory
-----------------------	--

6. AUTHOR(S)	Gary Moore
--------------	------------

7. PERFORMING ORGANIZATION NAME(S) AND ADDRESS(ES)	Research & Development Laboratories (RDL) 5800 Uplander Way Culver City, CA 90230-6608
--	--

8. PERFORMING ORGANIZATION
REPORT NUMBER

9. SPONSORING/MONITORING AGENCY NAME(S) AND ADDRESS(ES)	Air Force Office of Scientific Research (AFOSR) 801 N. Randolph St. Arlington, VA 22203-1977
---	--

10. SPONSORING/MONITORING
AGENCY REPORT NUMBER

11. SUPPLEMENTARY NOTES

12a. DISTRIBUTION AVAILABILITY STATEMENT	Approved for Public Release
--	-----------------------------

12b. DISTRIBUTION CODE

13. ABSTRACT (Maximum 200 words)	The United States Air Force Summer Research Program (SRP) is designed to introduce university, college, and technical institute faculty members to Air Force research. This is accomplished by the faculty members, graduate students, and high school students being selected on a nationally advertised competitive basis during the summer intersession period to perform research at Air Force Research Laboratory (AFRL) Technical Directorates and Air Force Air Logistics Centers (ALC). AFOSR also offers its research associates (faculty only) an opportunity, under the Summer Research Extension Program (SREP), to continue their AFOSR-sponsored research at their home institutions through the award of research grants. This volume consists of a listing of the participants for the SREP and the technical report from each participant working at the AF Wright Laboratory.
----------------------------------	---

14. SUBJECT TERMS	Air Force Research, Air Force, Engineering, Laboratories, Reports, Summer, Universities, Faculty, Graduate Student, High School Student
-------------------	---

15. NUMBER OF PAGES

16. PRICE CODE

17. SECURITY CLASSIFICATION OF REPORT	18. SECURITY CLASSIFICATION OF THIS PAGE	19. SECURITY CLASSIFICATION OF ABSTRACT	20. LIMITATION OF ABSTRACT
Unclassified	Unclassified	Unclassified	UL

PREFACE

This volume is part of a five-volume set that summarizes the research of participants in the 1997 AFOSR Summer Research Extension Program (SREP.)

Reports presented in this volume are arranged alphabetically by author and are numbered consecutively – e.g., 1-1, 1-2, 1-3; 2-1, 2-2, 2-3. Reports in the five-volume set are organized as follows:

VOLUME	TITLE
1	Armstrong Laboratory
2	Phillips Laboratory
3	Rome Laboratory
4A	Wright Laboratory
4B	Wright Laboratory
5	Arnold Engineering Development Center Air Logistics Centers United States Air Force Academy Wilford Hall Medical Center

1997 SREP Final Technical Report Table of Contents

Armstrong Laboratory

Volume 1

Principle Investigator	Report Title University/Institution	Laboratory & Directorate
1 Dr. Richelle M. Allen-King	Trans-1,2-Dichloroethene Transformation Rate in a Metallic Iron/Water System: Effects of Concentration and Temperature Washington State University	AL/EQC
2 Dr. Anthony R. Andrews	Development of Multianalyte Electrochemiluminescence Sensors & Biosensors Ohio University	AL/EQC
3 Dr. Jer-Sen Chen	Development of Perception Based Video Compression Algorithms Using Reconfigurable Hardware Wright State University	AL/CFHV
4 Dr. Cheng Cheng	Investigation & Eval of Optimization Algorithms Guiding the Assignment of Recruits to Training School Seats John Hopkins University	AL/HRM
5 Dr. Randolph D. Glickman	Optical Detection of Intracellular Photooxidative Reactions University of Texas Health Science Center	AL/OEO
6 Dr. Nandini Kannan	Predicting Altitude Decompression sickness Using Survival Models University of Texas at San Antonio	AL/CFTS
7 Dr. Antti J. Koivo	Skill Improvements Via Reflected Force Feedback Purdue Research Foundation	AL/CFBA
8 Dr. Suk B. Kong	Degradation & Toxicology Studies of JP-8 Fuel in Air, Soil & Drinking Water Incarnate Word College	AL/OEA
9 Dr. Audrey D. Levine	Biogeochemical Assessment of Natl Attenuation of JP-4 Contaminated Ground in the Presence of Fluorinated Surfactants Utah State University	AL/EQC
10 Dr. Robert G. Main	The Effect of Video Image Size & Screen Refresher Rate On Mess Retention Cal State University, Chico	AL/HRT
11 Dr. Phillip H. Marshall	On the Resilience of Time-to-Contact Judgements: The Determination of Inhibitory and Facilitory Influences, and Factor Structure Texas Tech University	AL/HRM
12 Dr. Bruce V. Mutter	Environmental cost Analysis: Calculating Return on Investment for Emerging Technologies Bluefield State College	AL/EQP

1997 SREP Final Technical Report Table of Contents

Armstrong Laboratory

Volume 1 (cont.)

Principle Investigator	Report Title University/Institution	Laboratory & Directorate
13 Dr. Sundaram Narayanan	Java-Based Interactive Simulation Architecture for Airbase Logistics Modeling Wright State University	AL/HRT
14 Dr. Barth F. Smets	Coupling of 2, 4-&2, 6-Dinitrotoluene Mineralization W/NO ₂ Removal by University of Cincinnati	AL/EQC
15 Dr. Mary Alice Smith	In Vitro Detection of Apoptosis in Differentiating Mesenchymal Cells Using Immunohistochemistry and Image Analysis University of Georgia	AL/OET
16 Dr. William A. Stock	Application of Meta-Analysis to Research on Pilot Training: Extensions to Flight Simulator Visual System Research Arizona State University	AL/HRA
17 Dr. Nancy J. Stone	Evaluation of a Scale Designed to Measure the Underlying Constructs of Engagement, Involvement, & Self-Regulated Learning Creighton University	AL/HRT
18 Dr. Mariusz Ziejewski	Characterization of Human Head/Neck Response in Z-Direction in Terms of Significant Anthropomorphic Parameters, Gender, Helmet Weight and Helmet Center North Dakota State University	AL/CFBV
19 Dr. Kevin M. Lambert	Magnetic Effects on the Deposition & Dissolution of Calcium Carbonate Scale Brigham Young University	AL/EQS
20 Dr. Jacqueline C. Shin	Coordination of Cognitive & Perceptual-Motor Activities Pennsylvania State University	AL/HRM
21 Dr. Travis C. Tubre	The Development of a General Measure of Performance Texas A&M University-College Station	AL/HRT
22 Dr. Robert B. Trelease	Development of Qualitative Process Modeling Systems for Cytokines, Cell Adhesion Molecules, and Gene Regulation University of California – Los Angeles	AL/AOH

1997 SREP Final Technical Report Table of Contents

Phillips Laboratory

Volume 2

Principle Investigator	Report Title University/Institution	Laboratory & Directorate
1 Dr. Graham R. Allan	Temporal & Spatial Characterization of a Synchronously-Pumped New Mexico Highlands University	PL/LIDN
2 Dr. Joseph M. Calo	Transient Studies of the Effects of Fire Suppressants in a Well-Stirred Combustor Brown University	PL/GPID
3 Dr. James J. Carroll	Examination of Critical Issues in the Triggering of Gamma Rays from $^{178}\text{Hfm}^2$ Youngstown State University	PL/WSQ
4 Dr. Soyoung S. Cha	Gradient-Data Tomography for Hartman Sensor Application to Aero-Optical Field Reconstruction University of Illinois at Chicago	PL/LIMS
5 Dr. Judith E. Dayhoff	Dynamic Neural Networks: Towards Control of Optical Air Flow Distortions University of Maryland	PL/LIMS
6 Dr. Ronald R. DeLyser	Computational Evaluation of Optical Sensors University of Denver	PL/WSTS
7 Dr. Andrew G. Detwiler	Analysis & Interpretation of Contrail Formation Theory & Observations South Dakota School of Mines – Technology	PL/GPAB
8 Dr. Itzhak Dotan	Measurements of Ion-Molecule Reactions at Very High Temperature The Open University of Israel	PL/GPID
9 Dr. George W. Hanson	Electromagnetic Modeling of Complex Dielectric/Metallic Mines In A Layered University of Wisconsin – Milwaukee	PL/WSQ
10 Dr. Mayer Humi	Optical & Clear Air Turbulence Worcester Polytechnic Inst.	PL/GPAA
11 Dr. Christopher H. Jenkins	Shape Control of an Inflated Circular Disk Experimental Investigation South Dakota School of Mines – Technology	PL/VT
12 Dr. Dikshitulu K. Kalluri	Numerical Simulation of Electromagnetic Wave Transformation in a Dynamic Magnetized Plasma University of Lowell	PL/GPIA
13 Dr. Aravinda Kar	Improved Chemical Oxygen-Iodine Laser (COIL) Cutting Models to to Optimize Laser Parameters University of Central Florida	PL/LIDB

1997 SREP Final Technical Report Table of Contents

Phillips Laboratory

Volume 2 (cont.)

Principle Investigator	Report Title University/Institution	Laboratory & Directorate
14 Dr. Andre Y. Lee	Characterization of Thermoplastic Inorganic-Organic Hybrid Polymers Michigan State University	PL/RKS
15 Dr. Feng-Bao Lin	Improvement in Fracture Propagation Modeling for Structural Ballistic Risk Assessment Polytechnic University of New York	PL/RKEM
16 Dr. Ronald A. Madler	Cross Sectional Area Estimation of Orbital Debris Embry-Riddle Aeronautical University	PL/WSAT
17 Dr. Carlos A. Ordóñez	Incorporation of Boundary condition Models into the AF Computer Simulation University of North Texas	PL/WSQA
18 Dr. James M. Stiles	Wide Swath, High Resolution, Low Ambiguity SAR Using Digital Beamforming Arrays University of Kansas	PL/VTRA
19 Dr. Charles M. Swenson	Balloon Retromodulator Experiment Post- flight Analysis Utah State University	PL/VTRA
20 Dr. Miguel Velez-Reyes	Development of Algorithms for Linear & Nonlinear Retrieval Problems in Atmospheric Remote Sensing University of Puerto Rico	PL/GPAS
21 Dr. John D. Holtzclaw	Experimental Investigation of Ipinging Jets University of Cincinnati	PL/RKS
22 Dr. Jeffrey W. Nicholson	Radar Waves with Optical Carriers University of New Mexico	PL/LIDB

1997 SREP Final Technical Report Table of Contents

Rome Laboratory

Volume 3

Principle Investigator	Report Title University/Institution	Laboratory & Directorate
1 Dr. A. F. Anwar	Deep Quantum Well Channels for Ultra Low Noise HEMTs for Millimeter and Sub-millimeter Wave Applications University of Connecticut	AFRL/SNH
2 Dr. Ahmed E. Barbour	Investigating the Algorithmic Nature of the Proof Structure of ORA Larch/VHDL Georgia Southern University	RL/ERDD
3 Dr. Milica Barjaktarovic	Specification & Verification of MISSI Architecture Using SPIN Wilkes University	RL/C3AB
4 Dr. Daniel C. Bukofzer	Analysis, Performance Evaluations, & Computer Simulations of Receivers Processing Low Probability of Intercept Signals Cal State Univ. Fresno	RL/C3BA
5 Dr. Xuesheng Chen	Non-Destructive Optical Characterization of Composition & Its Uniformity in Multilayer Ternary Semiconductor Stacks Wheaton College	RL/ERX
6 Dr. Jun Chen	Amplitude Modulation Using Feedback Sustained Pulsation as Sub-Carrier in Rochester Inst of Technol	RL/OCPA
7 Dr. Everett E. Crisman	Development of Anti-Reflection Thin Films for Improved Coupling of Laser Energy into Light Activated, Semiconductor Re-Configurable, Microwave Source/Antenna Brown University	RL/ERAC
8 Dr. Digendra K. Das	Development of a Stimulation Model for Determining the Precision Of Reliability SUNYIT	RL/ERSR
9 Dr. Matthew E. Edwards	An Application of PROFILER for Modeling the Diffusion of Of Aluminum-Copper on a Silicon Substrate Spelman College	RL/ERDR
10 Dr. Kaliappan Gopalan	Analysis of Stressed Speech Using Cepstral Domain Features Purdue University – Calumet	RL/IRAA
11 Dr. James P. LeBlanc	Multichannel Autoregressive Modeling & Multichannel Innovations Based New Mexico State University	RL/OCSS
12 Dr. Hrushikesh N. Mhaskar	Multi-Source Direction Finding Cal State University, Los Angeles	RL/ERAA
13 Dr. Ronald W. Noel	An Evolutionary Sys for Machine Recognition of Software Source Code Rensselaer Polytechnic Inst	RL/C3CA

1997 SREP Final Technical Report Table of Contents

Rome Laboratory

Volume 3 (cont.)

Principle Investigator	Report Title University/Institution	Laboratory & Directorate
14 Dr. Glenn E. Prescott	Rapid Prototyping of Software Radio Sys Using Field Programmable Gate Arrays University of Kansas Center for Research	RL/C3BB
15 Dr. Mysore R. Rao	Wavelet Transform Techniques for Isolation, Detection & Classification of Concealed Objects in Images Rochester Institute of Technology	RL/OCSM
16 Dr. Scott E. Spetka	IPL HTML Interface Performance Evaluation SUNY of Tech Utica	RL/IRD
17 Dr. Gang Sun	Investigation of Si/ZnS Near Infrared Intersubband Lasers University of Massachusetts-Boston	RL/EROC
18 Mr. Parker E. Bradley	Development of a User-Friendly Computer Environment for Blind Source Syracuse University	RL/C3BB

1997 SREP Final Technical Report Table of Contents

Wright Laboratory

Volume 4A

Principle Investigator	Report Title University/Institution	Laboratory & Directorate
1 Dr. Mohammad S. Alam	Infrared Image Registration & High Resolution Reconstruction Using Rotationally Translated Video Sequences* Purdue University	WL/AAJT
2 Dr. Pnina Ari-Gur	Optimizing Microstructure, Texture & Orientation Image Microscopy of Hot Rolled Ti-6Al-4V Western Michigan University	WL/MLLN
3 Dr. James D. Baldwin	Multi-Site & Widespread Fatigue Damage in Aircraft Structure in the Presence of Prior Corrosion University of Oklahoma	WL/FIB
4 Dr. Armando R. Barreto	Deconvolution of the Space-Time Radar Spectrum Florida International University	WL/AAMR
5 Dr. Marc M. Cahay	Improved Modeling of Space-Charge Effects in a New Cold Cathode Emitter University of Cincinnati	WL/AADM
6 Dr. Reaz A. Chaudhuri	Interfacing of Local Asyptotic Singular & Global Axisymmetric Micromechanical University of Utah	WL/MLBM
7 Dr. Robert J. DeAngelis	Texture Formation During the Thermo-Mechanical Processing of Copper Plate University of Nebraska – Lincoln	WL/MNMW
8 Dr. Gregory S. Elliott	The Study of a Transverse Jet in a Supersonic Cross-Flow Using Advanced Laser Rutgers: State University of New Jersey	WL/POPT
9 Dr. Altan M. Ferendeci	Development of Multiple Metal-Dielectric Layers for 3-D MMIC University of Cincinnati	WL/AADI
10 Dr. Allen G. Greenwood	Development of a Prototype to Test & Demonstrate the MODDCE Framework Mississippi State University	WL/MTI
11 Dr. Michael A. Grinfeld	Mismatch Stresses & Lamellar Microstructure of TiAl-Alloys Rutgers University- Piscataway	WL/MLLM
12 Dr. Michael C. Larson	Interfacial Sliding in Brittle Fibrous Composites Tulane University	WL/MLLM
13 Dr. Douglas A. Lawrence	Tools for the Analysis & Design of Gain Scheduled Missile Autopilots Ohio University	WL/MNAG

1997 SREP Final Technical Report Table of Contents

Wright Laboratory (cont.)

Volume 4A

Principle Investigator	Report Title University/Institution	Laboratory & Directorate
14 Dr. Junghsen Lieh	Determination of 3D Deformations, Forces & Moments of Aircraft Wright State University	WL/FIVM
15 Dr. Zongli Lin	Control of Linear Sys w/Rate Limited Actuators & Its Applications to Flight Control Systems SUNY Stony Brook	WL/FI
16 Dr. Paul Marshall	Experimental & Computational Investigations of Bromine & Iodine Chemistry in Flame Suppression University of North Texas	WL/MLBT
17 Dr. Hui Meng	Development of Holographic Visualization & Holographic Velocimetry Techniques Kansas State University	WL/POSC
18 Dr. Douglas J. Miller	Band Gap Calculations on Squarate-Containing Conjugated Oligomers for the Prediction of Conductive and Non-Linear Optical Properties of Polymeric Materials Cedarville College	WL/MLBP
19 Dr. Timothy S. Newman	Classification & Visualization of Tissue in Multiple Modalities of Brain MR University of Alabama at Huntsville	WL/AACR
20 Dr. Mohammed Y. Niamat	FPGA Implementation of the Xpatch Ray Tracer University of Toledo	WL/AAST
21 Dr. Anthony C. Okafor	Development of Optimum Drilling Process for Advanced Composites University of Missouri – Rolla	WL/MTI
22 Dr. George A. Petersson	Absolute Rates for Chemical Reactions Wesleyan University	WL/MLBT
23 Dr. Mohamed N. Rahaman	Process Modeling of the Densification of Granular Ceramics Interaction Between Densification and Creep University of Missouri – Rolla	WL/MLLN

1997 SREP Final Technical Report Table of Contents

Wright Laboratory (cont.)

Volume 4B

Principle Investigator	Report Title University/Institution	Laboratory & Directorate
24 Dr. Martin Schwartz	Quantum Mechanical Modeling of the Thermochemistry of Halogenated Fire Suppressants University of North Texas	WL/MLBT
25 Dr. Marek Skowronski	Investigation of Slip Boundaries in 4H-SiC Crystals Carnegie Melon University	WL/MLPO
26 Dr. Yong D. Song	Guidance & Control of Missile Sys Under Uncertain Flight Conditions North Carolina A&T State University	WL/MNAG
27 Dr. Raghavan Srinivasan	Models for Microstructural Evolution During Dynamic Recovery Wright State University	WL/MLIM
28 Dr. Scott K. Thomas	The Effects of Transient Acceleration Loadings on the Performance of a Copper-Ethanol Heat Pipe with Spiral Grooves Wright State University	WL/POOS
29 Dr. James P. Thomas	The Effect of Temperature on Fatigue Crack Growth of TI-6AL-4V in the Ripple University of Notre Dame	WL/MLLN
30 Dr. Karen A. Tomko	Scalable Parallel Solution of the 3D Navier-Stokes Equations Wright State University	WL/FIM
31 Dr. J. M. Wolff	Off Design Inviscid/Viscous Forced Response Prediction Model for High Cycle Wright State University	WL/POTF
32 Mr. Todd C. Hathaway	Experiments on Consolidation of Aluminum Powders Using Simple Shear University of North Texas	WL/MLLN
33 Ms. Diana M. Hayes	Error Correction & Compensation for Mueller Matrices Accounting for Imperfect Polarizers University of North Texas	WL/MNGA

1997 SREP Final Technical Report Table of Contents

Volume 5

Principle Investigator	Report Title University/Institution	Laboratory & Directorate
Arnold Engineering Development Center		
1 Dr. Frank G.Collins	Development of Laser Vapor Screen Flow Visualization Sys Tennessee University Space Institute	AEDC
United States Air Force Academy		
2 Mr. Derek E. Lang	Experimental Investigation of Liquid Crystal Applications for Boundary Layer Characterization University of Washington	USAFA/DFA
Air Logistics Centers		
3 Dr. Sandra A. Ashford	Development of Jet Engine Test Facility Vibration Signature & Diagnostic System University of Detroit Mercy	OCALC/TIE
4 Dr. Roger G. Ford	Use of Statistical Process Control in a Repair/Refurbish/ Remanufactureg Environment St. Mary's University	SAALC
Wilford Hall Medical Center		
5 Dr. Stedra L. Stillmana	Metabolite Profile Following the Administration of Fenproporex University of Alabama at Birmingham	WHMC

**ABSOLUTE RATES
for
CHEMICAL REACTIONS**

George A. Petersson
Professor of Chemistry
Chemistry Department

Wesleyan University
Middletown, CT 06459 - 0180

Final Report for:
Summer Faculty Research Extension Program
Wright Laboratory

Sponsored by:
Air Force Office of Scientific Research
Bolling Air Force Base, DC

and

Wright Laboratory

December 1997

ABSOLUTE RATES
for
CHEMICAL REACTIONS

George A. Petersson
Professor of Chemistry
Chemistry Department
Wesleyan University
Middletown, CT 06459 - 0180

Abstract

There are a number of problems in atmospheric chemistry and flame chemistry that are of considerable importance to the Air Force. A fundamental understanding of the absolute rates of the pertinent chemical reactions will provide the basis for improved solutions to these problems.

A new computational procedure for the characterization of transition states for chemical reactions has been developed. Previous calculations have frequently employed a single point high-level energy calculation at a transition state geometry obtained with a less expensive computational method, Energy[Method(1)]//Geom[Method(2)]. If we instead search the "inexpensive" intrinsic reaction coordinate (IRC) for the maximum of Energy[Method(1)] along this reaction path, the resulting "IRCMax method", Max{Energy[Method(1)]}/IRC{Geom[Method(2)]}, reduces errors in transition state geometries by a factor of four to five, and reduces errors in classical barrier heights by as much as a factor of ten. When applied to the CBS-4, G2(MP2), G2, CBS-Q, and CBS-QCI/APNO model chemistries, the IRCMax method reduces to the standard model for the reactants and products, and gives RMS errors in the classical barrier heights for ten atom exchange reactions of 1.3, 1.2, 1.0, 0.6, and 0.3 kcal/mol respectively.

The CBS barriers are incorporated into Eyring's absolute rate theory including tunneling through an Eckart potential barrier which includes variations in the zero-point vibrational energies. These calculations reproduce the experimental absolute rates (which vary over eight orders-of magnitude) for five hydrogen transfer reactions with barriers ranging from 1 to 20 kcal/mol at temperatures from 250 K to 2500 K to within 20% RMS relative error.

These methods can now be used to obtain rate constants for important reactions of halon replacements at combustion temperatures. It is now possible to experiment with many known and potential agents in many fire scenarios without ever lighting a match or otherwise starting a fire. This is the first step in the construction of a virtual fire laboratory where the computer takes the place of hardware, fuels and suppressants to make possible safe, fast, and effective evaluations of fire suppressants.

ABSOLUTE RATES
for
CHEMICAL REACTIONS

George A. Petersson

Introduction

There are a number of problems in atmospheric chemistry and flame chemistry that are of considerable importance to the Air Force. A fundamental understanding of the absolute rates of the pertinent chemical reactions will provide the basis for improved solutions to these problems.

Halon 1301, trifluoromethyl bromide, has been used as a fire suppressant for everything from computer labs to F-16s for forty years. It is an effective, clean, nontoxic agent that has one major flaw; it is harmful to the earth's protective ozone layer. Because halon was such an ideal agent, research in fire suppression agents had a low priority in Air Force labs and elsewhere until the ozone connection was established. The manufacture of halon has now ceased, and the Air Force is operating on "banked" halon until it runs out, its use is curtailed, or until a satisfactory replacement is found. The last option is preferred, and it is for this reason that the Air Force has major programs to find a replacement.

The Center for Computational Modeling of Nonstructural Materials employs considerable DoD MSRC resources to learn exactly how halon and potential replacement agents work. This program seeks to describe in precise terms all of the important chemical reactions of agents in a flame. Achieving this goal has required the development of improved theoretical methods.

Rate constants describe how fast individual chemical reactions occur, absolutely and in comparison to other reactions. The relative magnitudes permit one to decide which reactions are sufficiently important to include in the overall description of a combustion/suppression mechanism. Because many reactions occur simultaneously, and many more sequentially, it is often impossible to obtain unambiguous individual rate constants in an experiment. This is particularly true at the elevated temperatures typical of combustion reactions. For the relevant reactions which have reliable experimental rate constants, it was found that computationally derived rate constants gave disappointing results. Thus, it was found to be necessary to explore new computational approaches. This required fundamental studies of the theory of chemical reaction kinetics.

The energy of the transition state is of primary importance, and we have developed a new computational method to improve the accuracy of these calculated energies. Also of great importance is the quantum mechanical tunneling, which depends on the width of the potential barrier. This barrier width controls the rates at low temperatures where comparisons with experiment are more easily made. We find that if variations in the zero-point vibrational energy along the reaction path are taken into account, the new kinetics program we have written quantitatively accounts for tunneling effects. By working with simple reactions, we demonstrate that our new methods give excellent agreement with experimental results for a wide range of temperatures and reaction rates.

The problem of predicting absolute rates for gas phase chemical reactions has been solved. However, much remains to be done. We must now systematically determine the minimum level of calculation necessary to maintain the accuracy of each part of these calculations. It is only through such a systematic study that we will be able to extend this very high accuracy to the much larger species (e.g. C₃F₇H) required for solution of the halon replacement problem. Nevertheless, the use of the IRCMax method with the G2 and CBS-Q computational models is giving immediate improvements in our ability to model flame chemistry.

These methods are already being used to obtain rate constants for important reactions of proposed halon replacements at combustion temperatures. It will soon be possible to experiment with many known and potential agents in many fire scenarios without ever lighting a match or otherwise starting a fire. This is the first step in the construction of a virtual fire laboratory where the computer takes the place of hardware, fuels and suppressants to make possible safe, fast, and effective evaluations of fire suppressants.

Background

The absolute rates of chemical reactions present a formidable challenge to theoretical predictions. An elementary bimolecular chemical reaction:



proceeds at a rate that is proportional to the concentrations of the reactants and the specific rate constant, $k_{rate}(T)$:

$$\frac{dP_1}{dt} = \frac{dP_2}{dt} = -\frac{dR_1}{dt} = -\frac{dR_2}{dt} = k_{rate}(T) R_1 R_2 \quad (2)$$

It is now over one hundred years since Arrhenius published the seminal article¹ on the variation of the rate constant with absolute temperature:

$$k_{rate}(T) = A e^{-\Delta E^\ddagger / RT} \quad (3)$$

The principal difficulty for theoretical predictions lies in the extreme sensitivity of $k_{rate}(T)$ to small errors in the activation energy, ΔE^\ddagger , which can be interpreted as the difference in energy between the “transition state” and the reactants. An error of only 1.4 kcal/mol in ΔE^\ddagger leads to an error of an order-of-magnitude in $k_{rate}(T)$ at room temperature.

More than sixty years ago, Eyring proposed² the use of statistical mechanics to evaluate the preexponential factor, A , in Eq.(3) using partition functions, Q , and the “collision velocity”, $k_B T/h$:

$$A(T) = \frac{Q^\ddagger(T)}{Q_{R_1}(T) Q_{R_2}(T)} \cdot \frac{k_B T}{h} \quad (4)$$

thereby accounting for the small temperature variations in A . The evaluation of the translational, vibrational, and rotational partition functions:

$$Q_{\text{translation}} = V (2\pi Mk_B T)^{3/2} / h^3 \quad (5)$$

$$Q_{\text{rotation}} = 2\pi (4\pi/\sigma) \prod_j (2\pi I_j k_B T)^{1/2} / h \quad (6)$$

$$Q_{\text{vibration}} = \prod_j (1 - e^{-h\nu_j/k_B T})^{-1} \quad (7)$$

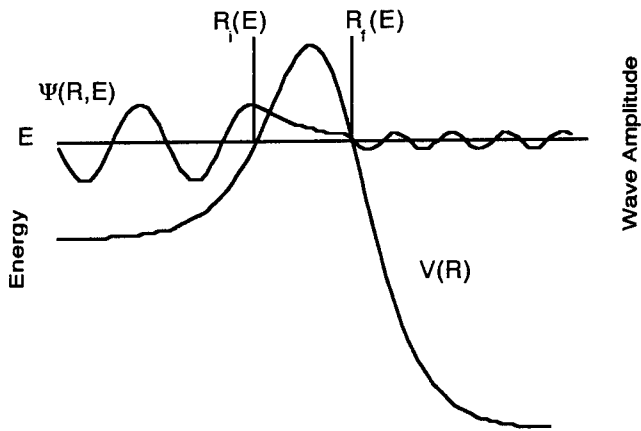
$$Q_{\text{electronic}} = \sum_j e^{-\Delta E_j/k_B T} \quad (8)$$

$$Q_{\text{total}} = Q_{\text{electronic}} Q_{\text{vibration}} Q_{\text{rotation}} Q_{\text{translation}} \quad (9)$$

requires only a knowledge of the mass (for $Q_{\text{translation}}$), geometry (for the moments of inertia, I_j , in Q_{rotation}), vibrational frequencies (ν_j for $Q_{\text{vibration}}$), and ΔE of any low-lying electronic states for the reactants and transition state ($Q_{\text{electronic}}$).

The electronic, vibrational, and rotational energy levels can often be determined from experiment for the reactants, but not for the transition state. The use of *ab initio* quantum mechanical methods to evaluate the required electronic, vibrational, and rotational energy levels is the subject of this proposal. We shall first be concerned with establishing the validity of transition state theory for quantitative absolute rate predictions if we use state of the art computational quantum methods. We shall then address the question of cost-effective compromises necessary for a widely applicable method.

Eyring presumed that motion along the path from reactants to products could be treated classically. However, if the reduced mass for this motion is finite, the quantum mechanical wave packet can tunnel through the barrier, $V(R)$, rather than climb over the top:



The probability of reactants with energy, E, tunneling through such a barrier is determined by the initial and final wave amplitudes:

$$K(E) = \left| \frac{\psi[R_f(E), E]}{\psi[R_i(E), E]} \right|^2 \quad (10)$$

Eckart introduced³ a simple mathematical form for the potential energy function, V(R):

$$V(R) = \frac{\Delta E_{reaction}}{e^{2\pi R/L} + 1} + \frac{\left(\sqrt{\Delta E_{forward}^+} + \sqrt{\Delta E_{reverse}^+} \right)^2}{e^{2\pi R/L} + 2 + e^{-2\pi R/L}} \quad (11)$$

for which he determined the exact transmission probability, $\kappa(E)$. This transmission probability must then be weighted by the Boltzmann distribution function. The final expression for the rate constant is therefore:

$$k_{rate}(T) = \frac{Q^\ddagger(T)}{Q_{R_1}(T)Q_{R_2}(T)} \cdot \frac{k_B T}{h} \int_0^\infty K(E) e^{-E/k_B T} dE \quad (12)$$

Truhlar and Kuppermann introduced⁴ the correct definition of the reaction path, R, in mass weighted coordinates, and were the first to recognize the importance of including in V(R), the quantum mechanical zero-point vibrational energy for all normal modes that are orthogonal to R. The challenge we face is to accurately determine all the quantities required to evaluate Eq.(12).

The geometry and energy of a stable molecule can often be measured experimentally to greater accuracy than is currently available computationally. However, transition states cannot generally be isolated for experimental study, and thus are obvious targets for computational studies. The development of analytical gradient and curvature methods⁵⁻¹¹ has made possible the rigorous determination of transition states within a given level of correlation energy and basis set (*e.g.* MP2/6-31G*).¹²

The geometries of stable molecules are relatively easy to predict.¹² Small basis set (*e.g.* 3-21G*) self-consistent field (SCF) calculations^{13,14} are generally sufficient to obtain bond lengths to within $\pm 0.03 \text{ \AA}$ and bond angles to within $\pm 3^\circ$. However, the prediction of molecular energies to chemical accuracy (*i.e.* $\pm 2 \text{ kcal/mol}$) requires large basis sets and near full configuration interaction (FCI) levels of correlation energy. The wide gap between the requirements for geometries and energies has spawned a variety of compound models ranging from the simple MP2/6-31G*/UHF/3-21G model to the G2 and CBS series of models.¹⁵⁻²² The compound model notation indicates that the second-order Møller-Plesset (MP2) energy²³ is evaluated with the 6-31G* basis set^{24,25} at the geometry obtained from unrestricted Hartree-Fock (UHF) calculations^{13,14} with the 3-21G basis set.^{26,27} The G2 and CBS models take the variable basis set approach a step farther, using large basis sets for the SCF energy, medium basis sets for the MP2 energy, and relatively small basis sets for the higher-order correlation energy.²¹ This compound model single point energy is evaluated at a geometry determined at a lower level of theory (*e.g.* CBS-4/UHF/3-21G or G2//MP2/6-31G*).

The optimal use of these compound methods for studies of transition states was the subject of the study I completed last Summer at the Center for Computational Modeling of Nonstructural Materials, Materials Directorate, Wright-Patterson AFB under the 1996 AFOSR Summer Faculty Research Program. I shall first review the results and conclusions from this study, and then describe the work that remains to be done to complete the development of optimized methods for the efficient prediction of absolute chemical reaction rates. The new studies will focus on the vibrational energy levels, not only at the transition state, but also along the reaction path before and after the actual transition state.

The IRCMax Method

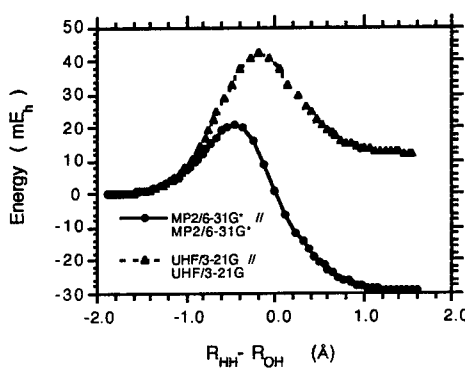
The potential energy surface (PES) for a typical bimolecular chemical reaction such as :



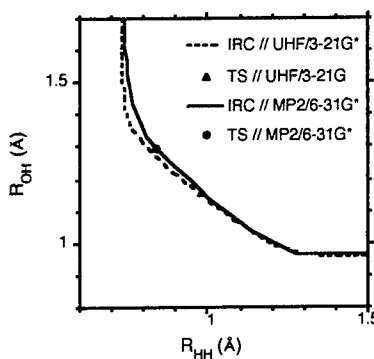
includes valleys (leading to the reactants and products) connected at the transition state (TS), which is a first-order saddle point (*i.e.* a stationary point with exactly one negative force constant). The reaction path or intrinsic reaction coordinate (IRC) is defined²⁸ as the path beginning in the direction of negative curvature away from the TS and following the gradient of the PES to the reactants and products.

If we move in a direction perpendicular to the reaction path, we find a potential energy curve (or surface) corresponding to a stable reactant or product molecule if we are far from the TS. Even around the TS, the variation of the PES perpendicular to the IRC is very similar to the PES for a stable molecule. Transition States differ from stable molecules in that they possess one negative force constant which defines the reaction coordinate. Calculated energies along the coordinates with positive force constants behave very much like their counterparts in stable molecules. However, the energy changes along the reaction coordinate are much more difficult to predict. It is the variation of the energy along this coordinate that is very sensitive to (and thus requires the inclusion of) the correlation energy.

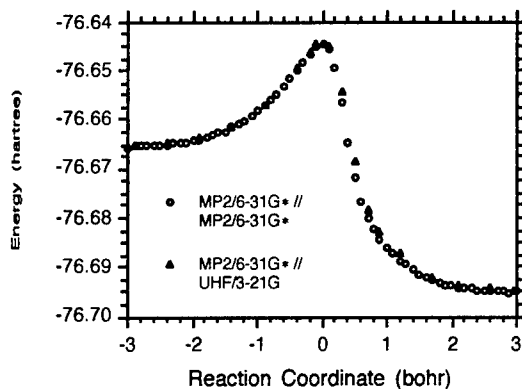
UHF calculations give notoriously bad results for transition states. For example, the UHF/3-21G energy profile for the transfer of a hydrogen atom from H₂ to OH is endothermic rather than exothermic and consequently places the transition state too close to the products:



One might erroneously conclude that such calculations provide no useful information about the reaction path. Fortunately, this is not the case. Although the variation of the energy along the reaction path is very poorly described by the UHF/3-21G method, the variation of the energy perpendicular to the reaction path is very nicely described by the UHF/3-21G method, just as in stable molecules. The UHF/3-21G reaction path very closely approximates the MP2/6-31G* reaction path:



However, the energy variation along this path, and hence the position of the UHF/3-21G transition state, is incorrect. Nevertheless, the UHF/3-21G reaction path passes through (or near) the MP2/6-31G* transition state. Hence, if we calculate the MP2/6-31G* energy along the UHF/3-21G reaction path, we obtain an energy profile that differs trivially from the MP2/6-31G* energy profile along the MP2/6-31G* reaction path:



This is rather remarkable for the H₂ + OH reaction, given the very poor UHF/3-21G//UHF/3-21G energy profile.

Based on these observations, we proposed the “*IRCMax*” transition state method, in which we select the maximum of the high-level Energy[Method(1)] along the low-level IRC obtained from the Geom[Method(2)] calculations.

The *IRCMax* transition state extension of the compound models takes advantage of the enormous improvement in computational speed achieved by using low-level, Geom[Method(2)], IRC calculations. We then perform several single point higher level, Energy[Method(1)], calculations along the Geom[Method(2)] reaction path to locate the Energy[Method(1)] transition state, that is, the maximum of Energy[Method(1)] along the Geom[Method(2)] IRC. Calculations at three points bracketing the transition state are sufficient to permit a parabolic fit to determine the transition state geometry and the activation energy.

Since we determine the maximum of Energy[Method(1)] along a path from reactants to products, the *IRCMax* method gives a rigorous upper bound to the high-level Method(1) transition state energy. In addition, when applied to the compound CBS and G2 models, the *IRCMax* method reduces to the normal treatment of bimolecular reactants and products, Energy[Method(1)]//Geom[Method(2)]. Thus the *IRCMax* method can be viewed as an extension of these compound models to transition states. The results below demonstrate the numerical superiority of this *IRCMax* method, Max{Energy[Method(1)]} // IRC{Geom[Method(2)]}, over conventional Energy[Method(1)]//Geom[Method(2)] calculations.

Computational Methods

The CBS-4, G2(MP2), G2, CBS-Q, and CBS-QCI/APNO model chemistries have been described in detail elsewhere.¹⁶⁻²¹ Here we shall simply note the RMS errors (2.47, 1.98, 1.54, 1.26, and 0.68 kcal/mol respectively)

for the 125 chemical energy differences (*i.e.* D₀'s, IP's, and EA's) of the "G2 test set" to provide a comparison for the activation energies reported in this proposal.

For the purposes of this proposal only, the notation for the compound single point energy models (CBS-4, G2, etc.) will refer to their use of varying basis sets for the different orders of perturbation theory, but will not include the geometry optimization methods normally contained in the definition of these methods. Thus the standard CBS-4 and G2 models will be denoted CBS-4//UHF/3-21G* and G2//MP2/6-31G* respectively. The notation, CBS-4, by itself will imply numerical optimization of the geometry with the single point energy method.

Numerical optimization of the geometry of stable molecules and transition state coordinates perpendicular to the reaction path employed parabolic fits on a 0.01 Å grid for bond lengths and 2° for bond angles. Reaction path following with a stepsize of 0.1 bohr (0.0529 Å) was used to determine the IRC's. Parabolic fits to the three highest points determined the position of transition states along the IRC. All calculations employed a modified version of the computer program, Gaussian94.²²

Results

The calibration of the accuracy of our calculated transition state geometries and activation energies makes the reasonable assumption that the CBS-QCI/APNO results are the most accurate of the models considered. The initial justification for this assumption rests on comparison with experiment for stable molecules, and comparison with Diedrich and Anderson's accurate numerical results²⁹ for the H₃ transition state (the CBS-QCI/APNO error for the H₃ activation energy is only 0.15 kcal/mol). However, the ultimate vindication comes from the final agreement of our kinetic models with experimental absolute reaction rates.

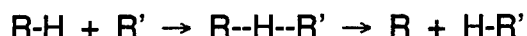
Transition State Geometry

The determination of molecular geometries is the first step in any computational study of molecular properties. Spectroscopic studies of diatomic molecules provide a convenient database³⁰⁻³² of molecular geometries known to within ±0.0001 Å, and thus can be used to calibrate the accuracy of our computational methods. We have used the diatomic species H₂, CH, NH, OH, FH, CN, and N₂, and the polyatomic species H₂O, HCN, CH₃, and CH₄ for this geometry calibration. The RMS errors in the UHF/3-21G, MP2/6-31G*, and MP2/6-31G† geometries are ±0.012, 0.016, and 0.015 Å respectively. The CBS-4 method is comparable in accuracy (±0.0048 Å) to (but much faster than) the QCISD/6-311G** method (±0.0052 Å). The G2(MP2), G2, and CBS-Q methods are very close in accuracy (±0.0036, 0.0038, and 0.0031 Å respectively). The compound methods (*i.e.* CBS-4, G2(MP2), G2, CBS-Q, and CBS-QCI/APNO) are clearly superior to the simple methods. In fact, the CBS-QCI/APNO method is sufficiently accurate (±0.0013 Å) to be used to calibrate the accuracy of any of the other computational methods.

The calculated geometries of the transition states for six degenerate atom exchange reactions:



where $A = H, F, CN, OH$, and CH_3 , and $B = H$ and F (with $A = H$) provide an indirect test of the IRCMax concept. Since the position of the transition state along the IRC is determined by symmetry, the accuracy of the calculated geometries depends only on the behavior of the calculated potential energy surface perpendicular to the IRC. Thus, the accuracy of these calculated transition state geometries should be comparable to the accuracy of calculated geometries for stable molecules. In fact, the RMS errors for each of the models ($\pm 0.035 \text{ \AA}$ for UHF/3-21G, $\pm 0.012 \text{ \AA}$ for MP2/6-31G*, $\pm 0.013 \text{ \AA}$ for MP2/6-31G † , $\pm 0.007 \text{ \AA}$ for QCISD/6-311G**, $\pm 0.009 \text{ \AA}$ for CBS-4, $\pm 0.0023 \text{ \AA}$ for G2(MP2), $\pm 0.0033 \text{ \AA}$ for G2, and ± 0.0032 for CBS-Q) is not too much larger than the corresponding error for stable molecules. We conclude that the behavior of these surfaces perpendicular to the IRC's is similar to that of stable molecules, but with somewhat smaller force constants accounting for the modest reduction in the accuracy of calculated geometries. The accuracy of calculated transition state energies should be unaffected, since the reduced force constants make the accuracy of the transition state geometry less critical. The calculated geometries of the transition states for four exothermic hydrogen abstraction reactions:



with $R = H$ and $R' = F, OH$, or CN , and $R = CH_3$ with $R' = OH$ provide a direct test of the IRCMax method. We first compare the UHF/3-21G and Max{MP2/6-31G*}//IRC{UHF/3-21G} optimized transition state geometries with the fully optimized MP2/6-31G* geometries, which are the presumed goal of these IRCMax calculations. The relative RMS errors indicate that the IRCMax method reduces geometry errors by a factor of five compared to the UHF/3-21G geometries. The residual relative RMS error ($\pm 0.027 \text{ \AA}$) is similar to the error in UHF/3-21G geometries for the symmetric transition states for degenerate reactions (± 0.035).

We next compare the MP2/6-31G* and Max{QCISD/6-311G**}//IRC{MP2/6-31G*} optimized transition state geometries with the fully optimized QCISD/6-311G** geometries, which are the goal for these IRCMax calculations. The relative RMS errors indicate that this time the IRCMax method reduces geometry errors by a factor of four compared to the MP2/6-31G* geometries. The residual relative RMS error here ($\pm 0.013 \text{ \AA}$) is similar to the error in MP2/6-31G* geometries for the symmetric transition states for degenerate reactions ($\pm 0.012 \text{ \AA}$).

Our third test compares the QCISD/6-311G** and Max{CBS-QCI/APNO}//IRC {QCISD/6-311G**} optimized transition state geometries with the fully optimized CBS-QCI/APNO geometries, which are the goal for these IRCMax calculations. The relative RMS errors indicate that this time the IRCMax method reduces geometry errors by a factor of five compared to the QCISD/6-311G** geometries. The residual relative RMS error here ($\pm 0.016 \text{ \AA}$) is more than twice as large as the error in QCISD/6-311G** geometries for the symmetric transition states for degenerate reactions ($\pm 0.007 \text{ \AA}$). These strongly exothermic reactions have “early” transition states in which the reactants are still quite far apart and only weakly interacting. This makes the transition states less well defined and difficult to locate to better than 0.01 \AA . Nevertheless, all three tests of the IRCMax method give

substantial improvement over the low level saddle points and demonstrate that the major error in calculated transition state geometries is the location along the IRC as we anticipated.

Activation Energy

The enthalpies of reaction, ΔH_{298}^0 , for the four exothermic reactions are known from experiment^{30,33} and thus can be used to calibrate the reliability of each of the computational methods for the energy changes along these reaction paths. The RMS errors are: UHF/3-21G* = 25.4, MP2/6-31G* = 16.3, QCISD/6-311G** = 5.3, CBS-4 = 1.41, G2(MP2) = 1.05, G2 = 1.20, CBS-Q = 0.79, and CBS-QCI/APNO = 0.70 kcal/mol. Given the small size of the current sample set, the agreement with the larger calibration studies^{18,21} is good.

Since the location of the transition state along the reaction path is completely determined by symmetry for the six degenerate reactions, the standard Energy[Method(1)]//Geom[Method(2)] procedure is equivalent to the IRCMax method for these cases. They thus provide a benchmark for the accuracy attainable when the location of the transition state is not in question. In comparison sets of three calculations each, we first calculate the classical barrier height using the simple geometry method, then the higher-level single point energy evaluated at the transition state geometry obtained from the simple geometry method, and finally the energy of the higher-level method evaluated at the transition state geometry obtained from the higher-level method. The relative RMS error is evaluated with respect to the higher-level/higher-level calculation, and the absolute RMS error is evaluated with respect to our best estimate of ΔE_e^\ddagger , the CBS-QCI/APNO model.

The calculated classical barrier heights for the four nondegenerate hydrogen abstraction reactions given in three sets of four calculations each provide a direct test of the IRCMax method. In each set of four calculations, the first row is the calculated classical barrier height using the simple geometry method, the second calculation is the more elaborate single point energy evaluated at the transition state geometry obtained from the simple geometry method, the third calculation is the maximum energy of the more elaborate method evaluated along the IRC obtained from the simple geometry method, and the fourth calculation is the energy of the more elaborate method evaluated at the transition state geometry obtained from the more elaborate method. The fourth calculation is used as the reference to evaluate the relative errors for the first three calculations.

Method/Basis St	RMS Error (kcal/mol)			
	6 Degenerate		4 Nondegenerate	
	Relative	Absolute	Relative	Absolute
UHF/3-21G*	6.37	9.49	13.19	20.87
MP2/6-31G* // UHF/3-21G*	3.38	9.75	6.48	3.70
Max{MP2/6-31G*} // IRC{UHF/3-21G*}			0.59	7.57
MP2/6-31G*	-	7.12	-	7.12
MP2/6-31G*	4.23	7.12	2.93	7.12
QCISD/6-311G**// MP2/6-31G*	1.63	5.13	0.40	4.72
Max{QCISD/6-311G**} // IRC{MP2/6-31G*}			0.14	4.88
QCISD/6-311G**	-	4.07	-	4.79
QCISD/6-311G**	3.93	4.07	4.64	4.64
CBS-QCI/APNO // QCISD/6-311G**	0.09	0.19	0.49	0.49
Max{CBS-QCI/APNO} // IRC{QCISD/6-311G**}			0.24	0.24
CBS-QCI/APNO	-	-	-	-

The first set of four calculations illustrates the behavior of the IRCMax method very clearly. This set compares the UHF/3-21G* method with the MP2/6-31G* energies calculated at UHF/3-21G* and MP2/6-31G* geometries. The UHF barrier heights are all much too high. This is an extreme example of the tendency of calculated barrier heights to converge to the exact value from above. The MP2//UHF barrier heights are all lower than the MP2//MP2 values. The UHF transition state geometry is at the wrong position along the reaction path and thus gives a value for the MP2//UHF transition state energy that is too low. The extreme case is the H-H-F barrier for which the MP2//UHF value is *negative*. In less extreme cases, this negative error can cancell the positive error (from the use of limited correlation/basis sets) to reduce the absolute RMS error . However, the results are erratic with no clear convergence pattern as the basis set and level of correlation treatment are improved. The IRCMax method gives an upper bound to the MP2 energy of the transition state, but the error from use of the UHF geometry for the reactants can exceed the IRCMax error for the MP2 transition state energy (as for H-H-CN) giving an IRCMax barrier that is below the MP2//MP2 barrier. Nevertheless, the difference between the IRCMax barriers and the MP2//MP2 barriers is minor, and we retain the inherent convergence pattern of calculated barrier heights. The Max{MP2/6-31G*} // IRC{UHF/3-21G*} procedure reduces the relative RMS error by a factor-of-ten (from 6.48 to 0.59 kcal/mol).

The calculated classical barrier heights of all ten test reactions are summarized in the table below for the simple UHF, MP2, and QCI methods and for the five recommended IRCMax methods. The eight sets of calculations are arranged in order of decreasing RMS errors. For each reaction, the sequence of improving calculations tends to

converge to the exact classical barrier height from above. The CBS-QCI/APNO barrier height for the H₂ + H reaction has converged to within 0.15 kcal/mol of the exact barrier obtained by numerical solution of the Schrödinger equation.²⁹ Having verified the accuracy of the CBS-QCI/APNO method in the one case for which the exact barrier height is known, we then use the CBS-QCI/APNO// CBS-QCI/APNO values for the nine remaining reactions to determine the errors in the less computationally demanding methods.

A graph of the barrier heights calculated with the less demanding methods vs the CBS-QCI/APNO barrier heights demonstrates the systematic tendency to overestimate barrier heights. Linear least-squares fits give straight lines with unit slope and nonzero intercept for all but the simple UHF/3-21G* calculations. Each of these computational methods consistently overestimates all ten barrier heights by about the same error. This suggests a simple empirical correction to the calculated classical barrier heights.

Recall that these compound model chemistries already include two empirical parameters, a one-electron correction and a two-electron correction.¹⁶⁻²¹ In the case of the G2 methods, the one-electron correction [Const₁(n_α + n_β)] was selected to give the exact energy for the hydrogen atom.¹⁶ The two-electron correction [Const₂(n_β=n_{pairs})] was selected to give the exact energy for the hydrogen molecule.¹⁶ We therefore propose a third empirical correction selected to give the exact energy for the H₃ transition state [Const₃(n_{k<0})]. The calculated classical barrier heights including this empirical correction are given in the table.

Table V. Calculated classical barrier heights, DEe‡ (kcal/mol), including empirical corrections.

Method/Basis Sct	H ₂ +F	H ₂ +CN	H ₂ +OH	CH ₄ +OH	H ₂ O +OH	H ₂ +H	HF +F	CH ₄ +CH ₃	HCN +CN	HF +H	Ave Error	RMS Error
UHF/3-21G*	19.11	-0.14	18.18	21.88	12.64	9.61	21.75	19.81	16.09	37.16	5.08	9.40
MP2/6-31G*	1.97	-3.59	5.21	6.40	4.08	9.61	12.45	14.47	21.24	42.93	-1.06	3.07
QCISD/6-311G**	4.82	5.10	8.06	9.39	9.51	9.61	19.67	18.18	19.46	45.91	2.44	2.80
IRCMax												
CBS-4 a	3.47	4.18	6.36	6.09	7.01	9.61	18.48	15.39	18.05	43.33	0.66	1.34
G2(MP2)	2.51	3.44	6.02	6.57	9.11	9.61	17.93	17.22	18.89	42.92	0.89	1.18
G2	2.30	3.31	5.96	6.53	8.87	9.61	17.45	17.17	18.80	42.75	0.74	1.02
CBS-Q b	1.97	3.86	5.57	5.77	8.27	9.61	16.98	16.79	18.38	41.79	0.37	0.62
CBS-QCI/APNO	2.04	3.95	4.95	5.45	7.59	9.61	15.75	16.50	18.26	42.14	0.10	0.17
CBS-QCI/APNO	-0.15	1.70	3.96	4.87	5.11	7.51	9.61	15.58	16.60	18.28	42.17	-

a. The CBS-4 barriers were increased by 3.63 kcal/mol for each CN group.

b. The CBS-Q barriers were increased by 0.43 kcal/mol for each CN group.

All nine methods now give the exact barrier height for H₃. The average errors are now generally small compared to the RMS errors, demonstrating that the dominant systematic errors have been removed. The correction based on H₃ gives a general improvement for all these atom exchange reactions. An additional empirical correction for the spin

contaminated cyano group significantly improved the CBS-4 and CBS-Q barriers. This suggests that a general bond additivity correction (BAC)^{34,35} might also be useful for calculations of activation energies.

Based on our experience²¹ that the CBS-Q errors are half as large as the CBS-4 errors and the CBS-QCI/APNO errors are half as large as the CBS-Q errors, we estimate the uncertainty in the CBS-QCI/APNO barrier heights to be ± 0.3 kcal/mol. This is consistent with the CBS-QCI/APNO overestimation of the H₃ barrier height by 0.15 kcal/mol before the empirical correction was applied. If we use the nonlinear CBS-QCI/APNO optimized geometry for the H₂ + F transition state, our empirically corrected CBS-QCI/APNO barrier height (1.70 ± 0.3 kcal/mol) for this highly exothermic reaction is in agreement with the best CCSD(T) (1.7 ± 0.2 kcal/mol)³⁶ and MRCI calculations (1.53 ± 0.15 kcal/mol).³⁷

All five compound models give chemically accurate barrier heights (*i.e.* RMS error < 2 kcal/mol). The RMS errors are consistently about half as large as those for the same models applied to dissociation energies, ionization potentials, and electron affinities.²¹

Vibrational Frequencies

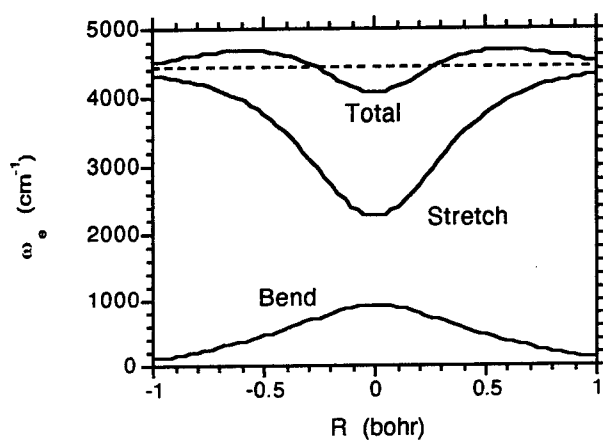
Vibrational energy levels include harmonic components linear in the quantum number, n, and anharmonic corrections:

$$E_n = (n + \frac{1}{2})\hbar\omega_e - (n + \frac{1}{2})^2 \hbar\omega_e X_e + \dots \quad (13)$$

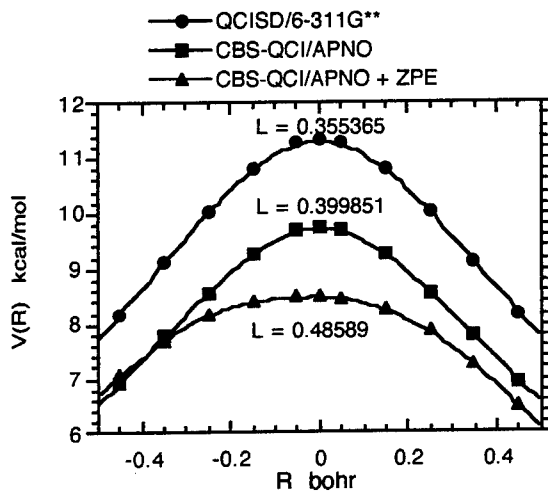
The harmonic term generally dominates the low-lying levels, especially for the stiff normal modes that dominate zero-point energies. For example, the values of ω_e and $\omega_e X_e$ for H₂ are 4401.23 cm⁻¹ and 121.34 cm⁻¹ respectively.³⁰ We therefore employ the harmonic approximation for all calculated frequencies and zero-point energies. The convergence of the harmonic frequencies obtained with the computational methods used for the IRC calculations is illustrated by the results for H₂ and the H₂+H transition state:

Method/Basis Set	H ₂		H ₃		Rxn Path
	Stretch		Stretch	Bend(2)	
UHF/3-21G	4657.1		2054.8	1121.4	2292.2 <i>i</i>
MP2/6-31G*	4533.6		2087.8	1164.6	2325.5 <i>i</i>
QCI/6-311G**	4420.1		2054.2	958.2	1589.1 <i>i</i>
QCI/6-311G(2df,2pd)	4404.1		2051.3	917.1	1530.9 <i>i</i>
Experiment	4401.23				

Note that polarization functions on the central hydrogen of the H-H-H transition state are necessary to obtain an accurate bending frequency. Without them, we would overestimate the ZPE of the transition state by 0.71 kcal/mol. To minimize such errors, we shall employ QCI/6-311G(2df,2pd) frequencies for our initial study of absolute reaction rates. The change in the total ZPE at the H₃ transition state decreases the barrier height, ΔE^\ddagger in Eq.(11), by 0.74 kcal/mol, and thus accelerates the reaction by more than a factor-of-three at room temperature. The variation of the H₃ stretch and bend as we move along the reaction path increases V(R) at R = ±0.5 bohr to either side of the maximum:



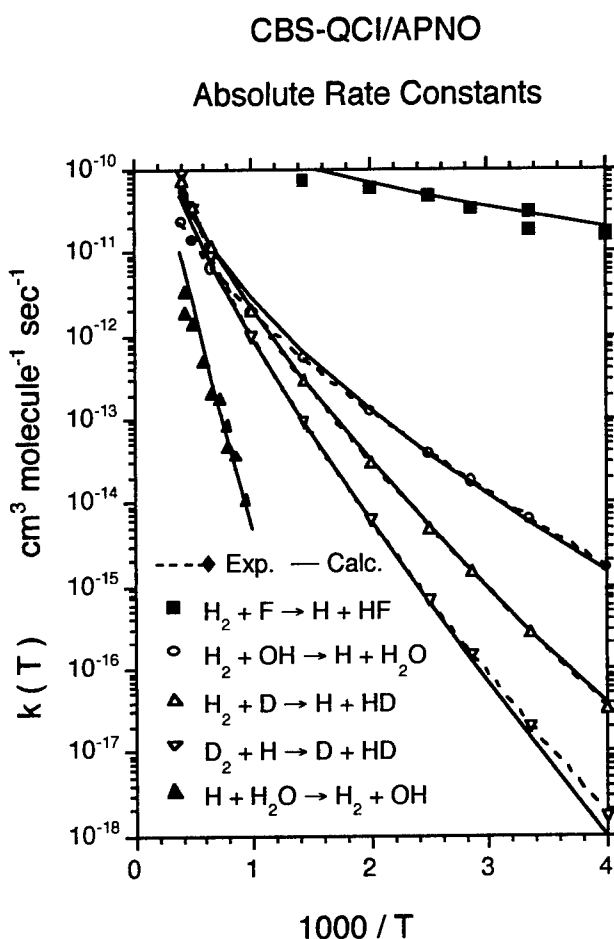
and thus broadens the Eckart barrier, Eq.(11), as illustrated for H₂ + D → H + HD:



This increase in the Eckart width parameter, L in Eq.(11), reduces the tunneling through the barrier and hence the calculated reaction rate by a factor-of-ten at low temperatures.

Absolute Reaction Rates

We are finally ready to evaluate all of the terms in Eq(12). We have selected six hydrogen abstraction reactions for the initial test of our methodology. The barrier heights for these reactions range from 1 kcal/mol ($\text{H}_2 + \text{F}$) to 20 kcal/mol ($\text{H}_2\text{O} + \text{H}$). We include temperatures from 250 K to 2500 K. The rate constants range from 10^{-18} up to $10^{-10} \text{ cm}^3 / \text{molecule sec}$. All absolute rate constants obtained from our CBS-QCI/APNO model are within the uncertainty of the experiments.³⁸



The dashed curves and open symbols for $\text{H}_2 + \text{OH}$, $\text{H}_2 + \text{D}$, and $\text{D}_2 + \text{H}$ represent the least-squares fits of smooth curves to large experimental data sets in an attempt to reduce the noise level in the experimental data.³⁸ The close agreement with theory suggests that this attempt was successful.

The problem of predicting absolute rates for gas phase chemical reactions has in principle been solved. We have made contact with experiment, demonstrating that a sufficiently accurate evaluation of Eq.(12) provides absolute rate constants within the uncertainty of experimental rates. The use of the IRCMax method with the G2 and CBS-Q

computational models is giving immediate improvements in our ability to model flame chemistry. However, much remains to be done. We must now systematically determine the minimum level of calculation necessary to maintain the accuracy achieved above for each part of these calculations. It is only through such a systematic study that we will be able to extend this very high accuracy to the much larger species (e.g. C_3F_7H) required for solution of the halon replacement problem.

We can partition the evaluation of Eq.(12) into several steps:

1. Find the transition state at a low-level of theory.
2. Determine a portion of the IRC at this low-level.

Determine the harmonic ZPE, $\Delta E_{ZPE}(\mathbf{R})$, at this low-level along this path.

3. Determine the high-level electronic energy, $E_e(\mathbf{R})$, along a portion of the low-level IRC. The maximum gives the IRCMax geometry, \mathbf{R}_e^\ddagger , and energy, E_e^\ddagger .
4. Add $\Delta E_{ZPE}(\mathbf{R})$ to $E_e(\mathbf{R})$ giving $E_o(\mathbf{R})$ along the path. The maximum of $E_o(\mathbf{R})$ gives the variational transition state (VTST) IRCMax geometry, \mathbf{R}_o^\ddagger , and energy, E_o^\ddagger .
5. The harmonic frequencies at this geometry, $\{\omega_o\}$, are used to evaluate the vibrational partition functions.
6. The rotational partition functions are evaluated at \mathbf{R}_o^\ddagger .
7. An Eckart function, $V_o(\mathbf{R})$ in Eq.(11), is least-squares fit to the potential function, $E_o(\mathbf{R})$. This is Eckart function is then used to evaluate the transmission probability, $\kappa(E)$, in Eq.(10).

Each of these steps must be converged to the desired accuracy (± 1.2 kcal/mol for CBS-4, ± 0.6 kcal/mol for CBS-Q, and ± 0.3 kcal/mol for CBS-QCI/APNO) with respect to both the one-electron expansion and the many-electron expansion. In addition, we must check for convergence with respect to the anharmonic expansion of the vibrational energy levels in Eq.(13), and complications such as centrifugal distortion.

Since we have a program capable of reproducing experimental rates, we can confidently use this code to evaluate effects such as anharmonicity and centrifugal distortion on the partition functions and thus on the absolute reaction rates. Examination of these effects is very important. They will be most significant at high temperatures when the higher vibrational and rotational energy levels become occupied. This is precisely the regime where experimental data is most difficult to come by. It is therefore imperative that we are careful to ensure the validity of our high temperature calculated rate constants. Inaccuracies at low temperatures (e.g. if we employ CBS-4 for a large molecule) can be empirically corrected with a single experimental rate measurement at room temperature, but we will then need the correct high temperature behavior from our calculations to usefully model flame chemistry.

The electronic energy of the transition state is of primary importance and has thus been the focus of our work to date. The IRCMax method in combination with our complete basis set (CBS) extrapolations¹⁹⁻²² provides a hierarchy of models achieving chemically useful accuracy for the calculated barrier heights (± 1.2 kcal/mol for CBS-

must be calculated to still higher accuracy (± 0.6 kcal/mol for CBS-4, ± 0.3 kcal/mol for CBS-Q, and ± 0.15 kcal/mol for CBS-QCI/APNO) so that we do not compromise these hard won gains.

The tunneling calculations presented in Section V did not include “bob sled” or “corner cutting” effects.^{39,40} The close agreement with experiment must therefore be a result of a cancellation of this omission internally or with some other error. If we are to have confidence in our final method, it is imperative that we identify the source of this effect, and adjust our methodology according to our findings.

The data in the table on page 15 suggest that vibrational frequencies in transition states are more sensitive to the basis set used than are vibrational frequencies in stable molecules. The minimum size basis set and order of perturbation theory must therefore be reevaluated for this application. Our preliminary conclusion is that polarization functions are necessary on hydrogens that migrate from donor to acceptor. The convergence of these vibrational frequencies must be examined along the entire portion of the reaction path that effects the tunneling through the Eckart barrier - not just at the transition state. One promising approach we are investigating is the use of different basis sets for different orders of perturbation theory - just as in our single point CBS models. For example, we might use the CBS-4 basis sets²¹ to optimize the geometry and calculate the frequencies for the CBS-QCI/APNO model. The number of possible combinations here is enormous, but we have developed a systematic method that will enable us to find the optimum combination.

We shall also need to make a related but separate study of the required accuracy for the vibrational energy levels and the effects of anharmonicity on the vibrational partition functions at high temperatures. The latter requires a numerical evaluation of the vibrational partition functions in place of the algebraic sum over an infinite geometric series that was used to obtain Eq.(7).

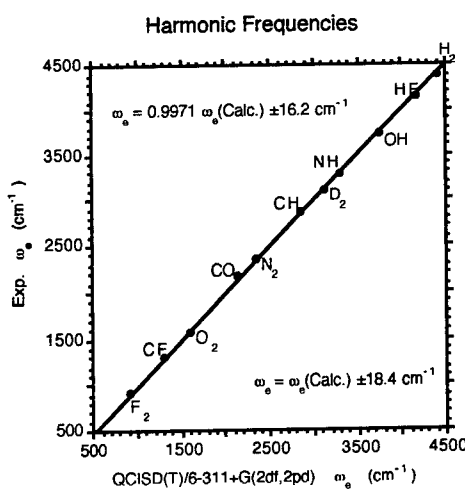
The sensitivity of the rotational partition functions, $Q_{rotation}$, to errors in the transition state geometry, R_0^\ddagger , and the sensitivity of the specific rate constant, $k_{rate}(T)$ to errors in $Q_{rotation}$ must also be determined. We shall also examine the effects of centrifugal distortion in the higher rotational energy levels that become populated at high temperatures.

The proposed method development will provide a hierarchy of kinetics models ranging from the very fast CBS-4 model applicable to up to twenty non hydrogen atoms giving absolute rates to within a factor of ten, through the CBS-Q model applicable to up to ten non hydrogen atoms giving absolute rates to within a factor of three, to the most accurate CBS-QCI/APNO model limited to only five non hydrogen atoms, but giving absolute rates to within fifty percent.

Once the development is complete, these methods will be used to obtain rate constants for important reactions of proposed halon replacements at combustion temperatures. It will then be possible to experiment with many known and potential agents in many fire scenarios without ever lighting a match or otherwise starting a fire. This will be the first step in the construction of a virtual fire laboratory where the computer takes the place of hardware, fuels and suppressants to make possible safe, fast, and effective evaluations of fire suppressants.

Improved Zero-Point Energies

We have begun a study of methods to improve the zero-point energies in the CBS IRCMax models for transition states. Very accurate vibrational frequencies are known for a number of diatomic molecules. Large basis set QCI calculations reproduce the harmonic frequencies to within $\pm 16 \text{ cm}^{-1}$. Such calculations are appropriate for the



demonstration kinetics calculations presented on page 17, but are clearly impractical for large molecules. We have therefore examined the convergence of the calculated harmonic frequencies with both the basis set and the level of theory:

Table IV. RMS errors in scaled harmonic constants, ω_0 , (cm^{-1}).

Basis Set	Level of Theory					
	HF	B3LYP	MP2	MP3	QCISD	QCISD(T)
3-21G	170.1	208.7	278.7	174.1	179.3	187.7
6-31G*	135.9	87.5	105.3	83.1	46.7	32.2
6-311G**	132.7	49.9	88.2	62.5	39.0	33.0
6-311+G(2df,2pd)	133.6	54.9	87.0	62.6	34.0	16.2

The results demonstrate the clear superiority of Becke 3-parameter Lee Yang Parr density functional theory over the more expensive MP2 methodology. It is probably necessary to accept the larger errors from HF/3-21G frequencies to maintain the speed of the CBS-4 model. However, it is definitely appropriate to develop an improved CBS-Q model employing B3LYP frequencies with at least a 6-311G** basis set. A manuscript describing such a method is in preparation. The RMS error for the G2 test set shows a very slight improvement over our previous CBS-Q model, which employed HF/6-31G* frequencies and MP2/6-31G* geometries. The new model employs a single B3LYP IRC for both the geometry and the frequencies, which is necessary to provide a practical implementation of the IRCMax model. Since the CBS-APNO model was developed more as a benchmark than as a practical computational method, we are inclined to employ QCISD/6-311G** geometries *and* frequencies so that we maintain a completely independent check on the CBS-Q model.

Finally we note that the IRCMax procedure has been completely automated and will be made available to the kinetics community with the release of Gaussian 98.

References

1. S. Arrhenius, Z. Physikal. Chem. **4**, 226 (1889).
2. H. Eyring, J. Chem. Phys. **3**, 107 (1935).
3. C. Eckart, Phys. Rev. **35**, 1303 (1930).
4. D. G. Truhlar and A. Kuppermann, J. Am. Chem. Soc. **93**, 1840 (1971).
5. C. Peng, and H. B. Schlegel, Israel J. Chem. **33**, 449 (1993).
6. N. C. Handy, and H. F. Schaefer, III, J. Chem. Phys. **81**, 5031 (1984).
7. J. A. Pople, R. Krishnan, H. B. Schlegel, and J. S. Binkley, Int. J. Quant. Chem. Symp **13**, 325 (1979).
8. H. B. Schlegel, J. Comp. Chem. **3**, 214 (1982).
9. M. Head-Gordon, and T. Head-Gordon, Chem. Phys. Lett. **220**, 122 (1994).
10. M. J. Frisch, M. Head-Gordon, and J. A. Pople, Chem. Phys. Lett. **166**, 275 (1990).
11. M. J. Frisch, M. Head-Gordon, and J. A. Pople, Chem. Phys. Lett. **166**, 281 (1990).
12. W. J. Hehre, L. Radom, P. v. R. Schleyer, and J. A. Pople *Ab Initio Molecular Orbital Theory*; John Wiley & Sons: New York, 1986.
13. C. C. J. Roothan, Rev. Mod. Phys. **23**, 69 (1951).
14. J. A. Pople, and R. K. Nesbet, J. Chem. Phys. **22**, 571 (1959).
15. J. A. Pople, M. Head-Gordon, D. J. Fox, K. Raghavachari, and L. A. Curtiss, J. Chem. Phys. **90**, 5622 (1989).
16. L. A. Curtiss, C. Jones, G. W. Trucks, K. Raghavachari, and J. A. Pople, J. Chem. Phys. **93**, 2537 (1990).
17. L. A. Curtiss, K. Raghavachari, G. W. Trucks, and J. A. Pople, J. Chem. Phys. **94**, 7221 (1991).
18. L. A. Curtiss, K. Raghavachari, and J. A. Pople, J. Chem. Phys. **98**, 1293 (1993).

19. J. A. Montgomery, Jr., J. W. Ochterski, and G. A. Petersson, *J. Chem. Phys.* **101**, 5900 (1994).
20. J. W. Ochterski, G. A. Petersson, and K. B. Wiberg, *J. Am. Chem. Soc.* **117**, 11299 (1995).
21. J. W. Ochterski, G. A. Petersson, and J. A. Montgomery, Jr., *J. Chem. Phys.* **104**, 2598 (1996).
22. Gaussian94, Revision B.3, M. J. Frisch, G. W. Trucks, H. B. Schlegel, P. M. W. Gill, B. G. Johnson, M. A. Robb, J. R. Cheeseman, T. Keith, G. A. Petersson, J. A. Montgomery, Jr., K. Raghavachari, M. A. Al-Laham, V. G. Zakrzewski, J. V. Ortiz, J. B. Foresman, C. Y. Peng, P. Y. Ayala, W. Chen, M. W. Wong, J. L. Andres, E. S. Replogle, R. Gomperts, R. L. Martin, D. J. Fox, J. S. Binkley, D. J. Defrees, J. Baker, J. P. Stewart, M. Head-Gordon, C. Gonzalez, and J. A. Pople; Gaussian, Inc.,: Pittsburgh PA, 1995; pp .
23. C. Møller, and M. S. Plesset, *Phys. Rev.* **46**, 618 (1934).
24. R. Ditchfield, W. J. Hehre, and J. A. Pople, *J. Chem. Phys.* **54**, 724 (1971).
25. W. J. Hehre, R. Ditchfield, and J. A. Pople, *J. Chem. Phys.* **56**, 2257 (1972).
26. J. S. Binkley, J. A. Pople, and W. J. Hehre, *J. Am. Chem. Soc.* **102**, 939 (1980).
27. M. S. Gordon, J. S. Binkley, J. A. Pople, W. J. Pietro, and W. J. Hehre, *J. Am. Chem. Soc.* **104**, 2797 (1982).
28. C. Gonzalez, and H. B. Schlegel, *J. Phys. Chem.* **90**, 2154 (1989).
29. D. L. Diedrich, and J. B. Anderson, *Science* **258**, 786 (1992).
30. K. P. Huber, and G. Herzberg *Constants of Diatomic Molecules*; Van Nostrand Reinhold: New York, 1979.
31. D. L. Gray, and A. G. Robiette, *Molecular Physics* **37**, 1901 (1979).
32. E. Hirota, *J. Molec. Spect.* **77**, 213 (1979).
33. J. Chase M. W. , C. A. Davies, J. Downey J. R. , D. J. Frurip, R. A. McDonald, and A. N. Syverud, *J. Phys. Chem. Ref. Data* **14**, Suppl. 1, (1985).
34. P. Ho, and C. F. Melius, *J. Phys. Chem.* **94**, 5120 (1990).
35. M. D. Allendorf, and C. F. Melius, *J. Phys. Chem.* **97**, 72 (1993).
36. G. E. Scuseria, *J. Chem. Phys.* **95**, 7426 (1991).
37. P. J. Knowles, P. Stark, and H. Werner, *Chem. Phys. Letters* **185**, 555 (1991).
38. NIST Chemical Kinetics Database, verson 6.0.
39. R. A. Marcus, *J. Chem. Phys.* **45**, 4493 (1966).
40. R. T. Skodje, D. G. Truhlar, and B. C. Garrett, *J. Chem. Phys.* **77**, 5955 (1982).

PROCESS MODELING OF THE DENSIFICATION OF GRANULAR CERAMICS:
INTERACTION BETWEEN DENSIFICATION AND CREEP

Mohamed N. Rahaman
Professor
Department of Ceramic Engineering

University of Missouri-Rolla
1870 Miner Circle
Rolla, MO 65409-0330

Final Report for:
Summer Research Extension Program

Sponsored by:
Air Force Office of Scientific Research
Bolling Air Force Base, Washington DC

and

University of Missouri-Rolla

December, 1997

PROCESS MODELING OF THE DENSIFICATION OF GRANULAR CERAMICS:
INTERACTION BETWEEN DENSIFICATION AND CREEP

Mohamed N. Rahaman
Professor
Department of Ceramic Engineering
University of Missouri-Rolla

Abstract

The effects of solid solution additives (dopants) on the densification and creep of CeO_2 powder compacts were investigated using the technique of loading dilatometry. Compacts of undoped CeO_2 and of CeO_2 doped with 6 atomic percent (at%) Y or Sc were sintered isothermally at temperatures in the range of 1050 to 1150 °C with applied uniaxial stresses of 0 and 0.35 MPa. With the applied stress, densification and creep occurred simultaneously and the effects of the two processes can be separated. For the three powder compositions, the ratio of the densification rate to the creep rate was almost independent of the density during sintering. However, the magnitude of the ratio was influenced by the presence of the dopant, with values of 5, 6 and 4 for CeO_2 , Y-doped CeO_2 and for Sc-doped CeO_2 , respectively. At an equivalent grain size, the creep rate decreased approximately exponentially with porosity. This dependence can be described in terms of a stress intensification factor, ϕ , of the form $\phi \approx \exp(aP)$ where a is a material parameter and P is the porosity. The magnitude of parameter a was influenced by the presence of the dopant and had values of 5.5, 6.5 and 5.0 for CeO_2 , Y-doped CeO_2 and for Sc-doped CeO_2 , respectively. The consequences of the data for modeling the densification process of granular powder compacts are discussed.

PROCESS MODELING OF THE DENSIFICATION OF GRANULAR CERAMICS: INTERACTION BETWEEN DENSIFICATION AND CREEP

Mohamed N. Rahaman

1. Introduction

The interaction between densification and creep has important consequences for the densification of granular materials. As outlined elsewhere [1], several attempts have been made in recent years to understand the interaction at both the practical and the theoretical levels. The interaction was explored further in a recent investigation by Rahaman et al [1] into the effect of a solid solution additive, Y_2O_3 , on the isothermal densification and creep of CeO_2 at temperatures of 1150-1200 °C. In the sintering of porous powder compacts, the additive was observed to reduce the diffusion coefficient for densification. The Y_2O_3 was also found to produce a corresponding decrease in the diffusion coefficient for creep of dense CeO_2 bodies. The effect of the additive on the diffusion coefficients provides further evidence that densification and creep commonly occur by the same mechanism in granular ceramics.

The occurrence of the same mechanism in densification and creep has important practical and theoretical implications. Practically, it may be possible to enhance the steady-state creep behavior from observations of the sintering behavior. Theoretically, it may be possible to predict the steady-state creep rate from physical and microstructural parameters determined from sintering experiments. Furthermore, theoretical models for the densification of granular materials must generally include the volumetric strain due to the hydrostatic component of the stress as well as the shear (creep) strain due the shear component of the stress. According to the sintering models [2], the densification rate can be described by an equation of the form:

$$\dot{\epsilon}_d = \frac{HD_d \phi^{(m+1)/2}}{G^m k T} (p_a + \Sigma) \quad (1)$$

where H is a numerical constant, D_d is the diffusion coefficient for the rate-controlling densification mechanism, G is the average grain size, p_a is the applied hydrostatic stress, k is the Boltzmann constant, T is the absolute temperature, Σ is the sintering stress defined as an equivalent externally applied hydrostatic stress which would have the same effect on the densification rate as the grain boundaries and pores, m is an exponent that depends

radial strains as a function of time.

2. Experimental Procedure

Fine powders of undoped CeO₂ and of CeO₂ solid solutions containing 6 at% Y and 6 at% Sc were used in this study. They were prepared by precipitation from solution under hydrothermal conditions (~300 °C and ~10 MPa). The synthesis and characterization of the powders are described in detail elsewhere [10,11]. The powders were crystalline and single phase with a cubic fluorite structure. The average particle sizes were in the range of 10-15 nm.

The powders were dried for 24 h at 200 °C and then compacted by uniaxial pressing in a stainless steel die (diameter = 6.25 mm) under a pressure of ~35 MPa, followed by cold isostatic pressing (pressure ≈ 400 MPa). The density of the green compacts was 0.54±0.02 of the theoretical density.

The compacts were sintered in flowing O₂ (~50 cm³/min) for 2 h in a loading dilatometer. The instrumentation and technique of loading dilatometry are described in detail elsewhere [5,9]. Sintering was performed at isothermal temperatures in the range of 1050-1150 °C under applied uniaxial stresses of 0 and 0.35 MPa. In the experiments, the sample was heated at 10 °C/min and the load was applied rapidly when the isothermal sintering temperature was reached. The isothermal sintering temperature used for CeO₂ was 1050 °C. However, it was found that the presence of the dopant delayed the densification to higher temperatures. In order to achieve approximately the same sintered densities, isothermal sintering temperatures of 1100 and 1150 °C were used for the compacts doped with Sc and Y, respectively.

The mass and dimensions of the compacts were measured before and after sintering and the density at any sintering time was determined from the initial density and the measured shrinkage. The final densities of the sintered compacts were also measured using Archimedes' principle. In a separate set of experiments, the sintering was terminated at fixed time intervals and the dimensions of the compacts were measured with a micrometer.

The grain sizes of the compacts sintered for fixed times were measured by X-ray line broadening [12]. This technique was used because the grain size values were <100 nm. The compacts were also fairly porous, thereby making the use of microscopy with polished and etched surfaces difficult. The values obtained from the

proportional to the stress and by using Eq. (8).

4. Results

Figure 1 shows the data for the relative density as a function of time during isothermal sintering of CeO_2 (at 1050 °C), Sc-doped CeO_2 (1100 °C) and Y-doped CeO_2 (1150 °C) under an externally applied stress of 0 MPa (i.e., during *conventional, pressureless sintering*). At the beginning of isothermal sintering, the density is ~0.70 and after sintering for 2 h the density reached a value of ~0.85.

In Fig. 2, the axial strain, ϵ_z , is plotted as a function of time for the sintering of CeO_2 (at 1050 °C) under applied stresses of 0 and 0.35 MPa. The data for ϵ_z versus the radial strain, ϵ_r , obtained in intermittent sintering experiments for CeO_2 under the same conditions of temperature and stress are shown in Fig. 3. Under zero applied stress, the shrinkage is isotropic, so that the slope [k in Eq. (6)] is equal to 1. As outlined earlier, the stress (0.35 MPa) was applied to the sample when the isothermal sintering temperature was reached. The application of the stress produced an increase in the slope k. Corresponding results for ϵ_z versus time and for ϵ_z versus ϵ_r are shown in Figs. 4 to 7 for Y-doped CeO_2 and for Sc-doped CeO_2 .

The linear densification rate, $\dot{\epsilon}_d$, was determined from the data using Eq. (4) and the results are shown in Fig. 8 as a function of relative density for CeO_2 , Y-doped CeO_2 and for Sc-doped CeO_2 . The curves are approximately parallel which may indicate that the densification mechanism is the same for the three compositions if it is assumed that the grain size is approximately the same at any given density. As discussed earlier, the isothermal sintering temperatures were higher for the Y-doped CeO_2 and for Sc-doped CeO_2 so that the densification rates at a given density do not directly yield the variation in the diffusion coefficient for the densification mechanism. The creep rate, $\dot{\epsilon}_c$, determined from the data of Figs. 2 to 7 using Eq. (5) are shown in Fig. 9 as a function of the relative density. The trends in the results are similar to those for the densification rates.

Figure 10 shows the ratio of the densification rate to the creep rate, $\dot{\epsilon}_d/\dot{\epsilon}_c$, as a function of the relative density. As observed in earlier work [5,6,13], the ratio is almost independent of the density. The values for $\dot{\epsilon}_d/\dot{\epsilon}_c$ are approximately 5, 6 and 4 for CeO_2 , Y-doped CeO_2 and for Sc-doped CeO_2 , respectively.

The grain size, G, as a function of relative density is shown in Fig. 11 for the three compositions. At

any given density, G is approximately independent of the presence of the dopant. It is known that Y and Sc has a marked effect on the grain boundary mobility of dense CeO_2 [10,14]. However, for the density range of the present experiments, the continuous pores are very effective for controlling the grain size [15]. As a result, the presence of the dopants do not have a significant effect on the grain size.

The grain size data of Fig. 11 were used to compensate for grain growth so that the creep rate as a function of density can be considered at an equivalent grain size. In this way, the true dependence of the creep rate on the density can be found. For the very fine particle size powders used in the present experiments, assuming that grain boundary diffusion is the rate controlling mechanism for densification and creep, then the measured creep rate was multiplied by the factor $(G/G_0)^3$, where G is the grain size at a given density and G_0 is the initial grain size, taken as the grain size at the beginning of isothermal sintering. Figure 12 shows the grain size compensated creep rate, $G^3\dot{\epsilon}_c/G_0^3$, as a function of relative density for the three compositions investigated. The logarithm of the grain size compensated creep rate decreases almost linearly with relative density. Assuming the relationship given in Eq. (3) for the stress intensity factor, ϕ , then the parameter a takes the values of 5.5, 6.5 and 5.0 for CeO_2 , Y-doped CeO_2 and for Sc-doped CeO_2 , respectively.

5. Discussion

The data allowed a determination of (i) the densification and creep rates as functions of the density during sintering and (ii) the stress intensification factor, ϕ , for undoped CeO_2 , Y-doped CeO_2 and for Sc-doped CeO_2 . The ratio of the densification rate to the creep rate is approximately independent of the relative density (Fig. 10), indicating that for each composition, the processes of densification and creep occur by the same mechanism. The occurrence of the same mechanism for densification and for creep was also found in earlier work [1] on undoped CeO_2 and Y-doped CeO_2 where the densification of porous powder compacts and the steady-state creep of dense bodies were investigated.

The values for the ratio of the densification rate to the creep rate, $\dot{\epsilon}_d/\dot{\epsilon}_c$, are found to be approximately 5, 6 and 4 for undoped CeO_2 , Y-doped CeO_2 and for Sc-doped CeO_2 , respectively. For the same mechanism, the dopant is expected to have the same effect on the separate processes of densification and creep so that the value of $\dot{\epsilon}_d/\dot{\epsilon}_c$ should be independent of the presence of the dopant. The relatively small variation in the measured value

theoretical predictions yielded dihedral angles of 120°, 110° and 135°, respectively for undoped CeO₂, Y-doped CeO₂ and for Sc-doped CeO₂, respectively.

References

1. M. N. Rahaman, R. E. Dutton and S. L. Semiatin, *Acta mater.*, **45** 3017-28 (1997).
2. M. N. Rahaman, *Ceramic Processing and Sintering*, Marcel Dekker, New York, 1995.
3. M. N. Rahaman, *AFOSR Summer Faculty Research Program Report*, August, 1995.
4. J. M. Vieira and R. J. Brook, *J. Am. Ceram. Soc.*, **67** 245-49 (1984).
5. M. N. Rahaman, L. C. De Jonghe and R. J. Brook, *J. Am. Ceram. Soc.*, **69** 53-57 (1986).
6. M. N. Rahaman and L. C. De Jonghe, *J. Mater. Sci.*, **22** 4326-30 (1987).
7. W. Beere, *Acta metall.*, **23** 131-38 (1975).
8. W. Beere, *Acta metall.*, **23** 139-45 (1975).
9. L. C. De Jonghe and M. N. Rahaman, *Rev. Sci. Instrum.*, **55** 2007-10 (1984).
10. M. N. Rahaman and Y.-C. Zhou, *J. Europ. Ceram. Soc.*, **15** 939-50 (1995).
11. Y.-C. Zhou and M. N. Rahaman, *J. Mater. Res.*, **8** 1680-86 (1993).
12. B. D. Cullity, *Elements of X-Ray Diffraction*, 2nd ed., Addison-Wesley, Reading, MA, 1978.
13. M.-Y. Chu, L. C. De Jonghe and M. N. Rahaman, *Acta metall.*, **37** 1415-20 (1989).
14. P.-L. Chen and I.-W. Chen, *J. Am. Ceram. Soc.*, **77** 2289-97 (1994).
15. M. N. Rahaman and C.-H. Hu, *Ceramic Trans.*, **32** 309-22 (1993).

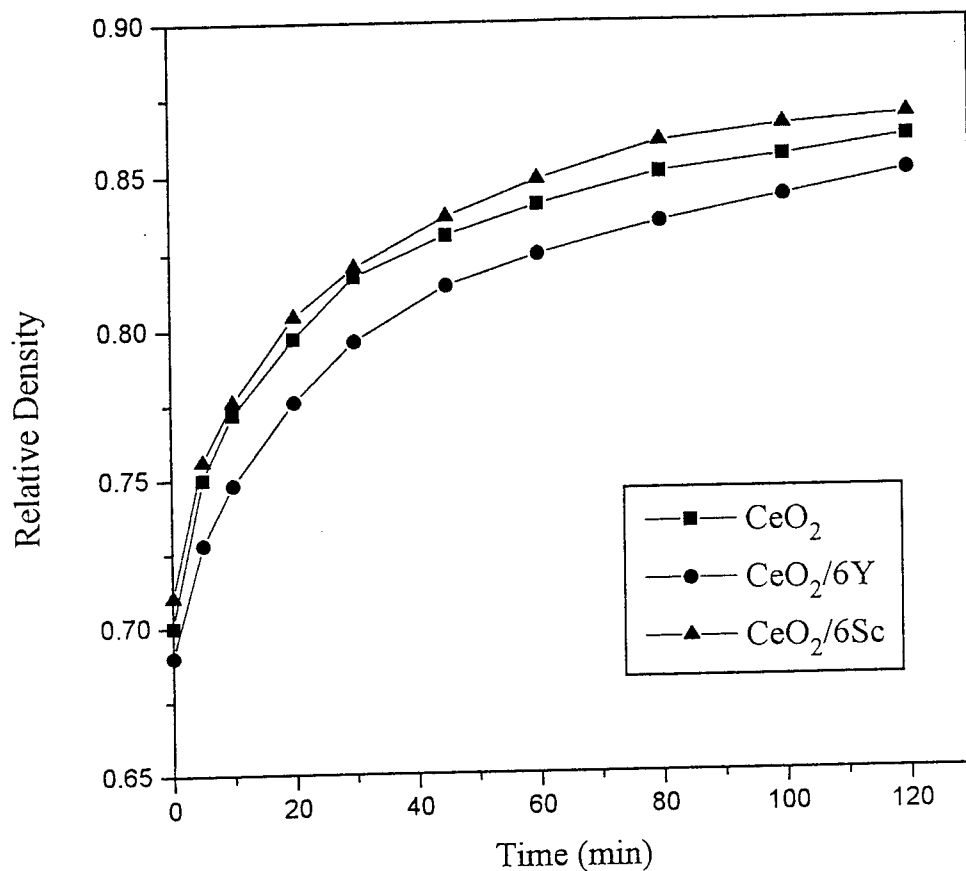


Fig. 1. Relative density versus time for powder compacts of undoped CeO_2 , CeO_2 doped with 6 at% Sc, and CeO_2 doped with 6 at% Y during isothermal sintering at 1050, 1100 and 1150 °C, respectively.

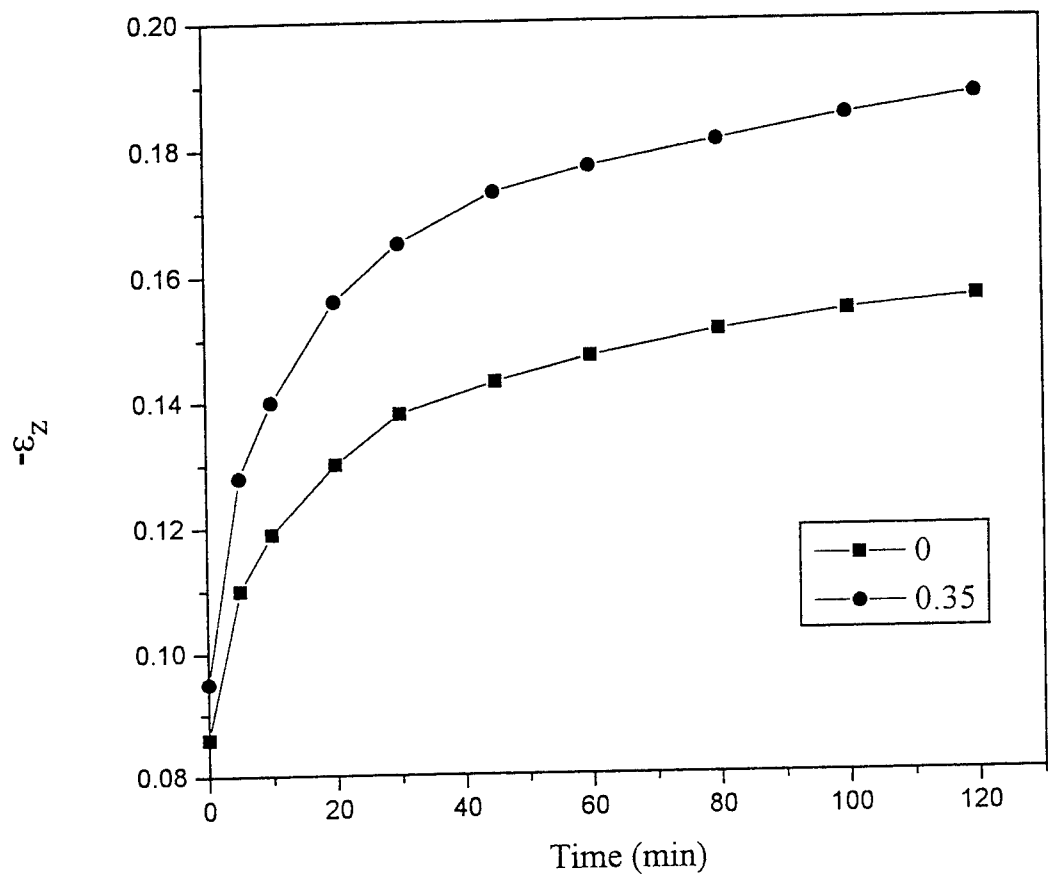


Fig. 2. Axial strain versus time for powder compacts of undoped CeO_2 during isothermal sintering at 1050 °C under applied uniaxial stresses of 0 and 0.35 MPa.

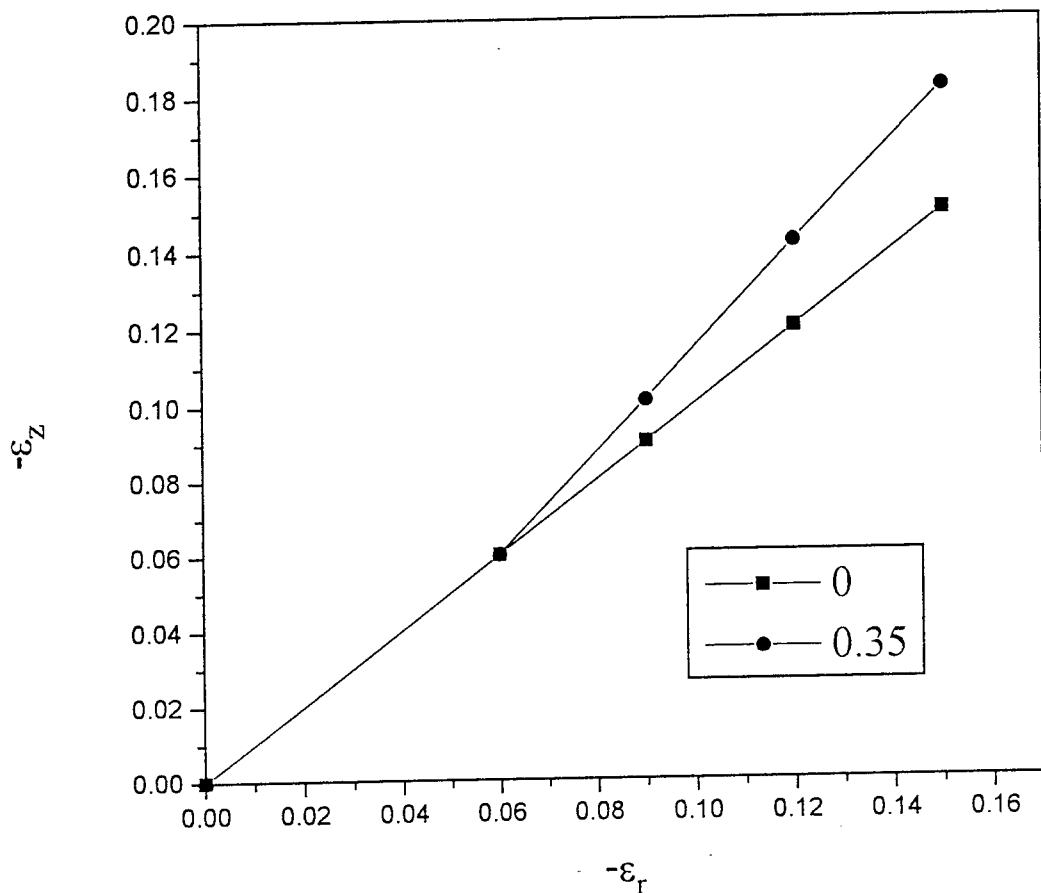


Fig. 3. Axial strain versus radial strain for powder compacts of undoped CeO_2 during sintering at $10\text{ }^{\circ}\text{C}/\text{min}$ to $1050\text{ }^{\circ}\text{C}$ followed by isothermal sintering for 2 h at this temperature under applied uniaxial stresses of 0 and 0.35 MPa . The stress was applied at the beginning of the isothermal sintering.

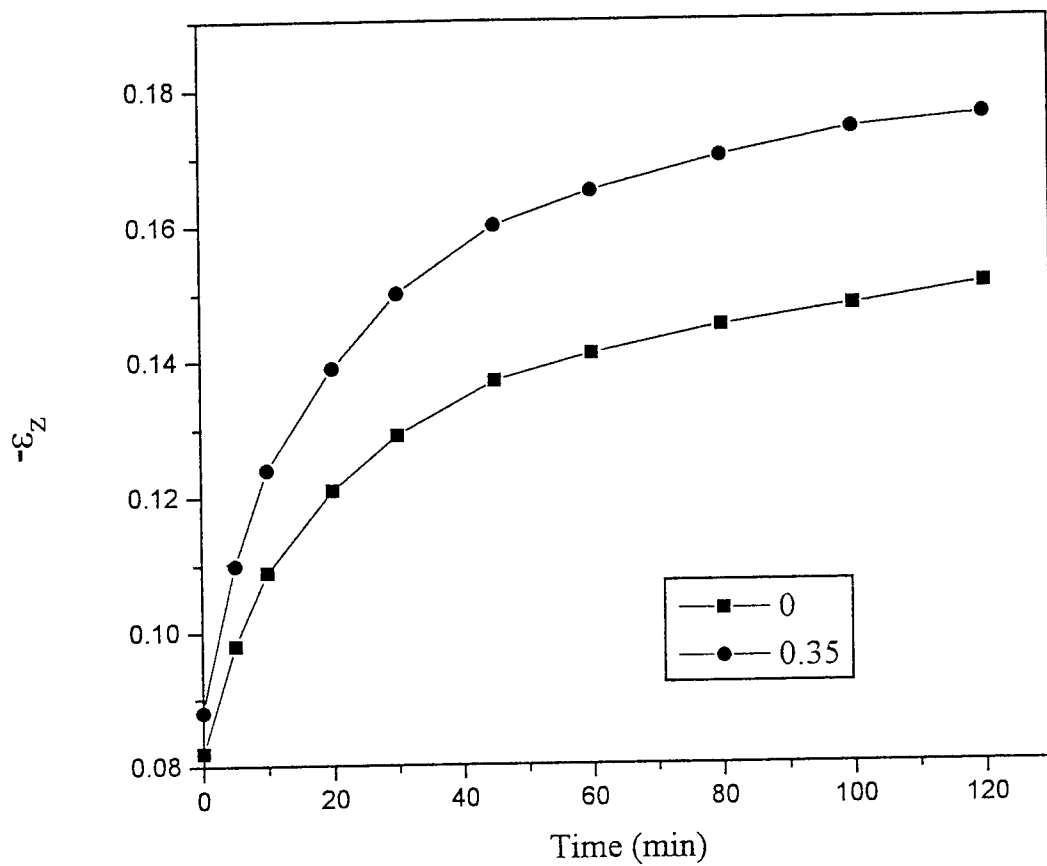


Fig. 4. Axial strain versus time for powder compacts of Y-doped CeO_2 during isothermal sintering at 1150 °C under applied uniaxial stresses of 0 and 0.35 MPa.

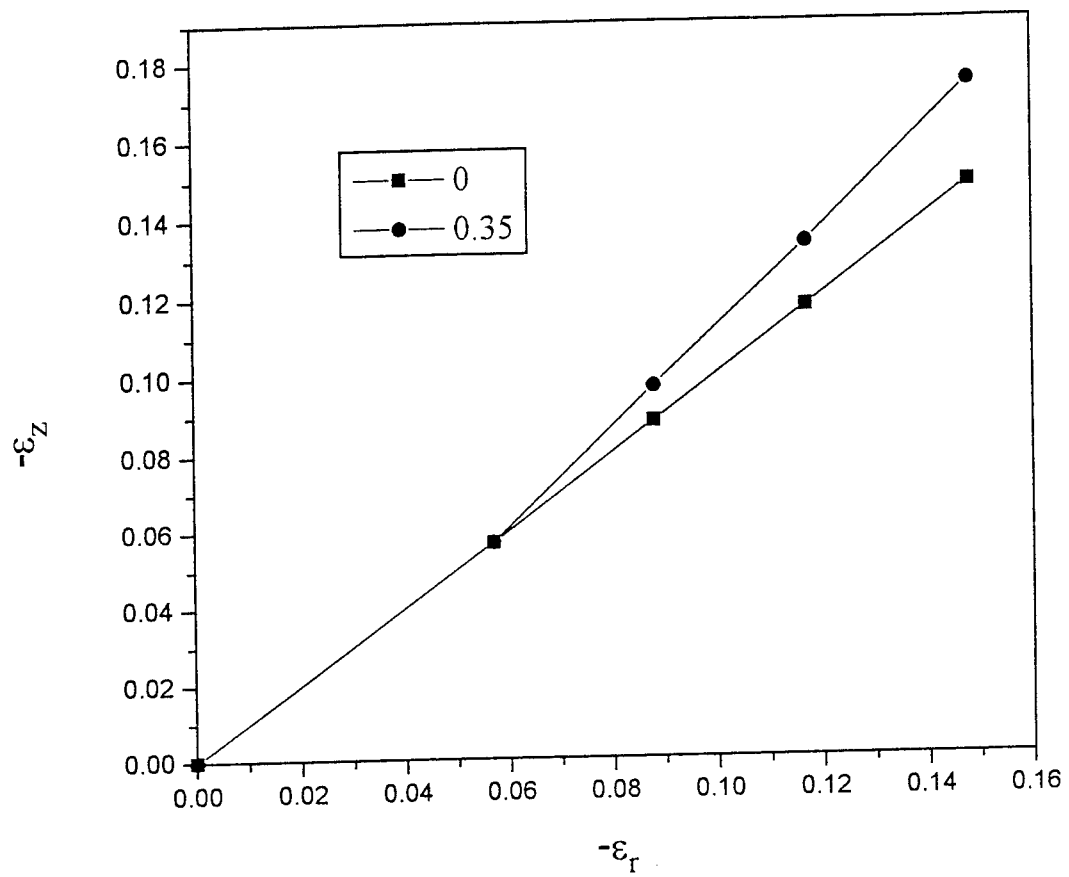


Fig. 5. Axial strain versus radial strain for powder compacts of Y-doped CeO_2 during sintering at $10^\circ\text{C}/\text{min}$ to 1150°C followed by isothermal sintering for 2 h at this temperature under applied uniaxial stresses of 0 and 0.35 MPa. The stress was applied at the beginning of the isothermal sintering.

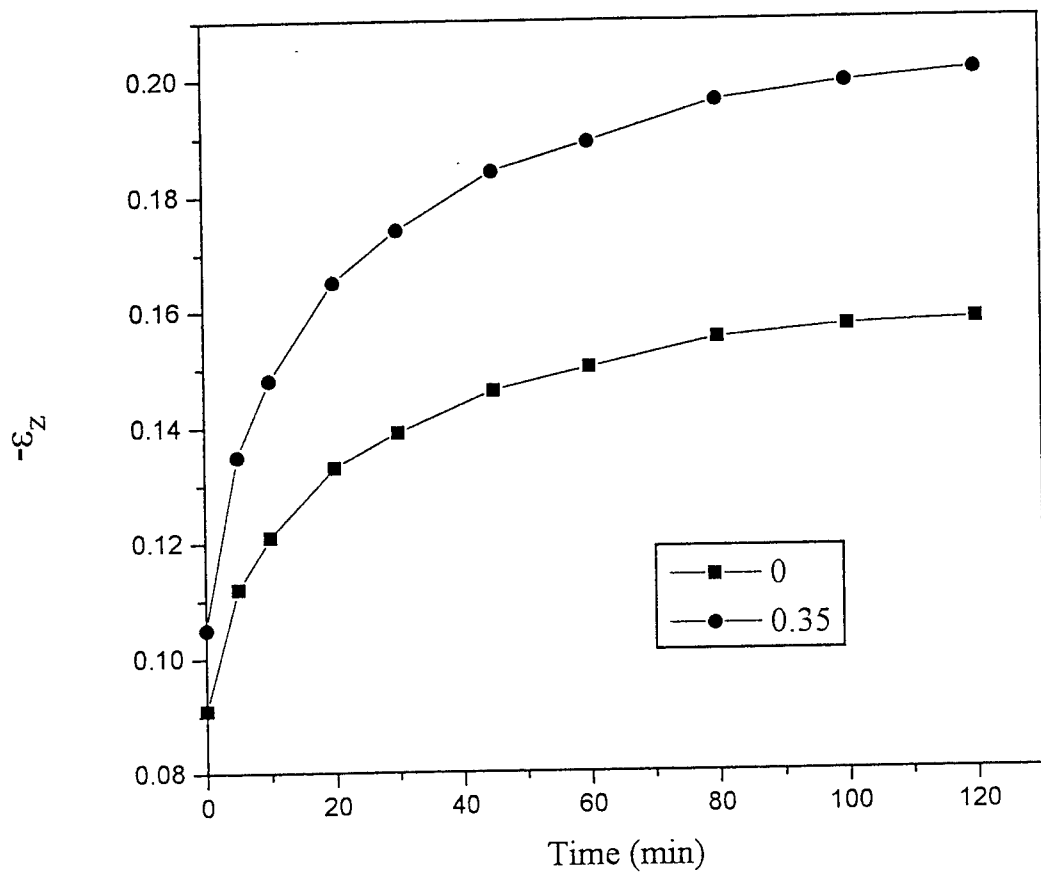


Fig. 6. Axial strain versus time for powder compacts of Sc-doped CeO_2 during isothermal sintering at 1100 °C under applied uniaxial stresses of 0 and 0.35 MPa.

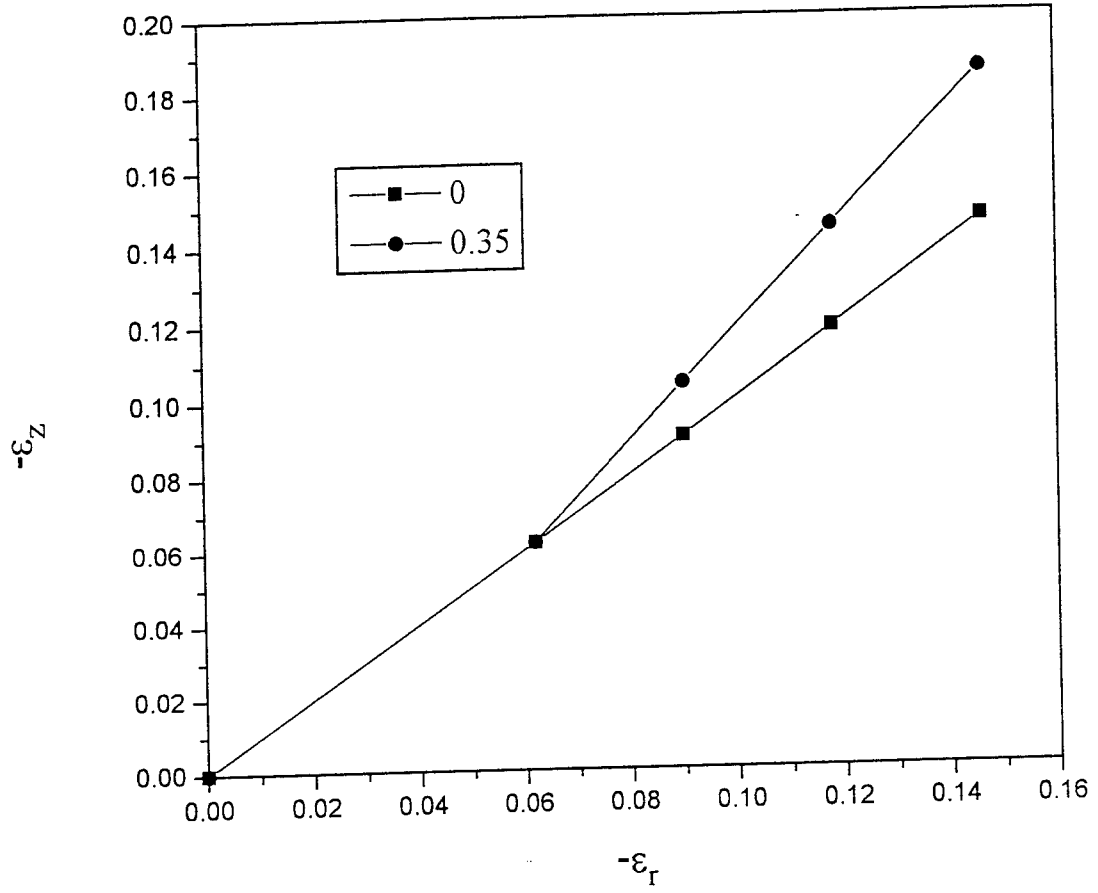


Fig. 7. Axial strain versus radial strain for powder compacts of Sc-doped CeO_2 during sintering at $10 \text{ }^{\circ}\text{C}/\text{min}$ to $1100 \text{ }^{\circ}\text{C}$ followed by isothermal sintering for 2 h at this temperature under applied uniaxial stresses of 0 and 0.35 MPa . The stress was applied at the beginning of the isothermal sintering.

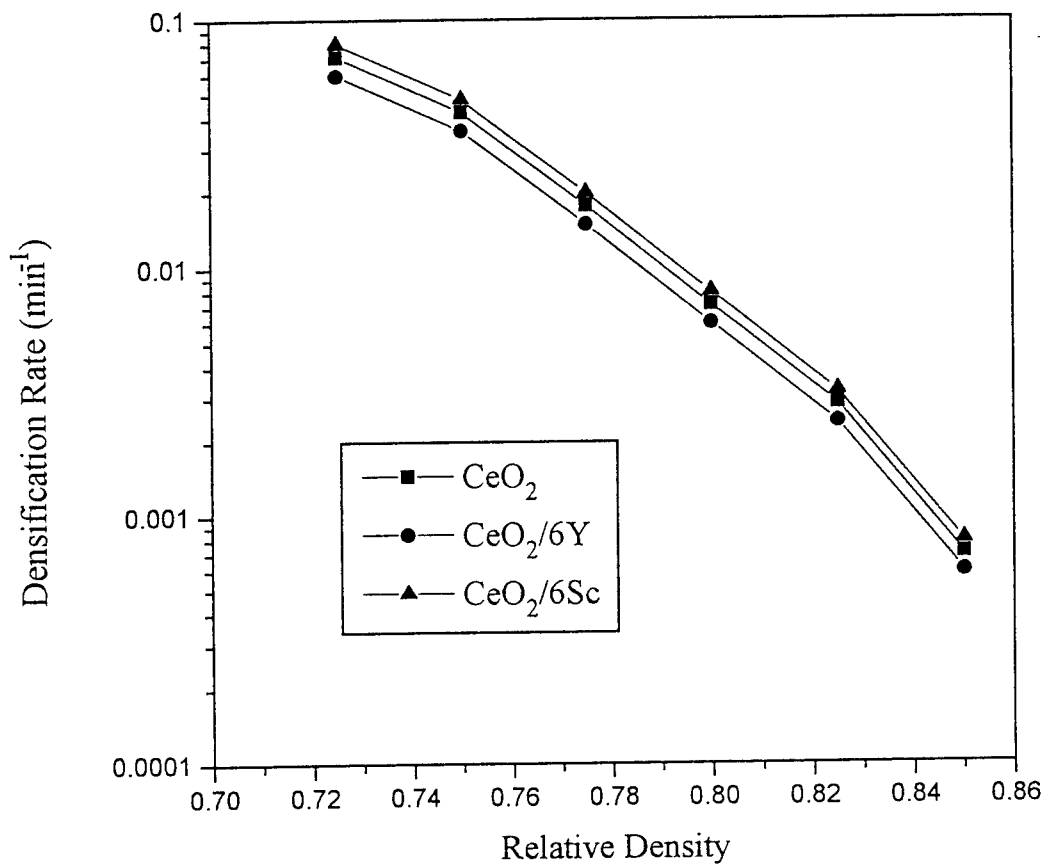


Fig. 8. Densification rate versus relative density for powder compacts of undoped CeO₂, Sc-doped CeO₂ and Y-doped CeO₂ during isothermal sintering at 1050, 1100 and 1150 °C, respectively.

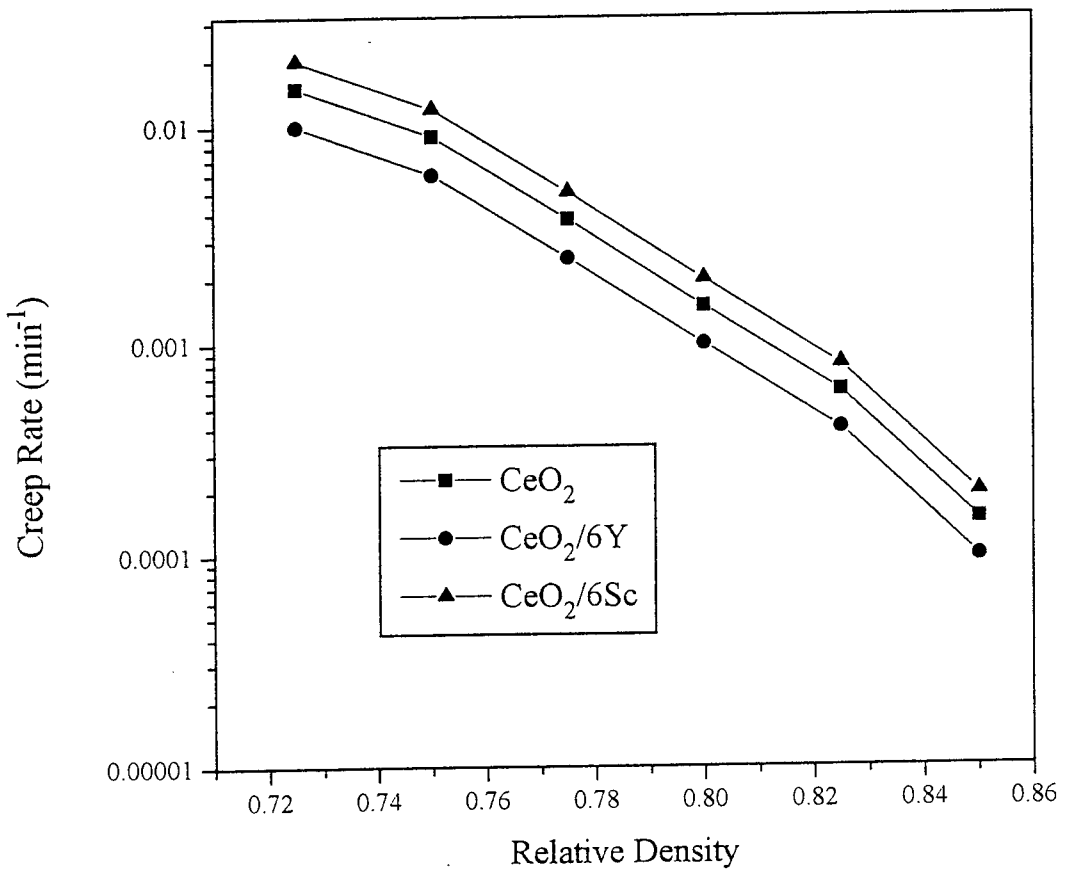


Fig. 9. Creep rate versus relative density for powder compacts of undoped CeO_2 , Sc-doped CeO_2 and Y-doped CeO_2 during isothermal sintering under an applied uniaxial stress of 0.35 MPa at 1050, 1100 and 1150 °C, respectively.

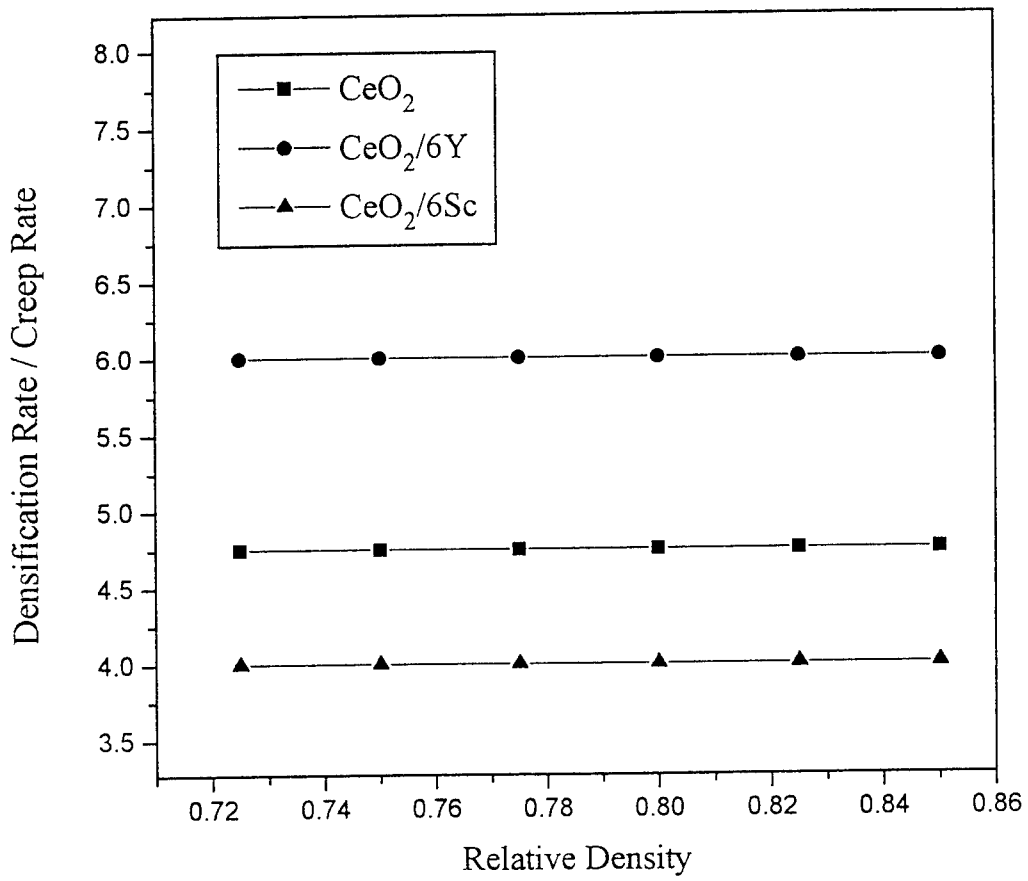


Fig. 10. Ratio of the densification rate to the creep rate for powder compacts of undoped CeO_2 , Sc-doped CeO_2 and Y-doped CeO_2 during isothermal sintering under an applied uniaxial stress of 0.35 MPa at 1050, 1100 and 1150 °C, respectively.

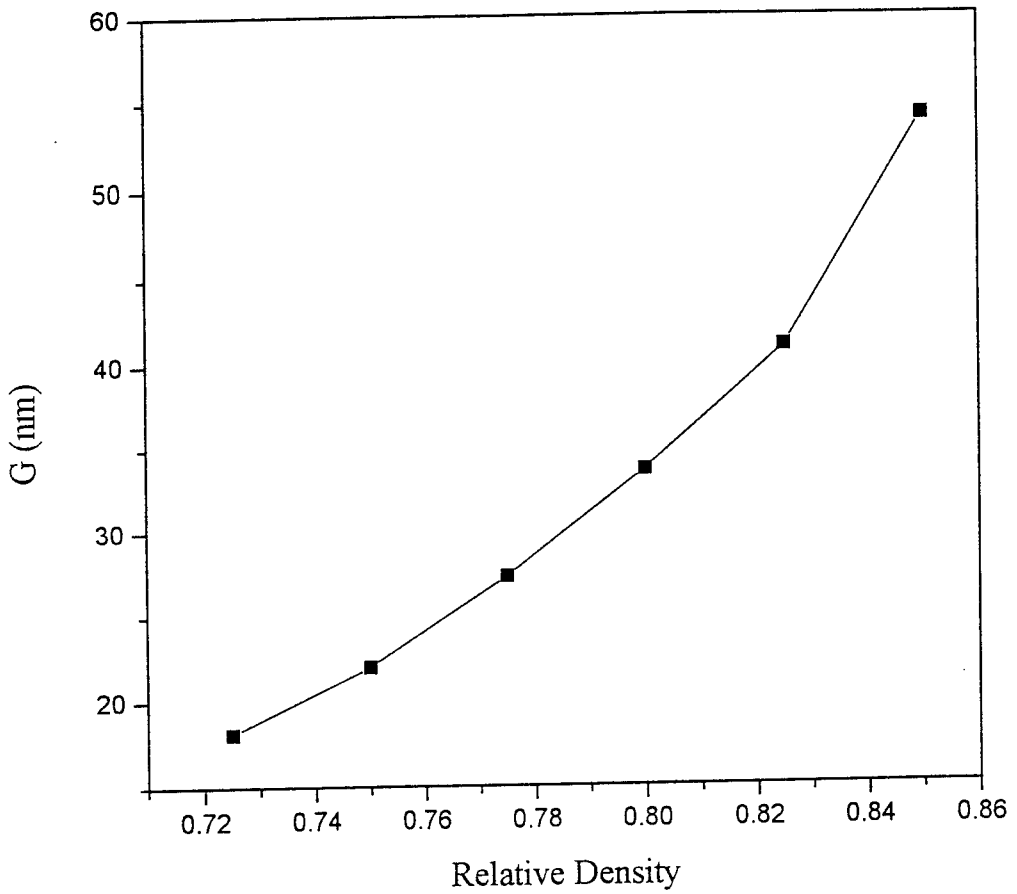


Fig. 11. Grain size versus relative density for powder compacts of undoped CeO_2 , Sc-doped CeO_2 and Y-doped CeO_2 during isothermal sintering at 1050, 1100 and 1150 °C, respectively.

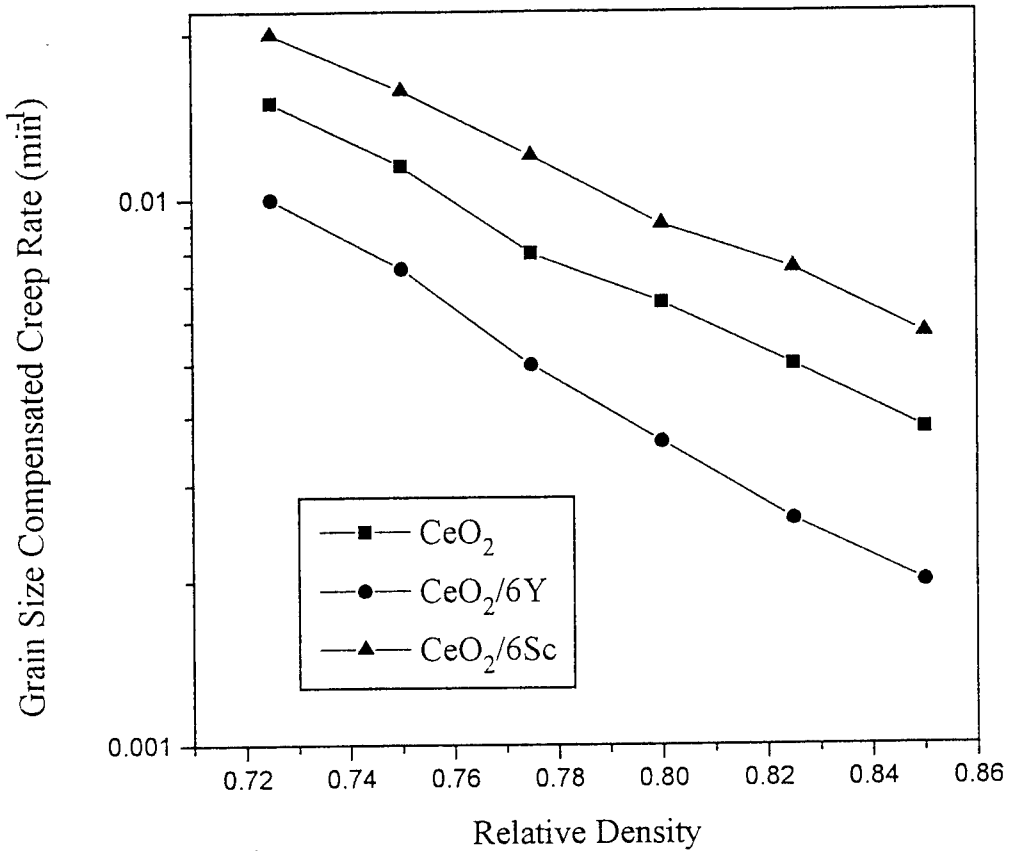


Fig. 12. Grain size compensated creep rate for powder compacts of undoped CeO_2 , Sc-doped CeO_2 and Y-doped CeO_2 during isothermal sintering under an applied uniaxial stress of 0.35 MPa at 1050, 1100 and 1150 °C, respectively.

QUANTUM MECHANICAL MODELING OF THE
THERMOCHEMISTRY OF HALOGENATED FIRE SUPPRESSANTS

Martin Schwartz
Regents Professor
Department of Chemistry

University of North Texas
215 W. Sycamore
Denton, TX 76203

Final Report for:
Summer Research Extension Program
Materials Directorate
Wright Laboratory

Sponsored by:
Air Force Office of Scientific Research
Bolling Air Force Base, DC

and

The University of North Texas

March 1999

QUANTUM MECHANICAL MODELING OF THE
THERMOCHEMISTRY OF HALOGENATED FIRE SUPPRESSANTS

Martin Schwartz
Regents Professor
Department of Chemistry
University of North Texas

Abstract

The *ab initio* G2, G2(MP2), CBS-4 and CBS-Q quantum mechanical protocols and the parameterized BAC-MP4 procedure were used to calculate the enthalpies of formation (ΔH°) of ethane and the complete series of fluoroethanes, $C_2H_xF_{6-x}$, $x=0-5$. Results from all methods exhibited significant negative deviations from experiment. With the exception of the CBS-4 and BAC-MP4 procedures, the negative errors in the calculated enthalpies were observed to be linearly dependent upon the number of C-F bonds in the molecule. Application of a Bond Additivity Correction (BAC) parameter, Δ_{CF} , derived in an earlier investigation of fluoro- and chlorofluoromethanes, removed some, although not all of the systematic deviations. Introduction of a heavy atom interaction parameter, representing the effect of an attached carbon on the C-F bond error yielded corrected enthalpies which agree with experiment to within the reported uncertainties. The BAC-MP4 method, which has already been parameterized with generalized BAC's, yields calculated enthalpies which average approximately 10 kJ/mol below the experimental values of ΔH° in the fluoroethanes.

The G2 and G2(MP2) quantum mechanical procedures have been used to calculate the enthalpies of formation () of ethylene, acetylene and all of their fluorinated derivatives, $C_2H_xF_{4-x}$, $x=0-4$ and $C_2H_xF_{2-x}$, $x=0-2$. Values obtained from both methods exhibit large, systematically negative, deviations from experiment, with errors that increase approximately linearly with the number of C-F bonds. For each method, application of a C-F bond additivity correction, Δ_{CF} , and heavy atom interaction parameter, whose values were derived from earlier studies of saturated HFC's, reduced the errors dramatically; the resulting RMS deviations from experiment are lower than the RMS uncertainties in the measured enthalpies. The only reported enthalpy of formation for fluoroacetylene, obtained from average bond enthalpies, has an extremely large uncertainty (> 60 kJ/mol). Based upon the overall good agreement of the calculated heats of formation with experiment, we recommend $\Delta H^\circ(H-C\equiv C-F) = 114 \pm 10$ kJ/mol.

QUANTUM MECHANICAL MODELING OF THE
THERMOCHEMISTRY OF HALOGENATED FIRE SUPPRESSANTS

Martin Schwartz

TABLE OF CONTENTS

	page
CHAPTER 1. AB INITIO CALCULATIONS OF THE ENTHALPIES OF FORMATION OF FLUOROETHANES	4
A. Introduction	4
B. Computational Methods	4
C. Results and Discussion	4
D. Bond Additivity Corrections	5
E. Summary and Conclusions	8
F. References	8
CHAPTER 2. CALCULATED ENTHALPIES OF FORMATION OF FLUOROETHYLENES AND ACETYLENES	10
A. Introduction	10
B. Calculations	11
C. Results and Discussion	11
D. References	13
 TABLES AND FIGURES	
Table 1. Enthalpies of Formation in Fluoroethanes	15
Table 2. Bond Additivity Correction Parameters in Fluoroethanes	17
Table 3. Enthalpies of Formation in Fluoroethylenes and Acetylenes	18
Figure 1. Errors in Enthalpies of Formation of Fluoroethanes	19
Figure 2. Errors in Enthalpies of Formation of Fluoroethylenes and Acetylenes	20

CHAPTER 1. INITIO CALCULATIONS OF THE ENTHALPIES OF FORMATION OF FLUOROMETHANES.

INTRODUCTION

Because of their lower ozone depletion potential, C₁ and C₂ hydrofluorocarbons (HFC's) have been proposed as interim replacements for the chlorofluorocarbons (CFC's) and halon fire suppressants [1]. In order to enable accurate modeling of the fire suppression capabilities of HFC's and other potential halon replacements, we have recently performed *ab initio* quantum mechanical calculations of the enthalpies of formation (ΔH°) of fluoromethanes [2] and chlorofluoromethanes [3,4].

In this study, we extend these calculations to the C₂ HFC's and report the results of G2(MP2), G2, CBS-4, CBS-Q and BAC-MP4 calculations of enthalpies of formation of ethane and the complete series of fluoroethanes, C₂H_xF_{6-x}, x=0-5. The results are presented below.

COMPUTATIONAL METHODS

The *ab initio* calculations were performed using the GAUSSIAN code [5-7] on HP-PARisk, CRAY Y-MP, CRAY X-MP, SUN-Sparc and SGI Power-Challenge computers [8]. Details of these calculations are described in an earlier paper [2] as well as the original articles that pertain to the BAC-MP4 [9-11], G2 [12-14], and CBS family of methods [15-18].

RESULTS AND DISCUSSION

The reported experimental enthalpies of formation of the fluoroethanes with their estimated uncertainties were taken from refs. [21-24] and are presented in the second column of Table 1A. The remaining columns of the table contain the enthalpies calculated by the various *ab initio* methods. The quantities in parentheses represent the deviations from experiment. The deviations in the *ab initio* enthalpies are also given in category A of Table 2 and plotted in Fig. 1 for the G2 and G2(MP2) methods [closed circles and solid lines].

One observes from the RMS and average errors in the table that the G2(MP2), G2 and CBS-Q enthalpies exhibit large negative deviations from experiment. Furthermore, from Figs. 1A, 1B and 1D, one sees that these negative errors are systematic with an approximately linear

dependence upon the number of C-F bonds in the molecule [25]. The CBS-4 enthalpies also show negative deviations from the experimental values. However, for this method the errors are approximately constant.

The four *ab initio* procedures have been found to yield very accurate enthalpies of formation in most non-halogenated species. From these results, and from previous work on fluorinated [2] and chlorinated [3] hydrocarbons it is clear that these methods exhibit severe, unacceptable errors relative to reported experimental enthalpies.

BOND ADDITIVITY CORRECTIONS

When the errors in Δ_f^{exp} are observed to be systematically dependent upon the number of bonds of a given type in a molecule, they can in principle be removed by the application of Bond Additivity Corrections (BAC's), originally introduced by Melius in his BAC-MP4 method [9-11]. The correction, Δ_{BAC} , is of the form: $\Delta_{\text{BAC}} = \Delta_{\text{C-F}} n_{\text{C-F}}$, where $n_{\text{C-X}}$ is the number of a given type of bond and $\Delta_{\text{C-X}}$ is the BAC parameter representing the error associated with this bond type. The parameters are determined via a linear fit of Eq. [1] to the calculated deviations of the *ab initio* enthalpies from experiment. In our earlier investigation on thermochemistry of the chlorofluoromethanes [3], it was found that, for the same four *ab initio* methods, the application of C-F and C-Cl BAC parameters, removed all systematic error and yielded corrected enthalpies of formation whose RMS deviations from experiment were significantly below the RMS uncertainties in the literature data. It was also observed that values of $\Delta_{\text{C-H}}$ were smaller than the parameter's standard deviation and that its exclusion had no impact on the quality of the fit.

Because of the close similarity of the fluoroethanes (C2's) to the fluoromethanes (C1's) in the earlier work, it would be reasonable to expect that the same C-F BAC parameter should also correct the systematic errors found in this study. The results of this procedure are displayed in category B of Table 2. The second column contains the values of $\Delta_{\text{C-F}}$ from Ref. [3], with their estimated standard deviations. The next two pairs of columns represent the RMS and average errors for the C1's and C2's, respectively. As noted above, the values of RMS1 and AVE1 demonstrate that the application of a single C-F BAC does indeed remove virtually all systematic errors in Δ_f^{exp} for the fluoromethanes; note that resulting RMS deviations are significantly smaller than the RMS experimental uncertainty of ± 4.1 kJ/mol. From RMS2 in Table 2, one

sees, of course, that the same BAC also yields a substantial decrease in RMS deviations in the C2's. However, in contrast to the C1's, the comparatively large negative values of AVE2 reveals that not all of the negative systematic error has been removed by the bond additivity correction. Furthermore, the resultant values of RMS2 are, in all cases, significantly greater than the RMS experimental uncertainty of ± 4.8 kJ/mol. In principle, this problem could be remedied by refitting to minimize the RMS residuals in the fluoroethanes. However, this yields a larger value for the parameter, which would overcorrect enthalpies in the C1's. Further, it is physically unrealistic that the error due to a C-F bond should differ in the two series.

An alternative approach to eliminate the remaining systematic error would be via the addition of a second BAC, Δ_{C-C} , to account for the presence of a C-C bond in the fluoroethanes. However, this has the effect of increasing the error in ethane, where the *ab initio* enthalpies are in excellent agreement with experiment for all but the CBS-4 method (Table 1A). Furthermore, these methods have been applied with great success to the prediction of in numerous non-fluorinated organic species with one or more C-C bonds. Hence, the introduction of a C-C bond additivity correction would not be consistent with these earlier results.

In order to explore further the source of the remaining systematic errors in the fluoroethanes, we refer to the results of our earlier investigation of the chlorofluoromethanes [3]. In that work, it was discussed at some length how trends and curvature in plots of (calc) - (expt) vs. n_{C-F} (at fixed n_{C-Cl}) and vs. n_{C-Cl} (at fixed n_{C-F}) provided definitive evidence of "heavy atom" interactions (also utilized by Melius in the BAC-MP4 method [9-11]); i.e. the presence of one C-F bond increases the error due to either a second fluorine or a chlorine atom on the same carbon. In the earlier work, it was decided not to include heavy atom interactions since the RMS residuals using linearly independent BAC's were already below the experimental uncertainties in the chlorofluoromethanes. In contrast, for the fluoroethanes, the the comparatively large residual errors (RMS2) and negative average deviations (AVE2) indicate that the introduction of a heavy atom interaction parameter is necessary in this series to account for enhanced errors due to the presence of a second carbon atom attached to the carbon containing the C-C bond. In the spirit of the BAC-MP4 procedure, one may write: $\Delta_{BAC} = n_{C-F}\Delta_{C-F}f_C$, where f_C is the interaction parameter representing the impact of a second attached carbon on the error due to

the C-F bond. This has no impact on the C1's since $\xi = 1$ if there is no second carbon.

One may solve for Δ_{BAC} via linear regression (constrained to pass through the origin) to fit Δ_{BAC} to the deviations of the *ab initio* enthalpies from experiment, with the product $n_{C-F}\Delta_{C-F}$ as the independent variable. The resultant values of the interaction parameter are shown in the third column of category C in Table 2. The estimated errors in Δ_{BAC} may be obtained from either (a) the standard deviation of the parameter obtained from the least squares fit, or (b) the variation in the parameter when Δ_{BAC} is varied between its upper and lower limits ($\pm \sigma$). The estimates given in the table represent the larger of these two values. The very large value of $\sigma(\Delta_{BAC})$ for the CBS-4 method is a consequence of the large error in Δ_{BAC} for this method and the fact that, as mentioned above, errors in the CBS-4 enthalpies of formation are largely random.

It is very satisfying to observe from RMS2 in category C that the RMS residuals using a C-F BAC with an Δ_{BAC} interaction parameters are reduced significantly for all but the CBS-4 method. Further, the much smaller negative values of AVE2, relative to category B, indicates that almost all of the remaining systematic error has been removed from the BAC corrected enthalpies of formation. With the exception of the CBS-4 method, values of RMS2 have been reduced to values comparable to the RMS experimental uncertainty. The removal of systematic error is also demonstrated in Fig. 1, in which, with the exception of the CBS-4 method, errors in the BAC corrected enthalpies of formation (open circles and dashed line) are clustered about zero.

Individual BAC corrected enthalpies of formation in the fluoromethanes, using Δ_{BAC} from Ref. [3] and Δ_{BAC} from this work (category C of Table 2) are presented in Table 1B. It is of interest to note that BAC-G2, BAC-G2(MP2) and BAC-CBS-Q enthalpies agree with experiment to within 10 kJ/mol (and are usually much closer), except for $\text{CH}_2\text{FCH}_2\text{F}$, where all three methods exhibit markedly negative deviations from the reported value. Since the reported uncertainty in the experimental enthalpy of this compound is quite large (Table 1A), it is tempting to speculate that the literature value may be in error. If this compound is excluded from the statistics, then all three methods show RMS errors significantly under 5 kJ/mol, and average errors under 1 kJ/mol.

Finally, the last column of Table 1B contains errors in enthalpies of formation of the fluoroethanes calculated using the Melius BAC-MP4 procedure [9-11]. It was shown in Ref. [3]

that calculated enthalpies using this method are in excellent agreement with experimental results for the fluoromethanes. There are, however, rather large residual systematic errors in predicted values of ΔH° of the fluoroethanes, as illustrated by the RMS and average errors of 11.5 and -10.2 kJ/mol, respectively. From the table, it is seen that calculated enthalpies of the C2 series are uniformly more negative than results from the literature. Thus, it would appear that the C-C BAC and interaction parameters derived in the BAC-MP4 method to fit data in predominantly non-halogenated organics do not adequately characterize the systematic errors in fluoroethanes.

SUMMARY AND CONCLUSIONS

Enthalpies of formation of the fluoroethanes calculated by the G2, G2(MP2), CBS-4 and CBS-Q quantum mechanical procedures were found to exhibit substantial negative deviations from experiment. With the exception of the CBS-4 technique, where the deviations are random, the errors are proportional to the number of C-F bonds in the molecule. The application of a C-F bond additivity correction, , derived in an earlier investigation of fluoro- and chlorofluoromethanes, removed some, although not all of the systematic errors. Introduction of a further heavy atom interaction parameter, , to account for the impact of a second attached carbon on the C-F bond error, yielded BAC corrected enthalpies with RMS errors comparable to experimental uncertainties.

Additional calculations on fluoroethylenes and acetylenes, fluorocarbon radicals and reactive transition states are in progress to assess the capability of *ab initio* procedures with bond additivity corrections to predict accurate enthalpies of formation in these species.

REFERENCES

- [1] Banks, R. E. *J. Fluorine Chem.* **1994**, *67*, 193
- [2] Berry, R. J.; Burgess, D. R., Jr.; Nyden, M. R.; Zachariah, M. R.; Schwartz, M. "Halon Thermochemistry: *Ab Initio* Calculations of the Enthalpies of Formation of Fluoromethanes," *J. Phys. Chem.* **1995**, *99*, 17145.
- [3] Berry, R. J.; Burgess, D. R., Jr.; Nyden, M. R.; Zachariah, M. R.; Schwartz, M. "Halon Thermochemistry: Calculated Enthalpies of Formation of Chlorofluoromethanes," *J. Phys. Chem.* **1996**, *100*, 7405.

- [4] The systems investigated in Ref. [3] include methane, the four fluoromethanes, the four chloromethanes, and the six mixed species.
- [5] Gaussian 90, Revision F, Gaussian, Inc.: Pittsburgh, PA, 1990.
- [6] Gaussian 92, Revision F.4., Gaussian, Inc.: Pittsburgh, PA, 1992.
- [7] Gaussian 94, Revision A.1, Gaussian, Inc., Pittsburgh, PA, 1995.
- [8] Certain commercial equipment, instruments, or materials are identified in this paper in order to specify the experimental procedure adequately. In no case does such identification imply recommendation or endorsement.
- [9] Melius, C. F. Thermochemistry of Hydrocarbon Intermediates in Combustion. Applications of the BAC-MP4 Method. In *Springer-Verlag DFVLR Lecture Notes*; Springer-Verlag: Berlin, 1990.
- [10] Melius, C. F. Thermochemical Modeling I. Application to Ignition and Combustion of Energetic Materials. *Chemistry and Physics of Energetic Materials*; S. N. Kluwer Academic: New York, 1992.
- [11] Ho, P.; Melius, C. F. *J. Phys. Chem.* **1990**, *94*, 5120
- [12] Pople, J. A.; Head-Gordon, M.; Fox, D. J.; Raghavachari, K.; Curtiss, L. A. *J. Chem. Phys.* **1989**, *90*, 5622.
- [13] Curtiss, L. A.; Jones, C.; Trucks, G. W.; Raghavachari, K.; Pople, J. A.; *J. Chem. Phys.* **1990**, *93*, 2537.
- [14] Curtiss, L. A.; Raghavachari, K.; Trucks, G. W.; and Pople, J. A. *J. Chem. Phys.* **1991**, *94*, 7221.
- [15] Petersson, G. A.; Al-Laham, M. A. *J. Chem. Phys.* **1991**, *94*, 6081
- [16] Ochterski, J. W.; Petersson, G. A.; Montgomery, J. A., Jr. *J. Chem. Phys.* submitted.
- [17] Nyden, M. R.; Petersson, G. A. *J. Chem. Phys.* **1981**, *75*, 1843. (b) Petersson, G. A.; Nyden, M. R. *J. Chem. Phys.* **1981**, *75*, 3423. (c) Petersson, G. A.; Licht, S. L. *J. Chem. Phys.* **1981**, *75*, 4556. (d) Petersson, G. A.; Yee, A. K.; Bennett, A. *J. Chem. Phys.* **1985**, *83*, 5105. (e) Petersson, G. A.; Braunstein, M. *J. Chem. Phys.* **1985**, *83*, 5129.
- [18] Petersson, G. A.; *Proc. Nat. Acad. Sci. (USA)* **1974**, *71*, 2795
- [19] Durig, J. R.; Liu, J.; Little, T. S.; Kalasinsky, V. F. *J. Phys. Chem.* **1992**, *96*, 8224.

- [20] Kalasinsky, V. F.; Anjaria, H. V.; Little, T.S. *J. Phys. Chem.* **1982**, *86*, 1351.
- [21] Tsang, W.; Hampson, R. F. *J. Phys. Chem. Ref. Data* **1986**, *15*, 1087.
- [22] Chen, S. S.; Rodgers, A. S.; Chao, J.; Wilhoit, R. C.; Zwolinski, B. J. *J. Phys. Chem. Ref. Data* **1975**, *4*, 441.
- [23] Burgess, D. R., Jr.; Zachariah, M. R.; Tsang, W.; Westmoreland, P. R. 'Thermochemical and Chemical Kinetic Data for Fluorinated Hydrocarbons.' *Prog. Energy Combust. Sci.* **1996**, *21*, 453.
- [24] Lacher, J. A.; Skinner, H. A. *J. Chem. Soc. (A)* **1968**, 1034.
- [25] Fits of $\Delta H^\circ(\text{calc}) - \Delta H^\circ(\text{expt})$ vs. n_{CF} to second order polynomials yielded statistically insignificant quadratic terms.
- [26] The standard errors in Δ_{CH} and Δ_{CF} (Table 2) are equal because of the multicollinearity of the two variables, n_{CH} and n_{CF} .
- [27] One observes from category B of Table 6 that, for all four methods, Δ_{CH} is relatively small and comparable to or less than the standard error in this parameter.
- [28] Kolesov, V. P. *Russ. Chem. Rev.* **1978**, *47*, 599.
- [29] For all four *ab initio* methods, the slopes of the plots of $\Delta H^\circ(\text{BAC}) - \Delta H^\circ(\text{expt})$ vs. n_{CF} [dashed lines in Fig. 1] are smaller than their standard deviations.

CHAPTER 2. Calculated Enthalpies of Formation of Fluoroethylenes and Acetylenes

INTRODUCTION

Because of their stratospheric ozone depletion potential [1], manufacture of currently used halon fire suppressants (e.g. CF_3Br , CF_2ClBr , $\text{CF}_2\text{BrCF}_2\text{Br}$) has been banned under the Montreal Protocols [2]. In order to obtain the requisite data to model the mechanism of flame suppression by potential halon replacements, we have utilized *ab initio* quantum mechanics to predict accurate thermochemical data [3-5] and rate constants [6] for the reactions of HFC's and CFC's and their decomposition products.

We have recently completed investigations on the application of various current methods

[G2, G2(MP2), CBS-Q and CBS-4] to calculate the enthalpies of formation [ΔH°] of fluoro-, chloro- and chlorofluoromethanes and fluoroethanes [3-5]. Fluoroethylenes are important intermediates in the flame chemistry of HFC's [7,8]. Hence, we have chosen to extend the G2 and G2(MP2) calculations to these species as well as the fluoroacetylenes to ascertain the capability of these methods to furnish accurate enthalpies of formation in unsaturated C2 fluorocarbons.

CALCULATIONS

The calculations were performed using the GAUSSIAN code [9,10] on HP-PARisk, CRAY Y-MP, IBM R6000, SUN-Sparc and SGI Power-Challenge computers. Geometries were calculated at both the HF/6-31G(d) and MP2(FU)/6-31G(d) levels for ethylene, acetylene and the eight fluorinated derivatives. Vibrational frequencies (scaled by 0.8929) were obtained using the HF/6-31G(d) basis. These quantities are required for determination of the ground state G2 and G2(MP2) electronic energies and for calculation of the temperature dependence of molecular heat capacities, entropies and reaction enthalpies. The G2 and G2(MP2) procedures have been presented in the original articles [11,12] as well as in an earlier paper from this laboratory [3].

Molecular and atomic electronic energies and heat capacities, together with elemental enthalpies of formation, were utilized to evaluate molecular enthalpies of formation at 298.15 K [(298)]. The computational procedures have been detailed elsewhere [3,13].

RESULTS AND DISCUSSION

Experimental and calculated enthalpies of formation are presented in Table 3. Recommended literature values, with their estimated uncertainties, are taken from the NIST compilation [7] for fluoroethylenes and from the JANAF tables for the fluoroacetylenes [13].

Calculated G2 and G2(MP2) enthalpies are given in columns 3 and 4 of Table 3; the quantities in parentheses represent deviations from the literature data. It is clear from the table that these deviations are quite large for both methods, as evidenced by the RMS errors for the

fluoroethylenes which are more than three times greater than the experimental uncertainties. One sees similarly large errors in calculated enthalpies of the fluoroacetylenes, although uncertainties in the experimental results are unusually high.

Significantly, one finds from the large negative average deviations that they are not randomly distributed. The systematic nature of errors in the calculated G2 and G2(MP2) enthalpies of formation are well illustrated in Figure 2, where values of [(calc) - (expt)] are plotted versus the number of C-F bonds (n_{CF}) for both the fluoroethylenes (closed circles) and fluoroacetylenes (open circles). Although there is significant scatter in the data, which may partially be attributed to errors in the experimental enthalpies, one sees that, for both methods, the negative deviations increase approximately linearly with n_{CF} .

This behavior is quite similar to that observed in our recent investigations of fluoro-, chloro- and chlorofluoromethanes [3-4], in which the errors in *ab initio* enthalpies of formation were linearly dependent upon the number of C-F and C-Cl bonds. In these studies, the quality of the calculated results were improved markedly by the application of linear Bond Additivity Corrections (BAC's) proportional to the number each type of carbon-halogen bond. For fluoromethanes, the use of a single BAC, Δ_{CF} , representing the error per C-F bond, reduced the RMS deviation from experiment to a value substantially less than the RMS uncertainties in the reported literature values. In a later investigation of predictions of in fluoroethanes [5], it was found that there is a "heavy atom" interaction between the second carbon the fluorine, which increased the errors due to the C-F bonds. Incorporating an interaction parameter, ξ , reduced RMS errors in this series to values comparable to the reported RMS experimental uncertainties.

It is straightforward to apply a BAC to the calculated *ab initio* enthalpies of formation, (calc) , to obtain corrected values, (BAC) , via the relation: $\Delta H_f^\circ(\text{BAC}) = \Delta H_f^\circ(\text{calc}) - \Delta_{CF} n_{CF}$. To test the transferability of BAC's between different series of halocarbons, we have chosen to utilize this equation with values of Δ_{CF} and determined for the saturated HFC's [4, 5,14] to obtain corrected G2 and G2(MP2) enthalpies of formation in the fluoroethylenes and acetylenes. The results are displayed in the last two columns of Table 3.

It is immediately apparent that there is a dramatic improvement in the quality of the calculated enthalpies. RMS deviations have dropped by a factor of 2 in the acetylenes and by 4-5 in the ethylenes and, for both series, are below the uncertainties in the reported experimental data. Additionally, as indicated by the small residual average deviations in both series, almost all of the systematic error has been removed.

As noted by Melius in his development of the BAC-MP4 method [15,16], the heavy atom interaction parameter is expected to be dependent upon bond length (increasing for shorter bonds). Thus, one expects that errors in the BAC-corrected enthalpies could be reduced still further by reoptimizing for the multiply bonded systems studied here [17]. However, we find it quite satisfying that use of a BAC and interaction parameter derived purely from data on fluoromethanes and ethanes yields such excellent agreement between theory and experiment in the unsaturated fluoroethylenes and acetylenes.

Finally, we discuss briefly the enthalpy of formation of fluoroacetylene. As shown in Table 3, there is an extremely high estimated uncertainty (63 kJ/mol) for this enthalpy, resulting directly from the fact that there has been no experimental determination of ; the value reported in the literature [13] was obtained using average bond enthalpies. However, based upon our observation that BAC-corrected enthalpies of formation in all of the fluorocarbons studied to date have been accurate to within approximately 10 kJ/mol (and usually much better) for molecules with accurately measured experimental heats, we propose that the value, $[\Delta H^\circ(H-C\equiv C-F)] = 114 \pm 10$ kJ/mol, furnishes a more reliable estimate, with reasonable error limits, than available from average bond enthalpy calculations.

REFERENCES

- [1] G. Baes, G. ANPI Mag. 112 (1992) 43.
- [2] W.Tsang and A. W. Mizolek, eds, Halon Replacements: Technology and Science; ACS Symposium Series 611, American Chemical Society, Washington, D. C. (1995).
- [3] R. J. Berry, D. R. Burgess, Jr., M. R. Nyden, M. R.; Zachariah and M. Schwartz, J. Phys. Chem. **99** (1995) 17145.
- [4] R. J. Berry, D. R. Burgess, Jr., M. R. Nyden, M. R.; Zachariah, C. F. Melius and M.

Schwartz, J. Phys. Chem. 100 (1996) 7405.

- [5] R. J. Berry, C. J. Ehlers, D. R. Burgess, Jr.; M. R. Zachariah, M. R. Nyden and M. Schwartz, "Halon Thermochemistry: Ab Initio Calculations of the Enthalpies of Formation of Fluoroethanes," J. Molec. Struct. (Theochem), (Submitted)
- [6] R. J. Berry, C. J. Ehlers, D. R. Burgess, Jr., M. R. Zachariah and P. Marshall, "A Computational Study of the Reactions of Atomic Hydrogen with Fluoromethanes: Kinetics and Product Channels," Chem. Phys. Letters, (Submitted)
- [7] "Thermochemical and Chemical Data for Fluorinated Hydrocarbons," D. R. F. Burgess, Jr., M. R. Zachariah, W. Tsang and P. R. Westmoreland, National Institute of Standards and Technology, Technical Note 1412, U. S. Government Printing Office, Washington (1995).
- [8] Fluoroethylenes are formed in flames by thermal decomposition of fluoroethanes, activated decomposition of fluoroethyl radicals, and fluoromethyl radical recombination reactions (Ref. 7)
- [9] Gaussian 92, Revision F.4, Gaussian, Inc.: Pittsburgh, PA, 1992.
- [10] Gaussian 94, Revision A.1, Gaussian, Inc., Pittsburgh, PA, 1995.
- [11] L. A. Curtiss, K. Raghavachari, G. W. Trucks and J. A. Pople, J. Chem. Phys. 94 (1991) 7221.
- [12] L. A. Curtiss, K. Raghavachari, and J. A. Pople, J. Chem. Phys. 98 (1993) 1293.
- [13] M. W. Chase, Jr., C. A. Davies, J. R. Downey, Jr., D. J. Frurip, R. A. McDonald and A. N. Syverud, JANAF Thermochemical Tables, 3rd. ed. J. Phys. Chem. Ref. Data, Suppl. 1, 14 (1985).
- [14] From Refs. [4,5], $\Delta_{\text{cf}}[\text{G}2] = -6.51 \text{ kJ/bond}$, $\text{fc}[\text{G}2] = 1.24$; $\Delta_{\text{cf}}[\text{G}2(\text{MP}2)] = -7.98 \text{ kJ/bond}$, $\text{fc} = 1.20$.
- [15] Melius, C. F. Thermochemistry of Hydrocarbon Intermediates in Combustion. Applications of the BAC-MP4 Method. In *Springer-Verlag DFVLR Lecture Notes*; Springer-Verlag: Berlin, 1990.
- [16] Melius, C. F. Thermochemical Modeling I. Application to Ignition and Combustion of Energetic Materials. *Chemistry and Physics of Energetic Materials*; S. N. Kluwer Academic: New York, 1992.
- [17] For example, if fc is reoptimized to minimize RMS errors in the G2 enthalpies of the fluoroethylenes, then the value of the parameter increases slightly (to fc=1.37) and the RMS and average errors are reduced to 4.1 and -0.2 kJ/mol, respectively.

Table 1. Enthalpies of Formation in Fluoroethanes.^a

A. Ab Initio Enthalpies

Species	Exp.	G2 ^b	G2(MP2) ^b	CBS-4 ^c	CBS-Q ^b
CH₃-CH₃	-84.1 ±0.4 [20]	-86.0 (-1.9)	-83.1 (1.0)	-92.1 (-8.0)	-81.5 (2.6)
CH₃-CH₂F	-263.2 ±1.6 [21]	-279.7 (-16.5)	-279.5 (-16.3)	-277.7 (-14.5)	-274.1 (-10.9)
CH₂F-CH₂F	-433.9 ±11.8 [22]	-461.4 (-27.5)	-464.1 (-30.2)	-450.9 (-17.0)	-454.8 (-20.9)
CH₃-CHF₂	-500.8 ±6.3 [21]	-516.4 (-15.6)	-518.3 (-17.5)	-508.5 (-7.7)	-510.0 (-9.2)
CH₂F-CHF₂	-664.8 ±4.2 [23]	-687.1 (-22.3)	-691.8 (-27.0)	-669.4 (-4.6)	-679.7 (-14.9)
CH₃-CF₃	-745.6 ±1.6 [21]	-772.1 (-26.5)	-775.4 (-29.8)	-760.0 (-14.4)	-764.4 (-18.8)
CHF₂-CHF₂	-877.8 ±17.6 [22]	-906.7 (-28.9)	-913.3 (-35.5)	-875.2 (2.6)	-898.2 (-20.4)
CH₂F-CF₃	-895.8 ±4.2 [21]	-934.2 (-38.4)	-940.2 (-44.4)	-911.9 (-16.1)	-925.0 (-29.2)
CHF₂-CF₃	-1104.6 ±4.6 [21]	-1145.9 (-41.3)	-1153.9 (-49.3)	-1116.0 (-11.4)	-1135.2 (-30.6)
CF₃-CF₃	-1342.7 ±6.3 [21]	-1383.7 (-41.0)	-1392.9 (-50.2)	-1348.4 (-5.7)	NA
RMS	±7.7	28.6	33.6	11.3	19.5
AVG	--	-26.0	-29.9	-9.7	-16.9

Table 1. (Cont'd.)**B. Enthalpies Calculated with Bond Additivity Corrections.**

Species	G2 ^b [BAC]	G2(MP2) ^b [BAC]	CBS-4 ^b [BAC]	CBS-Q ^b [BAC]	BAC-MP4 ^b
CH ₃ -CH ₃	-86.0 (-1.9)	-83.1 (1.0)	-92.1 (-8.0)	-81.5 (2.6)	-86.94 (-2.8)
CH ₃ -CH ₂ F	-271.6 (-8.4)	-269.9 (-6.7)	-275.5 (-12.3)	-267.9 (-4.7)	-272.35 (-9.2)
CH ₂ F-CH ₂ F	-445.3 (-11.4)	-444.9 (-11.0)	-446.5 (-12.6)	-442.3 (-8.4)	-445.96 (-12.1)
CH ₃ -CHF ₂	-500.3 (0.5)	-499.1 (1.7)	-504.1 (-3.3)	-497.5 (3.3)	-505.34 (-4.5)
CH ₂ F-CHF ₂	-662.9 (1.9)	-663.1 (1.7)	-662.8 (2.0)	-661.0 (3.8)	-671.5 (-6.7)
CH ₃ -CF ₃	-747.9 (-2.3)	-746.7 (-1.1)	-753.4 (-7.8)	-745.7 (-0.1)	-755.44 (-9.8)
CHF ₂ -CHF ₂	-874.4 (3.4)	-875.0 (2.8)	-866.3 (11.5)	-873.2 (4.6)	-883.31 (-5.5)
CH ₂ F-CF ₃	-901.9 (-6.1)	-901.9 (-6.1)	-903.0 (-7.2)	-900.0 (-4.2)	-913.3 (-17.5)
CHF ₂ -CF ₃	-1105.5 (-0.9)	-1106.0 (-1.4)	-1104.9 (-0.3)	-1104.0 (0.6)	-1124.1 (-19.5)
CF ₃ -CF ₃	-1335.3 (7.4)	-1335.4 (7.3)	-1335.1 (7.6)	NA	-1357 (-14.3)
RMS	5.6	5.2	8.3	4.3	11.5
AVG	-1.8	-1.2	-3.0	-0.3	-10.2

a) $\Delta_f H^\circ$ at 298.15 K in units of kJ/mol.

b) Values in parentheses represent deviations from experiment.

Table 2. Bond Additivity Correction Parameters in Fluoroethanes.

Method	Δ_{CF}	f_c	RMS1 ^b	AVE1 ^a	RMS2 ^c	AVE2 ^c
Expt.			±4.1	±4.8		
A. Ab Initio						
G2	0.0	0.0	14.8	-13.1	28.6	-26.0
G2(MP2)	0.0	0.0	18.4	-15.7	33.6	-29.9
CBS-4	0.0	0.0	2.8	-1.7	11.3	-9.7
CBS-Q	0.0	0.0	8.6	-7.0	19.5	-16.7
B. Δ_{CF}						
BAC-G2	-6.51 ± 0.41	0.0	3.2	-0.1	7.9	-6.5
BAC-G2(MP2)	-7.98 ± 0.38	0.0	2.6	0.2	7.6	-6.0
BAC-CBS-4	-1.28 ± 0.74	0.0	3.3	0.9	8.9	-5.8
BAC-CBS-Q	-3.51 ± 0.55	0.0	1.6	0.1	9.4	-7.6
C. $\Delta_{CF} + f_c$						
BAC-G2	-6.51 ± 0.41	1.24 ± 0.08	3.2	-0.1	5.6	-1.8
BAC-G2(MP2)	-7.98 ± 0.38	1.20 ± 0.06	2.6	0.2	5.2	-1.2
BAC-CBS-4	-1.28 ± 0.74	1.73 ± 1.50	3.3	0.9	8.8	-3.0
BAC-CBS-Q	-3.51 ± 0.55	1.78 ± 0.29	1.6	0.1	4.3	-0.3

- a) in units of kJ/mol
- b) fluoromethanes (C1)
- c) fluoroethanes (C2)

Table 3. Enthalpies of Formation in Fluoroethylenes and Acetylenes.^a

Species	expt ^{b,c}	G2 ^c	G2(MP2) ^c	G2 ^c [BAC]	G2(MP2) ^c [BAC]
CH ₂ =CH ₂	52.4 ± 0.8	53.4 (1.0)	55.5 (3.1)	53.4 (1.0)	55.5 (3.1)
CH ₂ =CHF	-140.1 ± 2.5	-146.1 (-6.0)	-146.5 (-6.4)	-138.0 (2.1)	-136.9 (3.2)
CHF=CHF[Z]	-297.1 ± 10.0	-315.0 (-17.9)	-318.0 (-20.9)	-298.9 (-1.8)	-298.8 (-1.7)
CHF=CHF[E]	-292.9 ± 10.0	-318.3 (-25.4)	-321.6 (-28.7)	-302.2 (-9.3)	-302.4 (-9.5)
CH ₂ =CF ₂	-336.4 ± 4.0	-359.0 (-22.6)	-361.4 (-25.0)	-342.9 (-6.5)	-342.2 (-5.8)
CHF=CF ₂	-491.0 ± 9.0	-512.4 (-21.4)	-517.7 (-26.7)	-488.2 (2.8)	-489.0 (2.0)
CF ₂ =CF ₂	-658.5 ± 2.9	-693.0 (-34.5)	-700.8 (-42.3)	-660.7 (-2.2)	-662.5 (-4.0)
RMS	6.7	21.3	25.2	4.6	4.9
AVG		-18.1	-21.0	-2.0	-1.8
CH≡CH	226.7 ± 0.8	234.6 (7.9)	236.8 (10.1)	234.6 (7.9)	236.8 (10.1)
CH≡CF	125.5 ± 63.0	106.2 (-19.3)	105.6 (-19.9)	114.3 (-11.2)	115.2 (-10.3)
CF≡CF	20.9 ± 21.0	0.5 (-20.4)	-3.1 (-24.0)	16.6 (-4.3)	16.0 (-4.9)
RMS	38.3	16.9	18.9	8.3	8.8
AVG		-10.6	-11.3	-2.5	-1.7

a) Enthalpies at 298.15 K and 1 atm in units of kJ/mol.

b) Experimental enthalpies taken from Refs. 7 (fluoroethylenes) and 13 (fluoroacetylenes).

c) Values in parentheses represent deviations from experiment.

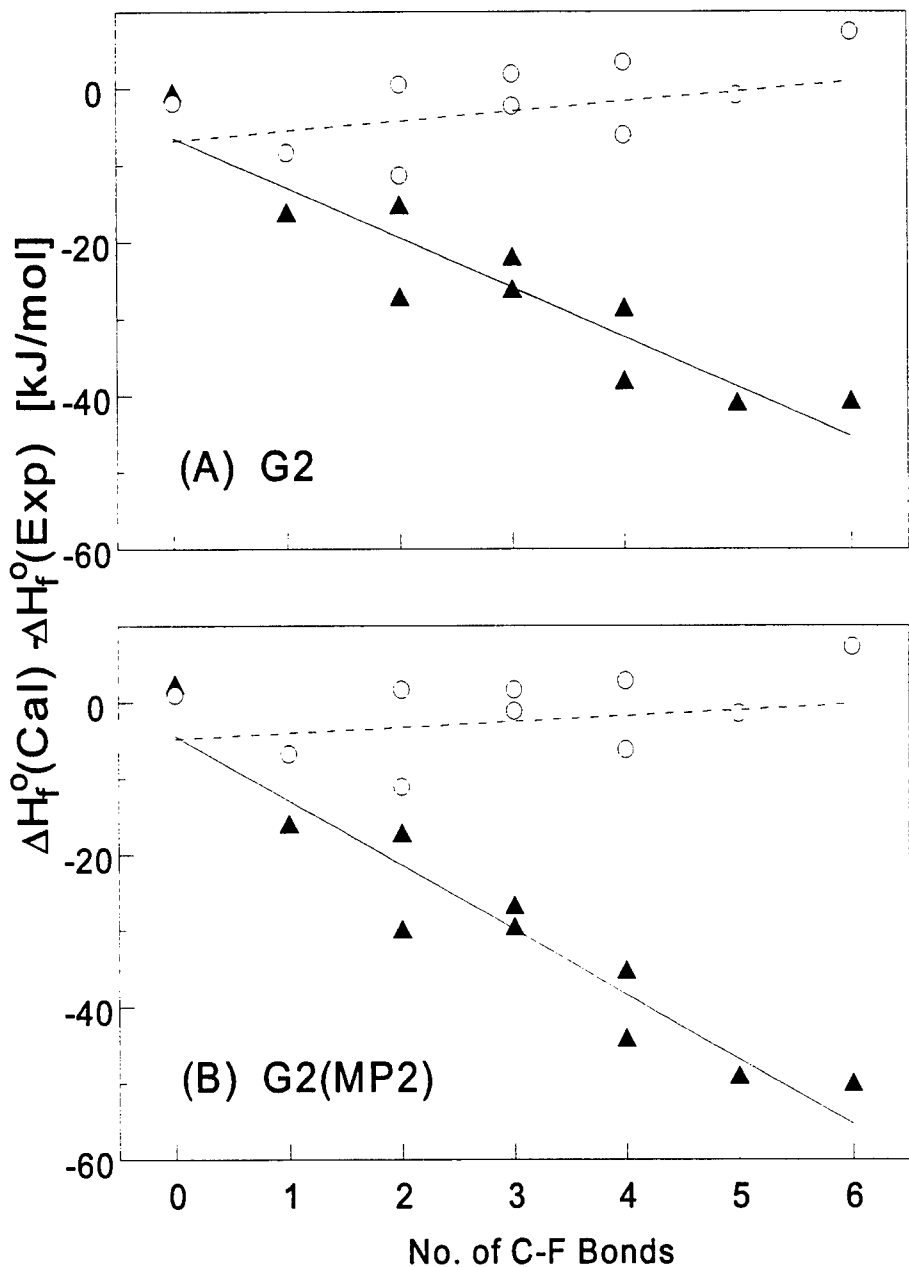


Figure 1. Errors in Enthalpies of Formation in Fluoroethanes. Closed symbols and solid lines - Ab Initio Enthalpies; Open Symbols and dashed lines - BAC corrected Enthalpies.

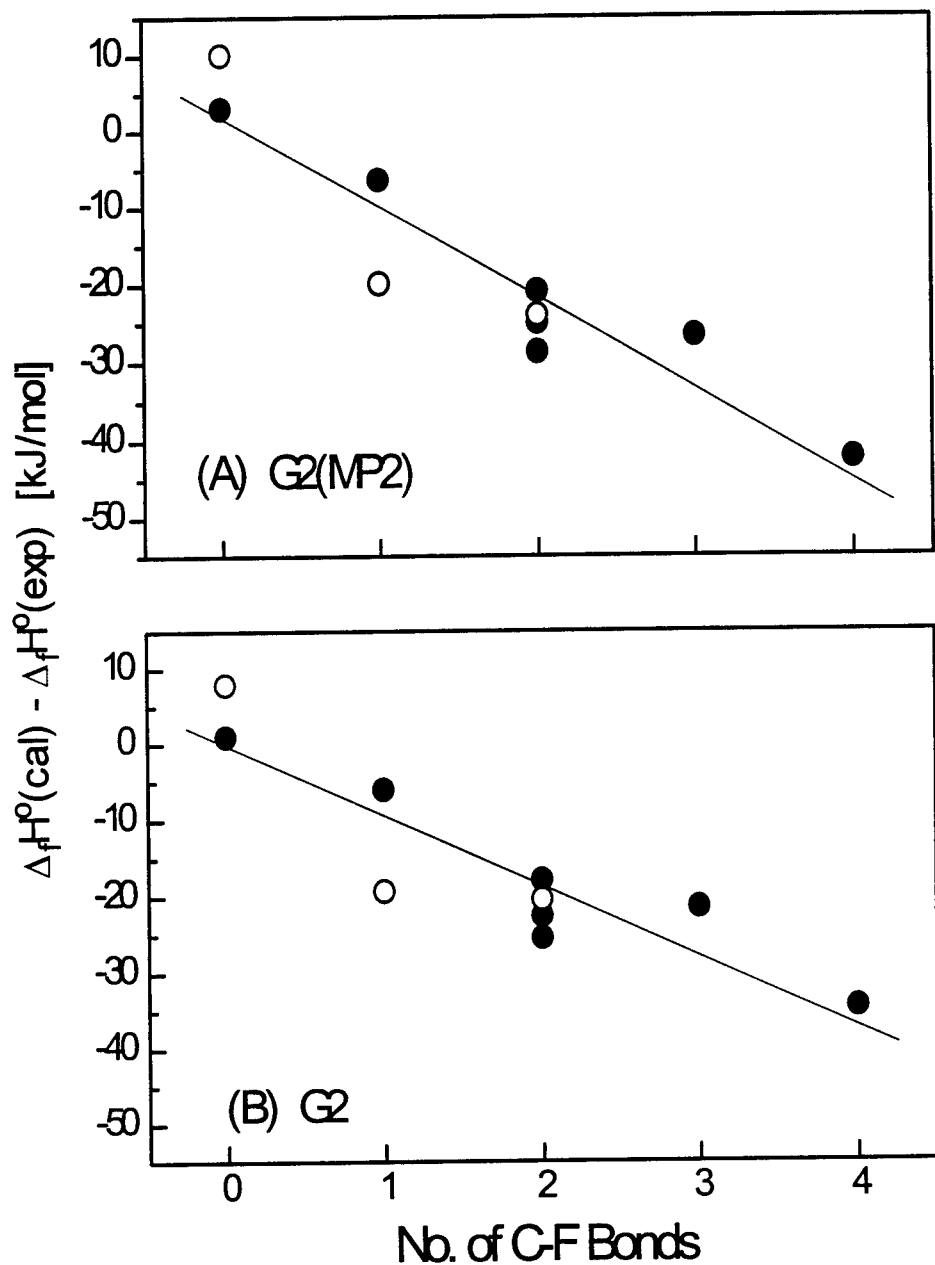


Figure 2. Errors in Enthalpies of Formation of Fluoroethylenes and Acetylenes.
Closed symbols - fluoroethylenes; Open symbols - fluoroacetylenes.

Investigation of SLIP Boundaries in 4H-SiC Crystals

Dr. Marek Skowronski
Professor
Department of Materials Science and Engineering

Carnegie Mellon University
Pittsburgh, PA

Final Report for:
Summer Research Extension Program
Wright Patterson Air Force Base

Sponsored by:
Air Force Office of Scientific Research
Bolling Air Force Base
Washington, D.C.

and

Wright Patterson AFB

December 1997

INVESTIGATION OF SLIP BOUNDARIES IN 4H-SiC CRYSTALS

Final Report

Dr. Marek Skowronski

Department of Materials Science and Engineering

Carnegie Mellon University

Abstract

The goal of the investigation was to describe the morphology of dislocation arrays observed in KOH-etched silicon carbide wafers and determine their origin. Number of wafers from several manufacturers has been etched and etch pit patterns have been analyzed. In addition to basal plane dislocation arrays, two types of etch pit arrays have been observed. The first type is interpreted as slip band traces due to $\langle 2\bar{1}\bar{1}0 \rangle \langle 1\bar{1}00 \rangle$ secondary slip system. The arrays start at the wafer periphery in proximity of misoriented grains and extend along $\langle 1\bar{1}00 \rangle$ directions for a distance of up to a centimeter. The second type of array is also made of edge dislocations with Burgers vector $\frac{a}{3} \langle 2\bar{1}\bar{1}0 \rangle$ and dislocation line direction [0001]. In distinction to the slip array, the etch pits are aligned along $\langle 2\bar{1}\bar{1}0 \rangle$ directions. It is proposed that $\langle 2\bar{1}\bar{1}0 \rangle$ arrays are produced by polygonization of slip bands during crystal growth. This interpretation is supported by high resolution x-ray diffraction mapping.

Introduction

High breakdown field (3.5×10^6 V/cm for $N_D = 10^{17}$ cm⁻³) and thermal conductivity (4.9 W/cmK) make silicon carbide well suited for the high power/high frequency/high voltage devices. Several different figures of merit have been proposed to estimate material suitability for these applications [1-4]. All of them indicate silicon carbide properties to be far superior to those of silicon and traditional III-V compounds and second only to diamond. This research project is particularly relevant to SiC application in devices intended for high voltage switching with applications in power transmission and conditioning. The device structures of primary interest are GTO and MTO thyristors rated for voltages in excess of 10 kV and currents above 1000 A. High blocking voltages and current ratings require low defect density / large active area of a device. Modern silicon-based thyristors occupy the entire area of a 3 inch diameter silicon wafer and this is the desired size of defect-free silicon carbide substrates.

High voltage devices are extremely demanding in terms of material quality including virtually zero extended defect density, and close tolerances on doping and thickness uniformity across the wafer. In silicon diodes premature breakdown was observed by non-formation of localized microplasma at precipitates [5-8], stacking faults [5,6], field non-uniformities due to obstructed diffusion [9], D-defects [10] misfit dislocations[7] and microcracks [11]. In silicon carbide one can expect most extended defects to cause premature breakdown as well. Currently available experimental evidence clearly shows micropipes to be the most detrimental defect for high voltage diodes [12,13]. They have been observed to cause catastrophic diode breakdown destroying the device [14]. Recently NASA Lewis / SUNY team demonstrated that a single c perfect screw dislocation can be responsible for lowering of the breakdown voltage [15]. It is clear, therefore, that the SiC material quality will be of utmost importance for the success of SiC power electronics. Current SiC power device technology relies almost exclusively on homoepitaxially grown SiC structures. Bearing in mind that threading defects will propagate from substrate into the active part of the device, it is critical to improve crystalline quality of SiC boules.

In order to reduce or eliminate the extended defects in SiC boules one has to start with identification of types of defects present. This step could lead to understanding of mechanisms responsible for defect nucleation.

Results and discussion

Figure 1 shows an optical micrograph of a KOH etched 4H-SiC (0001) wafer (Si face). On the right side of the figure, it is possible to see an edge of a wafer with a misoriented grain of 15R polytype. Starting at the grain boundary is a horizontal band of etch pits. The width of the band is approximately 100 μm with the length of 5 mm (not all of the band is shown in the figure). The long axis of the band extends along $\langle 1\bar{1}00 \rangle$ type direction. Many such bands have been observed in the proximity of similar polytypic inclusions at the crystal periphery with all three $\langle 1\bar{1}00 \rangle$ equivalent directions present.

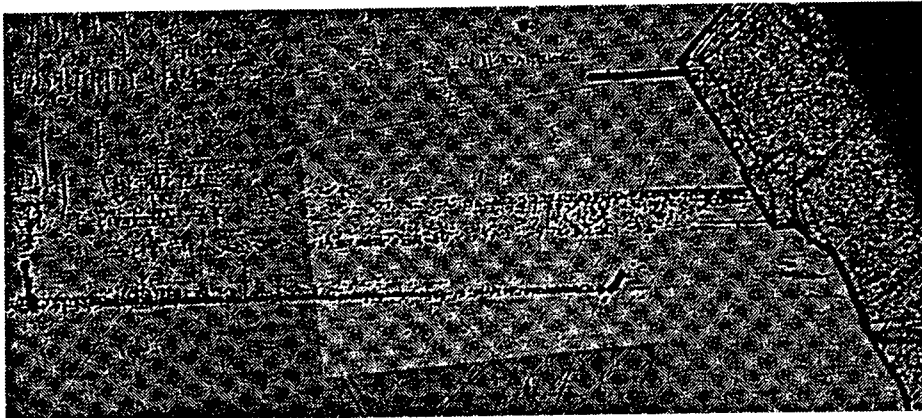


Fig. 1 Slip band extending along $[1\bar{1}00]$ on the (0001) wafer surface (Si-face of (0001) 4H-SiC wafer etched in molten KOH at 530 °C for 10 minutes, optical image, magnification x100).

The band has a typical characteristics of a slip trace. The polytypic inclusion served as a source of stress during crystal cool down due to the difference in thermal expansion coefficient between crystal and the inclusion. At some point during cool down, the stress exceeded critical resolved shear stress and the crystal deformed plastically. Hexagonal materials are known to have two slip systems. The primary slip system is $\frac{a}{3}\langle 2\bar{1}\bar{1}0 \rangle(0001)$ but at high temperatures an additional $\frac{a}{3}\langle 2\bar{1}\bar{1}0 \rangle\{10\bar{1}0\}$ slip system can be activated. The intersection of $\{10\bar{1}0\}$ type plane with basal plane gives $\langle 10\bar{1}0 \rangle$ type direction in agreement experimental etch pit pattern shown in Fig. 1.

An additional evidence supporting the above interpretation was obtained by high resolution x-ray diffraction mapping. Two basal-plane reflection ω -scans across the slip band shown in Fig. 1 were obtained and are shown in Fig. 2 and 3. All data have been obtained by performing ω -scan in triple axis mode. This scan allows for precise measurement of tilt of the basal plane across the boundary. Fig. 2(a) shows a (0008) peak position with the diffraction plane parallel to the slip band while the Fig. 2b shows the change of the reflection's full width at half maximum (FWHM). The slip band was located at approximately 7 mm. It is clear that at the band location the reflection FWHM broadens considerably but the total misorientation across the band is less than 20 arc seconds. Two other slip bands were present in the scanned part of the crystal (located at -4 and -1 mm) and show similar characteristics.

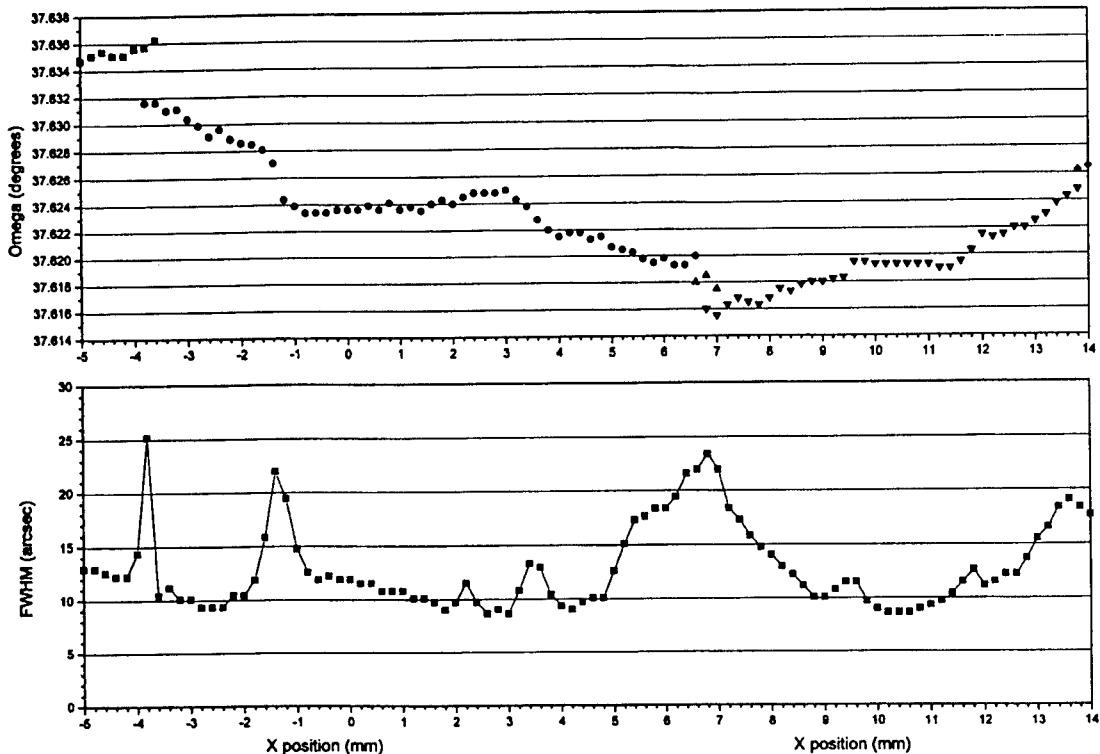


Fig. 2 (a) (0008) peak position versus location on the wafer. Spatial scan performed across the slip band shown in Fig. 1 with diffraction plane parallel to the slip band direction. 2 (b) Full width and half maximum for the same reflection.

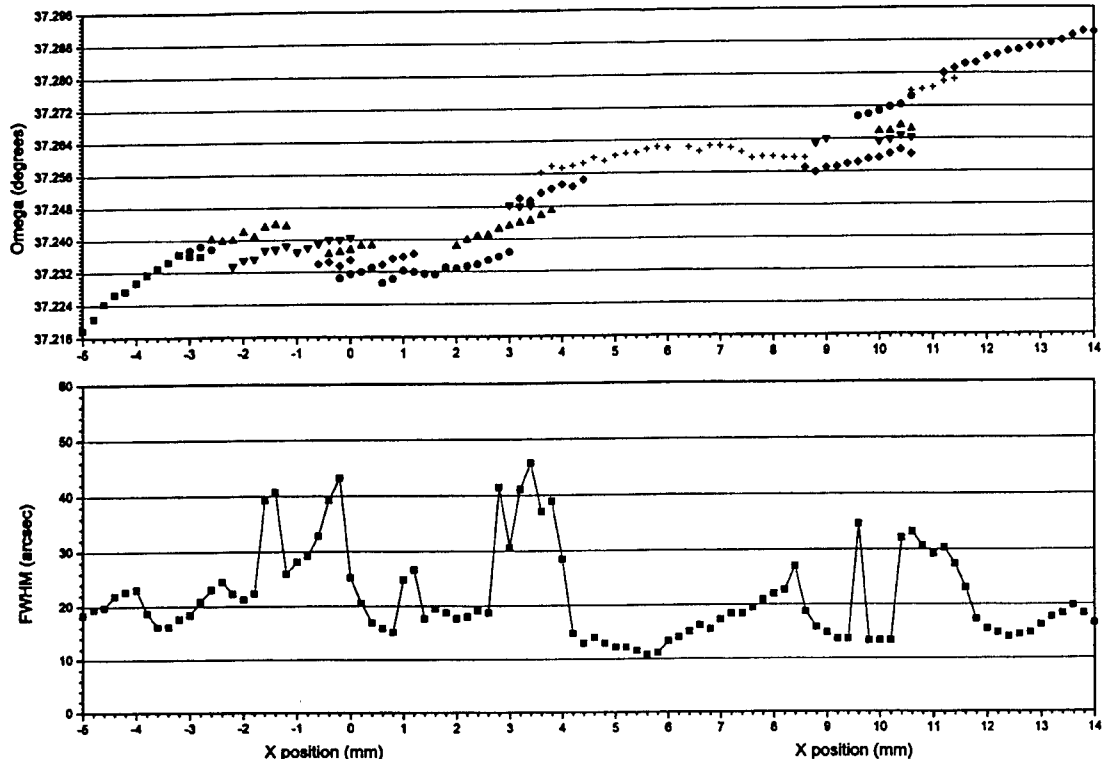
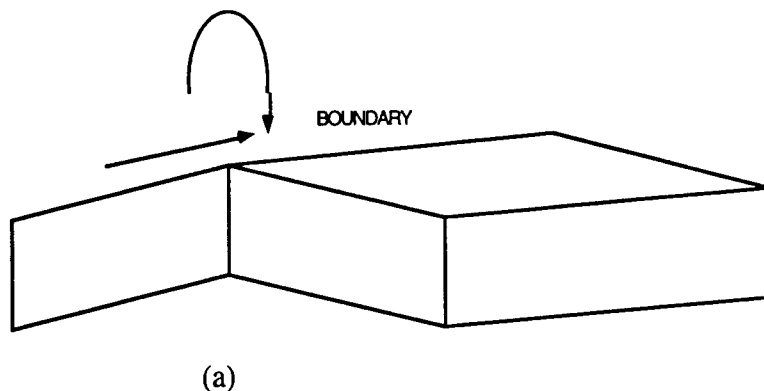
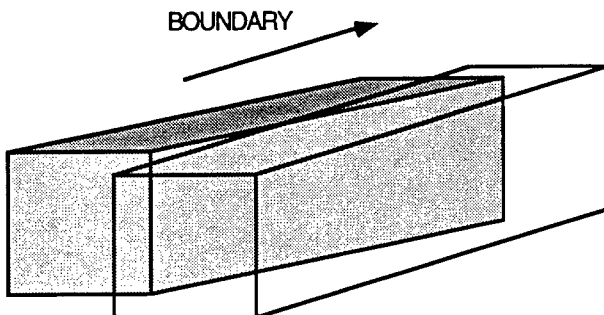


Fig. 3 (a) (0008) peak position versus location on the wafer. Spatial scan performed across the slip band shown in Fig. 1 with diffraction plane perpendicular to the slip band direction. 2 (b) Full width and half maximum for the same reflection.

Fig. 3 shows similar data with diffraction plane perpendicular to the slip band direction. The slip band is located at 10 mm. Again there is no measurable misorientation across the slip band. Since both scans used basal plane reflection, only the tilt components of misorientation could be determined. Fig. 4 shows the tilt misorientation measured in Fig. 2 while Fig. 5 shows misorientation measured in scan presented in Fig. 3. Absence of either type of tilt indicates that the slip band could only be associated with the twist in the basal plane. This is the type of misorientation expected if the dislocations making up the slip band belong to the $\frac{a}{3}\langle 2\bar{1}\bar{1}0 \rangle\{10\bar{1}0\}$ slip system.



(a)



(b)

Fig. 4 Two types of basal plane tilt boundaries

Independent supporting evidence of the nature of observed dislocations and dislocation arrays was obtained by observation of dislocation motion during annealing. At high temperatures, the edge dislocations within the slip band can arrange themselves “on top of each other” in order to minimize the total strain energy of the crystal. An example of such an arrangement is shown in Fig. 5.

The etch pit patterns observed on etched SiC wafers show clear evidence of such process being active in SiC during cool down (Fig. 6). The dislocations in the slip band generated at high temperature are aligning themselves in fine structure of lines perpendicular to the slip band trace.

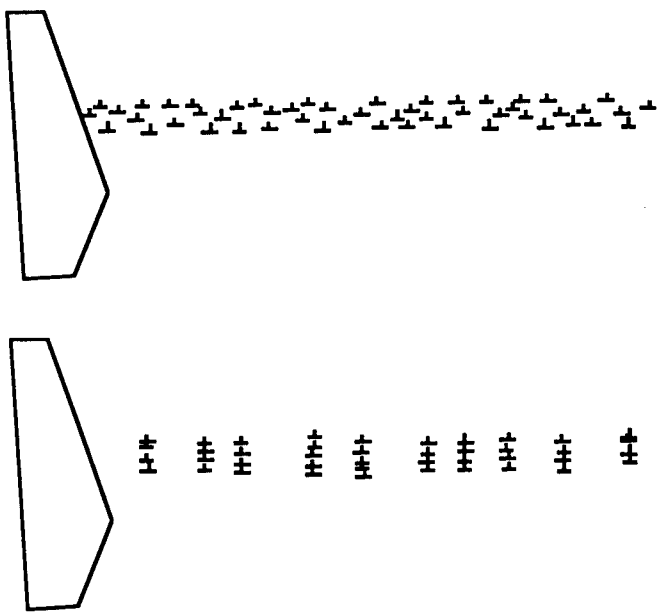


Fig. 5 (a) Slip band of edge dislocations, the inverted T symbol corresponds to location of a dislocation and the extra half plane of material. Slip plane contains Burgers vector (horizontal in the drawing) and dislocation line direction (perpendicular to the plane of drawing) (b) During annealing dislocations form arrays in direction perpendicular to Burgers vector.

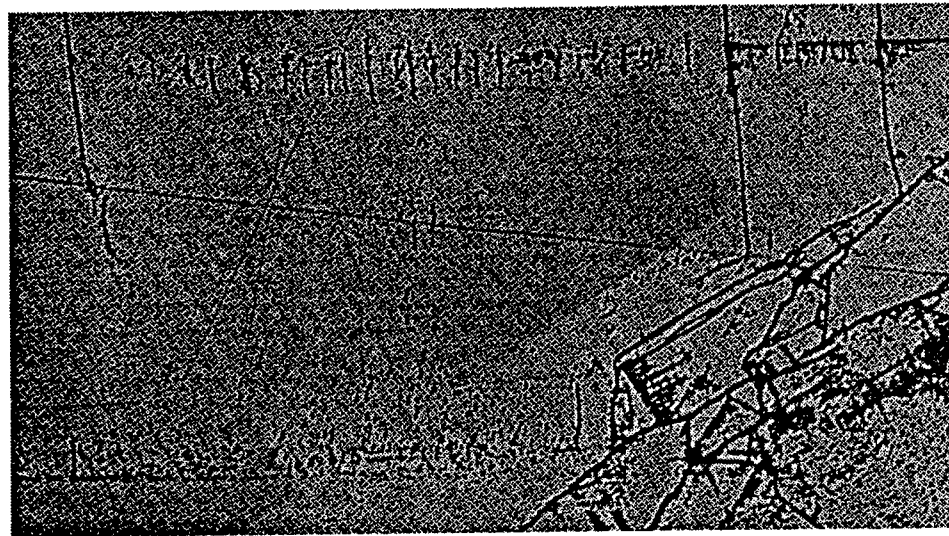


Fig. 6 Two slip bands on the etched SiC wafer surface. The band direction is $[1\bar{1}00]$. The fine structure of the bands consist of lines roughly perpendicular to the slip band direction ($[11\bar{2}0]$).

Conclusions

Experimental evidence of a new slip system $\frac{a}{3}\langle 2\bar{1}\bar{1}0 \rangle\langle 1\bar{1}00 \rangle$ in 4H-SiC crystals was obtained by KOH etching and high resolution x-ray diffraction. This slip was observed to be activated during crystal growth and post-growth cooling. The dislocations are mobile at high temperatures and polygonize forming dislocation arrays along $\langle 1\bar{1}00 \rangle$.

References:

1. E.O. Johnson, *Physical limitations on frequency and power parameters of transistors* , RCA Rev. 163-177 (1965).
2. R.W. Keyes, *Figure of merit for semiconductors for high-speed switches* , Proc. IEEE **60**, 225-226 (1972).
3. B.J. Baliga, *Semiconductors for high voltage, vertical channel field effect transistors* , J. Appl. Phys. **53**, 1759-1764 (1982).
4. B.J. Baliga, *Power semiconductor device figure of merit for high-frequency applications* , IEEE Electron. Device Lett. **10**, 455-457 (1989).
5. K.V. Ravi, C.J. Varker and C.E. Volk, *Electrically active stacking faults in silicon* , J. Electrochem. Soc. **120**, 533-541 (1973).
6. C.J. Varker and K.V. Ravi, *Oxidation-induced stacking faults in silicon. II. Electrical effects in pn diodes* , J. Appl. Phys. **45**, 272-287 (1974).
7. M. Lesniak and D.B. Holt, *Defect microstructure and microplasmas in silicon avalanche photodiodes* , J. Mater. Sci. **22**, 3547-3555 (1987).
8. C. Donolato, P.G. Merli and J. Vecchi, , J. Electrochem. Soc. **124**, 473 (1977).
9. J.W. Gaylord, *Microplasma observation in silicon junctions using a scanning electron beam* , J. Electrochem. Soc. **113**, 753-754 (1966).
10. H.J. Schulze and B.O. Kolbesen, *Influence of silicon defects on the electrical behavior of semiconductor power devices* , Mat. Res. Soc. Symp. Proc. **483**, 381-392 (1998).
11. N.F.B. Neve, K.A. Hughes and P.R. Thornton, *Scanning electron microscope as a means of studying microplasmas at high resolution* , J. Appl. Phys. **37**, 1704-1709 (1966).
12. P.G. Neudeck and J.A. Powell, *Performance limiting micropipe defects in silicon carbide wafers* , IEEE Electron Dev. Lett. **15**, 63-65 (1994).
13. P.G. Neudeck, *Progress in silicon carbide semiconductor electronics technology* , J. Electronic Materials **24**, 283-288 (1995).

14. P.G. Neudeck, D.J. Larkin, J.A. Powell, L.G. Matus and C.S. Salupo, *2000V 6H-SiC p-n junction diodes grown by chemical vapor deposition* , Appl. Phys. Lett. **64**, 1386-1388 (1994).
15. P.G. Neudeck, W. Huang and M. Dudley, *Breakdown degradation associated with elementary screw dislocations in 4H-SiC p+n junction rectifiers* , Mat. Res. Soc. Symp. Proc. **483**, 285-293 (1998).

GUIDANCE AND CONTROL OF MISSILE SYSTEMS UNDER UNCERTAIN FLIGHT CONDITIONS

**Yong D. Song
Assistant Professor
Department of Electrical Engineering**

**North Carolina A&T State University
Greensboro, NC 27411**

**Final Report for:
Summer Research Extension Program
Wright Laboratory**

**Sponsored by:
Air Force Office of Scientific Research
Bolling AFB, Washington DC Sponsorship**

and

Wright Laboratory

March 1998

GUIDANCE AND CONTROL OF MISSILE SYSTEMS UNDER UNCERTAIN FLIGHT CONDITIONS

Yong D. Song
Assistant Professor
Department of Electrical Engineering
North Carolina A&T State University, Greensboro, NC 27411

Abstract

This project developed and tested a memory-based control scheme for EMRAAT missiles. The main idea behind the memory-based method is to build the control scheme upon certain memorized information such as current system response, previous system response and past control experience. Fundamentally, the desired steering signal in the scheme is generated from observing and processing the most recent experience stored in a memory. System performance can be continuously improved during system operation. There is no need to repeatedly run the system for the same task (a process that is not allowed in missile systems). Another advantage of this approach is that the overall required memory space does not grow with time and is much smaller than most existing learning control methods. The effectiveness of proposed method is verified via simulation under varying flight conditions.

Guidance and Control of Missile Systems Under Uncertain Flight Conditions

Yong D. Song

1. Introduction

This project is concerned with autopilot design for the Extended Medium Range Air-to-Air Technology (EMRAAT) missile. The characteristics of EMRAAT missile were defined in the late 1980's by the U.S. Air Force Armament Laboratory, Eglin Air Force Base, Florida. The 2-D airframe of the EMRAAT missile is illustrated in Figure 1.

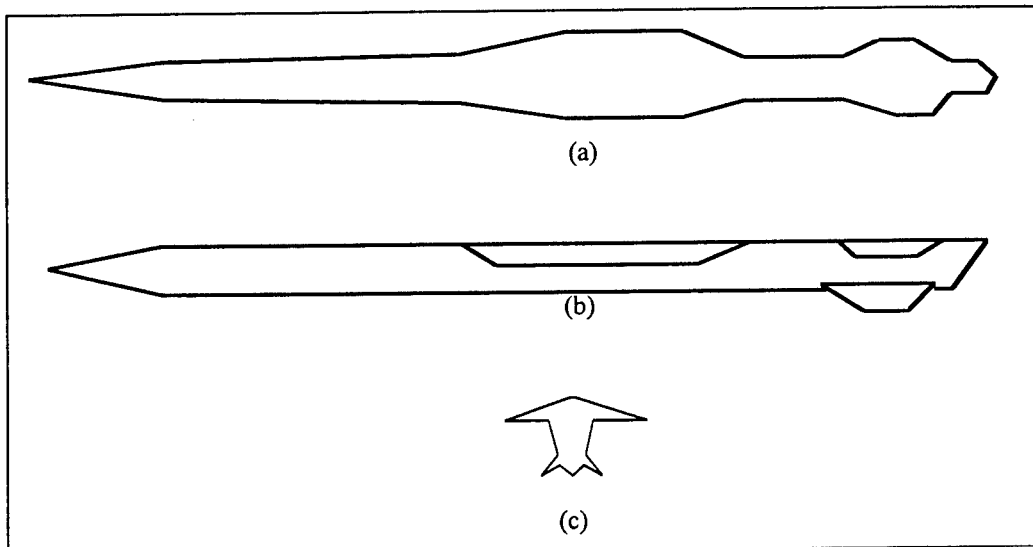


Figure 1. EMRAAT Airframe. (a) top view, (b) side view and (c)

Note that the missile of this type is a longitudinally nonaxisymmetrical airframe with four tail fins for control which are placed in a non-cruciform. Because of the asymmetric configuration, the missile exhibits many attractive features, such as high-lift, low-drag, air intake, internal carriage, and low-observability. While the asymmetric high-lift configuration gives the missile large maneuverability in its pitch plane, the available load factor in the yaw plane is limited. Therefore, to intercept an incoming target, a bank-to-turn (BTT) steering

strategy must be employed. The BTT maneuver is fulfilled through the control of roll and pitch motions. That is, to achieve the desired orientation, a BBT missile rolls the normal plane to the desired direction. The magnitude of the maneuver is controlled by pitch control devices. In contrast to a skip-to-turn autopilot which can be designed without worrying about the coupling among pitch, yaw and roll motions, a BBT autopilot must take into account the Coriolis and gyroscopic couplings due to roll motion. It is also imperative to accommodate the coupling between sideslip, angle of attack and roll rates to achieve rapid and precise response. Furthermore, it should be realized that almost all the aerodynamic coefficients are not constant, but time varying, depending on the flight conditions such as altitude, mach number and angle of attack etc. Some of the parameters may change by up to 50% of nominal value. Such a wide range of change demands a highly robust and adaptive control scheme.

In this project we investigated a methodology referred to as *memory-based* approach for controlling missile systems. The fundamental idea behind this approach is somewhat different from traditional methods. More specifically, our control method is not to assume the system is described by a linear model plus perturbations; not to linearize the system; not to estimate certain parameters based on the linear parametric assumption, not to determine the bounds on certain nonlinear functions; not to use infinite switch frequencies; not involve ad hoc membership functions; not to run the system repeatedly for the same task.

Instead, the control scheme is solely based upon certain memorized information such as current system response, previous system response and past control experience. Fundamentally, the desired control signal in the scheme is “learned” and generated from observing and processing the most recent experience stored in a memory. System performance can be continuously improved during system operation. There is no need to repeatedly run the system (a process that is not allowed in missile systems). Another advantage of this approach is that the overall required memory space does not grow with time and is much smaller than most existing methods (Atkeson and Reinkensmeyer 1992, Schaal and Atkeson 1994).

The remainder of the report is organized as follows. In Section 2 we explore the fundamental structure of memory-based control and present a set of memory-based control algorithms. Section 3 examines the EMRAAT model and addresses memory-based missile

autopilot design. Simulation on EMRAAT is presented in Section 4. Finally, we conclude this report in Section 5.

2. Memory-based Control

We begin with background review of memory-based technique. The fundamental structure of memory-based control and its application to autopilot design for EMRAAT missile are addressed in next subsections.

2.1 Background

Memory-based approach for solving engineering problems has a long history. Several researchers have contributed to this method. An early effort using memory-based concept was made by Fix and Hodges (1951) for a new pattern classification. Steinbuch and Piske (1963) implemented the direct storage of experience and nearest-neighbor search process with a neural network for pattern recognition. Memory-based method has also been applied to weather prediction (Lorenz, 1969), speech recognition -- learning of pronunciation (Stanfill and Waltz, 1986), medical diagnosis, protein structure prediction (Waltz, 1987) and others (Atkeson and Reinkensmeyer 1992). Application of memory-based method to control systems such as robot manipulators has also been reported (Schaal and Atkeson 1994). In fact, conventional PID control and any dynamic control can be viewed as a memory-based control. Also the Cerebellar Model Articulation Controller (CMAC) is essentially memory-based control.

While there exist many approaches to utilizing memory-based concepts for control systems, our special interest in this project lies in introducing a simple method to build a controller using certain memorized information. To begin, we introduce the following *information sets*

$$S_u = \{u_{k-1}, u_{k-2}, \dots, u_1, u_0\} - \text{control history}$$

$$S_x = \{x_k, x_{k-1}, \dots, x_1, x_0\} - \text{current and past system responses}$$

$$S_{x^*} = \{x_k^*, x_{k-1}^*, \dots, x_1^*, x_0^*\} - \text{current and past desired system responses}$$

Here (and hereafter), u_k , x_k and x^*_k stand for $u(kT)$ -- control signal, $x(kT)$ -- state vector of the system, and $x^*(kT)$ -- the desired trajectory vector, respectively, and T is the sampling period.

Simply speaking, the development of memory-based control algorithms involves two issues: *selecting appropriate memorized information* and *processing the selected information*. There could be many different approaches to addressing these issues, leading to different type of memory-based control algorithms. A typical approach is to make use of all the memorized information and process such information by the "average-weighting" method, i.e.

$$u_k = \frac{1}{h} \sum_{i=1}^h z_i w_i \quad (1)$$

where

$$z \in R^h \subset S_u \cup S_x \cup S_{x^*}$$

is a vector associated with the stored system information and w_i 's represent memory coefficients (MCs).

While the memory-based controller as shown in (1) is simple in structure, it suffers from the following drawbacks: 1) the required memory size may become extremely large as time goes by because it makes use of all the past information of the system (h is proportional to k); 2) due to large amount of information to be processed in (1), extensive computation and lengthy memory search are involved; and 3) there is no guarantee of stability for close-loop system because the MCs are not derived from system stability consideration.

2.2 Structure

We now develop a memory-based control scheme in which the above limitations are removed. As a first step, we define the following subsets
 $S'_u \subset S_u$, $S'_x \subset S_x$ and $S'_{x^*} \subset S_{x^*}$, such that

$$S'_u = \{u_{k-1}, u_{k-2}, \dots, u_{k-r}\} \cdot \text{control experience beyond } r\text{-step}$$

$$S'_x = \{x_k, x_{k-1}, \dots, x_{k-r}\} \cdot \text{current and } r\text{-step back system responses}$$

$$S'_{x^*} = \{x_k^*, x_{k-1}^*, \dots, x_{k-r}^*\} \cdot \text{current and } r\text{-step back desired system responses}$$

Here $1 \leq r \ll k$ is an integer. These sets form the database of experiences which are retrieved and processed via

$$u_k = \phi(z_r; w_r) \quad (2)$$

where

$$z_r \in R^p \subset S_u^r \oplus S_x^r \oplus S_{x^*}^r$$

and $\phi(\cdot)$ is a mapping function that converts the selected information z_r into u_k (through certain MCs). The controller, referred to as r^{th} -order memory-based control, is conceptually illustrated as in Figure 2. The difference between (1) and (2) is that only the most recent experiences are honored in (2) while the past information beyond r -step is forgotten. This is motivated by the fact that for a practical system the latest system statuses have more influence on its future behavior. Moreover, the selected information is processed through the mapping function $\phi(\cdot)$.

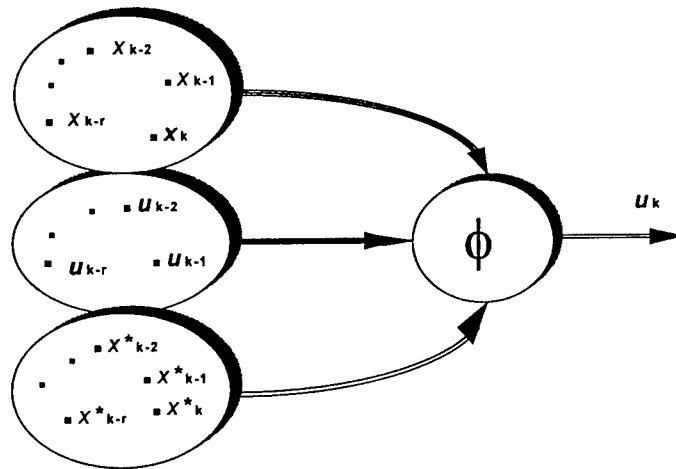


Figure 2. The r^{th} -order Memory-based Control Scheme

One of the favorable advantages of the proposed method is that the required memory size does not grow with time and is much smaller as compared with other methods (e.g., CMAC (Albus, 1975) and ACAM (Atkeson et al 1992)). To make this point clearer, let us consider building a first order memory-based controller. Essentially in this case we only need the following information:

$$S_u^1 = \{u_{k-1}\}$$

$$S_x^1 = \{x_{k-1}, x_k\}$$

and

$$S_x^{1*} = \{x_{k-1}^*, x_k^*\}$$

which is processed/generalized as in Figure 3. Similarly, to construct a second order memory-based controller we only need the stored information (Figure 4)

$$S_u^2 = \{u_{k-1}, u_{k-2}\}$$

$$S_x^2 = \{x_{k-2}, x_{k-1}, x_k\}$$

and

$$S_x^{2*} = \{x_{k-2}^*, x_{k-1}^*, x_k^*\}$$

As can be seen, memory space is not an issue here because the required memory does not grow with time.

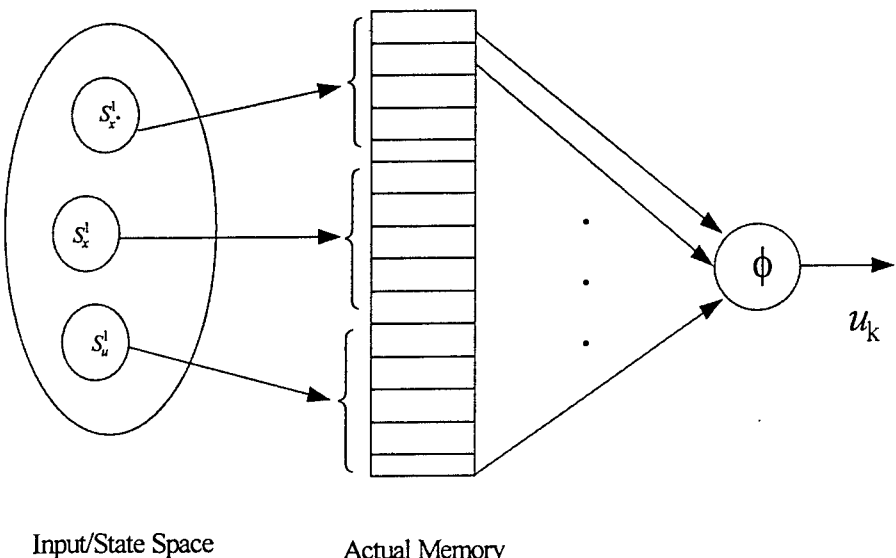


Figure 3. A First-order Memory-based Control

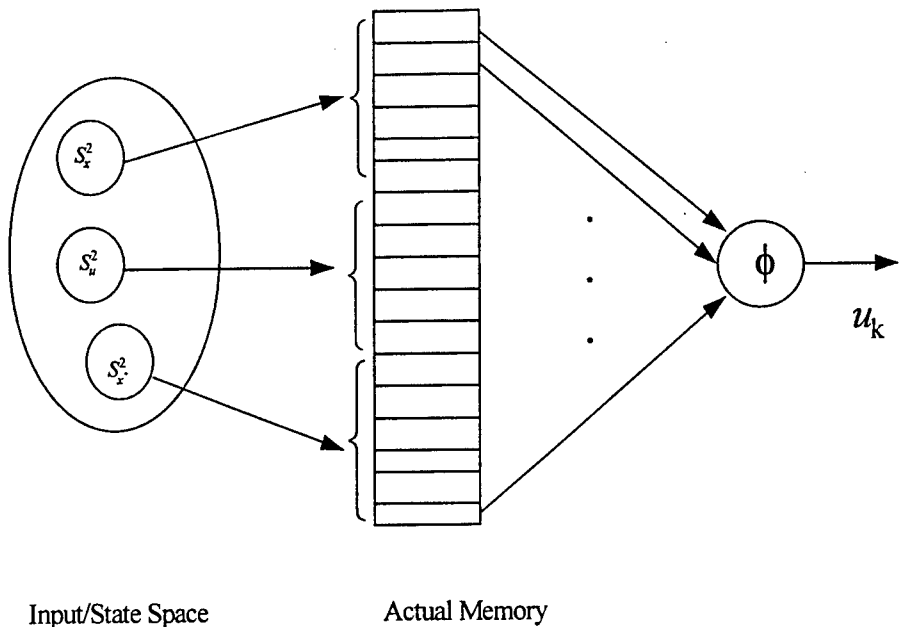


Figure 4. A Second-order Memory-based Controller

Regarding the memory-based controller (2), if we view the memory-based controller as a *mechanism (network)* that *on-line* processes the memorized information and produces a control action at time instant $t = kT$, then design of a memory-based controller boils down to specifying such a mechanism, i.e., specifying the mapping function $\phi(\cdot)$ and the memory coefficients (MCs) w_i . In this project, we use the following mapping function, among others,

$$\phi(\sigma, y) = \frac{2}{\sigma} \left(\frac{1 - e^{-\sigma y}}{1 + e^{-\sigma y}} \right), \quad \sigma > 0$$

It is interesting to note that such a mapping function exhibits two salient properties

- i) $|\phi(\sigma, y)| \leq \frac{2}{\sigma}$
- ii) $\lim_{\sigma \rightarrow 0} \phi(y, \sigma) \rightarrow y$

The first property allows us to adjust the magnitude of the control signal by choosing a proper value of σ and the second property implies that $\phi(\cdot)$ behaves like a linear function as σ tends to a small number. This property is useful in our stability analysis.

2.3 Memory-based Control Algorithms

First let us consider the following simple nonlinear system

$$\dot{x} = f_0(x) \pm \delta f(x) + u \quad (3)$$

where x is the system state, u is the control input, $f_0(\cdot)$ is *a priori* information regarding system nonlinearities (could be zero if no such information is available), and $\delta f(\cdot)$ models system nonlinearities/perturbations. Note that $\delta f(\cdot)$ is completely unpredictable both in magnitude and in direction, as usually the case in practice. To emphasize this fact we *exclusively* include the sign “ \pm ” in the model.

- The 1st-order memory-based controller is of the form

$$u_k = \phi(\sigma, w_0 u_{k-1} + w_{e_1} e_{k-1} / T + w_{e_2} e_k / T + w_{c_0} \eta_k(\cdot) + w_{c_1} \eta_{k-1}(\cdot)) \quad (4a)$$

where

$$\begin{aligned} e &= x - x^* \\ \eta(\cdot) &= f_0(x) - \dot{x}^* \end{aligned} \quad (4b)$$

The MCs are determined by backward time-shift method as follows,

$$w_0 = 1, \quad w_{e_1} = 1, \quad w_{e_2} = -2, \quad w_{c_0} = -1, \quad w_{c_1} = 1 \quad (4c)$$

Note that in (4a) the actual and desired system responses are processed through the tracking error e , which reduces the total number of MCs. Also note that the additional available information η is included in (4a). It is worth mentioning that η bears the same dimension as u , while e does not. To make the summation meaningful in (4a), both e_k and e_{k-1} are divided by T , which is intuitively understandable from dimensional analysis point of view. The condition for the controller to apply is that for a sufficiently small T ,

$$|\Delta h_k| = |\delta f(x_k, t_k) - \delta f(x_{k-1}, t_{k-1})|_{t_k=kT} \leq \delta_1 < \infty \quad (5)$$

As long as the system's perturbed dynamics do not change infinitely fast, the above condition is always satisfied.

- The r^{th} -order memory-based controller is of the form

$$u_k = \phi \left(\sigma, \sum_{i=1}^r w_{u_i} u_{k-i} + \sum_{i=0}^r w_{e_i} e_{k-i} / T + \sum_{i=0}^r w_{c_i} \eta_{k-i}(\cdot) \right) \quad (6)$$

where the MCs w_{u_i} and w_{e_i} are determined as in the table (where memory coefficients up to 8th-order are provided)

	$w_{u_i} (i=1, \dots, r)$	$w_{e_i} (i=0, 1, \dots, r)$
$r = 1$	1	-2 1
$r = 2$	2 -1	-3 3 -1
$r = 3$	3 -3 1	-4 6 -4 1
$r = 4$	4 -6 4 -1	-5 10 -10 5 -1
$r = 5$	5 -10 10 -5 1	-6 15 -20 15 -6 1
$r = 6$	6 -15 20 -15 6 -1	-7 21 -35 35 -21 7 -1
$r = 7$	7 -21 35 -35 21 -7 1	-8 28 -56 70 -56 28 -8 1
$r = 8$	8 -28 56 -70 56 -28 8 -1	-9 36 -84 126 -126 84 -36 9 -1

$$r = 1 \rightarrow |e_k| = |x_k - x_k^*| \leq T^2 c_1$$

$$r = 2 \rightarrow |e_k| = |x_k - x_k^*| \leq T^3 c_2$$

and

$$w_{c_0} = -1$$

$$w_{c_i} = w_{u_i} \ (\forall i = 1, \dots, r)$$

The condition for the controller to apply is

$$|\Delta^r h_k| = |\Delta^{r-1} h_k - \Delta^{r-1} h_{k-1}| \leq \delta_r < \infty \quad (7)$$

The above control algorithms can be extended to the following systems:

- The n^{th} -order nonlinear systems with unit gain

$$x^{(n)} = f_0(x) + u \pm h(\cdot) \quad (8)$$

for which the r^{th} -order memory-based tracking controller is

$$u_k = \phi\left(\sigma, \sum_{i=1}^r w_{u_i} u_{k-i} + \sum_{i=0}^r w_{e_i} s_{k-i}(.) / T + \sum_{i=0}^r w_{c_i} \eta_{k-i}(.)\right) \quad (9a)$$

where

$$s(.) = \dot{e} + \gamma_0 e, \quad \gamma_0 > 0 \quad (9b)$$

$$\eta(.) = f_0 + x^{*(n)} - \sum_{m=1}^{n-1} C_{n-1}^m q^{n-m} \gamma_0^m e, \quad q = d/dt \quad (9c)$$

The condition for the controller to apply is the same as in (7).

- The n^{th} -order nonlinear systems with constant non-unit gain

$$x^{(n)} = f_0(x) + g_0 u \pm h(.) \quad (10)$$

The γ^{th} -memory-based tracking controller is

$$u_k = \phi\left(\sigma, \sum_{i=1}^r w_{u_i} u_{k-i} + g_0^{-1} \left[\sum_{i=0}^r w_{e_i} s_{k-i}(.) / T + g_0^{-1} \sum_{i=0}^r w_{c_i} \eta_{k-i}(.) \right] \right) \quad (11a)$$

where

$$s(.) = \dot{e} + \gamma_0 e, \quad \gamma_0 > 0 \quad (11b)$$

$$\eta(.) = f_0(x) + x^{*(n)} - \sum_{m=1}^{n-1} C_{n-1}^m q^{n-m} \gamma_0^m e, \quad q = d/dt \quad (11c)$$

- For a more general nonlinear system with time varying gain

$$x^{(n)} = f_0(x) + g_0(x) u \pm h(.) \quad (12)$$

where $h(.)$ represents the lumped uncertainties of the system. The γ^{th} -order memory-based tracking controller is

$$u_k = \phi\left(\sigma, g_{0_k}^{-1} \left\{ \sum_{i=1}^r w_{u_i} g_{0_{k-1}} u_{k-i} + \sum_{i=0}^r w_{e_i} s_{k-i}(.) / T + \sum_{i=0}^r w_{c_i} \eta_{k-i}(.) \right\} \right) \quad (13a)$$

where

$$s(.) = \dot{e} + \gamma_0 e, \quad \gamma_0 > 0 \quad (13b)$$

$$\eta(.) = f_0(x) + x^{*(n)} - \sum_{m=1}^{n-1} C_{n-1}^m q^{n-m} \gamma_0^m e, \quad q = d/dt \quad (13c)$$

The condition for the controller to apply is the same as before.

2.4 Stability Analysis

To facilitate the analysis, we only consider system (3) with the 1st-order memory-based controller (the other cases can be shown in the same way).

Rewrite (3) in terms of tracking error as

$$\dot{e} = u + \eta \pm \delta f \quad (14)$$

where η is the generalized signal defined as in (4b). To make use of the memorized information, we now consider the discretized version of (14) using Euler differentiation¹

$$e_{k+1} = e_k + T(\eta_k + u_k \pm \delta f_k) \quad (15)$$

where, again, T is the sampling period. To use the memorized information (as needed in the first order memory-based controller), we consider one step backward time-shift in (15),

$$e_k = e_{k-1} + T(\eta_{k-1} + u_{k-1} \pm \delta f_{k-1}) \quad (16)$$

Subtracting (16) from (15) gives

$$e_{k+1} = 2e_k - e_{k-1} + T[\eta_k - \eta_{k-1} + u_k - u_{k-1} \pm (\delta f_k - \delta f_{k-1})] \quad (17)$$

With the first order memory-based controller (4a) and the corresponding MCs, it can be shown that the error dynamics (17) become

$$e_{k+1} = \pm T(\delta f_k - \delta f_{k-1}) \quad (18)$$

where the second property of $\phi(\cdot)$ is used. Now consider $d/dt(\delta f)$, the first derivative of δf w.r.t. time t which can be viewed as the perturbing rate of the system. For a practical system, such a rate cannot be infinitely fast (otherwise no feasible control exists for such a system). Hence it is assumed that

¹ A well known fact is that for a digital control system the controller can be designed in two ways, i.e., design a controller based on the continuous system model and then discretize the controller for digital implementation; or discretize the system first and then synthesize a digital controller for the system. The second method is used here.

$$\max \left| \frac{d}{dt} (\delta f) \right| \leq c_1 < \infty$$

which, for a sufficiently small T , leads (18) to (Kreyszig 1968)

$$|e_{k+1}| \leq T [T \left| \frac{d}{dt} (\delta f) \right|]_{t=kT} \leq T^2 c_1 \quad (19)$$

Consider the Lyapunov candidate function

$$V_{k+1} = e_{k+1}^2$$

From (19) it is seen that

$$\begin{aligned} \nabla V_k &= V_{k+1} - V_k \\ &= e_{k+1}^2 - e_k^2 \\ &\leq (T^2 c_1)^2 - e_k^2 \\ &< 0 \quad \forall |e_k| > T^2 c_1 \end{aligned}$$

Tracking stability with the proposed memory-based control algorithms is then ensured from Lyapunov stability theory. The tracking precision is measured by

$$|e_k| \leq T^2 c_1 \quad (20)$$

where T is the sample period and c_1 is the growth rate of the system uncertainties. Similarly, if the r^{th} -order memory-based control (9) is applied, it can be shown that

$$|e_{k+1}| \leq T |\nabla^r h_k| \leq T^{r+1} c_r$$

where

$$c_r = \max \left| \frac{d^r}{dt^r} h(\cdot) \right|$$

Remarks

1. There is no need to find c_1 . In stability analysis we only use the fact that such a constant exists. This can be ensured as long as the nonlinearities in the system do not change infinitely fast.
2. It is interesting to note that the memory-based control is a nonlinear and dynamic compensator. In contrast to traditional dynamic control, however, the design procedure

of the memory-based control is much simpler and the overall computation is much smaller. Furthermore, the condition for the controller to apply is much weaker than other methods.

3. To see the novelty of the proposed control strategy, it is worth examining what information is required in the proposed control scheme. It is seen that only memorized information is needed, while detailed description of the system nonlinearities are not involved. Furthermore, there is no need to estimate any parameters, no need to find the upper bound of the nonlinear function, no need to conduct intensive training or repetitively run the system.

3. Application to EMRAAT Missile

In this section we examine the applicability of the proposed memory-based approach to EMRAAT missile. First we discuss the missile's dynamics under varying flight conditions.

3.1 Modeling of EMRAAT Missile

Consider a rigid missile performing 3-D maneuvers. Using the standard body fixed coordinate system (i.e., the origin is at the center of mass of the missile, the positive x -axis extends forward through the nose of the missile, the positive z -axis extends downward, and the y -axis completes the right-handed triad), we can establish the following motion equations (Schumacher 1994)

$$\dot{\alpha} = q - \tan(\beta)[p \cos(\alpha) - r \sin(\alpha)] + \frac{g}{V \cos(\beta)} (\cos(\alpha) \cos(\phi) + \sin(\alpha) \sin(\theta)) \quad (22)$$

$$+ \frac{gQS}{WV \cos(\beta)} (C_{N_a} \alpha + C_{N_a} \dot{\alpha} + C_{N_q} q + C_{N_{\delta_q}} \delta_q) \cos(\alpha)$$

$$\dot{\beta} = p \sin(\alpha) - r \cos(\alpha) + \frac{gQS}{WV} (C_{Y_p} \beta + C_{Y_p} p + C_{Y_r} r + C_{Y_{\delta_p}} \delta_p + C_{Y_{\delta_r}} \delta_r) \cos(\beta) \quad (23)$$

$$+ \frac{g}{V} \cos(\theta) \sin(\phi) \cos(\beta)$$

$$J \begin{bmatrix} \dot{p} \\ \dot{q} \\ \dot{r} \end{bmatrix} + \begin{bmatrix} p \\ q \\ r \end{bmatrix} \times J \begin{bmatrix} p \\ q \\ r \end{bmatrix} = Q S d \left\{ \begin{bmatrix} n_1(\beta, p, r, c) \\ n_2(\alpha, \dot{\alpha}, q, c) \\ n_3(\beta, p, r, c) \end{bmatrix} + C(c) \begin{bmatrix} \delta_p \\ \delta_q \\ \delta_r \end{bmatrix} \right\} \quad (24)$$

with

$$J = \begin{bmatrix} I_{xx} & -I_{xy} & -I_{xz} \\ -I_{xy} & I_{yy} & -I_{yz} \\ -I_{xz} & -I_{yz} & I_{zz} \end{bmatrix} = \begin{bmatrix} 1.08 & -0.274 & 0.704 \\ -0.274 & 70.13 & -0.017 \\ 0.704 & -0.017 & 70.66 \end{bmatrix}$$

$$n_1(.,c) = C_{l_\beta} \beta + C_{l_p} p + C_{l_r} r$$

$$n_2(.,c) = C_{m_\alpha} \alpha + C_{m_q} \dot{\alpha} + C_{m_q} q$$

$$n_3(.,c) = C_{n_\beta} \beta + C_{n_p} p + C_{n_r} r$$

$$C(c) = \begin{bmatrix} C_{l_{\delta_p}} & 0 & C_{l_{\delta_r}} \\ 0 & C_{m_{\delta_q}} & 0 \\ C_{n_{\delta_p}} & 0 & C_{n_{\delta_r}} \end{bmatrix}$$

where c denotes the generalized aerodynamic coefficients/parameters² (the definition of each other variable can be found from Appendix A). These equations are related to translational motions as well as rotational motions. Note that yaw-pitch-roll motion depends on sideslip and angle of attack, as explicitly reflected in the above equations. Also it is observed that for the EMRAAT missile, the first diagonal element of the inertia matrix is not “dominant” as compared with the off-diagonal elements. Physically, this implies that the motions in yaw, pitch and roll are not decoupled. Consequently, the diagonal assumption of the inertia matrix commonly used is not well justified for EMRAAT missile. For this reason, the coupling motion equations as listed in the Appendix B is considered in this project.

Define

$$\Theta = \begin{bmatrix} \phi \\ \theta \\ \psi \end{bmatrix}, \omega = \begin{bmatrix} p \\ q \\ r \end{bmatrix}, n(.,c) = \begin{bmatrix} n_1(.,c) \\ n_2(.,c) \\ n_3(.,c) \end{bmatrix}, u = \begin{bmatrix} \delta_p \\ \delta_q \\ \delta_r \end{bmatrix}$$

It is well known that Θ and ω share the relation [37]

² These parameters depend heavily on flight conditions such as altitude, mach number and angle of attack etc

$$\omega = A(\theta, \phi)\dot{\Theta} \quad \text{and} \quad \dot{\omega} = \dot{A}\dot{\Theta} + A\ddot{\Theta} \quad (25)$$

where

$$A(\theta, \phi) = \begin{bmatrix} 1 & 0 & -\sin(\theta) \\ 0 & \cos(\phi) & \cos(\theta)\sin(\phi) \\ 0 & -\sin(\phi) & \cos(\theta)\cos(\phi) \end{bmatrix}$$

which is non-singular as long as $\theta \neq \pm\pi/2$. The case that A becomes singular is known as *gimbal lock*. In our analysis, we shall assume such unusual flight condition will not occur. If the system under consideration may experience gimbal lock, a different rotation order may be employed. With the above notations, the dynamic motion equations as listed in Appendix B can be re-expressed in terms of $\phi - \theta - \psi$ as

$$\ddot{\Theta} = f(., c) + g(., c)u \quad (26)$$

where

$$f(., c) = (JA)^{-1} \left\{ QSdn(., c) - J\dot{A}\dot{\Theta} - (A\dot{\Theta}) \times J(A\dot{\Theta}) \right\} \quad (27)$$

$$g(., c) = (JA)^{-1} Q SdC(c) \quad (28)$$

It is seen that the missile model is highly nonlinear and strongly coupled.

3.2 Memory-based Control

With above discussion, we are ready to address the application of the memory-based control method to EMRAAT missile. The missile autopilot design problem is as follows:

Given a set of commands in terms of yaw, pitch and roll angle $\psi^ \Rightarrow \theta^* \Rightarrow \phi^*$ and its velocity $\dot{\psi}^* \Rightarrow \dot{\theta}^* \Rightarrow \dot{\phi}^*$, design control algorithm u to automatically adjust the surface deflections such that the actual yaw, pitch and roll motions of the missile track the desired motions closely.*

We focus on the first order memory-based control due to its simplicity. Taking into account the varying flight conditions, let us re-express (26) as

$$\ddot{\Theta} = f_0(.) + g_0(.)u + h(.)$$

where

$$f_0(.) = f(., c)|_{c=c_0}, \quad g_0(.) = g(., c)|_{c=c_0}$$

and c_0 denotes the aerodynamic coefficients corresponding to the initial flight (launch) position, which is assumed to be known. Here $h(\cdot)$ represents the lumped uncertainties in the system, which is apparently time-varying and non-computable. However, for a controllable missile system, the variation rate of $h(\cdot)$ cannot be infinitely fast. Hence in what follows, it is assumed that

$$\left\| \frac{d}{dt} h(\cdot) \right\| \leq \delta < \infty \quad (30)$$

The following information is needed in building the first order memory-based missile controller,

$$\begin{aligned} & \{\Theta_k, \Theta_{k-1}, \dot{\Theta}_k, \dot{\Theta}_{k-1}\} \\ & \{\Theta_k^*, \Theta_{k-1}^*, \dot{\Theta}_k^*, \dot{\Theta}_{k-1}^*\} \\ & \{u_{k-1}\} \end{aligned}$$

Note that the total number of input/state variables in this case is 27. If these inputs/states are processed individually, we would require at least 27 MCs. While this is not a big number as compared with other methods, we still wish to reduce the actual MCs to facilitate on-line computation. This can be accomplished by introducing the following auxiliary variables (this process can be viewed as the information association in CMAC method (Albus 1975)),

$$s_k = \dot{e}_k + \gamma_0 e_k \quad (31)$$

where $\gamma_0 > 0$ is a design parameter and $e_k = \Theta_k - \Theta_k^*$ is the tracking error vector. To make use of the available system information such as $f_0(\cdot)$ and $\ddot{\Theta}^*$ etc, we also introduce a new "input" η_k

$$\eta_k = f_{0_k} - \ddot{\Theta}_k^* + \gamma_0 \dot{e}_k \quad (32)$$

With the above associated inputs, we now have the following generalized memory information

$$S_s = \{s_k, s_{k-1}\}$$

$$S_u = \{u_{k-1}\}$$

$$S_\eta = \{\eta_k, \eta_{k-1}\}$$

The 1st-order EMRAAT missile control scheme that makes use of the above memorized information is

$$u_k = \phi(\sigma, g_{0_k}^{-1}[w_0 g_{0_{k-1}} u_{k-1} + w_{e_1} s_{k-1}(.) / T + w_{e_2} s_k(.) / T + w_{c_0} \eta_k(.) + w_{c_1} \eta_{k-1}(.)])$$

where the MCs are determined by backward time-shift method as follows,

$$w_0 = 1, \quad w_{e_1} = 1, \quad w_{e_2} = -2, \quad w_{c_0} = -1, \quad w_{c_1} = 1$$

To show the stability, let us consider the following Lyapunov candidate function

$$V_{k+1} = s_{k+1}^T s_{k+1}$$

It can be verified that

$$\begin{aligned} \nabla V_k &= V_{k+1} - V_k \\ &= s_{k+1}^T s_{k+1} - s_k^T s_k \\ &< (T^2 \delta)^2 - s_k^T s_k \\ &\leq 0 \quad \forall \|s_k\| > T^2 \delta \end{aligned}$$

i.e., V_k decreases as long as $\|s_k\| > T^2 \delta$, thus $\|s_k\|$ remains bounded with the proposed memory-based control. In view of the definition of s , it is readily concluded that the boundedness of both $\|e_k\|$ and $\|\dot{e}_k\|$ are ensured.

With more memorized information, we can build a control up to r^{th} -order as follows,

$$u_k = \phi\left(\sigma, g_{0_k}^{-1}\left\{\sum_{i=1}^r w_{u_i} g_{0_{k-i}} u_{k-i} + \sum_{i=0}^r w_{e_i} s_{k-i}(.) / T + \sum_{i=0}^r w_{c_i} \eta_{k-i}(.)\right\}\right) \quad (33)$$

where w_i denotes the MCs as specified in the table in Section 2.

3.3 Memory-based Guidance

It should be mentioned the desired missile trajectory in terms of yaw, pitch and roll angle $\psi^* - \theta^* - \phi^*$ and its velocity $\dot{\psi}^* - \dot{\theta}^* - \dot{\phi}^*$ are to be obtained from the guidance unit. If the missile is to hit a known and static target, the desired trajectory for the missile to track could be obtained using a proper model based guidance law. However, if the missile is to intercept an incoming target that involves varying and uncertain flying conditions, it becomes nontrivial to obtain the trajectory of the moving target because of the uncertain dynamics of the target.

It is interesting that the memory-based method can be applied to predict the flying trajectory of the target with a reasonably good accuracy in spite of the unknown flight condition of the target. The main idea is as follows. Denote the dynamic model of the target by

$$\dot{x}^* = F(x^*, u^*) \quad (34)$$

where x^* and u^* are the state and control variables of the target, $F(\cdot)$ is a nonlinear and unknown function. The only information about $F(\cdot)$ is

$$\max_{t \geq 0} \left| \frac{d}{dt} F(\cdot) \right| \leq \mu_0 < \infty$$

implying that the target does not change its speed infinitely fast. By using the current and previous flying information, we can construct a memory-based algorithm to predict the trajectory of the target at the next step.

The algorithm is of the form

$$\hat{x}_{k+1}^* = \aleph(\omega, x_k^*, x_{k-1}^*) \quad (35)$$

where \hat{x}_{k+1}^* denotes the estimation of x^* at the time instant $t = kT$ and $\aleph(\cdot)$ is a mapping function of ω (memory coefficients), x_k^* and x_{k-1}^* (current and previous state of the target). Many possible specifications for (35) can be made. In our simulation, we note that a simple linear mapping function can lead to a good prediction.

4. Simulation Study

Simulation on EMRAAT missile was conducted aiming at verifying the effectiveness of the proposed method. The system parameters are taken from Schumacher (1994). Table 1 is the Aerodynamic coefficients at the flight condition: $M = 2.0$, Altitude = 30,000ft., Air Density = 5.87×10^{-4} slug/ft³. In general, these parameters are not constant because they depend on flight conditions. In the simulation, the values in the table are only used as the nominal values. Perturbed aerodynamic coefficients are considered to reflect the effect of varying flight conditions.

Table 1. EMRAAT Aerodynamic Coefficients

($M = 2.0$, Altitude = 30,000 ft., Air Density = 5.87×10^{-4} slug/ft³)

$C_{N_\alpha} = 36.6$	$C_{l_{\delta_r}} = -5.16$
$C_{N_\alpha} = 0.0274$	$C_{m_\alpha} = -82$
$C_{N_q} = 0.0145$	$C_{m_\alpha} = -0.014$
$C_{N_{\delta_q}} = 6.0165$	$C_{m_q} = -0.202$
$C_{Y_\beta} = -14.9$	$C_{m_{\delta_q}} = -40.7$
$C_{n_r} = -0.2$	$C_{n_\beta} = 35.52$
$C_{n_{\delta_p}} = 1.72$	$C_{n_p} = 0.006$
$C_{Y_p} = -0.00073$	$C_{n_{\delta_r}} = -28.65$
$C_{Y_r} = 0.0161$	$C_{l_\beta} = 5.44$
$C_{l_p} = 0.0021$	$C_{l_{\delta_p}} = -6.30$

The physical properties of the missile are given in Table 2. Note that these parameters except for V and Q are independent of flight conditions.

Table 2. EMRAAT Physical Properties
 $(M = 2.0, \text{Altitude} = 30,000 \text{ ft.}, \text{Air Density} = 5.87 \times 10^{-4} \text{ slug/ft}^3)$

$g = 32.2 \text{ ft/s}^2$	$I_{xx} = 1.08 \text{ slug}\cdot\text{ft}^2$
$d = 0.625 \text{ ft.}$	$I_{yy} = 70.13 \text{ slug}\cdot\text{ft}^2$
$S = 0.3067 \text{ ft}^2$	$I_{zz} = 70.66 \text{ slug}\cdot\text{ft}^2$
$W = 227.00 \text{ lbs}$	$I_{xz} = -0.704 \text{ slug}\cdot\text{ft}^2$
$V = 1936.16 \text{ ft/s}$	$I_{xy} = 0.274 \text{ slug}\cdot\text{ft}^2$
$Q = 1100.75 \text{ lb/ft}^2$	$I_{xz} = 0.017 \text{ slug}\cdot\text{ft}^2$

The control objective is to achieve quick missile tracking in yaw, pitch and roll motion. The desired trajectories are given as,

$$\phi = 40(1 - e^{-t}) \text{ (deg)}$$

$$\psi = 10(1 - e^{-t}) \text{ (deg)}$$

$$\theta = 30(1 - e^{-t}) \text{ (deg)}$$

As mentioned earlier, the aerodynamic coefficients depend heavily on flight conditions. For this reason, the simulations were conducted with one set of controller parameters. The focus is the flight condition variance, which is addressed by introducing a time-varying perturbation of the form

$$v = v_0 + \Delta v(t)$$

into *all* of the aerodynamic coefficients, where v_0 represents the nominal value as specified in Table 1 and $\Delta v(\cdot)$ denotes the coefficient deviation from its nominal value due to the variation of flight conditions. Clearly, during the whole course of flight the missile's aerodynamic coefficients may involve large variations, as illustrated in Figure 5 and Figure 6 for the case of $C_{m\delta_q}$ and $C_{l\beta}$ (the nominal values of these parameters used in the control scheme are $C_{m\delta_q} = -40.7$ and $C_{l\beta} = 5.44$). For the same reason, large variations of flight

speed (V) and dynamic pressure (Q) as depicted in Figure 7-Figure 8 are also considered in the simulation.

The first order memory-based control algorithms are used. The sampling period is $T = 0.015$ (sec) and $\gamma_0 = 4$. The dynamic equations as shown in Appendix B are used for computer simulation. The initial orientation of the missile is:

$$\phi(0) = 6^0, \quad \psi(0) = 5^0, \quad \theta(0) = 6^0$$

Tracking results with the memory-based control scheme are presented in Figure 9 and Figure 10, where Figure 9 represents the tracking error of roll angle, pitch angle and yaw angle under several different flight conditions and Figure 10 is the overall tracking profile (actual and desired trajectories) under the varying flight conditions. It is seen that the proposed control scheme achieves satisfactory tracking performance. The robust and adaptive features of the control scheme are also obvious.

5. Concluding Remarks

This project has investigated a memory-based approach for guidance and control of missile systems. The preliminary investigation indicates that the proposed memory-based control method exhibits attractive features. The control scheme, purely built upon past control experience and most recent system responses, is quite effective in dealing with system nonlinearities, modeling uncertainties and external disturbances. The proposed method demonstrates robust and adaptive properties, while these properties are achieved through an avenue somewhat different from traditional methods -- there is no need for parameter estimation, repetitive actions, infinite switching frequencies, ad hoc design process or extensive off-line training. It is noted that the structure of the controller remains unchanged for different nonlinear functions $\delta f(\cdot)$ and $\delta g(\cdot)$ (due to the change of flight conditions). Furthermore, the memory size does not grow with time, which could significantly facilitate real-time implementation.

While memory-based approach for solving engineering problems has a long history, applying this method to control systems is a new attempt. Our current results show that memory-based control has potential for missile control applications.

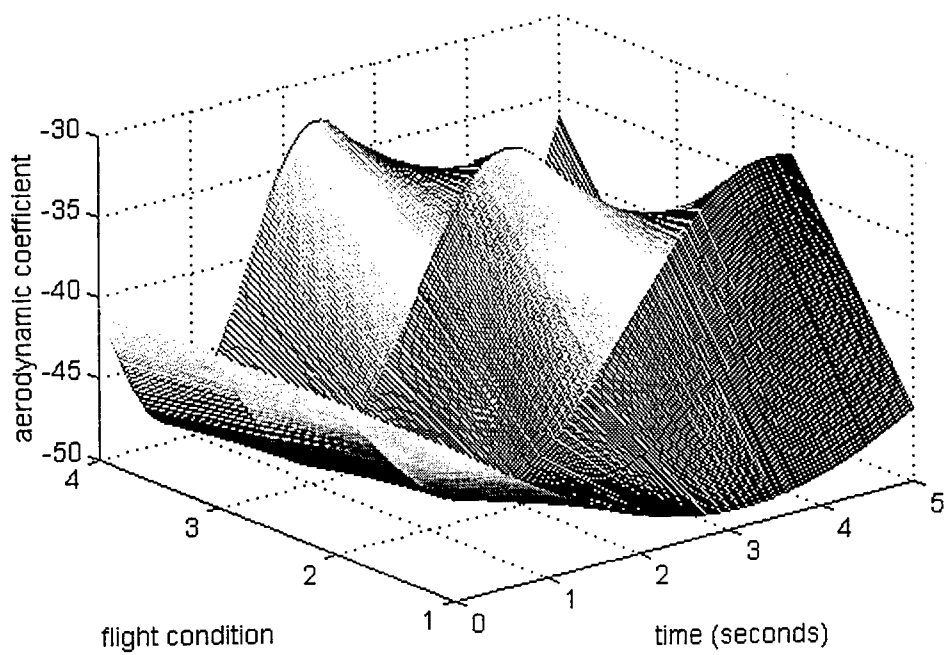


Figure 5. The variation of $C_{m\delta_q}$ with flight conditions

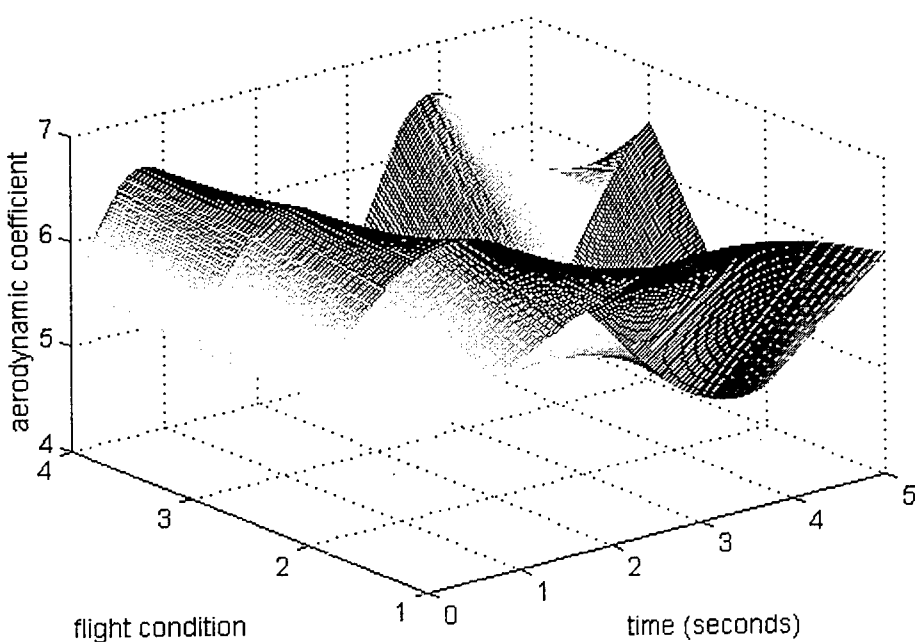


Figure 6. The variation of $C_{l\beta}$ with flight conditions

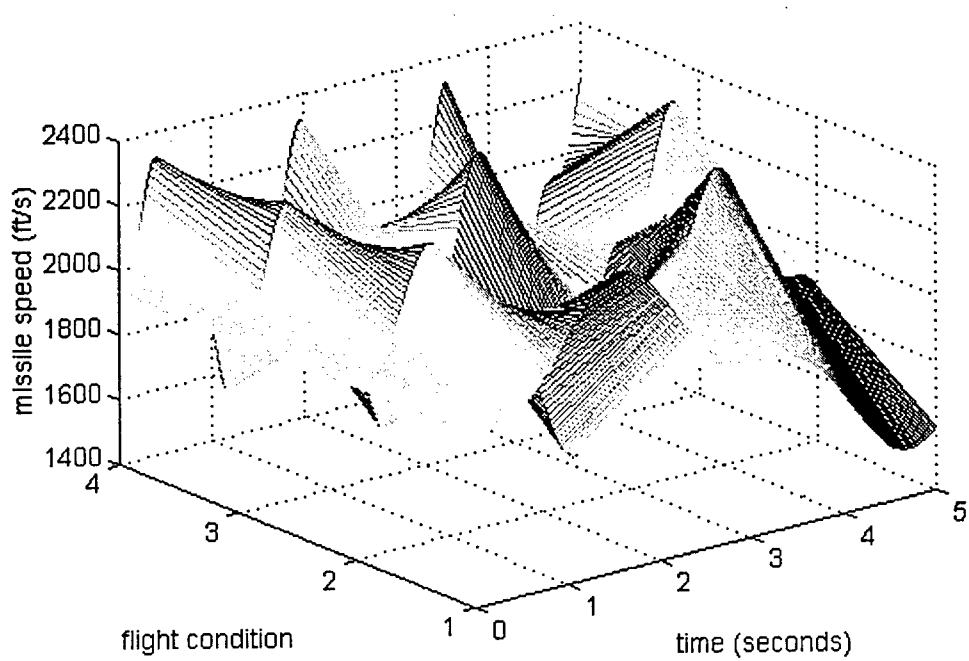


Figure 7. The variation of missile speed V with flight conditions

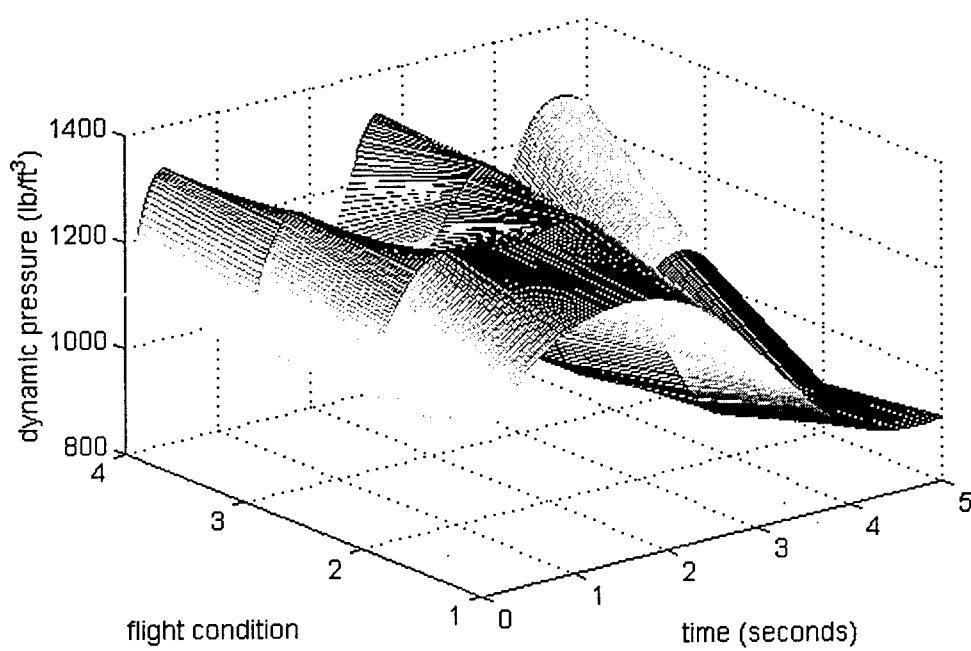


Figure 8. The variation of dynamic pressure Q with flight conditions

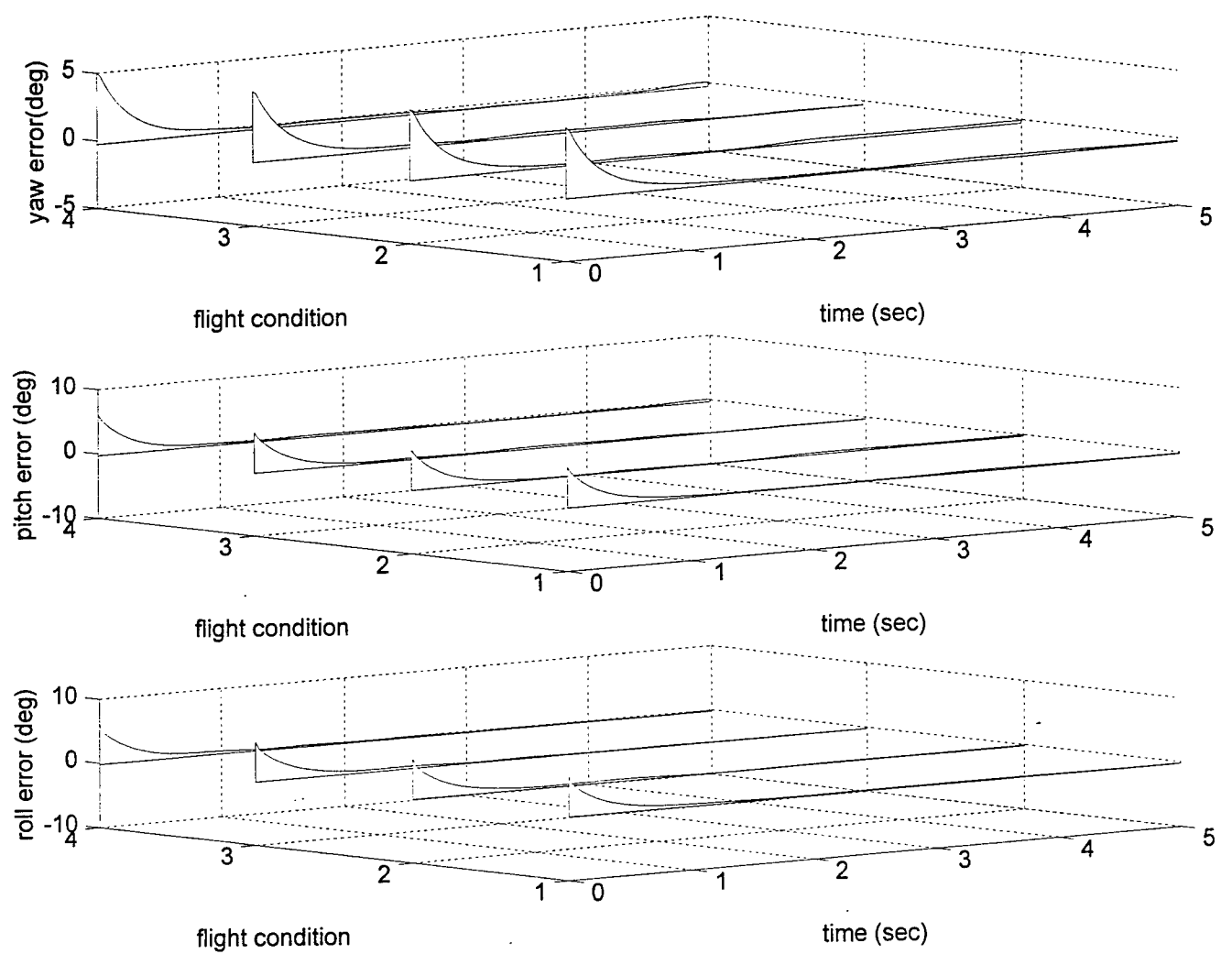


Figure 9. Tracking error under varying flight conditions

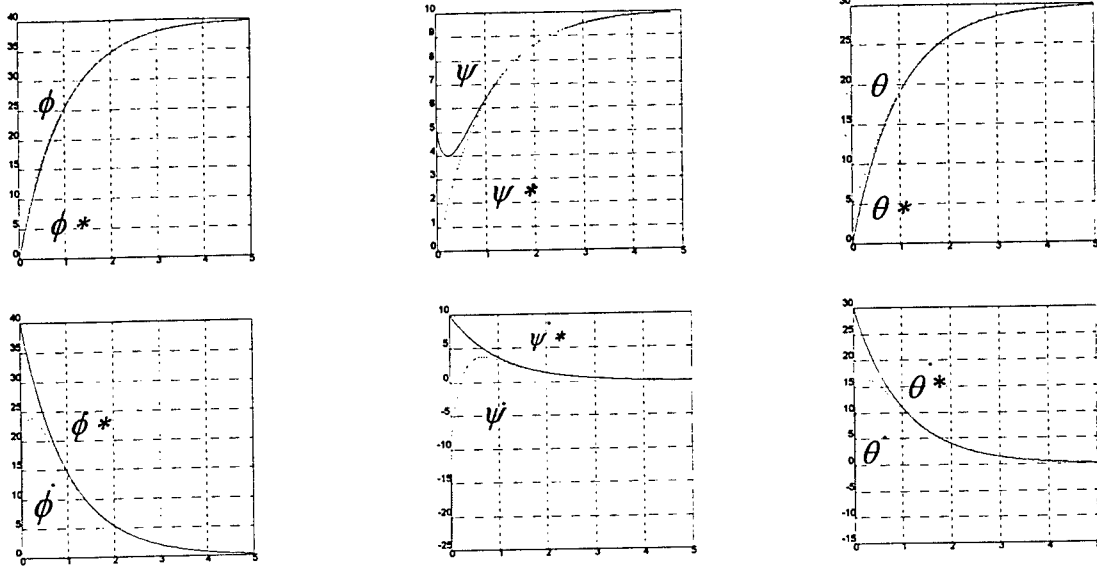


Figure 10. Yaw-pitch-roll motion tracking

Acknowledgment

Technical help from Dr. J. Cloutier, a senior research scientist at Eglin Air Force Base, is gratefully acknowledged.

References

- [1] S. Arimoto, S. Kawamura, F. Miyazaki and S. Tamaki, "Learning Control Theory for Dynamic Systems," *IEEE Int. Conf. on Decision and Control*, 1985, pp.1375-1380.
- [2] C. G. Atkeson and D. J. Reinkensmeyer, "Using Associate Content-addressable Memories to Control Robots," *Neural Networks for Control*, Edited by W. T. Miller, R. S. Sutton, and P. J. Werbos, 1992, pp. 255-285.
- [3] A. G. Barto, C. V. Hollot and B. E. Ydstie, "Neural Networks for Adaptive Control", NSF Research Proposal, 1989.
- [4] F. C. Chen and C. C. Liu, "Adaptively Controlling Nonlinear Contiguous-Time Systems Using Multilayer Neural Networks," *IEEE Trans. on Auto. Control*, Vol. 39, No. 6, 1994, pp. 1306-1310.
- [5] F. C. Chen and H. K. Khalil, "Adaptive Control of a Class of Nonlinear Discrete-Time Systems Using Neural Networks," *IEEE Trans. Auto. Control*, Vol. 40, No. 5, 1995, pp. 791-801.
- [6] J. M. Elzebda, A. H. Nayfeh and D. T. Mook, "Development of an Analytical Model of Wing Rock for Slender Delta Wings," *J. of Aircraft*, Vol. 26, No. 8, 1989.
- [7] G. Cybenko, "Approximation by Superposition of a Sigmoidal Function," *Mathematics of Control, Signals, and Systems*, No. 2, 1989, pp. 303-314.
- [8] E. Fix and J. L. Hodges, Jr., "Discriminatory Analysis, Non-parameteric Regression: Consistency Properties," *Technical Report No. 4, USAF School Aviation Medicine Randolph Field, TX AF- 41-(128)-31*, 1951.
- [9] M. Hagan, *Matlab Neural Networks Tool Box*, 1993, pp. 8-11.
- [10] S. Hara, Y. Yamamoto, T. Omata and M. Nakano, "Repetitive Control Systems: A New Type of Servo System for Periodic Exogenous Signals," *IEEE Trans. on Auto. Control*, Vol. 33, No. 7, 1988, pp. 659-668.
- [11] K. J. Hunt et al, "Neural Networks for Control Systems -- A survey," *Automatica*, Vol. 26, No. 8, 1992, pp. 1085-1112.
- [12] E. Kreyszig, *Advanced Engineering Mathematics*, Second Edition, John Wiley & Sons Inc., 1968.
- [13] F. L. Lewis, K. Liu and A. Yesildirek, "Neural Net Robot Controller with Guaranteed Tracking Performance," *IEEE Trans. on Neural Networks*, Vol. 6, No. 3, 1995, pp. 703-715.
- [14] A. Isidori, *Nonlinear Control Systems*. Berlin: Springer-Verlag, 1989.
- [15] A. Karakasoglu, S. I. Sudharsanan and M. K. Sundareshan, "Identification and Decentralized Adaptive Control Using Dynamical Neural Networks with Application to Robotic Manipulators," *IEEE Trans. on Neural Networks*, Vol. 4, No. 6, 1993, pp. 919-930.
- [16] E. N. Lorenz, "Atmospheric Predictability as Revealed by Naturally Occurring Analogues," *J. of the Atmospheric Science*, Vol. 26, 1969, pp. 636-646.

- [17] B. Kosko and S. Isaka, "Fuzzy logic," *Scientific American*, Vol. 269, No. 1, 1993, pp. 76-81.
- [18] K. S. Narendra and A. M. Parthasarathy, "Identification and Control of Dynamical Systems Using Neural Networks," *IEEE Trans. on Neural Networks*, Vol. 1, No. 1, 1990, pp. 4-27.
- [19] W. T. Miller, R. S. Sutton and P. J. Werbos (Eds), *Neural Networks for Control*, The MIT Press (Third Printing) 1992.
- [20] A. W. Moore, "Efficient Memory-based Learning for Robot Control," Ph. D. Thesis, Tech. Rep. 229, Computer Laboratory, University of Cambridge, Oct., 1990.
- [21] M. M. Polycarpou and A. T. Vemuri, "Learning Methodology for Failure Detection and Accommodation," *IEEE Control Systems*, Vol. 15, No. 3, 1995, pp. 16-25.
- [22] Z. R. Novakovic, "The Principle of self-support in Robot Control Synthesis," *IEEE Trans. on Systems, Man, and Cybernetics*, Vol. 21, No. 1, 1991, pp. 206- 220.
- [23] S. Schaal and C. G. Atkeson, "Robot Juggling: Implementation of Memory-based Learning," *IEEE Control Systems*, Vol. 14, No. 1, 1994, pp. 57-71.
- [24] H. Seraji, "Decentralized Adaptive Control of Manipulators: Theory, Simulation and Experimentation," *IEEE Trans. on Robotics and Automation*, Vol. 5, No. 2, 1989, pp. 183-201.
- [25] S. N. Singh, W. Yim and W. R. Wells, "Direct Adaptive and Neural Control of Wing-Rock Motion of Slender Delta Wings," *AIAA J. of Guidance, Control and Dynamics*, Vol. 18, No. 1, 1995, pp. 25-31.
- [26] J. E. Slotine and W. Li, *Applied Nonlinear Control*, Englewood Cliffs, NJ: Prentice-Hall, Inc., 1991.
- [27] C. Stanfill, and D. Waltz, "Toward Memory-based Reasoning," *Communications of the ACM*, Vol. 29, No. 12, 1986, pp. 1213-1228.
- [28] K. Steinbuch and U. A. Piske, "Learning Matrices and Their Applications," *IEEE Trans. on Electronic Computers*, Vol. 12, 1963, pp. 846-862.
- [29] M. Teshnehab and K. Watanabe, "Self Tuning of Computed Torque Gains by Using Neural Networks with Flexible Structures," *IEE Proc.-Control Theory Appl.*, Vol. 141, No. 4, 1994, pp. 235-242.
- [30] D. L. Waltz, "Applications of the Connection Machine," *Computer*, Vol. 20, No. 1, 1987, pp. 85-
- [31] J. S. Albus, "A New Approach to Manipulator Control: the Cerebellar Model Articulation Controller (CMAC)," *ASME Trans. on J. of Dynamic Systems, Measurement and Control*, Vol. 97, 1975, pp. 220-227.
- [32] J. S. Albus, "Data Storage in the Cerebellar Model Articulation Controller (CMAC)," *ASME Trans. on J. of Dynamic Systems, Measurement and Control*, Vol. 97, 1975, pp. 228-233.

- [33] P. Werbos, "Beyond regression: New Tools for Prediction and Analysis in Behavioral Science," Ph.D. dissertation, Harvard University, Cambridge, MA, Aug. 1974.
- [34] T. Yamada and T. Yabuta, "Neural Network Controller Using Autotuning Method for Nonlinear Functions," *IEEE Trans. on Neural Networks*, Vol. 1, No. 4, July, 1992, pp. 595-601.
- [35] K. Youcef-Toumi and S. Reddy, "Analysis of Linear Time Invariant Systems with Time Delay," *ASME Trans.J. f Dynamic Systems, Measurement, and Control*, Vol. 114, No. 12, 1992, pp. 544-555.
- [36] D. A. Schumacher, "Tactical Missile Autopilot Design Using Nonlinear Control," Ph.D. Thesis, Aerospace Engineering Dept., University of Michigan, 1994.
- [37] R. C. Nelson, *Flight Stability and Automatic Control*, McGraw-Hill, Inc. 1989

Appendix A: Glossary of Terms

α :	Angle of attack	
β :	Angle of sideslip	δ_p : Roll control input (surface deflection)
ψ :	Yaw angle	δ_q : Pitch control input (surface deflection)
θ :	Pitch angle	δ_r : Yaw control input (surface deflection)
ϕ :	Roll angle	N: Normal force
p :	Roll rate	Y: Side force
q :	Pitch rate	C_{a_b} : Aerodynamic coefficient - a due to b
r :	Yaw rate	l : Aerodynamic moment about x - axis
Q:	Dynamic pressure	m : Aerodynamic moment about y - axis
S:	Reference area	n : Aerodynamic moment about z - axis
d:	Reference length / diameter	I_{ij} : Moment or product of inertia
V:	Missile velocity	g : acceleration due to gravity
W:	Missile weight	M : Moment Vector
		F : Force Vector

Appendix B: Dynamic Equations of EMRAAT Missile

$$\begin{aligned}
\dot{p} = & \frac{1}{(I_{xx}I_{yy}I_{zz} - I_{xy}^2I_{zz} - I_{xx}I_{yz}^2 - 2I_{xy}I_{xz}I_{yz} - I_{xx}^2I_{yy})} [(-I_{xy}I_{xz}I_{zz} - I_{xz}^2I_{yz} + I_{xy}^2I_{yz} + I_{xy}I_{xz}I_{yy})p^2 + \\
& (I_{yy}I_{yz}I_{zz} - I_{yz}^3 - I_{xy}^2I_{yz} - I_{xy}I_{xz}I_{yy})q^2 + (-I_{yy}I_{yz}I_{zz} + I_{xy}I_{xz}I_{zz} + I_{yz}^3 + I_{xz}^2I_{yz})r^2 + \\
& (-I_{xy}I_{yz}I_{zz} + I_{xz}I_{yy}I_{zz} - 2I_{yz}^2I_{xz} - I_{xy}I_{yy}I_{yz} + I_{xx}I_{xy}I_{yz} - I_{xz}I_{yy}^2 + I_{xx}I_{xz}I_{yy})pq + \\
& (I_{xy}I_{zz}^2 + I_{xz}I_{yz}I_{zz} - I_{xy}I_{yy}I_{zz} - I_{xx}I_{xy}I_{zz} + 2I_{xy}I_{yz}^2 + I_{xz}I_{yy}I_{yz} - I_{xx}I_{xz}I_{yz})pr + \\
& (-I_{yy}I_{zz}^2 + I_{yz}^2I_{zz} + I_{yy}^2I_{zz} + I_{xy}^2I_{zz} - I_{yy}I_{yz}^2 - I_{xz}^2I_{yy})qr + QSD(C_{l_p}(I_{yy}I_{zz} - I_{yz}^2) + \\
& C_{n_p}(I_{xy}I_{yz} + I_{xz}I_{yy}))p + QSD(C_{m_q}(I_{xy}I_{zz} + I_{xz}I_{yz}))q + QSD(C_{l_r}(I_{yy}I_{zz} - I_{yz}^2) + \\
& C_{n_r}(I_{xy}I_{yz} - I_{xz}I_{yy}))r + QSD(C_{m_a}(I_{xy}I_{zz} + I_{xz}I_{yz}))\dot{\alpha} + QSD(C_{m_a}(I_{xy}I_{zz} + I_{xz}I_{yz}))\alpha + \\
& QSD(C_{l_\beta}(I_{yy}I_{zz} - I_{yz}^2) + C_{n_\beta}(I_{xy}I_{yz} + I_{xz}I_{yy}))\beta + QSD(C_{l_{\delta_p}}(I_{yy}I_{zz} - I_{yz}^2) + \\
& C_{n_{\delta_p}}(I_{xy}I_{yz} + I_{xz}I_{yy}))\delta_p + QSD(C_{m_{\delta_q}}(I_{xy}I_{zz} + I_{xz}I_{yz}))\delta_q + QSD(C_{l_{\delta_r}}(I_{yy}I_{zz} - I_{yz}^2) + \\
& C_{n_{\delta_r}}(I_{xy}I_{yz} + I_{xz}I_{yy}))\delta_r]
\end{aligned}$$

Appendix B: Dynamic Equations of EMRAAT Missile (Cont'd)

$$\begin{aligned}
\dot{q} = & \frac{1}{(I_{xx}I_{yy}I_{zz} - I_{xy}^2I_{xx} - I_{xx}I_{yz}^2 - 2I_{xy}I_{xz}I_{yz} - I_{xx}^2I_{yy})} [(-I_{xx}I_{xz}I_{xz} + I_{xx}I_{xy}I_{yz} + I_{xy}^3 + I_{xy}^2I_{xz})p^2 + \\
& (I_{xy}I_{yz}I_{zz} + I_{yz}^2I_{xz} - I_{xz}I_{xy}I_{yz} - I_{xy}^2I_{xz})q^2 + (-I_{xy}I_{yz}I_{zz} + I_{xx}I_{xz}I_{zz} - I_{xz}I_{yz}^2 - I_{xz}^3)r^2 + \\
& (-I_{xz}I_{yz}I_{zz} + I_{xy}I_{xz}I_{zz} + 2I_{xz}^2I_{yz} - I_{xx}I_{yy}I_{yz} - I_{xy}I_{xz}I_{yy} + I_{yz}I_{xz}^2 + I_{xx}I_{xy}I_{xz})pq + \\
& (I_{xx}I_{zz}^2 - I_{xz}^2I_{zz} - I_{xy}^2I_{zz} - I_{xz}^2I_{zz} + I_{xx}I_{yz}^2 + I_{xz}^2I_{xz})pr + \\
& (-I_{xy}I_{zz}^2 - I_{xz}I_{yz}I_{zz} + I_{xy}I_{yy}I_{zz} + I_{xx}I_{xy}I_{zz} + I_{xz}I_{yy}I_{yz} - I_{xz}I_{xz}I_{yz} - 2I_{xx}^2I_{xy})qr + \\
& QSD(C_{l_p}(I_{xy}I_{zz} - I_{xz}I_{yz}) + C_{n_p}(I_{xx}I_{yz} + I_{xy}I_{xz}))p + QSD(C_{m_q}(I_{xx}I_{zz} - I_{xz}^2))q + \\
& QSD(C_{l_r}(I_{xy}I_{zz} + I_{xz}I_{yz}) + C_{n_r}(I_{xx}I_{yz} + I_{xy}I_{yz}))r + QSD(C_{m_a}(I_{xx}I_{zz} - I_{xz}^2))\dot{\alpha} + \\
& QSD(C_{m_a}(I_{xx}I_{zz} - I_{xz}^2))\alpha + QSD(C_{l_p}(I_{xy}I_{zz} + I_{xz}I_{yz}) + C_{n_p}(I_{xx}I_{yz} + I_{xz}I_{xy}))\beta + \\
& QSD(C_{l_{\delta_p}}(I_{xy}I_{zz} + I_{xz}I_{yz}) + C_{n_{\delta_p}}(I_{xx}I_{yz} + I_{xz}I_{xy}))\delta_p + QSD(C_{m_{\delta_q}}(I_{xx}I_{zz} - I_{xz}^2))\delta_q + \\
& QSD(C_{l_{\delta_r}}(I_{xy}I_{zz} + I_{xz}I_{yz}) + C_{n_{\delta_r}}(I_{xx}I_{yz} + I_{xz}I_{xy}))\delta_r]
\end{aligned}$$

Appendix B: Dynamic Equations of EMRAAT Missile (Cont'd)

$$\begin{aligned}
\dot{r} = & \frac{1}{(I_{xx}I_{yy}I_{zz} - I_{xy}^2I_{xx} - I_{xx}I_{yz}^2 - 2I_{xy}I_{xz}I_{yz} - I_{xx}^2I_{yy})} [(-I_{xx}I_{xz}I_{yz} + I_{xx}I_{xy}I_{yy} - I_{xy}^3 - I_{xz}^2I_{xy})p^2 + \\
& (I_{xz}I_{yy}I_{yz} + I_{yz}^2I_{xy} - I_{xx}I_{xy}I_{yy} + I_{xy}^3)q^2 + (-I_{xy}I_{yz}^2 - I_{xz}I_{yy}I_{yz} + I_{xx}I_{xz}I_{yz} + I_{xy}I_{xz}^2)r^2 + \\
& (-I_{xx}I_{yz}^2 - I_{yy}^2I_{xx} + I_{xz}^2I_{yy} + I_{xy}^2I_{yy} + I_{yy}I_{xx}^2 - I_{xy}^2I_{xx})pq + \\
& (I_{xx}I_{yz}I_{zz} + I_{xy}I_{xz}I_{zz} + I_{xx}I_{xy}I_{yz} - 2I_{xy}^2I_{yz} - I_{yz}I_{xx}^2 - I_{xy}I_{xz}I_{yy} - I_{xx}I_{xy}I_{xz})pr + \\
& (-I_{xy}I_{yz}I_{zz} - I_{xz}I_{yy}I_{zz} + I_{xy}I_{yy}I_{yz} + I_{xx}I_{xy}I_{yz} + I_{xz}I_{yy}^2 - I_{xx}I_{xz}I_{yy} + 2I_{xy}^2I_{xz})qr + \\
& QSD(C_{l_p}(I_{xy}I_{yz} - I_{xz}I_{yy}) + C_{n_p}(I_{xx}I_{yy} - I_{xy}^2))p + QSD(C_{m_q}(I_{xx}I_{yz} + I_{xy}I_{xz}))q + \\
& QSD(C_{l_r}(I_{xy}I_{yz} + I_{xz}I_{yy}) + C_{n_r}(I_{xx}I_{yy} - I_{xy}^2))r + QSD(C_{m_a}(I_{xx}I_{yz} - I_{xy}I_{xz}))\dot{\alpha} + \\
& QSD(C_{m_a}(I_{xx}I_{yz} - I_{xy}I_{xz}))\alpha + QSD(C_{l_\beta}(I_{xy}I_{yz} + I_{xz}I_{yy}) + C_{n_\beta}(I_{xx}I_{yy} - I_{xy}^2))\beta + \\
& QSD(C_{l_{\delta_p}}(I_{xy}I_{yz} + I_{xz}I_{yy}) + C_{n_{\delta_p}}(I_{xx}I_{yy} - I_{xy}^2))\delta_p + QSD(C_{m_{\delta_q}}(I_{xx}I_{yz} - I_{xy}I_{xz}))\delta_q + \\
& QSD(C_{l_{\delta_r}}(I_{xy}I_{yz} + I_{xz}I_{yy}) + C_{n_{\delta_r}}(I_{xx}I_{yy} - I_{xy}^2))\delta_r]
\end{aligned}$$

MICROSTRUCTURAL EVOLUTION
DURING HOT DEFORMATION OF IN-718

Raghavan Srinivasan
Associate Professor
Steve Medeiros
Graduate Student
Department of Mechanical and Materials Engineering

Wright State University,
3640 Colonel Glenn Highway
Dayton, Ohio 45435

Final Report for:
Summer Research Extension Program
Wright Laboratory/Materials Directorate

Sponsored by:
Air Force Office of Scientific Research
Bolling Air Force Base

and

Wright Laboratory

March 1998

MICROSTRUCTURAL EVOLUTION
DURING HOT DEFORMATION OF IN-718

Raghavan Srinivasan

Associate Professor

Steve Medeiros

Graduate Student

Department of Mechanical and Materials Engineering
Wright State University

Abstract

Microstructural changes that occur during hot deformation of the nickel base superalloy, IN-718, were studied. Isothermal tests were conducted in vacuum at constant strain rates at different temperatures. Samples were sectioned and examined after deformation to a final strain of 0.69 (50% reduction in height). Both the volume fraction and size of the recrystallized grains varied with temperature and strain rate within the processing window. Complete recrystallization was observed at deformation temperatures of 1000° and 1025°C, whereas only partial recrystallization was observed at 950° and 975°C. No recrystallization was observed in specimens deformed at 900°C. At deformation temperatures of 1050° and 1100°C, the grain size after deformation was very large. Within the processing conditions that yielded a fine recrystallized microstructure, the activation energy for deformation was 400 kJ/mol.

MICROSTRUCTURAL EVOLUTION DURING HOT DEFORMATION OF IN-718

Raghavan Srinivasan and Steve Medeiros

Introduction

The properties and performance of a material in service is strongly influenced by the microstructure, which, in-turn, depends upon the thermo-mechanical processing that the material experiences. These so-called *performance-property-microstructure-processing* relationships have been the subject of research for many decades, and form the basis for the field of Materials Science of Engineering. A number of empirical relationships between processing parameters, such as strain, strain-rate, and temperature, and the resulting microstructure of an alloy have been developed for particular alloys. Recently, a new approach to metal forming process design was developed at the Process Design Branch of Wright Laboratory/Materials Directorate (WL/MLIM) [1,2]. A state-space representation of the microstructure of AISI 1030 steel was constructed from an existing set of empirical equations developed by Yada, et al. [3]. A two-stage analysis and optimization approach then obtained first the processing conditions necessary for achieving a particular microstructure, and then the design of a metal forming operation that would deliver these processing conditions. Yada's model predicted the evolution of γ or austenite grains during deformation at temperatures greater than 900°C. However, due to phase transformations occur between the deformation temperature and room temperature, and the austenite grain size had to be inferred from the distribution of the α phase or ferrite (that forms upon cooling) along the austenite grain boundaries. This indirect measure of the design parameter, namely the dynamically recrystallized austenite grain size at the forming temperature, meant the results were left with some uncertainty. The present study was undertaken to characterize an alloy that does not exhibit phase changes between the deformation temperature and room temperature. Data from this study will be provided to the Process Design group (WL/MLIM) for application of the methodology.

Materials and Experimental Procedures

Forging grade IN-718 with a nominal composition shown in Table-1 was obtained from Teledyne Alivac in the form of a 10-inch (254-mm) billet. Compression specimens 0.6 inch high and 0.4-inch diameter were machined by EDM and then surface ground to remove the recast layer. Compression tests were carried out in the Deformation Testing Facility at Wright State University. This facility consists of a 220 kip (1000 kN) hydraulic test frame with a vacuum furnace. Radiant heating from tungsten mesh heating elements permit test temperatures up to 2000°C in a hot zone with a maximum size of 5 inches diameter and 12 inches long. The displacement of the ram was controlled by a signal from the microcomputer. Load and stroke data was collected on a digital oscilloscope. A schematic drawing of the facility is shown in Figure-1. Prior to the start of the testing program, and several times during the program, the furnace was calibrated using a specimen with an inserted thermocouple.

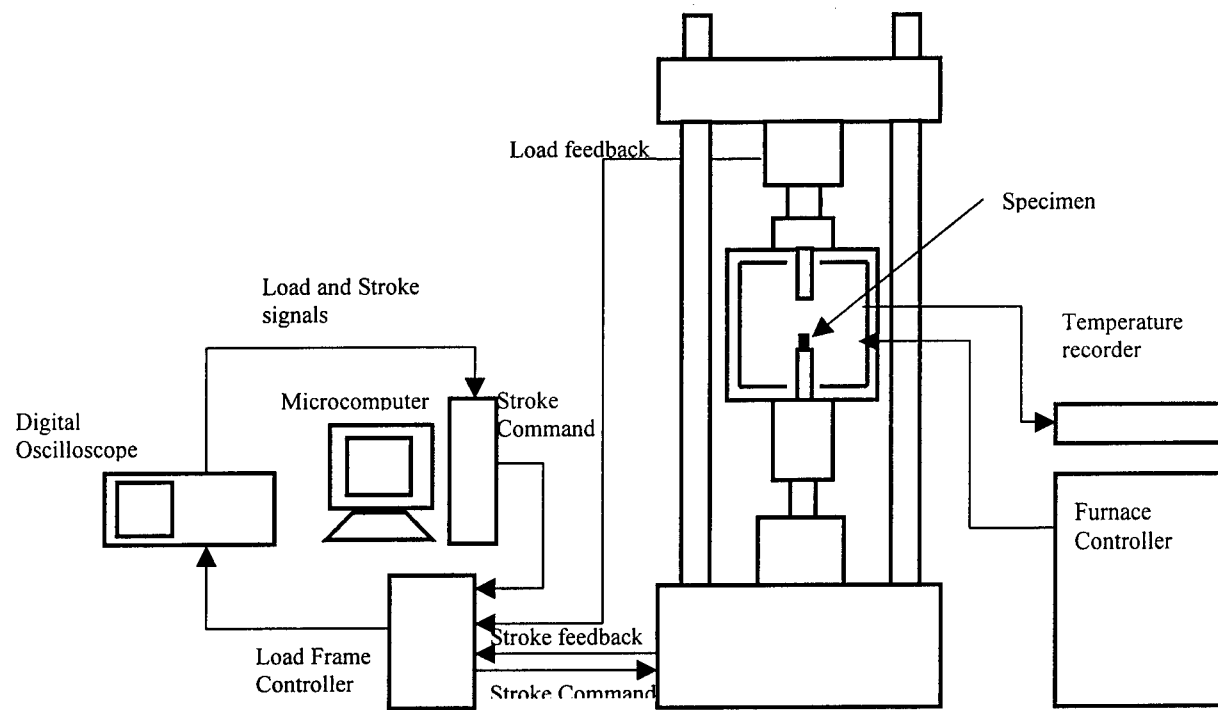


Figure 1: Schematic of the Deformation Testing System

Table-1 Nominal composition of the starting material

Alloying Element	C	S	Mn	Si	Cr	Mo	Co	Ti
Weight Fraction	0.025	0.0004	0.07	0.09	18.07	2.86	0.26	1.02

Alloying Element	Al	B	Fe	Cu	Ni	P	Nb	Ta
Weight Fraction	0.50	0.003	17.74	0.04	53.90	0.004	5.41	0.01

For each compression test, a sample was coated with graphite lubricant, and placed on similarly coated platens made of TZM. The system was heated in vacuum to the test temperature and held for 10 minutes. The specimen was then deformed at the appropriate strain rate to the desired final strain (discussed below). After testing, the heating elements were switched off, and the furnace chamber was filled with helium. The specimen was removed from the chamber after it had cooled to approximately 50°C. The load and stroke data collected by the oscilloscope was transferred to the microcomputer and converted to true-stress vs. true-strain curves. These curves were then corrected for deformation heating by assuming a fraction of the work of deformation was converted to heat, resulting in the change in temperature of the specimen [4].

In order to identify the regime of temperature and strain rate over which this material undergoes recrystallization, the following test matrix was selected.

Temperatures: **900°, 950°, 1000°, 1050°, 1100°C**

Strain rates: **0.001, 0.01, 0.1, 1 s⁻¹**

This matrix was selected because of the range of deformation rates available in forging presses used in the manufacture of superalloy components, and the known γ'' and Ni_3Nb solvus temperatures for the material, of approximately 925° and 1040°C respectively. Below the γ'' solvus temperature, fine particles of γ'' and carbide strengthen the alloy by impeding free movement of dislocations. The Ni_3Nb particles help to stabilize the grain structure. Above the Ni_3Nb solvus, excessive grain growth occurs. All compression tests in this matrix were carried out to a final strain of 0.69 (50% reduction in height). The deformed specimens were sectioned and examined to identify the range of temperatures over which recrystallization occurred, i.e., between the two solvus temperatures. The test matrix within the recrystallization domain was refined to include two additional temperatures, namely 975° and 1025°C. All samples were sectioned after deformation, and grain size was measured using the line-intercept method [5].

Results and Discussion

Figures 2 to 5 show the flow curves obtained from the compression tests. These flow stress values have been corrected for deformation heating, as mentioned earlier. The flow curves show the normal variation of stress with temperature and strain rate; namely faster strain rate and lower temperatures result in higher flow stresses. The flow stress appears to attain steady state after a true strain of about 0.3. Stress values at a strain of 0.4 were extracted and the apparent activation energy for deformation was calculated using the method described by Malas [6]. Figure 6 shows apparent activation energy contours over the entire test matrix. As can be seen in Figure 6, the activation energy for deformation of IN-718 between the two solvus temperatures is about 400 kJ/mol., which agrees with previously reported values for this material [7].

Figure 7 shows the starting microstructure for the test material. The average grain size was $16.4 \pm 1.1 \mu\text{m}$. Figures 8 to 14 show micrographs from specimens deformed to a true strain of 0.69 (50% reduction in height) at a strain rate of 0.01s^{-1} at different temperatures. Below the γ - γ'' solvus temperature, the grains appear deformed, and no recrystallization is observed. Upon exceeding the γ - Ni_3Nb solvus, the grain size after deformation is considerably larger than the starting grain size. The processing window is, therefore, bounded by the two solvus temperatures. At temperatures of 950° and 975°C, partial recrystallization of the deformed grains is observed, while complete recrystallization occurs at temperatures of 1000° and 1025°C. Figures 15 to 18 show microstructures of the samples deformed at 975°C and Figures 19 to 22 show microstructures of samples deformed at 1000°C. These figures show the effect of strain rate on the recrystallized grain size.

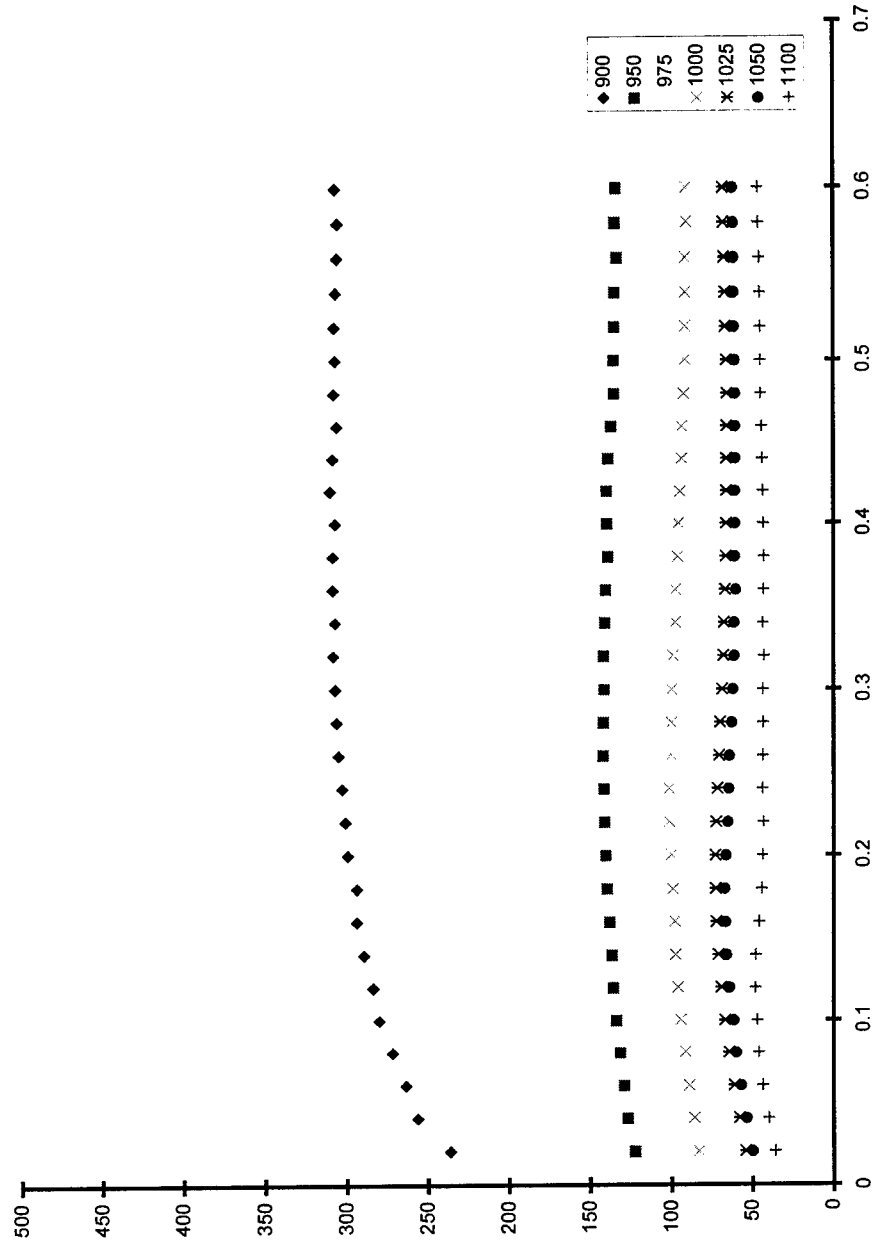


Figure 2: Flow curves for IN-718 deformed at a strain rate of 10^{-3}s^{-1} at temperatures of
 900°, 950°, 975°, 1000°, 1025°, 1050°, and 1100°C

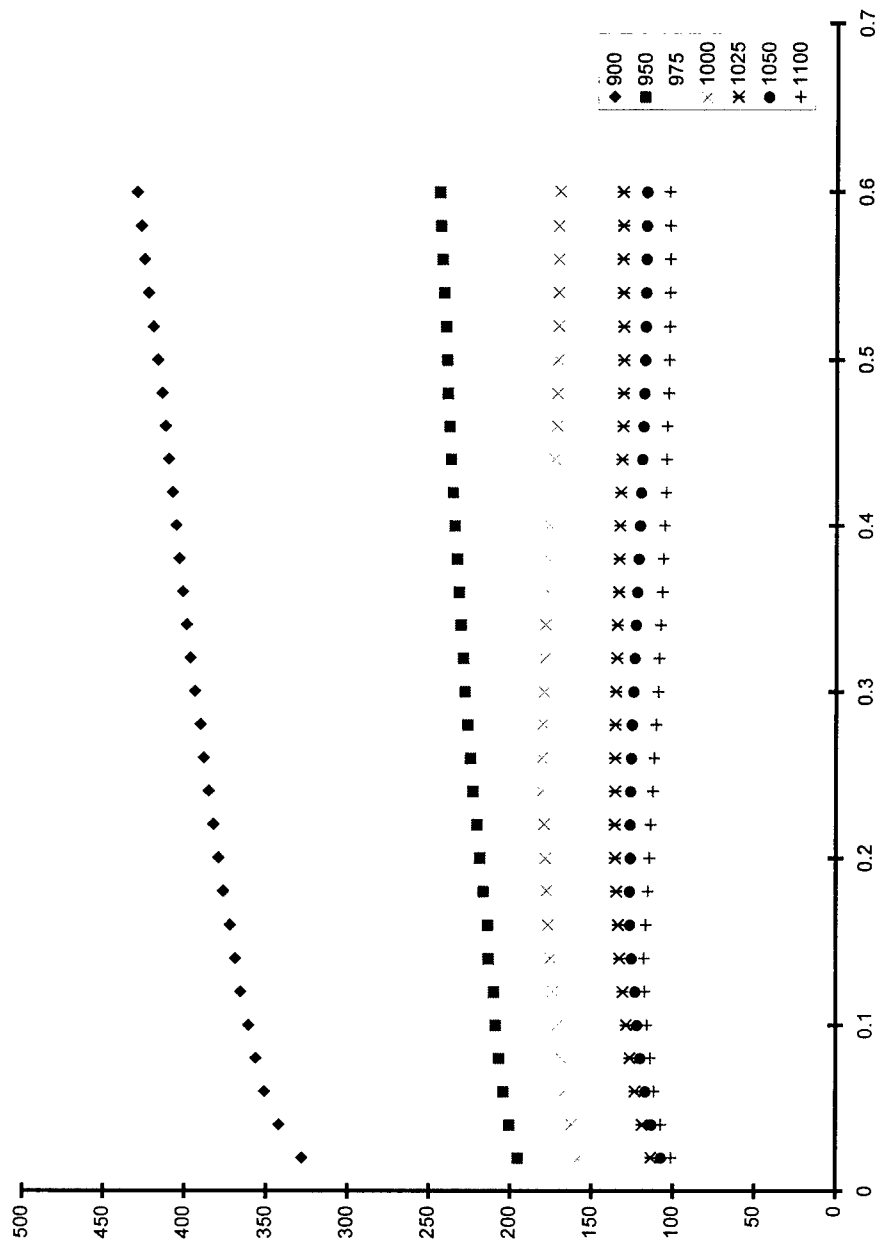


Figure 3: Flow curves for IN-718 deformed at a strain rate of 10^{-2}s^{-1} at temperatures of $900^\circ, 950^\circ, 975^\circ, 1000^\circ, 1025^\circ, 1050^\circ$, and 1100°C

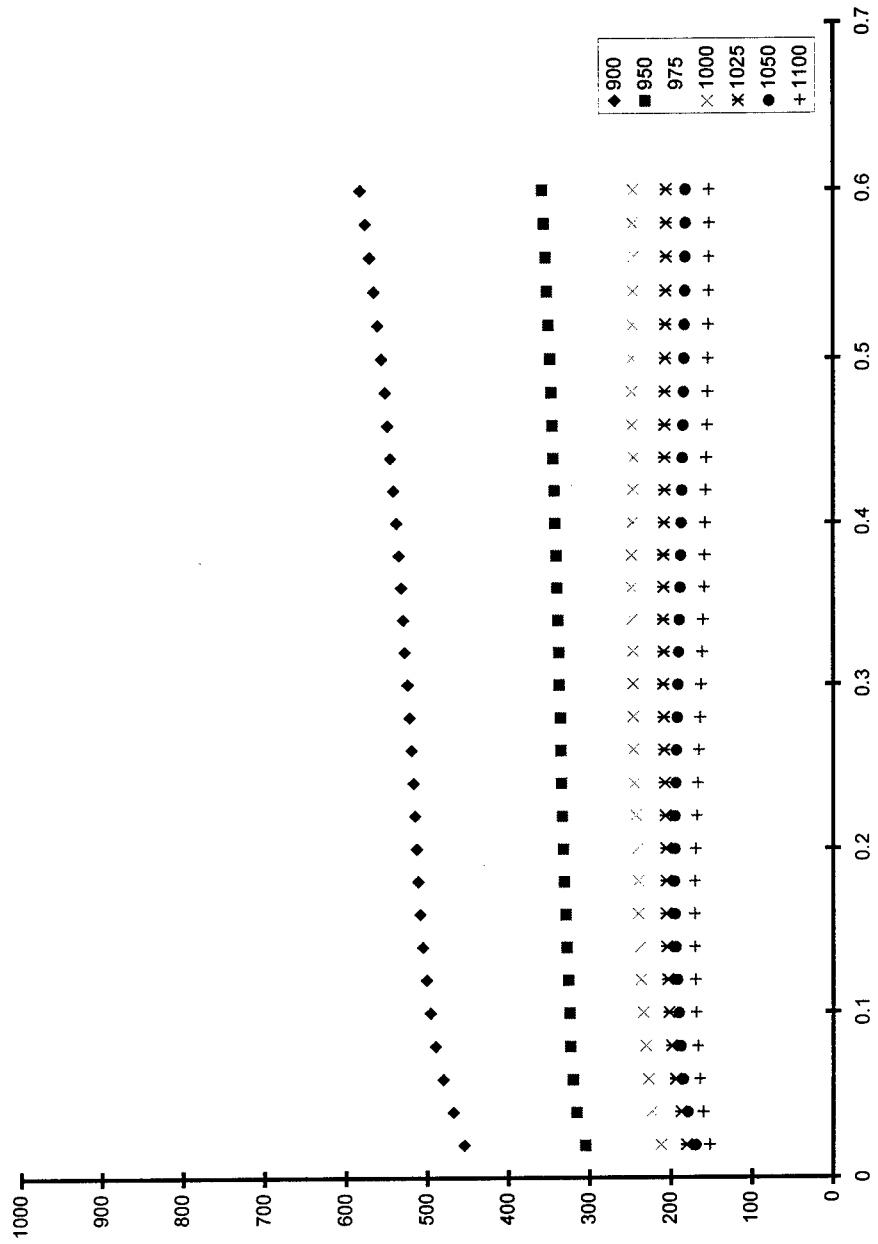


Figure 4: Flow curves for IN-718 deformed at a strain rate of 10^{-1}s^{-1} at temperatures of 900° , 950° , 975° , 1000° , 1025° , 1050° , and 1100°C

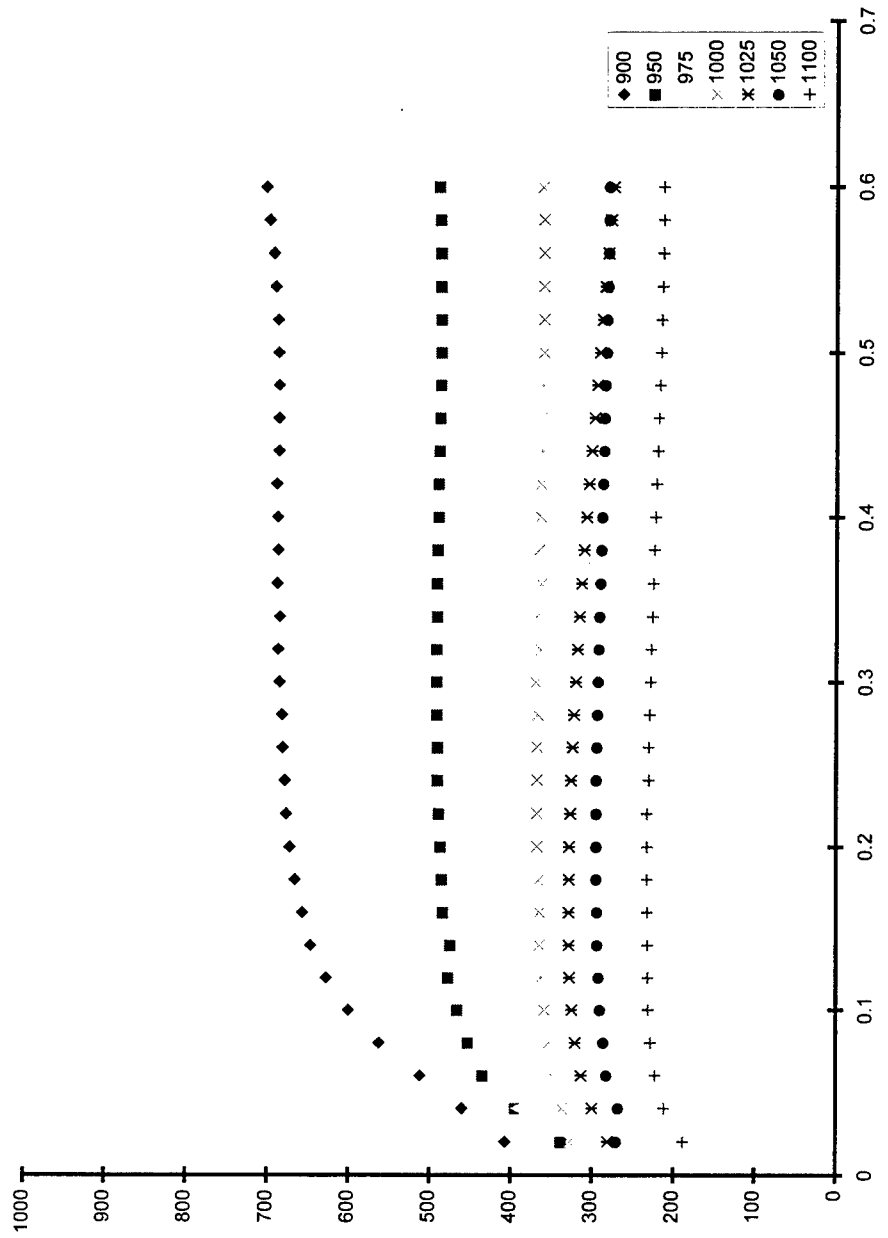


Figure 5: Flow curves for IN-718 deformed at a strain rate of 10^0 s^{-1} at temperatures of
 $900^\circ, 950^\circ, 975^\circ, 1000^\circ, 1025^\circ, 1050^\circ$, and 1100°C

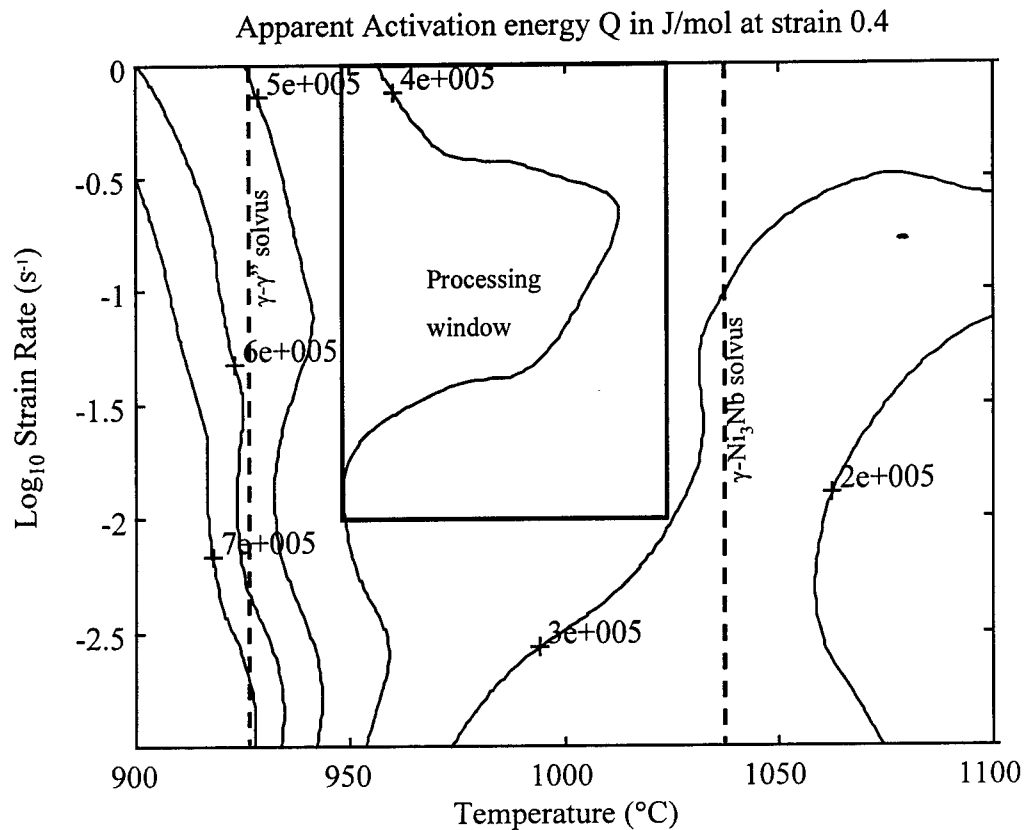


Figure 6: Apparent Activation energy contours at a strain of 0.4 for the deformation of IN-718

The fraction of grains that have recrystallized after deformation changes with deformation conditions. As can be seen in Figures 9, 10, 15 to 18, at deformation temperatures of 950° and 975°C, only partial recrystallization has occurred. Table-2 shows volume fraction of recrystallized grains under various deformation conditions. These measurements were made using the point count method. The average grain size of the recrystallized grains as a function of deformation temperature and strain rate is shown in Table-3. At temperatures of 1000° and 1025°C, when complete recrystallization occurs, the recrystallized grain size increases when strain rate increases from 10^{-3}s^{-1} to 10^{-2}s^{-1} , and then decreases upon further increase in strain rate. As seen in Figure 6, the activation energy for deformation at 10^{-3}s^{-1} at these temperatures is about 300kJ/mol, which is lower than that obtained for higher strain rates. The observed variation in grain size with strain rate may be related to metadynamic recrystallization that occurs in this material [8]. For the purposes of this study, the grain size reported is that observed in the deformed samples after deformation and cooling to room temperature. No attempt is made to distinguish whether recrystallization occurred during deformation or after deformation while cooling to room temperature.

Table-2: Fraction recrystallized after deformation of IN-718

	$\dot{\varepsilon} = 10^{-3} s^{-1}$	$\dot{\varepsilon} = 10^{-2} s^{-1}$	$\dot{\varepsilon} = 10^{-1} s^{-1}$	$\dot{\varepsilon} = 10^0 s^{-1}$
T=900°C	0	0	0	0
T = 950°C	0.52	0.32	0.56	0.52
T = 975°C	0.59	0.63	0.90	0.84
T = 1000°C	1.0	1.0	1.0	1.0
T = 1025°C	1.0	1.0	1.0	1.0
T = 1050°C	1.0	1.0	1.0	1.0
T = 1100°C	1.0	1.0	1.0	1.0

Table-3: Recrystallized grain size after deformation of IN-718

	$\dot{\varepsilon} = 10^{-3} s^{-1}$	$\dot{\varepsilon} = 10^{-2} s^{-1}$	$\dot{\varepsilon} = 10^{-1} s^{-1}$	$\dot{\varepsilon} = 10^0 s^{-1}$
T = 950°C	3.5	4.2	4.7	4.4
T = 975°C	4.9	4.7	4.3	4.1
T = 1000°C	$8.0 \pm 0.7 \mu\text{m}$	$8.3 \pm 0.3 \mu\text{m}$	$7.3 \pm 0.3 \mu\text{m}$	$7.1 \pm 0.7 \mu\text{m}$
T = 1025°C	$10.4 \pm 0.7 \mu\text{m}$	$11.5 \pm 0.7 \mu\text{m}$	$10.8 \pm 0.7 \mu\text{m}$	$10.0 \pm 0.7 \mu\text{m}$

Summary

Microstructural changes that occur during deformation of IN-718 were studied under isothermal-constant-strain-rate deformation conditions. After deformation to a strain of 0.69 (50% reduction in height) no recrystallization was observed at a deformation temperature of 900°C. Partial recrystallization was observed at temperatures of 950° and 975°C, and complete recrystallization at 1000° and 1025°C. At deformation temperatures of 1050° and 1100°C, there was considerable grain growth in the deformed specimens. This can be attributed to the dissolution of the Ni₃Nb particles above the solvus temperature of about 1040°C. Within the regime of dynamic recrystallization, the activation energy for deformation was approximately 400-kJ/mol. The grain size after recrystallization within the processing regime decreased with increasing strain rate from 10^{-2} to $10^0 s^{-1}$ both at 1000° and 1025°C. At all strain rates, the grain size after deformation at 1000°C was smaller than that observed after deformation at 1025°C.



Figure 7: Microstructure of the as-received material

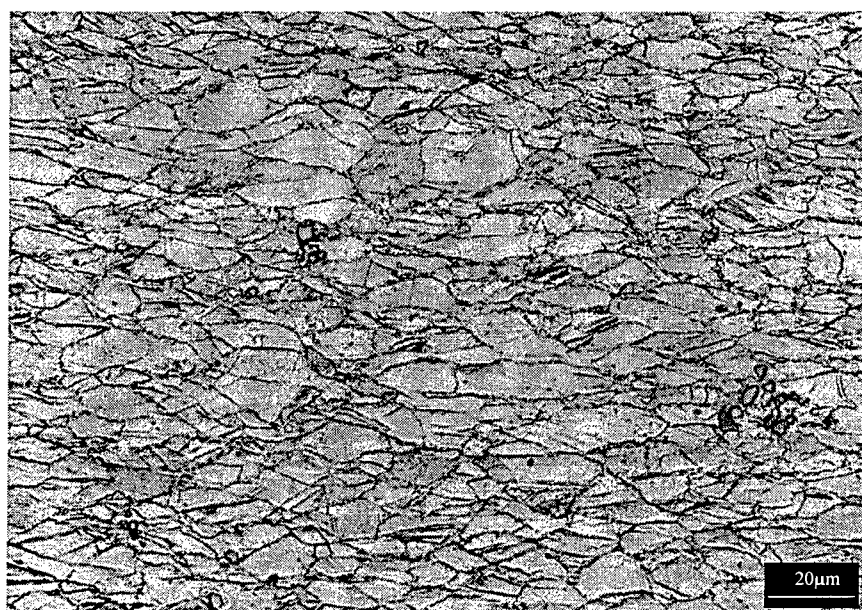


Figure 8: Microstructure of IN-718 after deformation to a strain of 0.69 at 900°C at a strain rate of 10^{-2}s^{-1} .

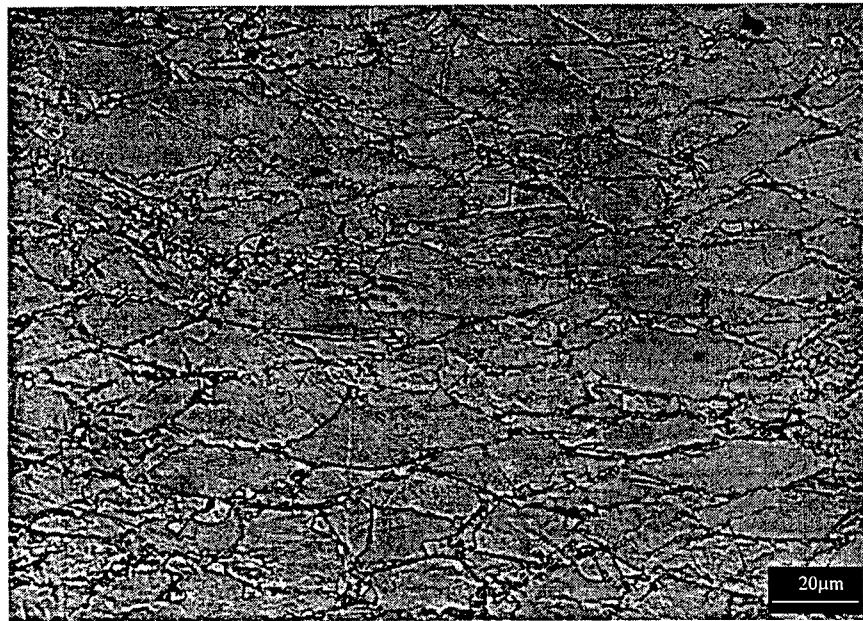


Figure 9: Microstructure of IN-718 after deformation to a strain of 0.69 at 950°C at a strain rate of 10^{-2}s^{-1} .

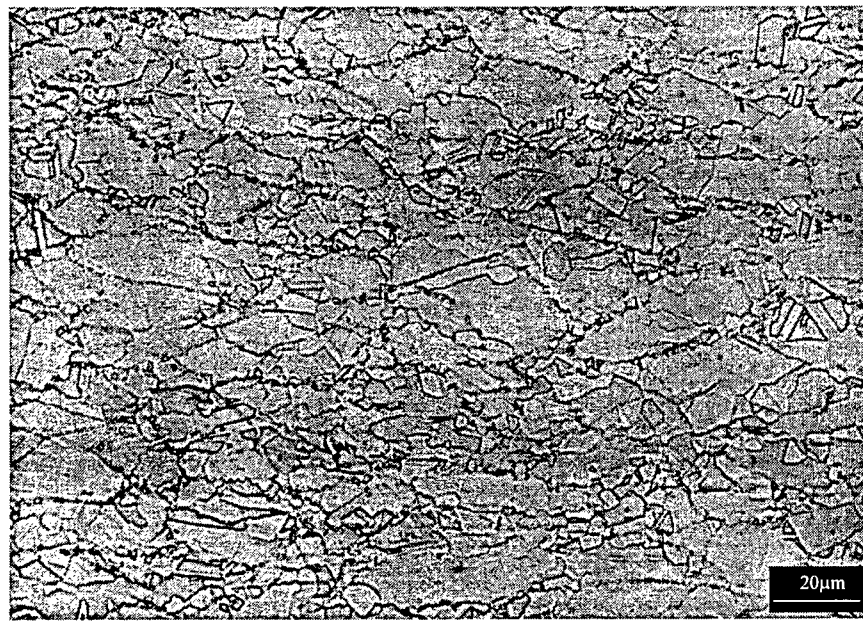


Figure 10: Microstructure of IN-718 after deformation to a strain of 0.69 at 975°C at a strain rate of 10^{-2}s^{-1} .

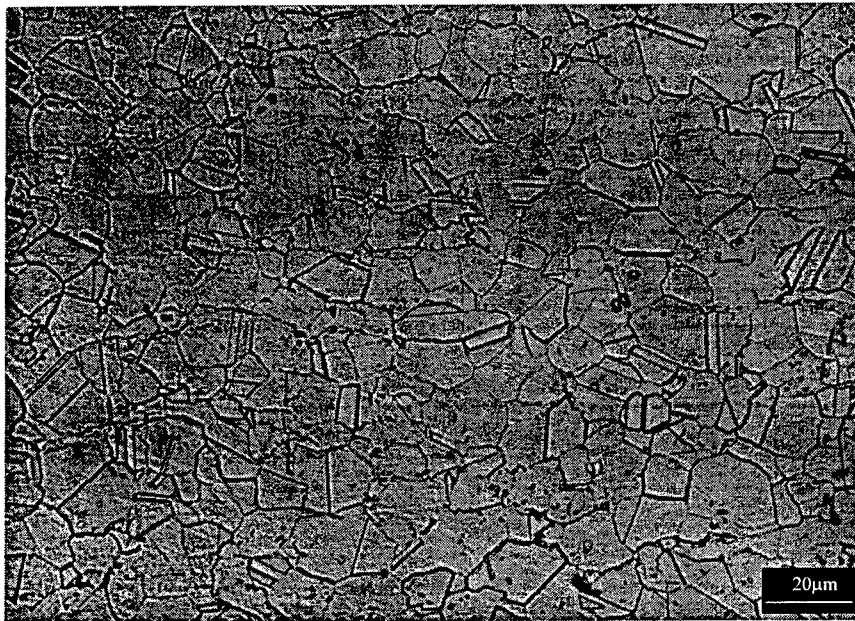


Figure 11: Microstructure of IN-718 after deformation to a strain of 0.69 at 1000°C at a strain rate of 10^{-2}s^{-1} .

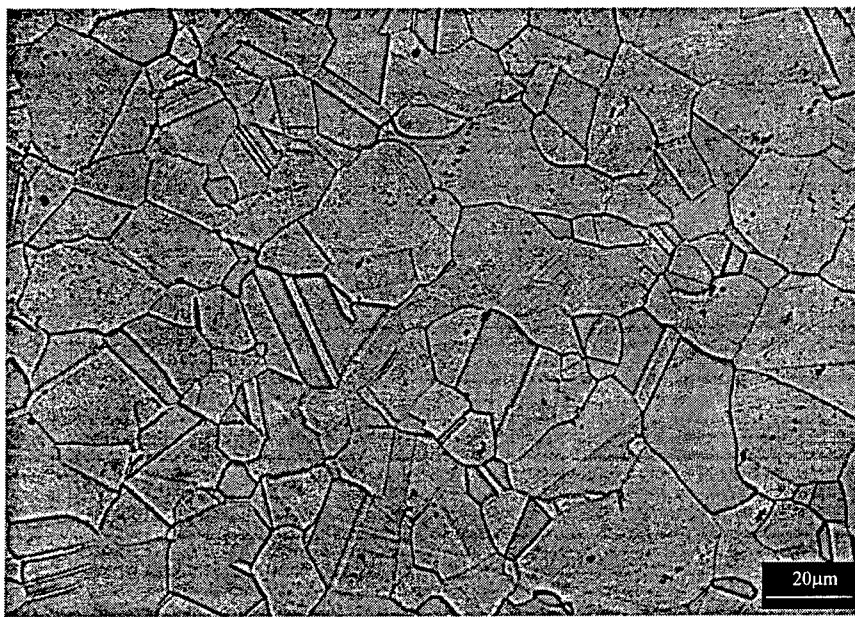


Figure 12: Microstructure of IN-718 after deformation to a strain of 0.69 at 1025°C at a strain rate of 10^{-2}s^{-1} .

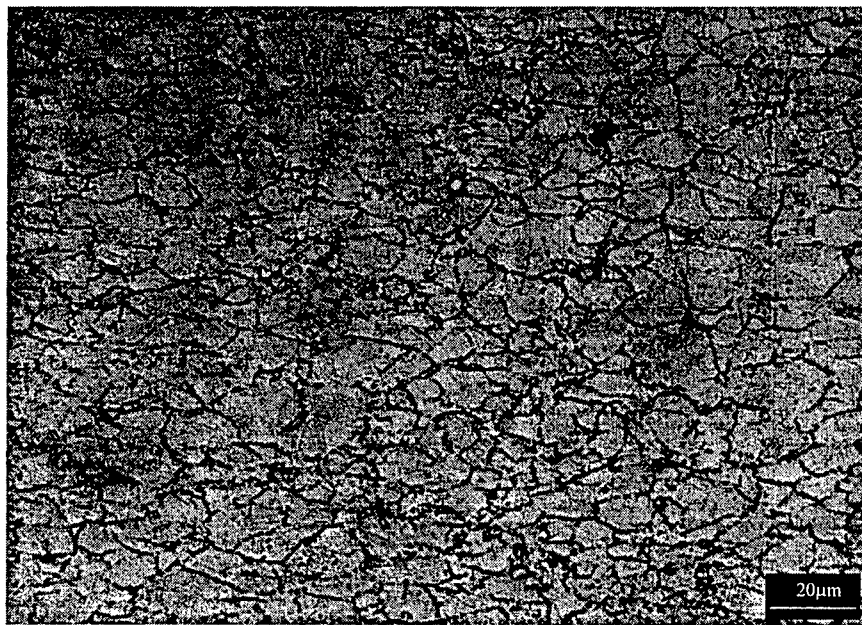


Figure 13: Microstructure of IN-718 after deformation to a strain of 0.69 at 1050°C at a strain rate of 10^{-2}s^{-1} .

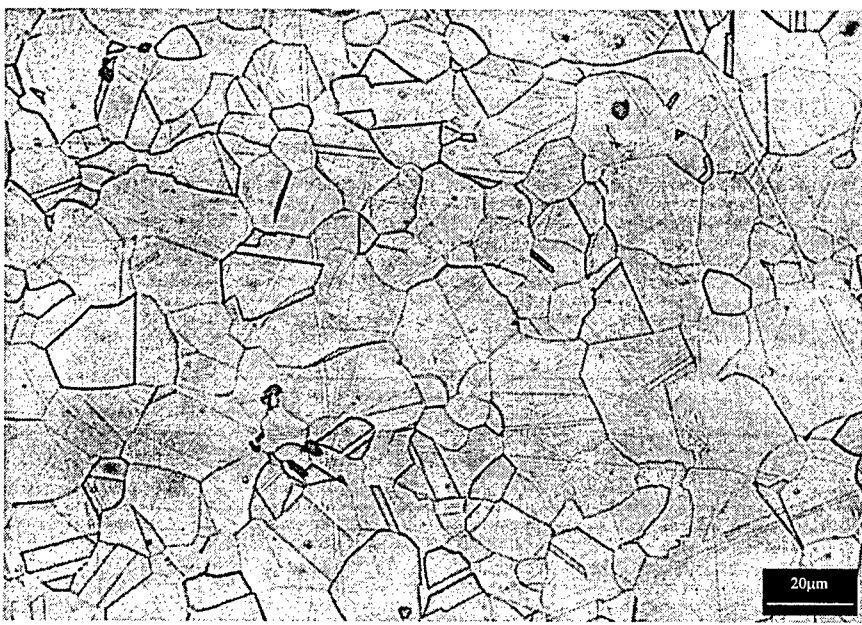


Figure 14: Microstructure of IN-718 after deformation to a strain of 0.69 at 1100°C at a strain rate of 10^{-2}s^{-1} .



Figure 15: Microstructure of IN-718 after deformation to a strain of 0.69 at 975°C at a strain rate of 10^{-3}s^{-1} .

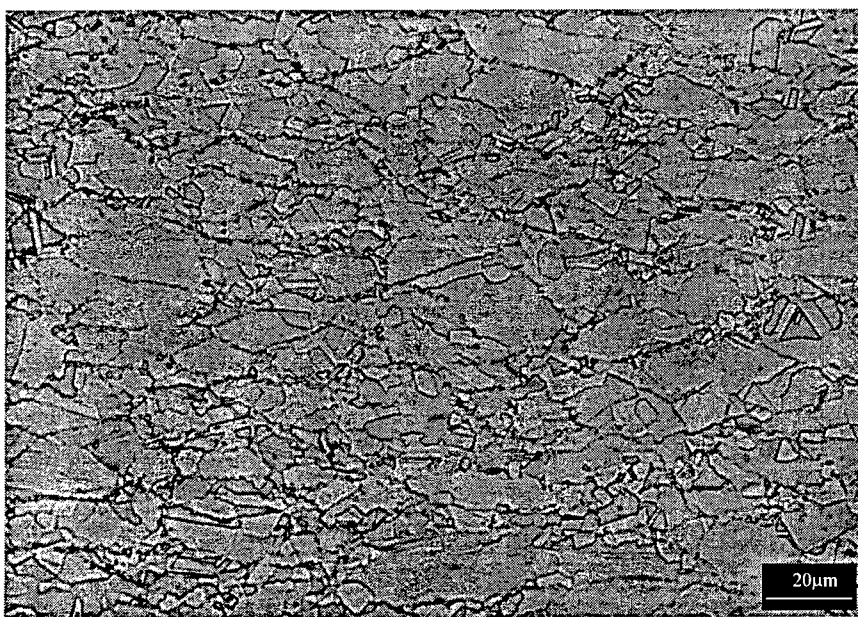


Figure 16: Microstructure of IN-718 after deformation to a strain of 0.69 at 975°C at a strain rate of 10^{-2}s^{-1} .



Figure 17: Microstructure of IN-718 after deformation to a strain of 0.69 at 975°C at a strain rate of 10^{-1}s^{-1} .

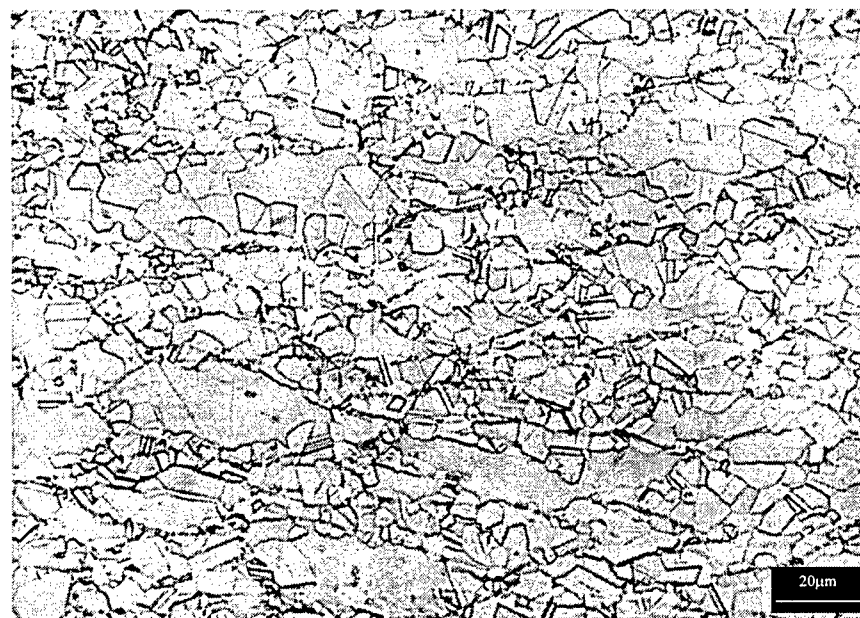


Figure 18: Microstructure of IN-718 after deformation to a strain of 0.69 at 995°C at a strain rate of 10^0s^{-1} .

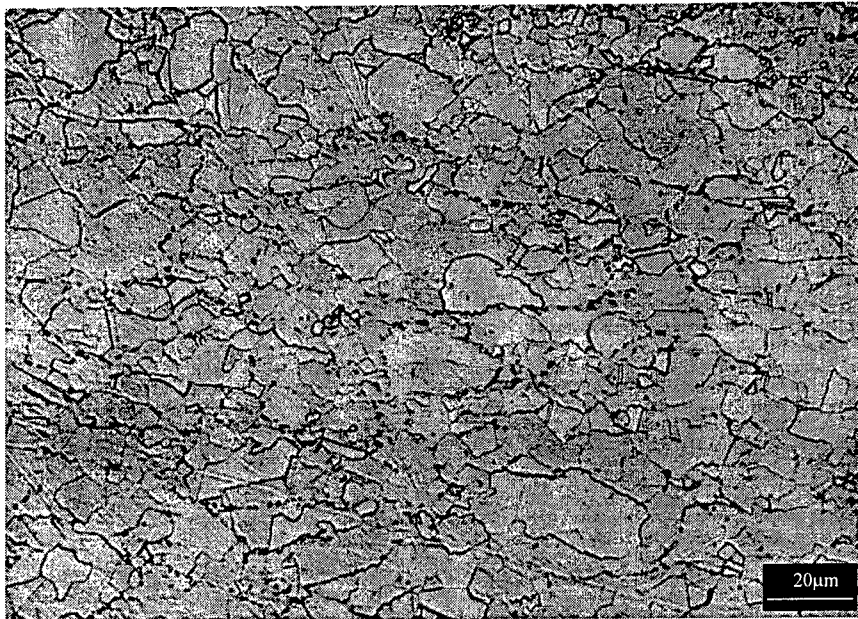


Figure 19: Microstructure of IN-718 after deformation to a strain of 0.69 at 1000°C at a strain rate of 10^{-3} s^{-1} .

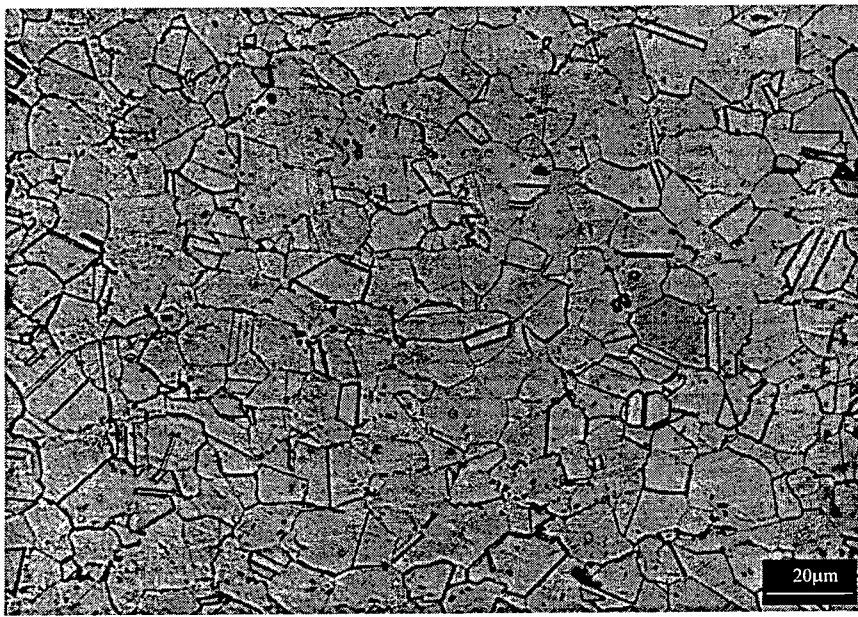


Figure 20: Microstructure of IN-718 after deformation to a strain of 0.69 at 1000°C at a strain rate of 10^{-2} s^{-1} .

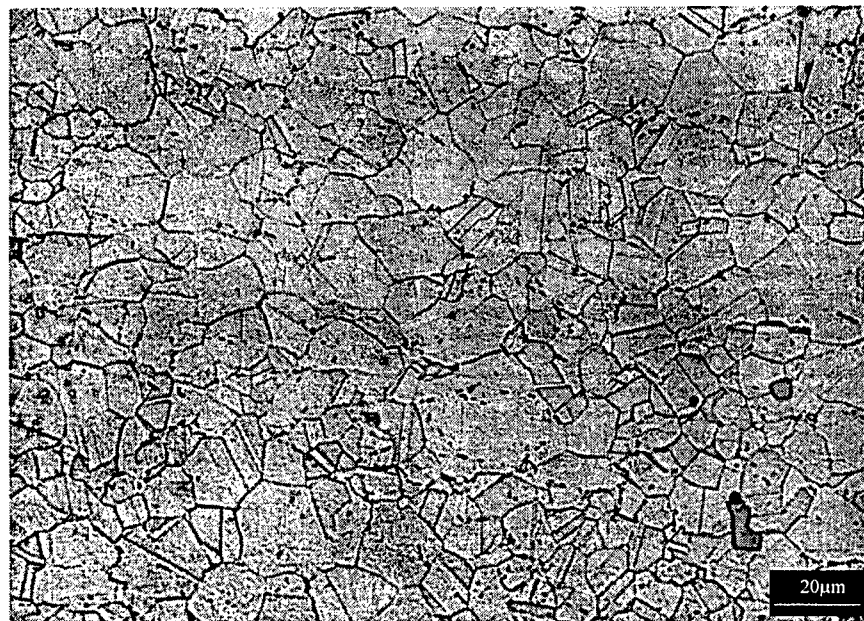


Figure 21: Microstructure of IN-718 after deformation to a strain of 0.69 at 1000°C at a strain rate of 10^{-1}s^{-1} .

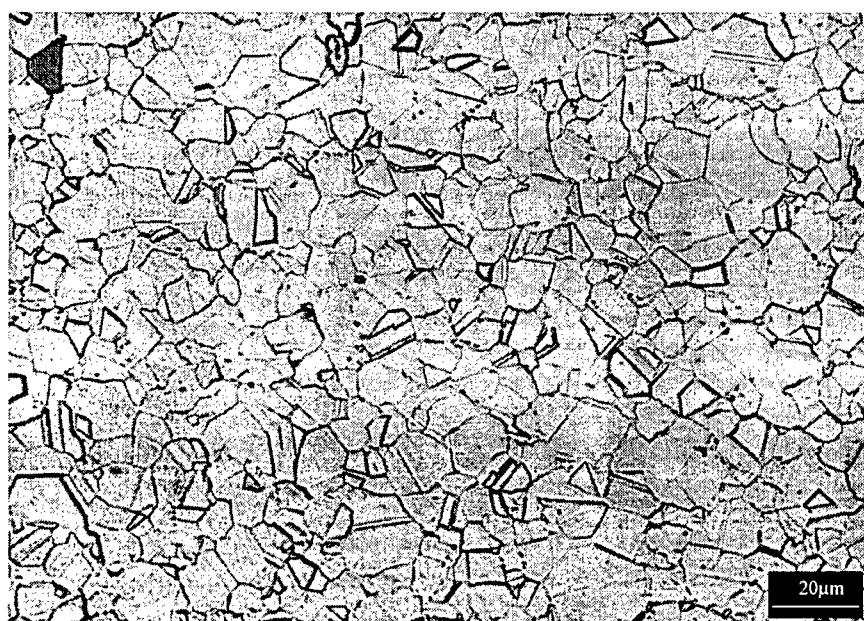


Figure 22: Microstructure of IN-718 after deformation to a strain of 0.69 at 1000°C at a strain rate of 10^0s^{-1} .

References

1. S. Venugopal, E.A. Medina, J.C. Malas, S. Medeiros, W.G. Frazier, W.M. Mullins, and R. Srinivasan, "Optimization of Microstructure Development during Deformation Processing using Control Theory Principles," Scripta Materialia, Vol. 36, No. 3, pp. 347-353, 1997
2. J.C. Malas, W.G. Frazier, S. Venugopal, E.A. Medina, S. Medeiros, R. Srinivasan, R.D. Irwin, W.M. Mullins, and A. Chaudhary, "Optimization of Microstructure Development during Deformation Processing using Control Theory," Metallurgical and Materials Transactions, Vol. 28A, No. 9, pp. 1921-1930, 1997.
3. H. Yada, Proc. Int. Symp. Accelerated Cooling of Rolled Steels, G.E. Ruddle and A.F. Crawley, Eds., Pergamon Press, Canada, p 105, 1987.
4. P. Dadras, and J.F. Thomas, Jr., "Characterization and modeling for forging deformation of Ti-6242," Metallurgical Transactions A., vol. 12A, p.1867, 1981.
5. ASTM Standard E112, American Society for Testing and Materials, Vol. 3.01, 1991.
6. J.C. Malas, "Methodology for Design and Control of Thermomechanical Processes," Ph.D. Dissertation, Ohio University, Athens, Ohio, 1991.
7. A.A. Guimaraes and J.J. Jonas, "Recrystallization and Aging Effects Associated with the High Temperature Deformation of Waspaloy and Inconel 718," Metallurgical Transactions A, Vol. 12A, pp. 1655-1666, 1981.
8. L.X. Zhou and T.N. Baker, "Effects of Dynamic and Metadynamic Recrystallization on Microstructures of Wrought IN-718 due to Hot Deformation," Materials Science and Engineering A, Vol. 196, pp. 89-95, 1995.

THE EFFECTS OF TRANSIENT ACCELERATION LOADINGS ON THE PERFORMANCE OF A
COPPER-ETHANOL HEAT PIPE WITH SPIRAL GROOVES

Scott K. Thomas
Assistant Professor
Department of Mechanical and Materials Engineering

Wright State University
Dayton, OH 45435

Final Report for:
Summer Faculty Research Program
Wright Laboratory

Sponsored by:
Air Force Office of Scientific Research
Bolling Air Force Base, Washington DC

and

Wright Laboratory

December 1997

THE EFFECTS OF TRANSIENT ACCELERATION LOADINGS ON THE PERFORMANCE OF A
COPPER-ETHANOL HEAT PIPE WITH SPIRAL GROOVES

Scott K. Thomas
Assistant Professor
Department of Mechanical and Materials Engineering
Wright State University

Abstract

A helically-grooved copper heat pipe with ethanol as the working fluid has been fabricated and tested on a centrifuge table. The heat pipe was bent to match the radius of curvature of the table so that uniform transverse (perpendicular to the axis of the heat pipe) body force fields could be applied along the entire length of the pipe. The steady-state performance of the curved heat pipe under transverse body force fields was determined by varying the heat input ($Q_{in} = 25$ to 250 W) and centrifuge table velocity (radial acceleration $|\ddot{a}_r| = 0$ to 10-g). The thermal resistance decreased with increasing heat input until dryout was reached. As dryout commenced, the thermal resistance increased. Due to the geometry of the helical grooves, the capillary limit increased by a factor of five when the radial acceleration increased from $|\ddot{a}_r| = 0$ to 6.0-g . This important result was verified by a mathematical model of the heat pipe system, wherein the capillary limit of each groove was calculated in terms of centrifuge table angular velocity, the geometry of the heat pipe and the grooves (including helix pitch), and temperature-dependent working fluid properties.

THE EFFECTS OF TRANSIENT ACCELERATION LOADINGS ON THE PERFORMANCE OF A COPPER-ETHANOL HEAT PIPE WITH SPIRAL GROOVES

Scott K. Thomas

Introduction

Heat pipes have been proposed to be used aboard fighter aircraft such as the Navy F/A-18 to act as heat sinks for electronics packages which drive aileron or trailing edge flap actuators (Gernert et al., 1991; Yerkes and Hager, 1992). During combat, transient acceleration fields of up to 9-g could be present on the aircraft. Therefore, knowledge of the thermal performance of heat pipes under elevated acceleration fields is of importance to designers of the electronics packages in need of cooling.

Yerkes and Beam (1992) analytically and experimentally studied a flexible copper–water arterial heat pipe in a transient heat flux and transient body force environment using a centrifuge table. The effects of transverse body forces on the liquid flow in the artery were analyzed by developing a relationship between the wicking height and the radial acceleration. With a constant heat input, the capillary limit of the heat pipe was reached as the radial acceleration increased above 8-g. It was hypothesized that the transverse body force field partially deprimed the artery.

Yerkes and Hallinan (1995a, 1995b) studied the effects of transient accelerations on an unheated meniscus in a capillary tube. A centrifuge table was used to experimentally examine the advancing or receding behavior of water and ethanol in the capillary tube. The analytical study involved the formulation of the transient nature of the acceleration field in the meniscus region and the dynamic behavior of the meniscus as a result of the temporal acceleration-induced body forces. The effects of the transverse body forces, the Bond number and the capillary number on the motion of the meniscus were predicted and compared to the experimental results with excellent agreement.

Thomas and Yerkes (1997) determined the quasi-steady state thermal resistance of a flexible copper–water heat pipe under transient acceleration fields with constant heat input using a horizontal centrifuge table. The performance of the heat pipe was examined for the following parameters: Heat input, $Q_{in} = 75$ to 150 W; condenser temperature, $T_{cw} = 3, 20$ and 35°C ; and sinusoidal acceleration frequency, $f = 0, 0.01, 0.05, 0.1, 0.15$ and 0.2 Hz. The centrifuge radial acceleration ranged from $|\vec{a}_r| = 1.1$ to 9.8-g for each frequency setting. In addition, the effects of the previous dryout history were noted. It was found that the thermal resistance of the heat pipe decreased with increasing acceleration frequency and condenser

temperature, and increased with the heat input. The occurrence of dryout prior to changing the frequency tended to result in higher thermal resistances as compared to the case when dryout did not occur due to the inability of the artery to fully reprime.

The objective of the present study was to determine the steady-state operating characteristics of a helically-grooved copper-ethanol heat pipe when subjected to constant heat input and constant transverse (perpendicular to the axis of the heat pipe) body force fields. The radial acceleration and gravity combine to impose a transverse body force on the heat pipe. This body force was varied by increasing the radial acceleration. The heat input and radial acceleration ranged from $Q_{in} = 25$ to 250 W and $|\vec{a}_r| = 0.0$ to 10.0-g. The thermal resistance of the heat pipe under various conditions is reported, as well as incidents of dryout. The effects of the transverse body force field on the temperature uniformity between the inboard and outboard sides of the pipe are shown. The influence of the external convective heat transfer from the heat pipe due to the motion of the centrifuge table on the total heat transported was determined. The capillary limit for $|\vec{a}_r| = 0.0, 2.0, 4.0$ and 6.0-g are presented. An iterative mathematical model to determine the capillary limit of helically-grooved heat pipes for various operating temperatures and body force fields has been developed, which includes the effects of the geometry of the heat pipe and the grooves (including helix pitch) and temperature-dependent working fluid properties.

Experimental Setup

The purpose of the experiment was to examine the steady-state performance of a helically-grooved copper-ethanol heat pipe under various heat inputs and transverse body force fields using a centrifuge table located at Wright-Patterson AFB (WL/POOS). To ensure uniform radial acceleration fields over the length of the heat pipe, the pipe was bent to match the 1.22 m radius of curvature of the centrifuge table. Physical information concerning the heat pipe is given in Table 1. It should be noted that the helix angle α was very small: Each groove rotated through an angle of 2.07 rad (120 arc degrees) over the length of the pipe. The heat pipe was mounted to a platform which overhung the edge of the horizontal centrifuge table. This allowed the heat pipe to be positioned such that the radius of curvature was equivalent to the outermost radius of the centrifuge table. Insulative mounting blocks were used to ensure that the heat pipe matched the prescribed radius as closely as possible. The horizontal centrifuge table was driven by a 20-hp dc motor. The acceleration field near the heat pipe was measured by a three-axis accelerometer. The acceleration field at the centerline of the heat pipe radius was calculated from these readings using a coordinate transformation.

Power was supplied to the heat pipe evaporator section by a precision power supply through power slip

rings to the table. The input power was calculated using the current and voltage readings. While the current reading could be made directly using a precision ammeter, the voltage across the electric heater had to be measured on the rotating table because voltage drops were noted between the control room and the table, regardless of the size of wire used. Therefore, the voltage at the heater was obtained through the instrumentation slip ring assembly and read by a precision voltmeter. A pressure-sensitive nichrome heater tape with an aluminized backing was wound uniformly around the circumference of the evaporator section for heat input.

The calorimeter consisted of a length of 1/8 in. OD copper tubing wound tightly around the condenser section. The size of the tubing was chosen to be small to minimize the effects of acceleration on the performance of the calorimeter. Thermal grease was used between the heat pipe and the calorimeter to decrease contact resistance. Type T thermocouples were inserted through brass T-branch connectors into the coolant inlet and exit streams, and a rotameter and high-resolution digital flow meter were used to measure the mass flow rate of the coolant (ethylene glycol/water mixture). The mass flow rate was controlled using a high-pressure booster pump, which aided the low-pressure pump in the recirculating chiller. The temperature of the coolant was maintained at a constant setting by the recirculating chiller ($T_{cw} = 20^\circ\text{C}$). Coolant was delivered to the centrifuge table via a double-pass hydraulic rotary coupling.

The rotameter and digital flow meter used to determine the mass flow rate of coolant through the calorimeter were calibrated by using a stop watch and precision scales. The mass flow rate was fixed during each experiment. Values of the specific heat of ethylene glycol/water mixtures were obtained from ASHRAE (1977), which were in terms of percent ethylene glycol by weight and temperature. Measuring the specific gravity resulted in a value of $50 \pm 5\%$ ethylene glycol by weight. The average temperature between the calorimeter inlet and outlet was used as the temperature at which the specific heat was evaluated. The specific heat did not vary appreciably since it is a weak function of temperature.

Heat pipe temperatures were measured by Type T surface-mount thermocouples, which were held in place using Kapton tape. Mounting locations for the thermocouples are shown in Fig. 1. A short unheated length next to the evaporator end cap was instrumented with two thermocouples specifically for the detection of dryout in the evaporator section. Temperature signals were conditioned and amplified on the centrifuge table. These signals were transferred off the table through the instrumentation slip ring assembly, which was completely separate from the power slip ring assembly to reduce electronic noise. Conditioning the temperature signals prior to leaving the centrifuge table eliminated difficulties associated with creating

additional junctions within the slip ring assembly. Temperature and acceleration signals were collected using a personal computer and data logging software.

The thermocouples used in the present experiment were calibrated using a NIST-traceable resistance temperature detector (RTD) and a low-deadband ($\pm 0.01^\circ\text{C}$) recirculating chiller. The uncertainty for the RTD was stated as $\pm 0.005^\circ\text{C}$. The chiller temperature was set at eleven equally-spaced values between 0.0 and 100.0°C , and readings were taken at each setting after the system had reached the steady state. This procedure was repeated on three different days to reduce systematic errors. The combined data were used to generate polynomial best-fit curves of various orders. A regression analysis was used to determine the polynomial order which minimized the absolute errors between the raw data and the curve fit.

Since the heat pipe assembly was subjected to air velocities up to 11 m/s (25 mi/hr) due to the rotation of the table, efforts were made to reduce convective heat losses from the exterior of the heat pipe. A thin-walled aluminum box was fitted around the heat pipe and fastened to the centrifuge table which allowed approximately 25 mm of ceramic wool insulation to be packed around the heat pipe. This insulation/box arrangement provided an effective barrier to convective losses from the heat pipe to the ambient.

The helically-grooved copper-ethanol heat pipe was tested in the following manner. The recirculating chiller was turned on and allowed to reach the setpoint temperature. The centrifuge table was started from the remote control room at a slow constant rotational speed to prevent damage to the power and instrumentation slip rings. In this case, the radial acceleration remained less than $|\vec{a}_r| \leq 0.01\text{-g}$. Power to the heater was applied, and the heat pipe was allowed to reach a steady-state condition, which was determined by monitoring various temperatures on the heat pipe until changes of less than 0.1°C over 2 min. were noted. The centrifuge table velocity was then increased until the radial acceleration reached the next level ($|\vec{a}_r| = 0.0, 2.0, 4.0, 6.0, 8.0, 10.0\text{-g}$). Again, steady-state values were obtained at each acceleration setting. In all cases, the centrifuge table rotated in a clockwise direction as seen from above. After all data had been recorded, the power to the heater was turned off, and the heat pipe was allowed to cool before shutting down the centrifuge table.

Uncertainty Analysis

Uncertainty estimates for the heat input, heat transported and thermal resistance are given in this section. The heat input to the electric heater was calculated using the measured amperage and voltage. In addition, a correction was made for the losses due to the heat generated by the short length of wire leading to the

heater.

$$Q_{\text{in}} = IV - I^2(R_{\text{wire}}) \quad (1)$$

The heat removed from the heat pipe by the calorimeter (transported heat) is given by

$$Q_t = \dot{m}C_p(T_{\text{out}} - T_{\text{in}}) \quad (2)$$

The thermal resistance of the heat pipe was defined as the ratio of the temperature drop across the heat pipe to the transported heat

$$R_{\text{th}} = \frac{T_{\text{eec}} - T_{\text{cec}}}{\dot{m}C_p(T_{\text{out}} - T_{\text{in}})} \quad (3)$$

Using the analysis given by Miller (1989), the maximum root-sum-square uncertainties for all of the measured and calculated values presented in this paper are given in Table 2.

Mathematical Modeling

The objective of the present analysis was to determine the effect of imposing a transverse body force field on a circular cross-section heat pipe with helical grooves with respect to the capillary limit. To determine the capillary limit, the total body force imposed on the liquid along the length of the helical grooves must be known. As shown in Fig. 2, the curved heat pipe was mounted to a centrifuge table at radius R . The angular velocity of the table resulted in an acceleration component directed toward the center of the table (\vec{a}_r). If the angular velocity of the centrifuge table changed with respect to time, a component of acceleration would be induced along a tangent to the heat pipe (\vec{a}_t). Since the liquid accelerated and moved in a curved path, centripetal and Coriolis accelerations were also present. In addition to the body force due to gravity ($\vec{F}_g = \{-m_t g\} \hat{\mathbf{e}}_{z_1}$), all of the above-mentioned acceleration components contributed to the total body force imposed on the fluid moving in the grooves.

To find the total body force on the liquid, an inertial reference frame (x_1, y_1, z_1) is placed at the center of the centrifuge table, with the z_1 direction oriented vertically [Fig. 3(a)]. A non-inertial reference (x_2, y_2, z_2) is located at any point on the centerline of the helix. The (x_3, y_3, z_3) coordinate system is in the center of the helical groove at the same s location as the (x_2, y_2, z_2) system [Fig. 3(b)]. The x_3 unit vector is directed along the tangent to the helix, z_3 is directed toward the centerline, and y_3 is orthogonal to x_3 and z_3 (Fig. 4). With respect to the liquid flow within the helical grooves, the following assumptions are made:

1. The grooves are completely filled along the length of the heat pipe with no puddling or depletion.

2. There is no communication of liquid between the grooves.
3. The liquid velocity vector is directed along the unit vector \hat{e}_{x_3} (tangent to the helical groove).
4. Condensation and evaporation are uniform along the lengths of the condenser and evaporator sections, respectively.
5. The liquid velocity may vary from one groove to another.

These assumptions result in the following liquid velocity profile along the length of a groove (Silverstein, 1992)

$$\vec{V}_\ell = \begin{cases} \left\{ \left(\frac{s}{L_c} \right) V_{\ell,\max} \right\} \hat{e}_{x_3} & 0 \leq s < L_c \\ \{V_{\ell,\max}\} \hat{e}_{x_3} & L_c \leq s < L_c + L_a \\ \left\{ \left(\frac{L_t - s}{L_e} \right) V_{\ell,\max} \right\} \hat{e}_{x_3} & L_c + L_a \leq s < L_t \end{cases} \quad (4)$$

where $V_{\ell,\max}$ is the liquid velocity in the adiabatic section. Note that $V_{\ell,\max}$ is allowed to vary from one groove to another. The velocity of the liquid \vec{V}_ℓ shown in Fig. 3(a) results in an angular velocity $\vec{\omega}_2$ of the (x_2, y_2, z_2) reference about the z_1 axis. Since the helix angle α is constant, the angular velocity and acceleration are

$$\vec{\omega}_2 = \left\{ - \frac{|\vec{V}_\ell| \sin \alpha}{R} \right\} \hat{e}_{z_1} \quad (5)$$

$$\frac{d\vec{\omega}_2}{dt} = \begin{cases} \left\{ - \frac{V_{\ell,\max}^2 \sin \alpha}{2L_c R} \right\} \hat{e}_{z_1} & 0 \leq s < L_c \\ 0 & L_c \leq s < L_c + L_a \\ \left\{ \frac{V_{\ell,\max}^2 \sin \alpha}{2L_e R} \right\} \hat{e}_{z_1} & L_c + L_a \leq s < L_t \end{cases} \quad (6)$$

In addition to $\vec{\omega}_2$, the liquid motion results in an angular velocity $\vec{\omega}_3$ around the centerline of the helix, as shown in Fig. 3(b) due to the fluid path around the circumference of the heat pipe. The angular parameter ϕ is related to the arc length s by

$$\phi = \phi_0 + \frac{2\pi s}{p} \quad (7)$$

where ϕ_0 corresponds to the starting angle of the helix at $s = 0$. With this notation, the angular velocity and acceleration of the liquid around the x_2 axis are

$$\vec{\omega}_3 = \left\{ \frac{2\pi |\vec{V}_\ell| \sin \alpha}{p} \right\} \hat{e}_{x_2} \quad (8)$$

$$\frac{d\vec{\omega}_3}{dt} = \begin{cases} \left\{ \frac{\pi V_{\ell,\max}^2 \sin \alpha}{pL_c} \right\} \hat{\mathbf{e}}_{x_2} & 0 \leq s < L_c \\ 0 & L_c \leq s < L_c + L_a \\ \left\{ -\frac{\pi V_{\ell,\max}^2 \sin \alpha}{pL_e} \right\} \hat{\mathbf{e}}_{x_2} & L_c + L_a \leq s < L_t \end{cases} \quad (9)$$

The acceleration vector at point P on the helix with respect to the inertial reference (x_1, y_1, z_1) is given by (Shames, 1980)

$$\vec{A} = \frac{d^2\vec{r}}{dt^2} = \frac{d^2\vec{\rho}}{dt^2} + \frac{d^2\vec{R}}{dt^2} + 2\vec{\omega} \times \left(\frac{d\vec{\rho}}{dt} \right) + \left(\frac{d\vec{\omega}}{dt} \right) \times \vec{\rho} + \vec{\omega} \times (\vec{\omega} \times \vec{\rho}) \quad (10)$$

The length of the position vector $\vec{\rho}$ is constant, and rotates with angular velocity $\vec{\omega}_3$. Therefore,

$$\frac{d\vec{\rho}}{dt} = \vec{\omega}_3 \times \vec{\rho} \quad (11)$$

and

$$\frac{d^2\vec{\rho}}{dt^2} = \left(\frac{d\vec{\omega}_3}{dt} \right) \times \vec{\rho} + \vec{\omega}_3 \times \left(\frac{d\vec{\rho}}{dt} \right) \quad (12)$$

The length of the position vector \vec{R} is also fixed and rotates with angular velocity $\vec{\omega} = (\vec{\omega}_1 + \vec{\omega}_2)$.

$$\frac{d\vec{R}}{dt} = (\vec{\omega}_1 + \vec{\omega}_2) \times \vec{R} \quad (13)$$

$$\frac{d^2\vec{R}}{dt^2} = \left[\frac{d}{dt}(\vec{\omega}_1 + \vec{\omega}_2) \right] \times \vec{R} + (\vec{\omega}_1 + \vec{\omega}_2) \times \left(\frac{d\vec{R}}{dt} \right) \quad (14)$$

Combining the above relations gives the acceleration vector at any point in the helical groove

$$\begin{aligned} \vec{A} = & \left(\frac{d\vec{\omega}_3}{dt} \right) \times \vec{\rho} + \vec{\omega}_3 \times (\vec{\omega}_3 \times \vec{\rho}) + \left[\frac{d}{dt}(\vec{\omega}_1 + \vec{\omega}_2) \right] \times \vec{R} + (\vec{\omega}_1 + \vec{\omega}_2) \times [(\vec{\omega}_1 + \vec{\omega}_2) \times \vec{R}] \\ & + 2(\vec{\omega}_1 + \vec{\omega}_2) \times (\vec{\omega}_3 \times \vec{\rho}) + \left[\frac{d}{dt}(\vec{\omega}_1 + \vec{\omega}_2) \right] \times \vec{\rho} + (\vec{\omega}_1 + \vec{\omega}_2) \times [(\vec{\omega}_1 + \vec{\omega}_2) \times \vec{\rho}] \end{aligned} \quad (15)$$

The position vectors \vec{R} and $\vec{\rho}$ are given by

$$\vec{R} = \{R \sin \theta\} \hat{\mathbf{e}}_{x_1} + \{R \cos \theta\} \hat{\mathbf{e}}_{y_1} \quad (16)$$

$$\vec{\rho} = \{r_h \cos \phi\} \hat{\mathbf{e}}_{y_2} + \{r_h \sin \phi\} \hat{\mathbf{e}}_{z_2} \quad (17)$$

Since $\vec{\rho}$, $\vec{\omega}_3$ and $d\vec{\omega}_3/dt$ are in terms of the (x_2, y_2, z_2) coordinate system, a transformation is needed between

this coordinate reference and the (x_1, y_1, z_1) reference

$$\begin{Bmatrix} \hat{e}_{x_2} \\ \hat{e}_{y_2} \\ \hat{e}_{z_2} \end{Bmatrix} = \begin{vmatrix} \cos \theta & -\sin \theta & 0 \\ \sin \theta & \cos \theta & 0 \\ 0 & 0 & 1 \end{vmatrix} \begin{Bmatrix} \hat{e}_{x_1} \\ \hat{e}_{y_1} \\ \hat{e}_{z_1} \end{Bmatrix} \quad (18)$$

Using this transformation, $\vec{\rho}$, $\vec{\omega}_3$ and $d\vec{\omega}_3/dt$ are

$$\vec{\rho} = \{r_h \cos \phi \sin \theta\} \hat{e}_{x_1} + \{r_h \cos \phi \cos \theta\} \hat{e}_{y_1} + \{r_h \sin \phi\} \hat{e}_{z_1} \quad (19)$$

$$\vec{\omega}_3 = \left\{ \frac{2\pi|\vec{V}_\ell|}{p} \sin \alpha \cos \theta \right\} \hat{e}_{x_1} + \left\{ -\frac{2\pi|\vec{V}_\ell|}{p} \sin \alpha \sin \theta \right\} \hat{e}_{y_1} \quad (20)$$

$$\frac{d\vec{\omega}_3}{dt} = \begin{cases} \left\{ \frac{B}{L_c} \cos \theta \right\} \hat{e}_{x_1} + \left\{ -\frac{B}{L_c} \sin \theta \right\} \hat{e}_{y_1} & 0 \leq s < L_c \\ 0 & L_c \leq s < L_c + L_a \\ \left\{ -\frac{B}{L_e} \cos \theta \right\} \hat{e}_{x_1} + \left\{ \frac{B}{L_e} \sin \theta \right\} \hat{e}_{y_1} & L_c + L_a \leq s < L_t \end{cases} \quad (21)$$

where $B = (\pi V_{\ell, \max}^2 \sin \alpha)/p$.

The components of the acceleration vector given in eqn. (15) can be found in terms of the (x_3, y_3, z_3) reference by using a coordinate transformation to relate the (x_1, y_1, z_1) and (x_3, y_3, z_3) coordinate systems

$$\begin{Bmatrix} \hat{e}_{x_3} \\ \hat{e}_{y_3} \\ \hat{e}_{z_3} \end{Bmatrix} = \begin{vmatrix} b_{11} & b_{12} & b_{13} \\ b_{21} & b_{22} & b_{23} \\ b_{31} & b_{32} & b_{33} \end{vmatrix} \begin{Bmatrix} \hat{e}_{x_1} \\ \hat{e}_{y_1} \\ \hat{e}_{z_1} \end{Bmatrix} \quad (22)$$

where b_{ij} is the transformation matrix made up of direction cosines between the coordinate systems. To determine the elements in the transformation matrix, the following geometric analysis is given. The position vector \vec{r} can be written as

$$\vec{r} = \{(R + r_h \cos \phi) \sin \theta\} \hat{e}_{x_1} + \{(R + r_h \cos \phi) \cos \theta\} \hat{e}_{y_1} + \{r_h \sin \phi\} \hat{e}_{z_1} \quad (23)$$

The sign on the last term determines whether the helix twist is clockwise (+) or counterclockwise (-). The unit vector \hat{e}_{x_3} is tangent to the helical groove, and is obtained by finding the derivative of the position

vector \vec{r} with respect to ϕ . The tangent vector is given by

$$\begin{aligned}\vec{t} = & \left\{ \left(\frac{p}{2\pi R} \right) (R + r_h \cos \phi) \cos \theta - r_h \sin \phi \sin \theta \right\} \hat{e}_{x_1} \\ & + \left\{ - \left(\frac{p}{2\pi R} \right) (R + r_h \cos \phi) \sin \theta - r_h \sin \phi \cos \theta \right\} \hat{e}_{y_1} + \{r_h \cos \phi\} \hat{e}_{z_1}\end{aligned}\quad (24)$$

The unit vector in the tangent direction is $\hat{e}_{x_3} = \vec{t}/|\vec{t}|$, where

$$|\vec{t}| = \sqrt{\left[\left(\frac{p}{2\pi R} \right) (R + r_h \cos \phi) \right]^2 + r_h^2} \quad (25)$$

\hat{e}_{z_3} is directed from a point on the helical curve to the centerline of the helix at a given s .

$$\hat{e}_{z_3} = -\frac{\vec{\rho}}{|\vec{\rho}|} = \{-\cos \phi \sin \theta\} \hat{e}_{x_1} + \{-\cos \phi \cos \theta\} \hat{e}_{y_1} + \{-\sin \phi\} \hat{e}_{z_1} \quad (26)$$

The vector directed along \hat{e}_{y_3} is orthogonal to the \hat{e}_{z_3} and \vec{t} vectors

$$\begin{aligned}\vec{h} = \hat{e}_{z_3} \times \vec{t} = & \left\{ -r_h \cos \theta - \left(\frac{p}{2\pi R} \right) (R + r_h \cos \phi) \sin \phi \sin \theta \right\} \hat{e}_{x_1} \\ & + \left\{ r_h \sin \theta - \left(\frac{p}{2\pi R} \right) (R + r_h \cos \phi) \sin \phi \cos \theta \right\} \hat{e}_{y_1} + \left\{ \left(\frac{p}{2\pi R} \right) (R + r_h \cos \phi) \cos \phi \right\} \hat{e}_{z_1}\end{aligned}\quad (27)$$

where the unit vector is $\hat{e}_{y_3} = \vec{h}/|\vec{h}| = \vec{h}/|\vec{t}|$. The elements of the transformation matrix [eqn. (22)] are

$$b_{11} = \left\{ \left(\frac{p}{2\pi R} \right) (R + r_h \cos \phi) \cos \theta - r_h \sin \phi \sin \theta \right\} / |\vec{t}| \quad (28)$$

$$b_{12} = \left\{ - \left(\frac{p}{2\pi R} \right) (R + r_h \cos \phi) \sin \theta - r_h \sin \phi \cos \theta \right\} / |\vec{t}| \quad (29)$$

$$b_{13} = (r_h \cos \phi) / |\vec{t}| \quad (30)$$

$$b_{21} = \left\{ -r_h \cos \theta - \left(\frac{p}{2\pi R} \right) (R + r_h \cos \phi) \sin \phi \sin \theta \right\} / |\vec{t}| \quad (31)$$

$$b_{22} = \left\{ r_h \sin \theta - \left(\frac{p}{2\pi R} \right) (R + r_h \cos \phi) \sin \phi \cos \theta \right\} / |\vec{t}| \quad (32)$$

$$b_{23} = \left\{ \left(\frac{p}{2\pi R} \right) (R + r_h \cos \phi) \cos \phi \right\} / |\vec{t}| \quad (33)$$

$$b_{31} = -\cos \phi \sin \theta \quad (34)$$

$$b_{32} = -\cos \phi \cos \theta \quad (35)$$

$$b_{33} = -\sin \phi \quad (36)$$

For the limiting case of axial grooves, the above mathematical model remains valid. By taking the limit as $p \rightarrow \infty$, eqn. (7) becomes

$$\phi = \phi_0 \quad (37)$$

Also, the transformation matrix given by eqn. (22) becomes

$$b_{ij} = \begin{vmatrix} \cos \theta & -\sin \theta & 0 \\ -\sin \phi_0 \sin \theta & -\sin \phi_0 \cos \theta & \cos \phi_0 \\ -\cos \phi_0 \sin \theta & -\cos \phi_0 \cos \theta & -\sin \phi_0 \end{vmatrix} \quad (38)$$

A pressure balance within the heat pipe results in the following expression for the capillary limit (Faghri, 1994; Chi, 1976)

$$\Delta P_{\text{cap,max}} \geq \Delta P_v + \Delta P_\ell + \Delta P_{\text{bf}} \quad (39)$$

The maximum capillary pressure is

$$\Delta P_{\text{cap,max}} = \frac{2\sigma}{r_c} \quad (40)$$

where the capillary radius is equal to the helical groove width $r_c = w$. For a circular cross section heat pipe with uniform heat input and output along the lengths of the evaporator and condenser, respectively, the pressure drop in the vapor is

$$\Delta P_v = \frac{4\mu_v Q_t}{\pi \rho_v h_{fg} r_v^4} (L_e + 2L_a + L_c) \quad (41)$$

The body forces imposed on the fluid within a particular groove may either aid or hinder the return of the fluid to the evaporator, depending on the groove pitch p and the angle of the starting point of the helix ϕ_0 . However, even if the body force hinders the return of the fluid, each groove contributes to the heat transported Q_t . Therefore, the capillary limit equation [eqn. (39)] is first solved for the heat transported by each individual groove Q_g , and the results are summed to determine the total heat transport Q_t . Since the pressure drop in the vapor space is based on the total heat transport, eqn. (39) must be solved iteratively.

The body forces in the tangent direction due to acceleration [eqn. (15)] and gravity are integrated over the length of the groove to find the average pressure drop due to body forces

$$\begin{aligned} \Delta P_{\text{bf}} &= -\rho_\ell \left(\int_0^{L_g} \hat{\mathbf{e}}_{x_3} \cdot (-\vec{A} + \{-g\} \hat{\mathbf{e}}_{z_1}) \, dx_3 \right) \\ &= -\rho_\ell \sqrt{\left(\frac{2\pi r_h}{p}\right)^2 + 1} \left[\int_0^{L_t} \hat{\mathbf{e}}_{x_3} \cdot (-\vec{A} + \{-g\} \hat{\mathbf{e}}_{z_1}) \, ds \right] \end{aligned} \quad (42)$$

where the length of a helical groove is given in terms of the s coordinate

$$L_g = s \sqrt{\left(\frac{2\pi r_h}{p}\right)^2 + 1} \quad (43)$$

The pressure drop in the liquid is given by (Faghri, 1994)

$$\Delta P_\ell = \int_0^{L_g} \frac{\mu_\ell \dot{m}_\ell}{\rho_\ell A_w K} dx_3 = \frac{\mu_\ell Q_g (f_\ell \text{Re}_\ell) (L_e + 2L_a + L_c)}{4\rho_\ell r_\ell^2 w h h_{fg}} \sqrt{\left(\frac{2\pi r_h}{p}\right)^2 + 1} \quad (44)$$

The coefficient of drag within a rectangular groove is given by Shah and Bhatti (1987)

$$f_\ell \text{Re}_\ell = 24(1 - 1.3553\beta + 1.9467\beta^2 - 1.7012\beta^3 + 0.9564\beta^4 - 0.2537\beta^5) \quad (45)$$

where the range of the aspect ratio is $0 \leq \beta \leq 1$.

Combining the above relations, the general expression for the maximum capillary limit for a single groove is

$$\frac{2\sigma}{w} \geq \frac{(L_e + 2L_a + L_c)}{h_{fg}} \left\{ \frac{4\mu_v Q_t}{\pi \rho_v r_v^4} + \frac{\mu_\ell Q_g (f_\ell \text{Re}_\ell)}{4\rho_\ell r_\ell^2 w h} \sqrt{\left(\frac{2\pi r_h}{p}\right)^2 + 1} \right\} - \rho_\ell \sqrt{\left(\frac{2\pi r_h}{p}\right)^2 + 1} \left[\int_0^{L_t} \hat{e}_{x_3} \cdot (-\vec{A} + \{-g\} \hat{e}_{z_1}) ds \right] \quad (46)$$

This equation was solved for each individual groove. However, the total heat transported Q_t was not known *a priori*, so an iterative solution procedure was necessary:

1. Input an initial value for the heat transported $Q_t = Q_{t,i}$.
2. Starting with the groove at $\phi_0 = 0$, let the heat transported by that groove be $Q_g = \Delta Q_g$, where ΔQ_g is the step size.
3. Calculate the right- and left-hand sides of eqn. (46).
4. If the inequality holds, increment Q_g by ΔQ_g until the inequality no longer holds.
5. Repeat steps 2 through 4 for each groove.
6. The heat transported by the heat pipe is the sum of the heat transported by each groove:

$$Q_t = \sum_{j=1}^{N_g} (Q_g)_j$$

7. Use the value of Q_t found in step 6 as the input value in step 1.
8. Steps 1 through 7 are repeated until converged values for Q_g and Q_t are obtained.

The temperature dependence of the thermo-fluid properties was accounted for using the polynomial curve fits (evaluated at the adiabatic temperature) given by Faghri (1994).

As previously mentioned, an assumption imposed on this analysis is that there is no communication of liquid between the grooves. However, it is possible under some conditions that this assumption may no longer hold. If at any point along the helical groove the body force on the liquid due to the acceleration components \vec{A}_{y_3} and \vec{A}_{z_3} becomes significant with respect to the surface tension force, it is possible that fluid could be torn from the groove. To quantify the assumption of no communication of liquid between the grooves, the Bond number is used, which is defined as

$$Bo = \frac{\rho_\ell r_\ell |\vec{A}_{\text{res}}|}{2\sigma/w} = \frac{\text{Body Force}}{\text{Surface Tension Force}} \quad (47)$$

where \vec{A}_{res} is the resultant acceleration vector between the y_3 and z_3 directions. If $Bo < 1$, it is assumed that the communication of liquid between grooves is negligible.

Results and Discussion

Experimental

The objective of this experiment was to gain a better understanding of the steady-state operating characteristics of a helically-grooved copper-ethanol heat pipe in a transverse body force field. The heat input and radial acceleration were varied to find information on dryout phenomena, circumferential temperature uniformity, heat lost to the environment, thermal resistance and the capillary limit.

Raw temperature and acceleration data versus time for a typical test run are presented in Fig. 5 for two different heat input settings. In Fig. 5(a), with a heat input of $Q_{\text{in}} = 20$ W, no dryout of the evaporator section was detected. As the radial acceleration was increased stepwise, the temperatures across the heat pipe did not vary significantly. In Fig. 5(b), however, with a heat input of $Q_{\text{in}} = 50$ W, partial dryout of the evaporator section was noted when $|\vec{a}_r| = 0.0\text{-g}$. This can be seen in the dramatic increase of the evaporator end cap temperature above the adiabatic section temperature. Once the radial acceleration was increased to $|\vec{a}_r| = 2.0\text{-g}$, the evaporator temperature decreased significantly, showing that the acceleration actually aided in the return of the working fluid back to the evaporator section. Dryout was also seen when the radial acceleration was decreased from $|\vec{a}_r| = 2.0$ to 0.0-g at the end of the test in Fig. 5(b). In this case,

regular fluctuations in the evaporator end cap temperature were seen. This indicated a pulsating rewetting phenomenon, where the liquid front advanced and receded within the evaporator section.

The circumferential temperature uniformity of the heat pipe was found using a series of thermocouples on the inboard and outboard sides, as shown in Fig. 1. The steady-state temperatures detected along the length of the heat pipe are shown in Fig. 6 for a radial acceleration of $|\vec{a}_r| = 10.0\text{-g}$ and heat transport values of $Q_t = 35, 71$ and 107 W . The temperatures in the evaporator section increased with heat transported. This phenomenon is commonly seen, and is due to the influence of the heater on the thermocouple readings. However, the inboard and outboard evaporator end cap temperatures were very close to those in the adiabatic section, indicating no partial dryout of the evaporator. Even at this acceleration, the temperature uniformity between the inboard and outboard sides of the heat pipe was excellent.

The heat transported is compared to the heat input for all of the data collected in Fig. 7. While a slight decrease in the heat transported was noted for increasing radial acceleration rates (increasing table angular velocity), the decrease was seen to be only marginally significant compared to the maximum percent uncertainty of the heat transported (Table 2). Therefore, the amount of heat lost due to external convection was quite small in comparison to that lost due to conduction through the insulation and mounting blocks.

Figure 8 shows the thermal resistance as a function of transported heat over the entire range of radial acceleration. In general, the thermal resistance decreased and then increased with transported heat when dryout commenced. When $|\vec{a}_r| = 0.0$ and 2.0-g , dryout resulted in a gradual increase in the thermal resistance, as shown in Fig. 8. In this case, the capillary limit was considered to be reached when the thermal resistance began to increase. For $|\vec{a}_r| \geq 4.0\text{-g}$, dryout occurred suddenly, as shown in Fig. 9. In this figure, the heat input was changed from $Q_{in} = 129$ to 142 W , where the evaporator end cap and heater temperatures increased by 40°C in less than 2 minutes. After dryout was confirmed, the heat input was returned to $Q_{in} = 129 \text{ W}$, at which time the heat pipe quickly reprimed and began to operate normally again. This runaway dryout behavior indicates an unstable operating condition near the capillary limit when under the influence of elevated transverse body force fields. While the capillary limit was reached for $|\vec{a}_r| = 0.0, 2.0, 4.0$ and 6.0-g , the capillary limit at 8.0 and 10.0-g could not be determined due to reaching the maximum allowable amperage through the heater ($Q_{in,max} = 250 \text{ W}$, $Q_{t,max} = 175 \text{ W}$). In the experimental study by Yerkes and Beam (1992), where the performance of a flexible copper-water heat pipe was examined, it was found that dryout occurred when the artery used for liquid return deprimed under radial acceleration fields greater than $|\vec{a}_r| > 8\text{-g}$. This shows that helically-grooved heat pipes have definite advantages over arterial heat

pipes under elevated transverse body force fields. The experimentally-determined capillary limit values for $|\vec{a}_r| = 0.0, 2.0, 4.0$, and 6.0-g are presented in the next section.

Numerical

A mathematical model which predicts the capillary limit of a helically-grooved heat pipe subjected to a transverse body force field has been developed. The effects of temperature-dependent working fluid properties, the geometry of the heat pipe and the grooves (including helix pitch), and body force field strength were accounted for. To validate the present solution, the closed-form solution presented by Klasing et al. (1997) was used, wherein the capillary limit of a heat pipe under gravity with straight axial grooves as the wick structure was calculated. The geometric values given in Table 1 were used in both models to calculate the capillary limit for adiabatic temperatures between 40 and 80°C . The solution of the capillary limit for a helically-grooved heat pipe was iterative in nature, so a convergence check on ΔQ_g was required. The maximum percentage error for $\Delta Q_g = 0.1, 0.01$, and 0.001 W was 7.65, 0.58, and 0.14, respectively, as compared to the closed-form solution. Therefore, in an effort to maintain a reasonable calculation time, ΔQ_g was chosen to be 0.01 W.

Figure 10 shows the capillary limit of each helical groove versus the starting angle of the groove. When $|\vec{a}_r| = 0.0\text{-g}$, the heat transported by the grooves has a peak in the upper right-hand quadrant, and a minimum in the lower left-hand quadrant. This was due to the presence of the body force due to gravity, which aided the liquid return in the grooves in the upper right-hand quadrant. As the resultant body force vector (gravity + acceleration due to rotation) increased in magnitude and changed in direction, the maximum heat transported by the grooves increased and shifted from the upper right-hand quadrant to the lower right-hand quadrant, as shown in Fig. 10(a). In addition, the increase in the resultant body force vector progressively deactivated the grooves where the body force acted in a direction unfavorable to the return of liquid back to the evaporator section. Faghri and Thomas (1989) showed that axial grooves are very sensitive to body force effects: A change in tilt angle from horizontal to -1° (unfavorable) resulted in a decrease in the capillary limit of a copper-water heat pipe from $Q_{\text{in}} = 700$ to less than 50 W in their study. In the present case, the benefits derived from the increase in the fluid flow rate through part of the grooves outweighed the loss of heat transport through those grooves which were hindered. For $|\vec{a}_r| \geq 4.0\text{-g}$, the location of the grooves where the maximum heat transport occurred did not vary appreciably, since the body force due to the radial acceleration was significantly greater than that due to gravity [Fig. 10(b)].

Figure 11 shows the acceleration components due to rotation and gravity in the (x_3, y_3, z_3) coordinate

system. The relative magnitudes of the acceleration in the x_3 , y_3 , and z_3 directions illustrate how the helical grooves contribute to the return of the fluid to the evaporator. Due to the curvature of the helical grooves, an acceleration component was induced in the x_3 direction. However, the magnitude of this acceleration component was relatively small due to the shallowness of the helix angle. The acceleration components in the y_3 and z_3 directions were significantly larger because their magnitude and direction were similar to that of \vec{a}_r . The acceleration for $\phi_0 = 0.0^\circ$ in Fig. 11(a) was less than zero along the entire length of the groove and $Q_{g,\text{cap}} < 0.01 \text{ W}$ (see Fig. 10). However, for the groove located at $\phi_0 = 180.0^\circ$ the acceleration in the x_3 direction was greater than zero along the groove length, which resulted in $Q_{g,\text{cap}} = 8.41 \text{ W}$. When compared to Fig. 10(b), it can be seen that the positive acceleration components in the x_3 direction enhanced the capillary limit by increasing the rate of fluid return to the evaporator. In contrast, the negative acceleration components in the x_3 direction greatly hindered the return of working fluid to the evaporator.

The capillary limit versus radial acceleration is given in Fig. 12 for various adiabatic temperatures. Figure 12(a) shows the results of the present model, where the capillary limit of the heat pipe increased monotonically with adiabatic temperature and radial acceleration. Figure 12(b) shows a comparison of the experimentally and analytically obtained capillary limits. Since no attempt was made in the experiments to maintain a constant adiabatic temperature, the model was evaluated at the same adiabatic temperatures as those seen in the experiments. Both curves in Fig. 12(b) have similar trends, but the mathematical model overpredicted the experimental capillary limit data by 27 to 50%. This overprediction is typical of the capillary limit analysis used in the present model (Richter and Gottschlich, 1994). However, since the trends between the analytical model and the experimental results are comparable, the present model can be very useful as a design tool to analyze various configurations. It should be noted that a five-fold increase in the capillary limit was achieved in the experiment by increasing the radial acceleration from $|\vec{a}_r| = 0$ to 6.0-g.

In regard to the assumption of no liquid communication between the grooves, the aforementioned Bond number analysis resulted in $Bo_{\max} = 0.32$ over the range of parameters reported. Therefore, the assumption concerning no communication of liquid between the grooves appears to be valid.

Conclusions

The steady-state performance of a helically-grooved copper-ethanol heat pipe has been examined experimentally as a function of heat input and transverse body force field strength. A mathematical model of the heat pipe system has been developed which accounts for the effects of increased transverse body forces,

the geometry of the heat pipe and the grooves (including helix pitch), and temperature-dependent working fluid properties. The following conclusions have been made concerning the results of the experimental and numerical analyses:

1. An increase in the transverse body force imposed on the heat pipe actually aided in the return of the working fluid back to the evaporator section. This resulted in a five-fold increase in the capillary limit when the radial acceleration was increased from $|\vec{a}_r| = 0$ to 6-g.
2. Even at the highest radial acceleration ($|\vec{a}_r| = 10\text{-g}$), the temperature uniformity between the inboard and outboard sides of the heat pipe was excellent.
3. In general, the thermal resistance decreased and then increased with transported heat when dryout commenced.
4. When $|\vec{a}_r| = 0.0$ and 2.0-g, dryout resulted in a gradual increase in the thermal resistance. For $|\vec{a}_r| \geq 4.0\text{-g}$, dryout occurred suddenly, which indicates an unstable operating condition near the capillary limit when under the influence of elevated transverse body forces.
5. As the resultant body force vector increased in magnitude and changed in direction, the maximum heat transported by the grooves increased and shifted from the upper right-hand quadrant to the lower right-hand quadrant of the heat pipe circumference. In addition, the increase in the resultant body force vector progressively deactivated the grooves where the body force acted in a direction unfavorable to the return of liquid back to the evaporator section.
6. The mathematical model overpredicted the experimental capillary limit data by up to 50%, but since the trends between the analytical model and the experimental results were comparable, the present model can be very useful as a design tool to analyze various groove structure configurations.

Acknowledgements

Funding for this work was provided by AFOSR Contract F49620-93-C-0063. The technical assistance of Dr. Kirk Yerkes, Mr. Keving Klasing, and Mr. Don Reinmuller are noted and appreciated.

Nomenclature

\vec{a}	acceleration vector, m/s ²
a	adiabatic length near evaporator end cap, m

\vec{A}	acceleration vector at any point in the helical groove, m/s ²
A_w	cross-sectional area of the wick, $\pi h (2r_v + h)$, m ²
b	adiabatic length near condenser end cap, m
b_{ij}	transformation matrix
Bo	Bond number, $\rho_\ell r_\ell w \vec{A}_{\text{res}} / 2\sigma$
C_p	specific heat at constant pressure, J/(kg·K)
\hat{e}	unit vector
D_o	tube outside diameter, m
D_v	vapor core diameter, m
f	acceleration frequency, Hz
$f_\ell \text{Re}_\ell$	drag coefficient
\vec{F}_g	body force due to gravity, N
g	gravity constant, 9.81 m/s ²
\vec{h}	vector aligned with \hat{e}_{y_3}
h	groove height, m
h_{fg}	heat of vaporization, J/kg
I	heater current, A
K	permeability, $2\epsilon r_\ell^2 / (f_\ell \text{Re}_\ell)$, m ²
L_a	adiabatic length, m
L_c	condenser length, m
L_e	evaporator length, m
L_g	groove length, m
L_t	total heat pipe length, m
m	mass, kg
\dot{m}	mass flow rate, kg/s
N_g	number of grooves
p	helix pitch, m
P	pressure, N/m ²
Q	heat transfer rate, W
Q_{cap}	capillary limit heat transfer rate, W

Q_{in}	heat input at the evaporator, W
Q_t	heat transported, W
\vec{r}	position vector to the helix from the (x_1, y_1, z_1) reference, m
r_c	capillary radius, m
r_h	radius of the helix, $r_v + h/2$, m
r_ℓ	liquid hydraulic radius, $2wh/(2h + w)$, m
r_v	radius of the heat pipe vapor space, m
\tilde{R}	position vector to the centerline of the helix from the (x_1, y_1, z_1) reference, m
R	radius of curvature of the centerline of the helix, m
R_{th}	thermal resistance, K/W
R_{wire}	electrical resistance of heater lead wires, Ω
s	coordinate along the centerline of the helix, m
\vec{t}	vector tangent to the helix
t	time, s
t_w	tube wall thickness, m
T_{cec}	condenser end cap temperature, K
T_{cw}	cooling water temperature, K
T_{eec}	evaporator end cap temperature, K
T_{in}	calorimeter inlet temperature, K
T_{out}	calorimeter outlet temperature, K
V	heater voltage, V
\vec{V}_ℓ	liquid velocity vector, m/s
$V_{\ell,max}$	liquid velocity in the adiabatic section, $Q_g/\rho_\ell whh_{fg}$, m/s
w	groove width, m
x_1, y_1, z_1	inertial coordinates at the center of the centrifuge table
x_2, y_2, z_2	non-inertial coordinates at the centerline of the helix
x_3, y_3, z_3	non-inertial coordinates in the helical groove
α	helix angle, $\tan^{-1}(p/2\pi r_h)$, rad
β	aspect ratio, w/h
Δ	uncertainty

ΔP	change in pressure, N/m ²
ϵ	porosity, whN_g/A_w
θ	s/R , rad
μ	absolute viscosity, kg/(m-s)
\vec{r}	position vector to the helix from the (x_2, y_2, z_2) reference, m
ρ	density, kg/m ³
σ	surface tension, N/m
ϕ	angular parameter, rad
ϕ_0	angle of the starting point of the helix, rad
$\vec{\omega}$	angular velocity vector, rad/s

Subscripts

a	adiabatic
bf	body force
c	condenser
cap	capillary
e	evaporator
g	gravity or groove
l	liquid
max	maximum
r	radial
res	resultant
t	tangential or transported
v	vapor

References

- ASHRAE Handbook of Fundamentals*, 1977, American Society of Heating, Refrigerating and Air-Conditioning Engineers, Inc., Atlanta, GA.
- Chi, S., 1976, *Heat Pipe Theory and Practice: A Sourcebook*, Hemisphere Publ. Corp., New York.

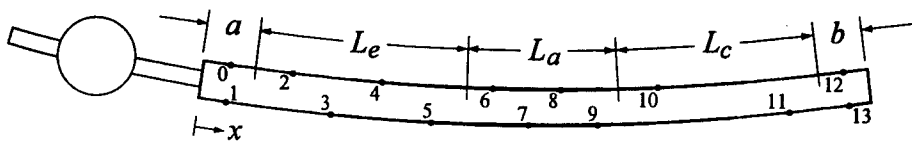
- Faghri, A., 1994, *Heat Pipe Science and Technology*, Taylor and Francis, Washington, DC.
- Faghri, A., and Thomas, S., 1989, "Performance Characteristics of a Concentric Annular Heat Pipe: Part I—Experimental Prediction and Analysis of the Capillary Limit," *ASME J. Heat Transfer*, Vol. 111, pp. 844-850.
- Gernert, N., et al., 1991, "Flexible Heat Pipe Cold Plates for Aircraft Thermal Control," *Proc. Aerospace Technology Conference and Exposition*, SAE Paper No. 912105.
- Klasing, K.S., Thomas, S.K., and Yerkes, K.L., 1997, "CAPLIM: A Visual Basic Program to Calculate the Capillary Limit of an Axially-Grooved Heat Pipe," *Proc. Intersociety Energy Conversion Engineering Conf.*, Vol. 2, pp. 1514-1518, Honolulu, HI.
- Miller, R., 1989, *Flow Measurement Engineering Handbook*, 2nd Ed., McGraw-Hill.
- Richter, R. and Gottschlich, F.M., 1994, "Thermodynamic Aspects of Heat Pipe Operation," *AIAA J. Thermophysics Heat Transfer*, Vol. 8, No. 2, pp. 334-340.
- Shah, R.K., and Bhatti, M.S., 1987, "Laminar Convective Heat Transfer in Ducts," in *Handbook of Single-Phase Convective Heat Transfer*, Eds., Kakac, S., Shah, R.K., and Aung, W., Wiley, New York.
- Shames, I., 1980, *Engineering Mechanics*, 3rd Edn., Prentice-Hall, New Jersey.
- Silverstein, C., 1992, *Design and Technology of Heat Pipes for Cooling and Heat Exchange*, Taylor & Francis, Washington, DC.
- Thomas, S., and Yerkes, K., 1997, "Quasi-Steady State Performance of a Heat Pipe Subjected to Transient Acceleration Loadings," *AIAA J. Thermophysics Heat Transfer*, Vol. 11, pp. 306-309.
- Yerkes, K., and Beam, J., 1992, "Arterial Heat Pipe Performance in a Transient Heat Flux and Body Force Environment," *Proc. Aerospace Atlantic Conf.*, Dayton, OH, SAE Paper No. 921944.
- Yerkes, K.L., and Hager, B., 1992, "Transient Response of Heat Pipes for Actuator Thermal Management," *Proc. Aerospace Atlantic Conf.*, Dayton, OH, SAE Paper No. 921024.
- Yerkes, K., and Hallinan, K., 1995a, "Dynamic Behavior of an Unheated Meniscus Subjected to Transient Acceleration Field," *AIAA J. Thermophysics Heat Transfer*, Vol. 9, No. 2, pp. 322-328.
- Yerkes, K., and Hallinan, K., 1995b, "Behavior of a Meniscus Subjected to Transient Accelerations for Increasing Capillary Numbers," *AIAA J. Thermophysics Heat Transfer*, Vol. 9, No. 3, pp. 543-549.

Table 1: Helically-grooved heat pipe specifications.

Working fluid	Ethanol
Working fluid charge	6.5 cm^3
Heat pipe length	$L_t = 457 \text{ mm}$
Evaporator length	$L_e = 152 \text{ mm}$
Adiabatic length	$L_a = 101 \text{ mm}$
Condenser length	$L_c = 152 \text{ mm}$
Tube outside dia.	$D_o = 15.88 \text{ mm}$
Tube wall thickness	$t_w = 0.766 \text{ mm}$
Vapor core diameter	$D_v = 13.46 \text{ mm}$
Radius of curvature	$R = 1.22 \text{ m}$
Wall/wick materials	Copper
Wick structure	Helical grooves
Helix pitch	$p = 139 \text{ cm clockwise}$
Groove height	$h = 0.442 \text{ mm}$
Groove width	$w = 0.474 \text{ mm}$
Number of Grooves	$N_g = 50$
Heater element	Nichrome heater tape
Fill valve	Nupro B-4HW bellows valve
Calorimeter	1/8 in. OD copper tubing

Table 2: Maximum uncertainties of measured and calculated values.

Measured Values	
Mass flow rate	$\Delta \dot{m} = \pm 1.4 \times 10^{-4} \text{ kg/s}$
Calorimeter inlet temp.	$\Delta T_{in} = \pm 0.14 \text{ K}$
Calorimeter outlet temp.	$\Delta T_{out} = \pm 0.14 \text{ K}$
Evaporator end cap temp.	$\Delta T_{eec} = \pm 0.17 \text{ K}$
Condenser end cap temp.	$\Delta T_{cec} = \pm 0.16 \text{ K}$
Heater voltage	$\Delta V = \pm 2\% \text{ of reading}$
Heater current	$\Delta I = \pm 2\% \text{ of reading}$
Radial acceleration	$\Delta a_r = \pm 0.1\text{-g}$
Electrical wire resistance	$\Delta R_{wire} = \pm 2.4 \times 10^{-3} \Omega$
Calculated Values	
Heat input	$\Delta Q_{in} = \pm 4\%$
Heat transported	$\Delta Q_t = \pm 14\%$
Thermal resistance	$\Delta R_{th} = \pm 14\%$
Capillary limit	$\Delta Q_{cap} = \pm 11\%$



$a = 25.4 \text{ mm}$
 $L_e = 152 \text{ mm}$
 $L_a = 101 \text{ mm}$
 $L_c = 152 \text{ mm}$
 $b = 25.4 \text{ mm}$
 $L_t = 457 \text{ mm}$

TC#	x (mm)	TC#	x (mm)
0,1	12.7	8	238.
2	55.8	9	259.
3	86.4	10	330.
4	116.	11	381.
5	147.	12,13	444.
6	198.	14	Coolant Outlet
7	218.	15	Coolant Inlet

Figure 1: Thermocouple locations and relevant lengths.

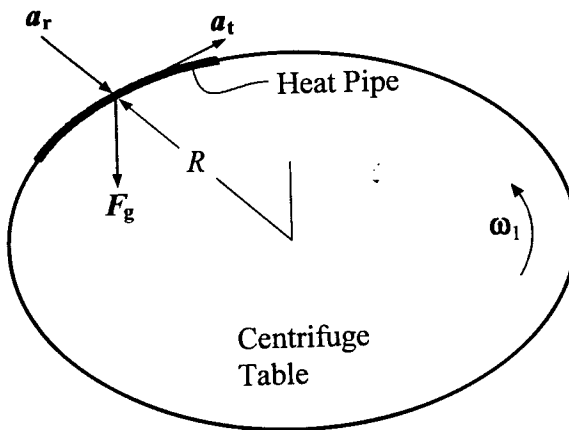


Figure 2: Heat pipe mounted to the centrifuge table.

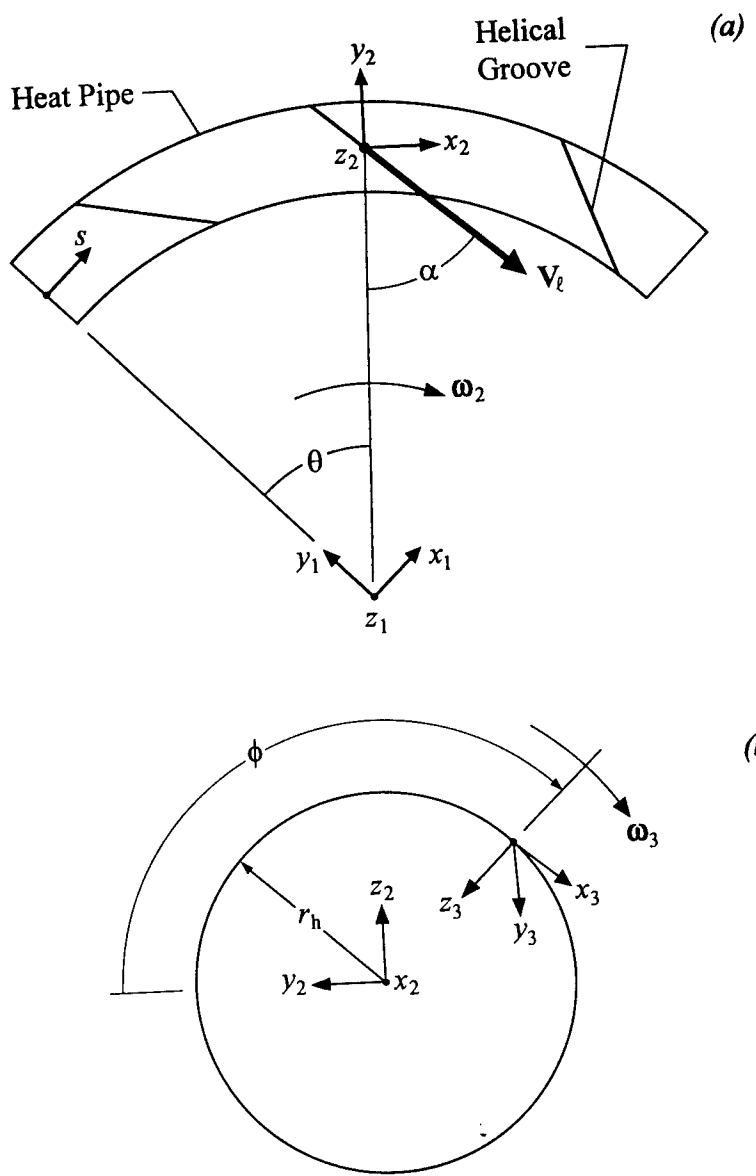


Figure 3: Geometric considerations between the three coordinate systems: (a) Top view of heat pipe mounted to the centrifuge table; (b) Cross-sectional view of the heat pipe at a particular s location.

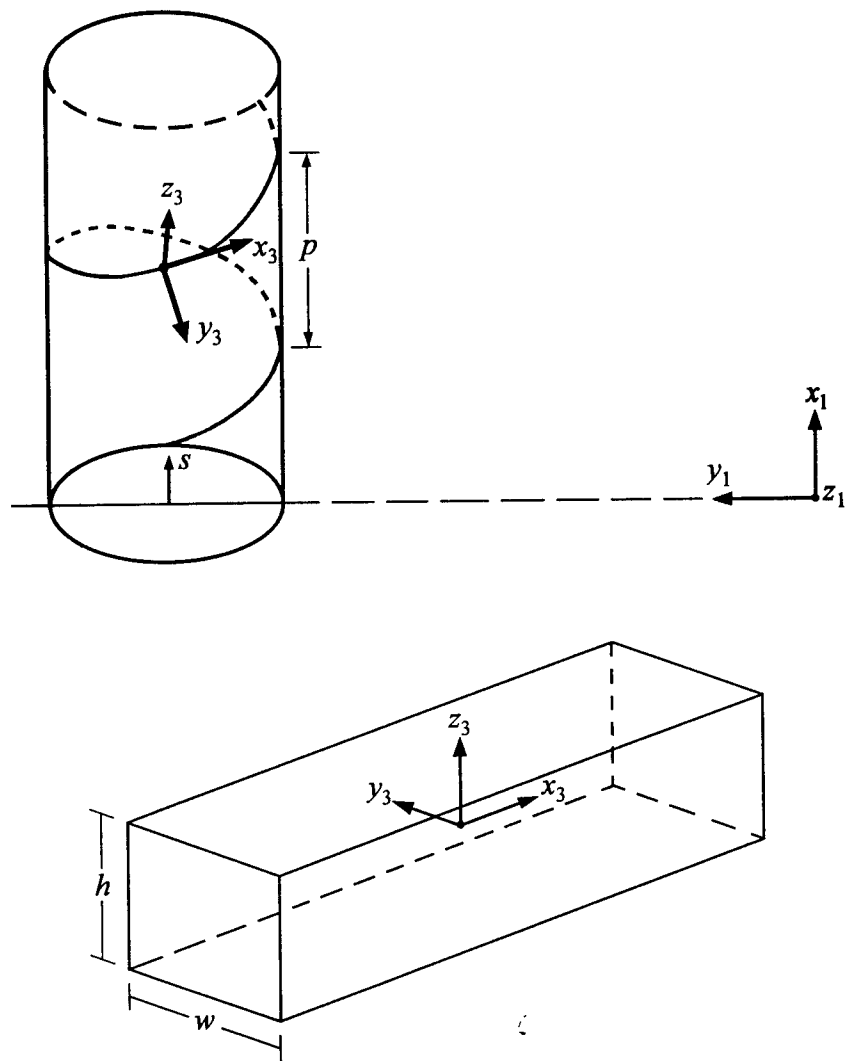


Figure 4: Coordinate system situated in the helical groove.

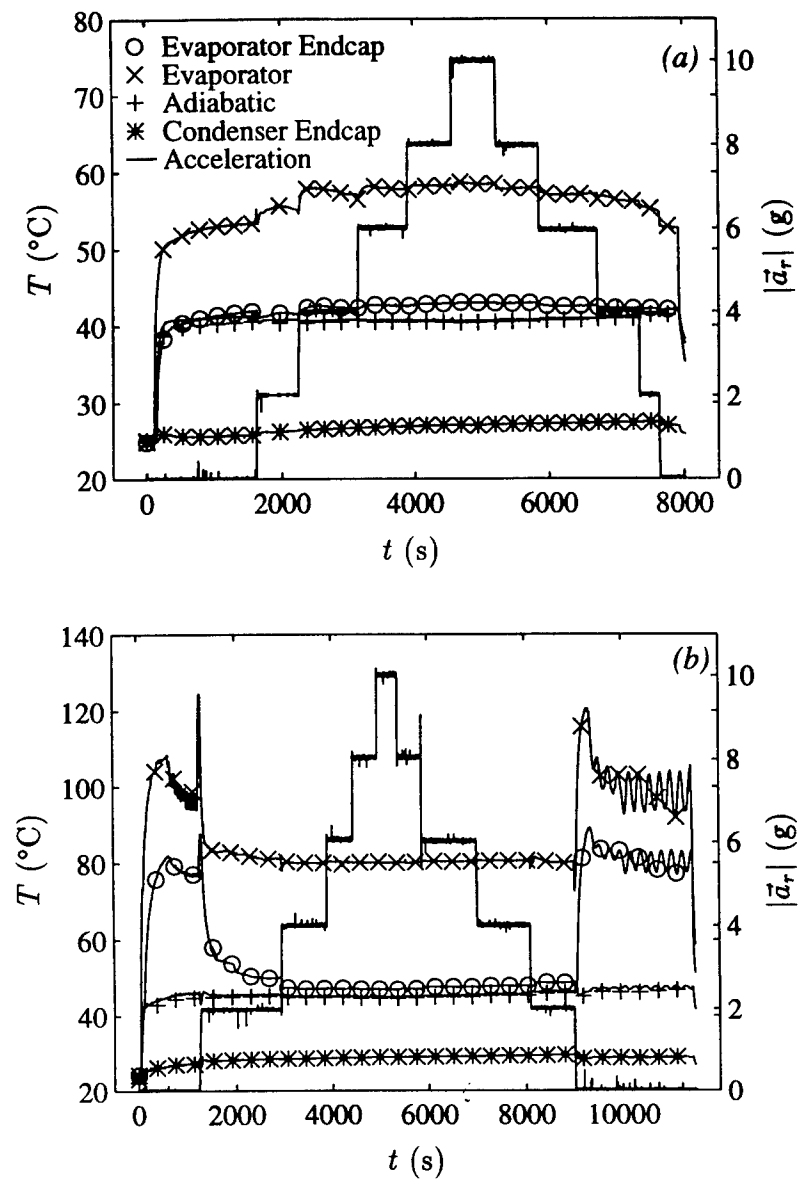


Figure 5: Temperature and acceleration versus time for a typical test run: (a) $Q_{in} = 20 \text{ W}$; (b) $Q_{in} = 50 \text{ W}$.

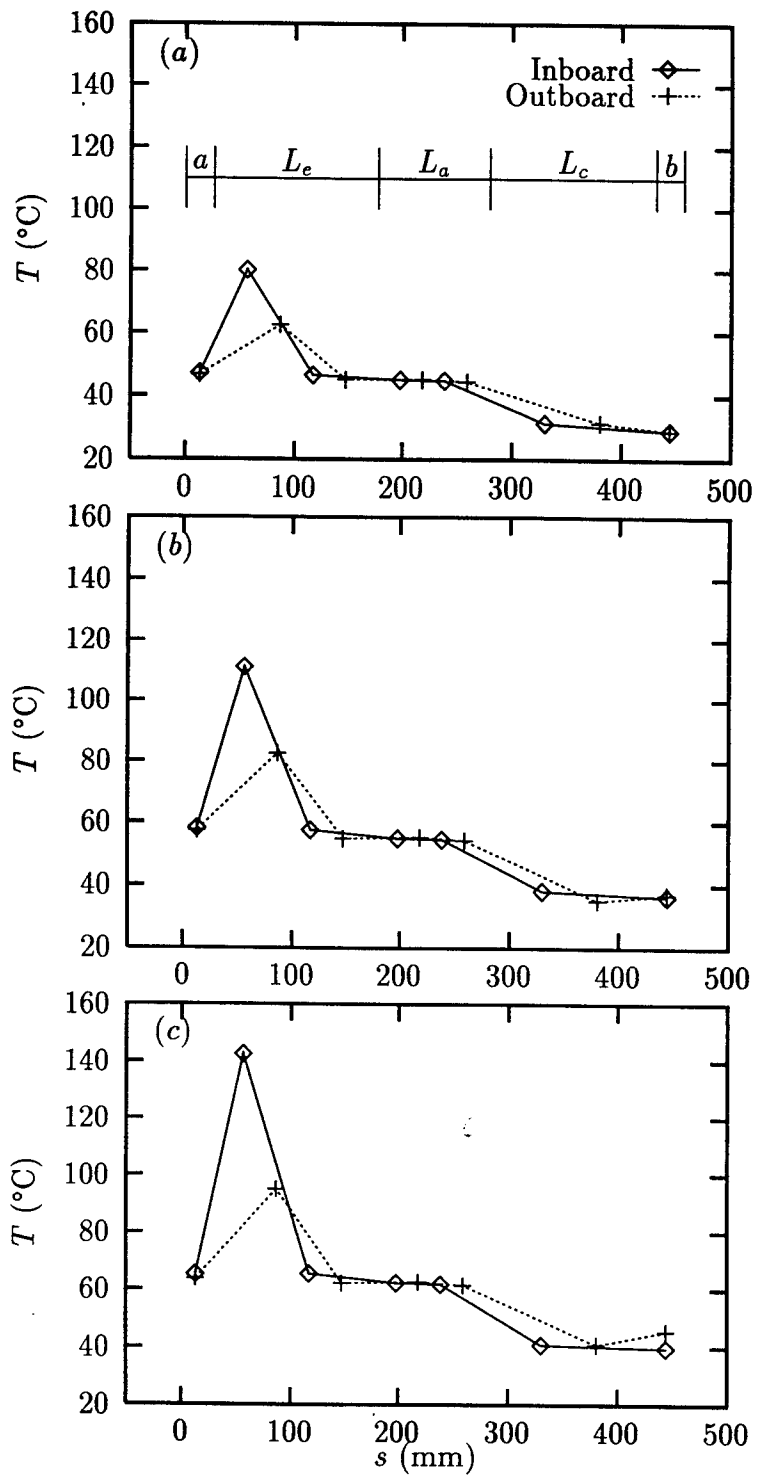


Figure 6: Steady state temperature distribution for $|\vec{a}_r|=10.0\text{-}g$: (a) $Q_t = 35 \text{ W}$; (b) $Q_t = 71 \text{ W}$; (c) $Q_t = 107 \text{ W}$

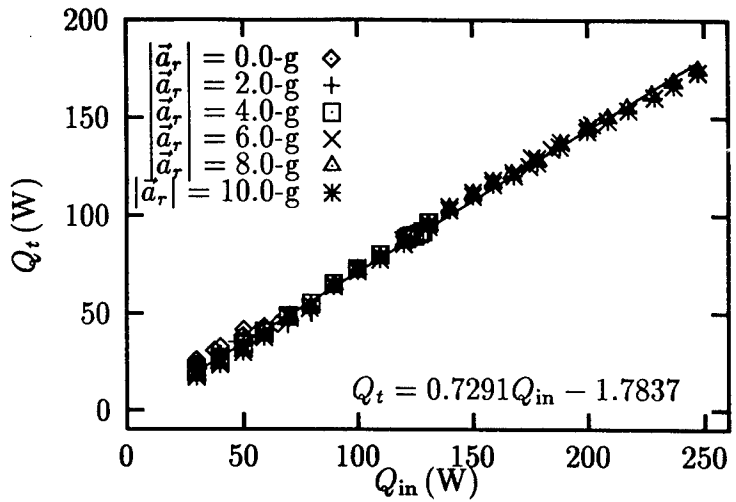


Figure 7: Heat transported versus heat input.

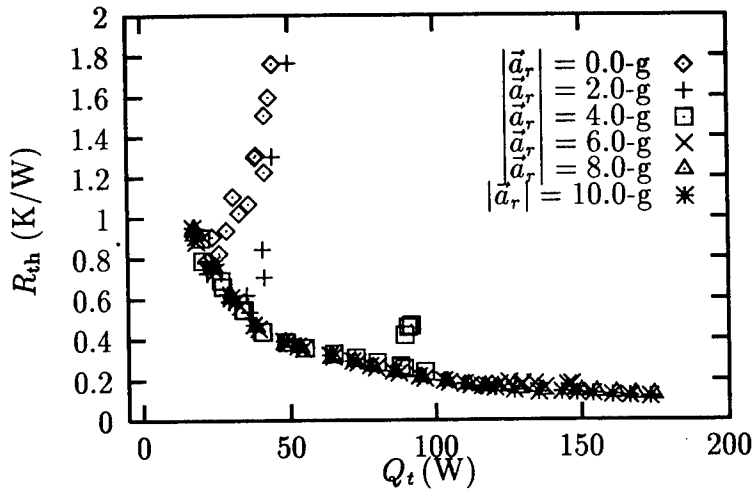


Figure 8: Thermal resistance versus heat transported.

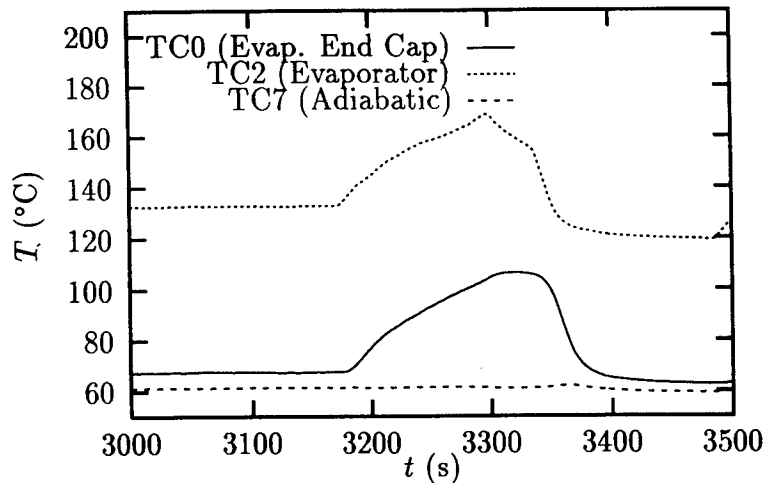


Figure 9: Temperature versus time during an incident of dryout for $|\vec{d}_r| = 4.0\text{-g}$.

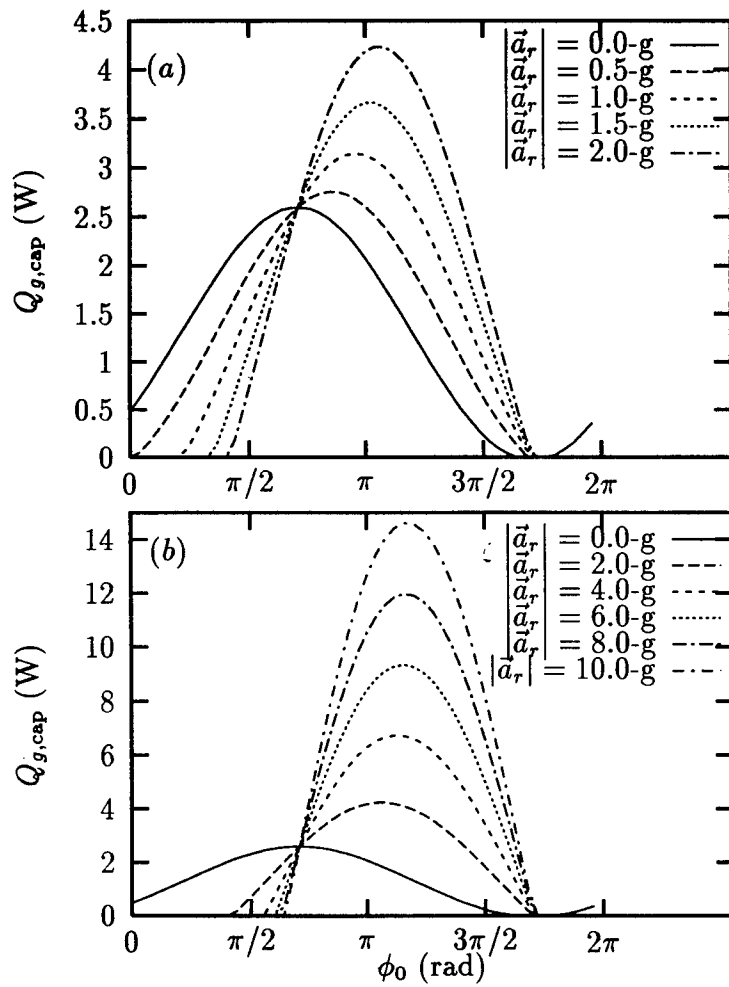


Figure 10: Capillary limit per groove versus groove starting angle ($T_a = 60^\circ\text{C}$): (a) $0 \leq |\vec{a}_r| \leq 2.0\text{-g}$; (b) $0 \leq |\vec{a}_r| \leq 10.0\text{-g}$.

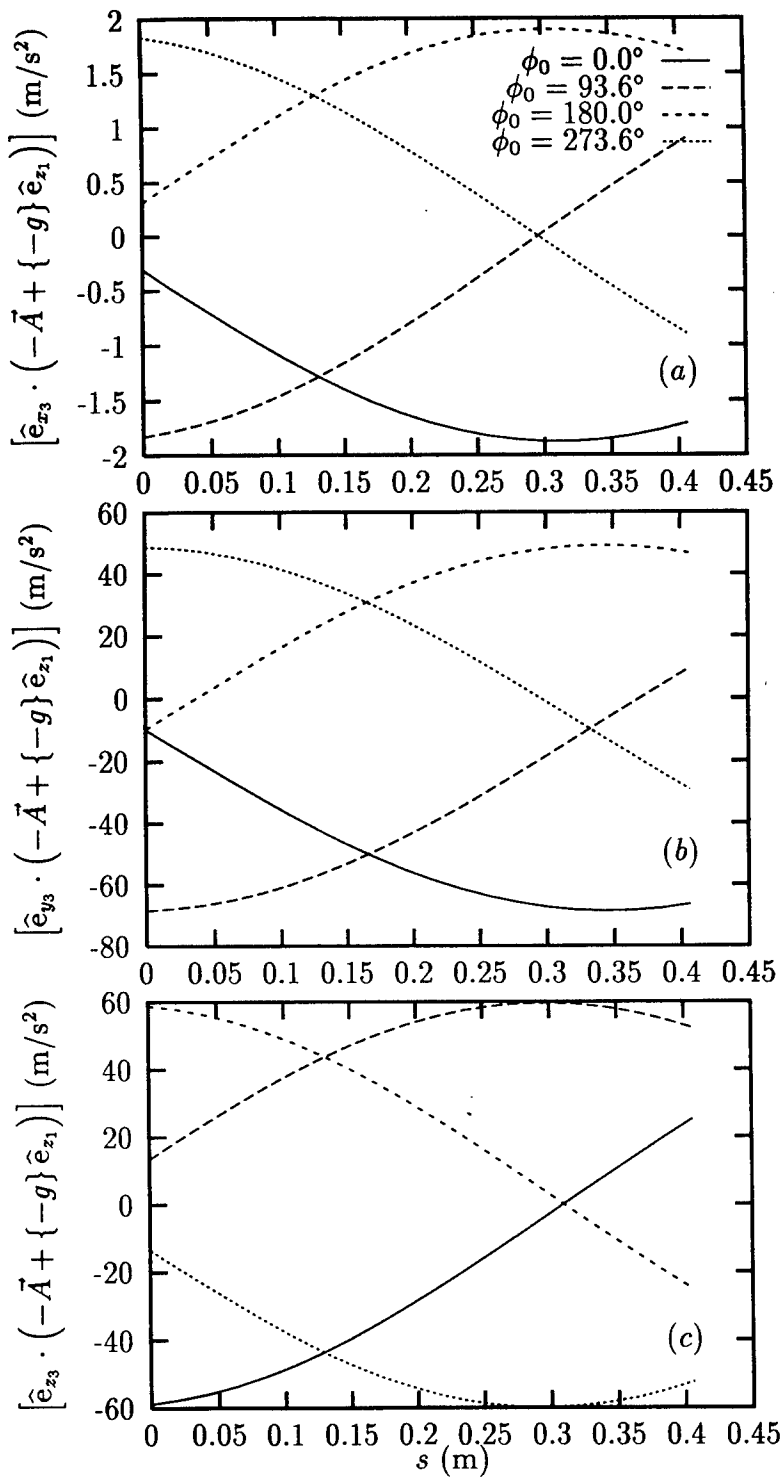


Figure 11: Acceleration components due to rotation and gravity in the (x_3, y_3, z_3) coordinate system with $|\vec{a}_r| = 6.0\text{-g}$: (a) \hat{e}_{x_3} direction; (b) \hat{e}_{y_3} direction; (c) \hat{e}_{z_3} direction.

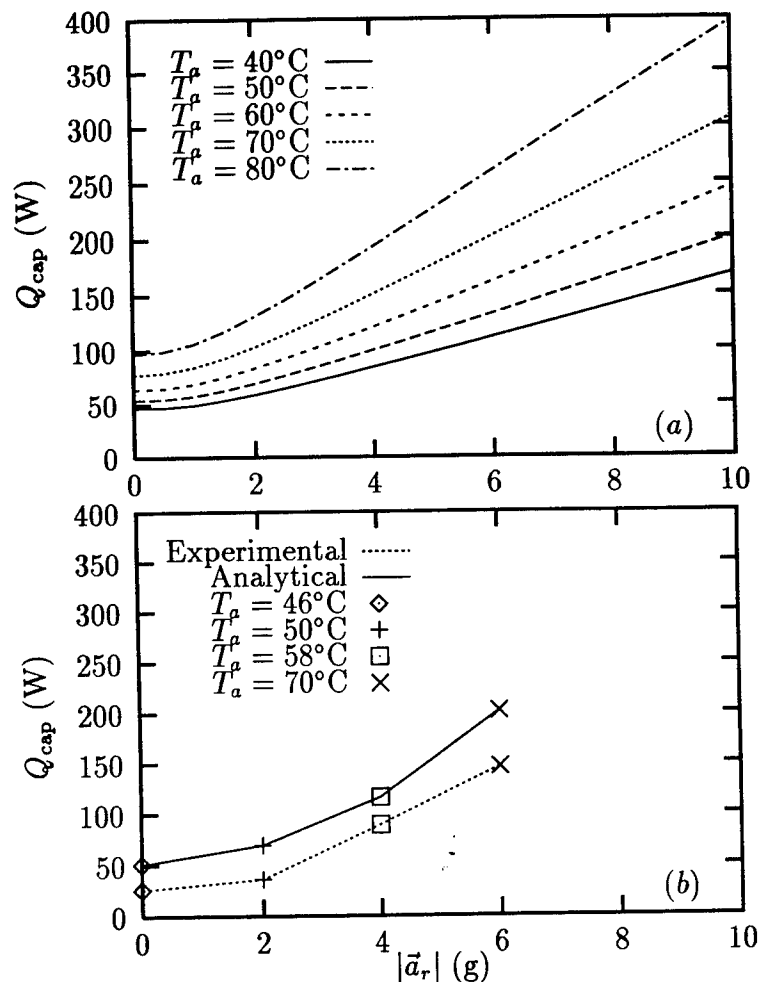


Figure 12: Capillary limit versus radial acceleration: (a) Present model; (b) Comparison of present model and experimental results.

**SUBCRITICAL CRACK GROWTH OF Ti-6Al-4V
IN THE RIPPLE-LOADING REGIME**

James P. Thomas
Assistant Professor
Department of Aerospace and Mechanical Engineering

University of Notre Dame
374 Fitzpatrick Hall
Notre Dame, IN 46556-5637

Final Report for:
Summer Research Extension Program
Wright Laboratory

Sponsored by:
Air Force Office of Scientific Research
Bolling Air Force Base, DC

and

Wright Laboratory

June 1998

SUBCRITICAL CRACK GROWTH OF Ti-6Al-4V IN THE RIPPLE-LOADING REGIME

James P. Thomas

Assistant Professor

Department of Aerospace and Mechanical Engineering
University of Notre Dame

Abstract

Recent premature failures of some titanium alloy fan blades and disks in various military and commercial jet engines have been attributed to high cycle fatigue (HCF). The rotating components in jet engines experience high frequency, low amplitude vibratory loads superposed on large, slowly varying centrifugal loads (i.e., "ripple loading"). The primary objective of this research was the development of an experimental data base for subcritical crack growth of Ti-6Al-4V under high stress-ratio ($R \geq 0.9$) loading. Mini-C(T) crack growth specimens were machined from the solution treated and aged WL PRDA-V HCF Ti-6Al-4V plate forging material in the L-T orientation. Crack growth rate tests were conducted using a MTS servohydraulic test system with automated computer control and data acquisition and indirect crack length measurement via the reversing current DC potential drop technique.

Room temperature fatigue crack growth behavior was characterized for $R = 0.9$ over the stress intensity range $\Delta K_{th} \leq \Delta K \leq (1 - R)K_c$ ($\Delta K_{th} \approx 2.1$ and $K_c \approx 63$ to $65 \text{ MPa}\sqrt{m}$). Logarithmic plots of crack growth rate (CGR) versus ΔK exhibited the classical three-stage behavior with a linear Paris-Erdogan region of CG at the intermediate ΔK levels. Room-temperature sustained-load cracking (SLC) tests were conducted using static K -control and constant K_{max} /exponentially decreasing ΔK ($R \geq 0.95$) ripple-loading tests. All attempts at inducing steady-state SLC proved unsuccessful despite the fact that K_{max} values (i.e., $\sim 63 \text{ MPa}\sqrt{m}$) very close to K_c were applied during testing. Small amounts of crack growth occurred at the start of each static K test as the crack tunneled, but eventually the CGR would decrease to a very low value. Significant crack tunneling occurred at the higher static K levels but not during the ripple-loading tests. The fractography showed evidence of transgranular fracture by quasi-cleavage with accompanying secondary cracking during fatigue and by ductile rupture during SLC.

The fatigue results are not particularly remarkable. The lack of steady-state sustained load cracking despite the moderate internal hydrogen level suggests that specimen orientation may be playing an important role in the subcritical crack growth process. Additional tests to characterize subcritical crack growth as a function of internal hydrogen level, temperature, and specimen orientation are recommended.

SUBCRITICAL CRACK GROWTH OF Ti-6Al-4V IN THE RIPPLE-LOADING REGIME

James P. Thomas

Introduction

Recent failures of fan and compressor components in Air Force gas turbine engines have been attributed to high stress-ratio, high cycle fatigue (HCF) [1,2]. These components are commonly made of Ti-6Al-4V, a two phase α - β titanium alloy known to be susceptible to hydrogen assisted cracking and low temperature creep. One goal of the current Air Force research efforts in this area is to reduce HCF related maintenance costs by 40%, in part through the development of a damage-tolerant design methodology for HCF [3]. Achievement of this goal will require better experimental and mechanistic understanding of the roles played by internal hydrogen and temperature in the hydrogen assisted cracking and low temperature creep damage processes under HCF conditions.

The crack growth behavior of Ti-6Al-4V is affected by *material related factors* such as: yield strength, microstructure, texture, and residual internal hydrogen concentration; and *environmental related factors* such as: hydrogen activity in the service environment, temperature, and applied and residual stress levels [4,5]. Two potentially important crack growth rate enhancement mechanisms in Ti-6Al-4V are hydrogen assisted cracking (HAC) and low temperature creep (LTC). Enhancement by hydrogen is generally attributed to precipitation and fracture of brittle hydrides that form in the α phase and α - β interphase regions [6,7,8]. Enhancement by LTC occurs via time dependent plastic deformations and/or vacancy diffusion and condensation at the crack tip [9,10,11,12].

Very little information is available on subcritical crack growth of Ti-6Al-4V at high stress ratios. Published literature on the effects of hydrogen, temperature, microstructure, loading, etc. on subcritical crack growth [4,5,6,12,13,14] have found that: a.) increases in internal hydrogen lead to decreased crack growth threshold K levels and increased crack growth rates (CGR); b.) the influence of temperature is complex, depending on the microstructure and loading conditions, but when temperature effects are present, a maximum in the CGR tends to occur at some intermediate level between – 70 and 200°C; and c.) the fracture surfaces show signs of both brittle cleavage, likely due to hydride formation and fracture, and ductile fracture, likely due to low temperature creep. The brittle/ductile nature of the fractography may indicate parallel action of the HAC and LTC damage mechanisms.

The objective of this research was to determine the influence of temperature on subcritical crack growth of the WL PRDA-V HCF Ti-6Al-4V plate forging material in the ripple-loading regime. Unfortunately, the material was not available from the manufacturer until October of 1997, 10 months into the yearlong research program. Because of this delay, only room temperature subcritical crack growth data can be reported at this time. Crack growth tests at sub- and above-ambient temperatures are currently in progress.

Specific results reported below include: 1.) fatigue and SLC threshold stress intensities, ΔK_{th} and $(K_{th})_{slc}$; 2.) critical stress intensity for fracture, K_c ; 3.) CGR's for fatigue over the stress intensity range: $\Delta K_{th} \leq \Delta K \leq (1 - R)K_c$; 4.) optical micrographs of the "as-received" microstructure; 5.) scanning electron fractographs of the fatigue and SLC fracture surfaces; and 6.) chemical analysis of the internal hydrogen level.

Material and Experimental Work

Mini-compact tension specimens with $W = 20$ and $B = 4.9\text{ mm}$ were machined from the WL PRDA-V HCF Ti-6Al-4V plate forging (#45) in the L-T orientation (Figures 1 & 2). The material's "as-received" heat treatment consisted of solution-treating at 932.3°C (1710°F) for 75 min . in air followed by air cooling. It was then vacuum annealed (batch #1451) at 704.4°C ($1300 \pm 25^\circ\text{F}$) and $5 \times 10^{-7}\text{ torr}$ for 2 hrs . followed by fan cooling in an Argon atmosphere. The resulting microstructure consists of approximately 57% alpha and 43% lamellar beta grains (ASTM G.S. ~ 5 to 6) that are slightly "flattened" in the forging plane (Figure 3). The nominal chemical composition and some material property values are reported below in Tables 1 and 2.

Table 1: Chemical composition of the Ti-6Al-4V test material.

Nominal Chemical Composition (Wgt. %)								
Al	V	O	Fe	C	N	H*		Ti
6.0	4.0	0.15	0.15	0.030	0.005	0.00505 ± 0.00029		Bal.

*: Actual value \pm 1 SD based on chemical analysis of 6 samples.

Table 2: Material properties for the Ti-6Al-4V test material.

Material Properties [†]				
S_u (MPa)	S_y (MPa)	Elongation (%)	Modulus (GPa)	Strain Rate (s^{-1})
979	930	20.1	120	5×10^{-4}
1014	1003	18.3	126.5	5×10^{-2}

†: Data from WL/MLLN.

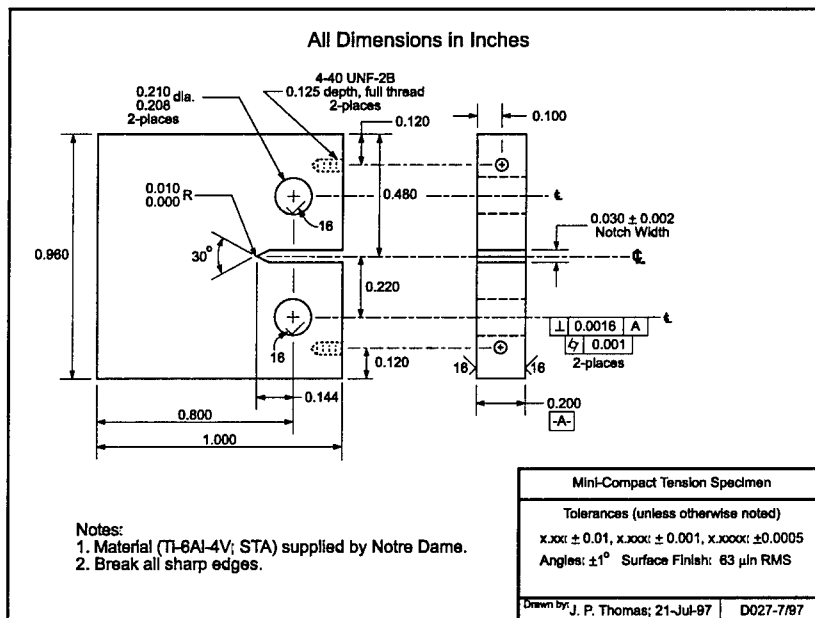


Figure 1: Machining print for the mini-C(T) specimen.

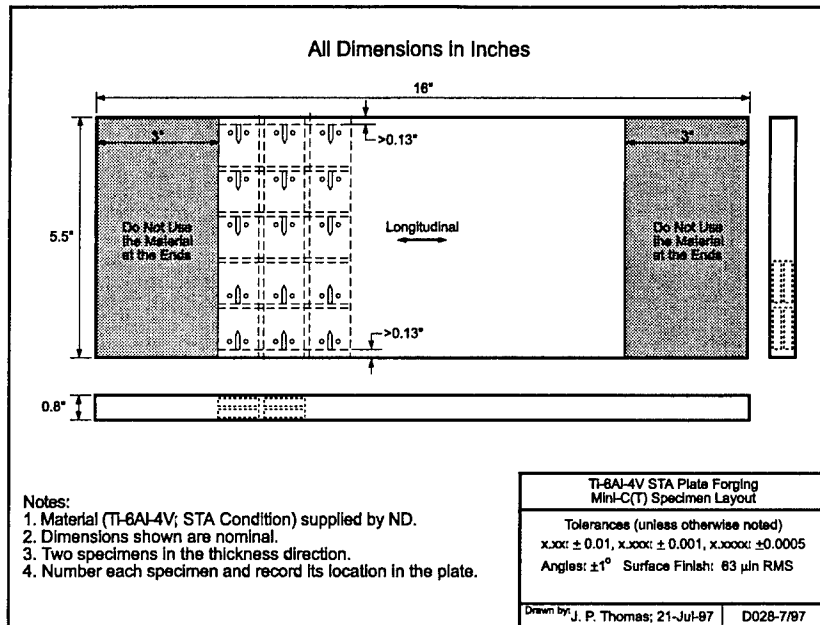


Figure 2: Specimen orientation in the plate.

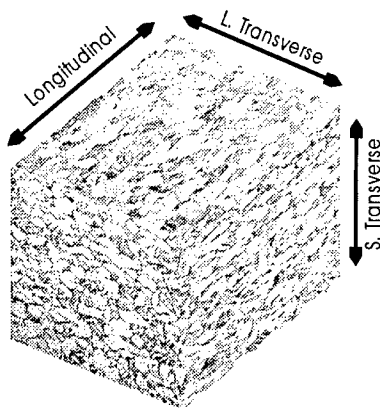


Figure 3: Microstructure for the WL PRDA-V HCF Ti-6Al-4V plate forging (#45) showing α grains (light) within a lamellar β matrix (dark). Anisotropy in the form of flattening of the grains in the forging (L-T) plane is present (Kroll's reagent; see Figure 68 in reference [15]).

Crack length was measured indirectly using a reversing current DC potential drop technique (Figure 4). The current leads were attached on the notch face using 4-40 screws, the potential leads were spot welded on opposite sides of the notch and then secured with epoxy to prevent inadvertent mechanical stressing of the welds (Figure 5).

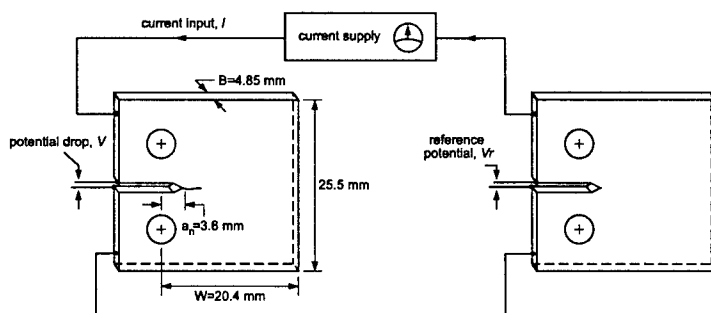


Figure 4: DC potential drop crack length measurement system wiring schematic.

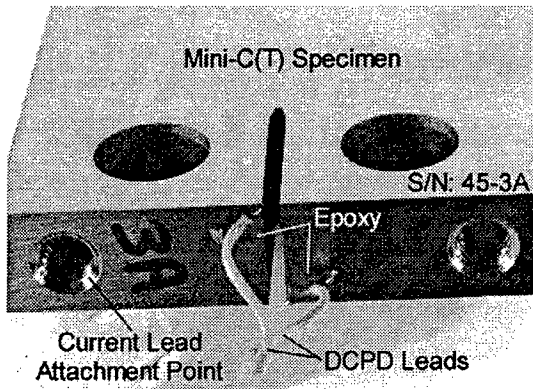


Figure 5: Mini-C(T) specimen showing wiring details for the crack length measurement system.

Calibration data (i.e., normalized crack length-vs.-normalized potential drop; Figures 6 and 7) were obtained from two specimens cracked in fatigue with $K_{max} \approx 25 MPa\sqrt{m}$ and alternating stress ratios (i.e., $R = 0.50$ for $\Delta a \sim 1 mm$ and $R = 0.85$ for $\Delta a \sim 0.5 mm$). Alternating the R -values led to demarcation of the crack front (see Figure 8); post test crack length measurements were made using a stereomicroscope and precision x - y measurement stage. The data was least squares fit to the following empirical calibration relationship:

$$\frac{a}{W} = -0.57456 + 0.77764\phi + 0.024940\phi^2 - 0.040995\phi^3 \quad (1)$$

where

$$\phi \equiv \frac{V}{V_0} \frac{V_{r0}}{V_r} \quad (2)$$

is the normalized potential, a is the crack length, W the specimen width, V the current test specimen potential drop, V_0 the initial test specimen notch potential, V_{r0} the initial reference specimen potential, and V_r the current reference specimen potential. The reference potential term, V_{r0}/V_r , corrects the normalized potential drop for small changes occurring in the current and temperature during the course of the test.

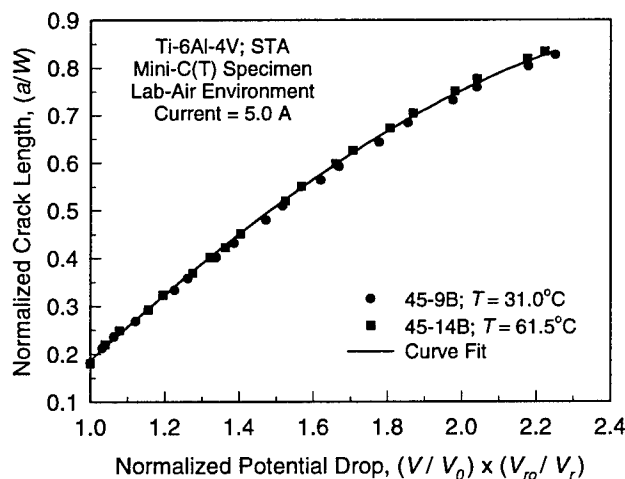


Figure 6: Scatter plot for the potential drop-crack length calibration data.

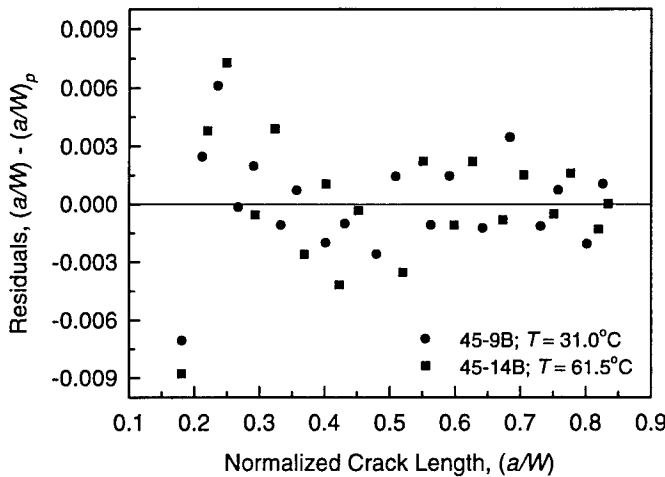


Figure 7: Residual plot for the potential drop-crack length calibration data.

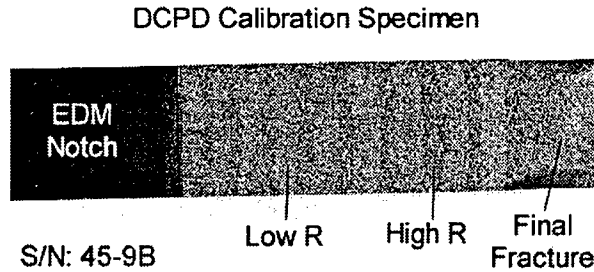


Figure 8: Fracture surface of a calibration specimen showing the surface demarcation achieved by varying the stress ratio R while holding K_{max} constant.

The CGR tests were conducted under ambient laboratory conditions on a 22-kip MTS servohydraulic test system with automated computer control and data acquisition. The tests were conducted under ΔK -control following the relationship:

$$\Delta K = \Delta K_0 \exp(C(a - a_0)) \quad (3)$$

ΔK_0 is the value of ΔK at some arbitrary starting crack length a_0 and C is the ΔK -gradient ($= 0.00$ or ± 0.08 mm^{-1}). All specimens were precracked at least 1 mm beyond the notch or starting crack length at K_{max} levels $\leq 50\%$ of the starting value for the particular test. The following stress intensity relation for C(T) specimens was used in these tests (ASTM E-647-93):

$$K = \frac{P}{B\sqrt{W}} \frac{(2 + a/W)}{(1 - a/W)^{3/2}} \times \left(0.886 + 4.64 \left(\frac{a}{W} \right) - 13.32 \left(\frac{a}{W} \right)^2 + 14.72 \left(\frac{a}{W} \right)^3 - 5.6 \left(\frac{a}{W} \right)^4 \right) \quad (4)$$

A summary of the CGR tests is given below in Table 3:

Table 3: Crack Growth Testing Summary

Test No.	Specimen S/N	Test Description
1	45-2B	DCPD Calibration
2	45-9B	DCPD Calibration
3	45-14B	DCPD Calibration
4	45-10A	Fatigue CGR: da/dN -vs- ΔK
5	45-6A	Fatigue CGR: da/dN -vs- ΔK
6	45-19B	SLC: $(K_{th})_{slc}$
7	45-11A	SLC: $(K_{th})_{slc}$
8	45-20B	SLC: $(K_{th})_{slc}$
9	45-17B	SLC: $(K_{th})_{slc}$
10	45-2A	Ripple-Loading SLC

Results and Discussion

The fatigue data are shown in Figures 9 through 11. A power-outage interruption and a change in load frequency from 50 to 25 Hz at the higher ΔK levels during Test #4 (i.e., 45-10A; Figure 9) has an influence on the crack growth behavior as can be seen on comparing with the data from Test #5 (45-6A; Figure 10). Figure 11 combines the data from Figures 9 and 10 minus that from Test #4 corresponding to the interruption and lower frequency data. The least squares fit power-law relationship for the Stage II data in Figure 11 is given by:

$$\frac{da}{dN} = 1.662 \times 10^{-8} \Delta K^{3.413} \quad (5)$$

where da/dN is given in $mm/cycle$ for ΔK expressed as $MPa\sqrt{m}$.

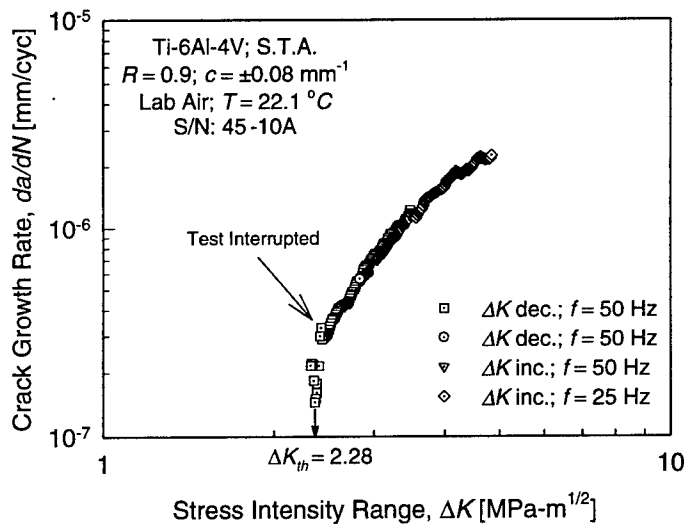


Figure 9: Fatigue crack growth data from Test #4.

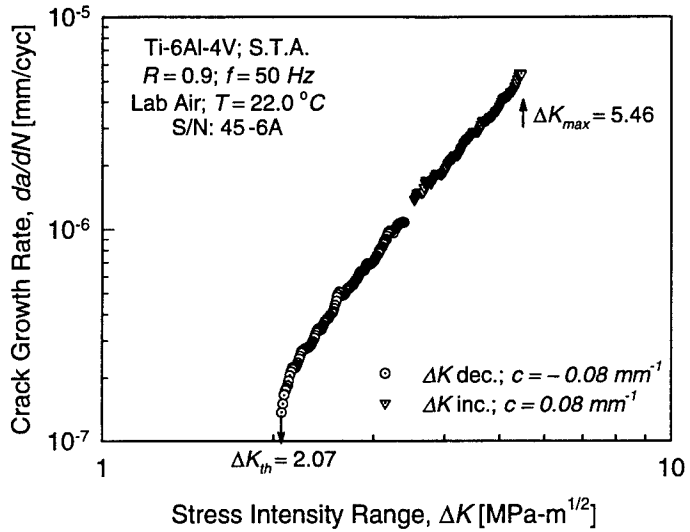


Figure 10: Fatigue crack growth data from the Test #5.

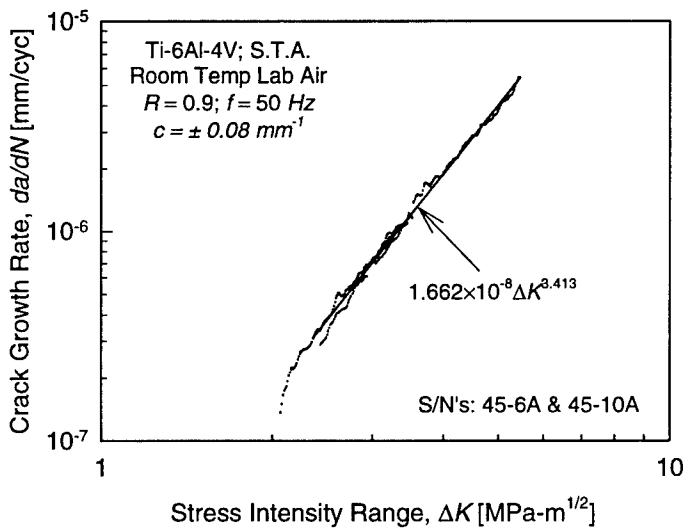


Figure 11: Combined data from Figures 9 & 10 not including that from Test #4 gathered after the test interruption and change in loading frequency.

The above fatigue data also provided the following estimates for the fatigue crack growth threshold stress intensity for $R = 0.9$: $\Delta K_{th} \approx 2.28$ and $2.07 \text{ MPa}\sqrt{\text{m}}$ corresponding to CGR's less than $2 \times 10^{-10} \text{ m/cycle}$. Another threshold stress intensity estimate was obtained from the ripple-loading SLC data corresponding to $R = 0.97$ (see Figure 14): $\Delta K_{th} \approx 1.88 \text{ MPa}\sqrt{\text{m}}$ for a CGR of $\sim 2 \times 10^{-11} \text{ m/cycle}$.

Several unsuccessful attempts were made to induce sustained load cracking in this material. Static K tests were conducted on three different specimens by first precracking in fatigue then quickly ramping to the starting K value. The K_{max} values used during fatigue precracking were limited to < 50% of the starting K values for the SLC

tests. Small amounts of crack growth occurred at the start of each test, but the CGR's eventually diminished to very small values. Significant crack tunneling occurred at the higher K levels as illustrated by the SLC crack in Figure 12 (45-17B; Test #9). The corresponding crack growth data is shown in Figure 13.

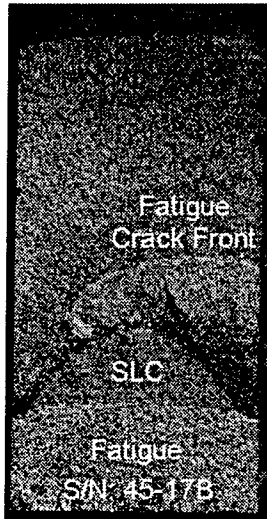


Figure 12: Crack tunneling during SLC at $K \approx 63.3 MPa\sqrt{m}$. The distance from the precrack to SLC peak is 1.585 mm.

The K value achieved during the SLC test on specimen 45-17B (Test #9) was very close to the critical fracture value K_c , and yet, no observable steady-state CG. This suggests that steady-state SLC may not be possible for this material in the L-T orientation or the mini-C(T) specimen configuration. The internal hydrogen level of $\sim 50 wppm$ is large enough to have an influence on the subcritical CG behavior of Ti-6Al-4V, based on studies reported in the literature (see, for example, [4,5,6]). The most important difference between the present situation and those reported in the literature is the specimen orientation; the published SLC studies use specimens machined in the T-L orientation. This factor will be investigated in a future study of this material.

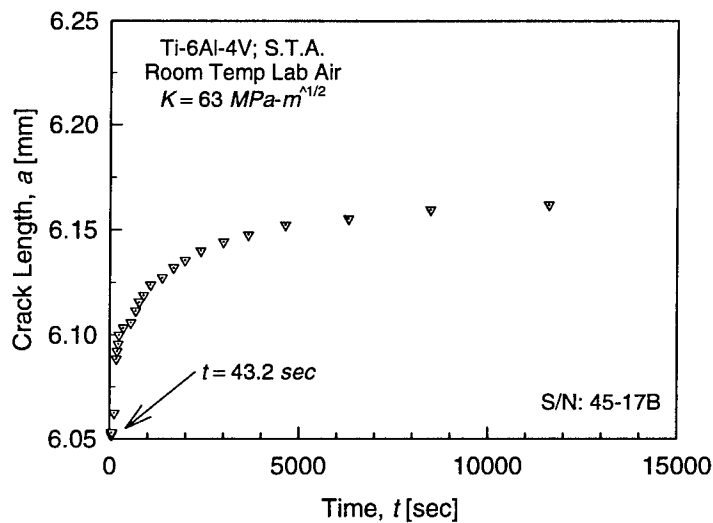


Figure 13: SLC data for 45-17B corresponding to the crack shown in Figure 12. The crack length at the start of the test was 5.66 mm and is not included in the above plot.

The K value achieved during the SLC test on specimen 45-17B (Test #9) was very close to the critical fracture value K_c , and yet, no observable steady-state CG. This suggests that steady-state SLC may not be possible for this material in the L-T orientation or the mini-C(T) specimen configuration. The internal hydrogen level of

$\sim 50 \text{ wppm}$ is large enough to have an influence on the subcritical CG behavior of Ti-6Al-4V, based on studies reported in the literature (see, for example, [4,5,6]). The most important difference between the present situation and those reported in the literature is the specimen orientation; the published SLC studies have all used specimens machined in the T-L orientation. This factor will be investigated in a future CGR study of this material.

One other item of interest with regard to the static- K SLC tests was the difficulty in getting a fatigue crack to propagate evenly in the through thickness direction following crack arrest. Significant plastic deformation (i.e., dimples) was evident at the crack tips on the outer surfaces of the specimen during static loading. The crack would grow a small amount, at the start of fatigue loading, but then cease until a large number of cycles were accumulated. It would then start growing again but usually on one side of the specimen only (see the fatigue crack front shown in Figure 12). A two stage fatigue cracking procedure was developed to speed up and even-out the crack growth process. A high K_{max} value (still less than 50% of the SLC K value) with $R = 0.2$ was used to "initiate" the crack from its SLC arrest position. The crack was allowed to grow about 0.5 mm . The fatigue K_{max} value was then dropped to either 15 or $20 \text{ MPa}\sqrt{m}$ with $R = 0.1$ and the crack allowed to grow for another 2 to 3 mm to guarantee that the fatigue crack front would be at least 1 mm beyond the tip of the SLC crack. The crack front would straighten out during this last stage of fatigue crack growth so that valid K values could be achieved in any subsequent SLC test.

The ripple-loading SLC test (45-2A; Test #10) results are shown in Figures 14 through 16. Two tests were conducted using this specimen; the first with $K_{max} = 50 \text{ MPa}\sqrt{m}$ and a starting $R = 0.95$ (Figure 14) and the second with $K_{max} = 60 \text{ MPa}\sqrt{m}$ and a starting $R = 0.96$ (Figure 15). Very little difference exists between the two sets of CGR data, as shown in Figure 16, despite the difference in K_{max} values. This is further evidence for lack of sustainable SLC; the CG process during ripple-loading SLC is dominated by fatigue. It is also manifested by the fractography (discussed below), by the small crack front curvature, and by the rapid diminishment in CGR as $\Delta K \rightarrow 1.88 \text{ MPa}\sqrt{m}$ and $R = 0.97$. Note that this value is approximately 10% lower than that corresponding to the constant $R = 0.9$ fatigue CG threshold test (45-6A, Test #6).

Critical fracture toughness, K_c , estimates for this material in the mini-C(T) specimen configuration were obtained using the data from two "unplanned" fractures during the SLC tests. The critical values fall within the range $63\text{-}65 \text{ MPa}\sqrt{m}$.

Fractographs corresponding to fatigue, static SLC, and ripple-loading SLC are shown in Figures 17 through 30. The fracture surface for low ΔK -level fatigue conditions is primarily transgranular quasi-cleavage with significant amounts of secondary cracking (Figure 17). At the high ΔK -levels (Figure 18), there is evidence of ductile rupture (voids) and perhaps a bit less secondary cracking. Figures 19 through 22 show fracture surfaces corresponding to mid ΔK -level fatigue conditions for a variety of magnifications. The observable features are similar to those developed on the low and high ΔK -level fatigue surfaces: transgranular quasi-cleavage with secondary cracking and voids.

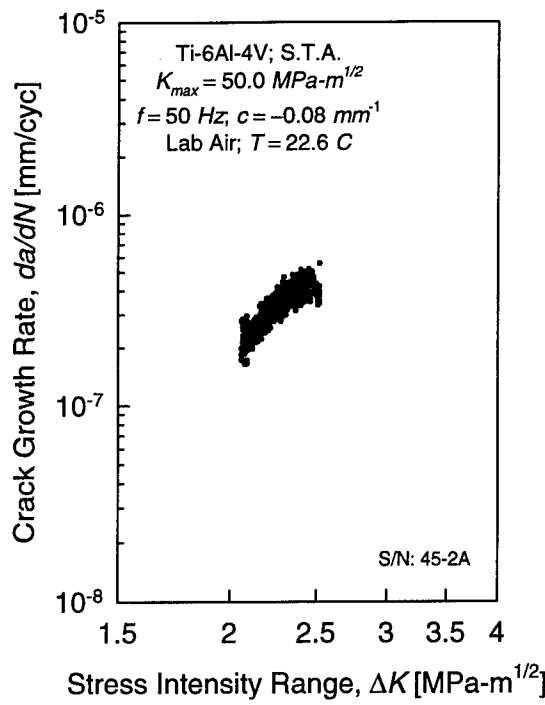


Figure 14: Ripple-loading SLC data for 45-2A at $K_{max} = 50 \text{ MPa}\sqrt{m}$.

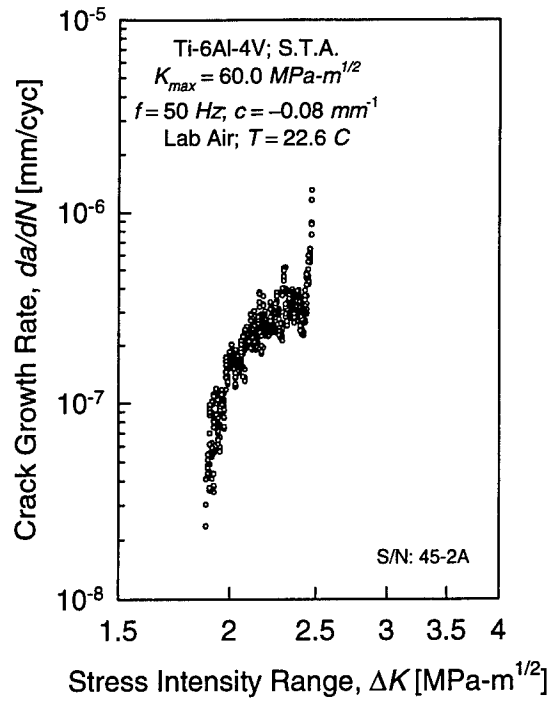


Figure 15: Ripple-loading SLC data for 45-2A at $K_{max} = 60 \text{ MPa}\sqrt{m}$.

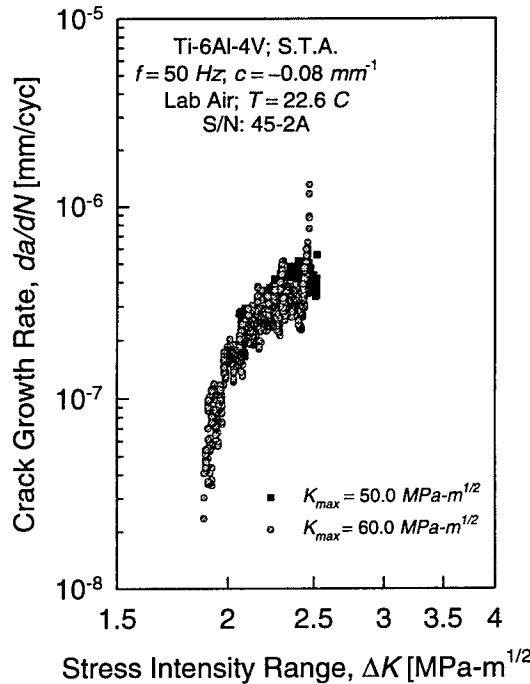


Figure 16: Combined data from Figures 14 and 15 for ripple-loading SLC.

Figures 23 through 27 show the fractographs for the static K SLC test specimen (45-17B; Test #9). These surfaces exhibit many inclusionless voids and some transgranular quasi-cleavage but no secondary cracking. These features are consistent with a ductile rupture (low temperature creep) process. The contrast between the fracture features developed during fatigue and SLC is demonstrated in Figures 26 and 27.

Figures 28 through 30 show fractographs for ripple-loading SLC (45-2A; Test #10). These fractures surfaces are both fatigue-like in nature with transgranular quasi-cleavage and some accompanying secondary cracking, but also SLC-like with the voids that are present. Consistent with the above fractographic observations is the fact that the curvature of the crack front during ripple-loading SLC is much smaller (i.e., more fatigue-like) than the large curvature crack fronts that develop during static SLC.

Summary

Room temperature fatigue and sustained-load crack growth behavior of the solution treated and aged WL PRDA-V HCF Ti-6Al-4V plate forging material was experimentally characterized. Fatigue crack growth data was generated for $R = 0.9$ over the stress intensity range $\Delta K_{th} \leq \Delta K \leq (1 - R)K_c$. The crack growth rate exhibited the classical three-stage behavior with a linear Paris-Erdogan region at the intermediate ΔK levels. Scanning electron microscopy of the fatigue fracture surfaces showed evidence of transgranular fracture by quasi-cleavage with accompanying secondary cracking and voids (especially at the higher ΔK levels).

Sustained-load cracking tests were conducted using static K -control and constant K_{max} /exponentially decreasing ΔK ripple-loading tests. Steady-state cracking could not be induced, even with K_{max} values close to the critical fracture toughness, K_c . Significant crack tunneling occurred at the higher static K levels but not during the ripple-loading tests. Scanning electron microscopy of the sustained-load fracture surfaces showed many voids with some accompanying transgranular quasi-cleavage (i.e., ductile rupture) consistent with a low temperature creep crack growth process.

The fatigue results are not particularly remarkable. The lack of steady-state sustained load cracking despite the moderate internal hydrogen level suggests that specimen orientation may be playing an important role in the subcritical crack growth process. Additional tests to characterize subcritical crack growth as a function of internal hydrogen level, temperature, and specimen orientation are recommended.

Acknowledgments

The financial support of AFOSR and Wright Laboratory for this Summer Faculty Research Extension grant (AFOSR Contract # F49620-93-C-0063; RDL Subcontract # 97-0810) is gratefully acknowledged. The advice and guidance of Dr. Ted Nicholas of Wright Laboratory on this project is also gratefully acknowledged. The Ti-6Al-4V plate material used in this testing program was received from the Materials Behavior Branch (MLLN) Branch of Wright Laboratory.

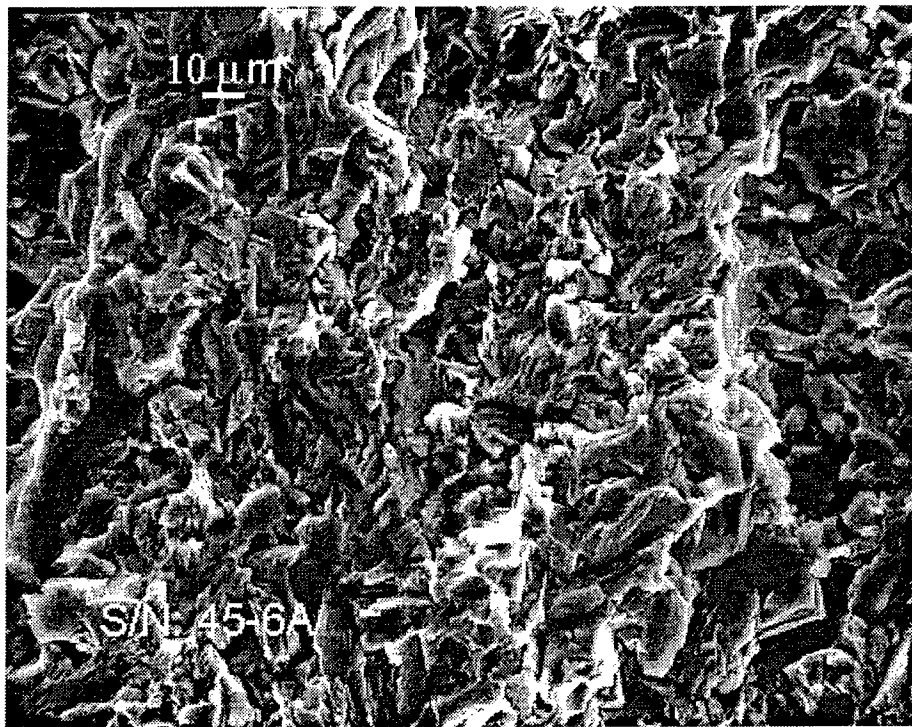


Figure 17: Fracture surface of fatigue specimen 45-6A from the Stage I (threshold ΔK) CG region showing transgranular quasi-cleavage and secondary cracking.

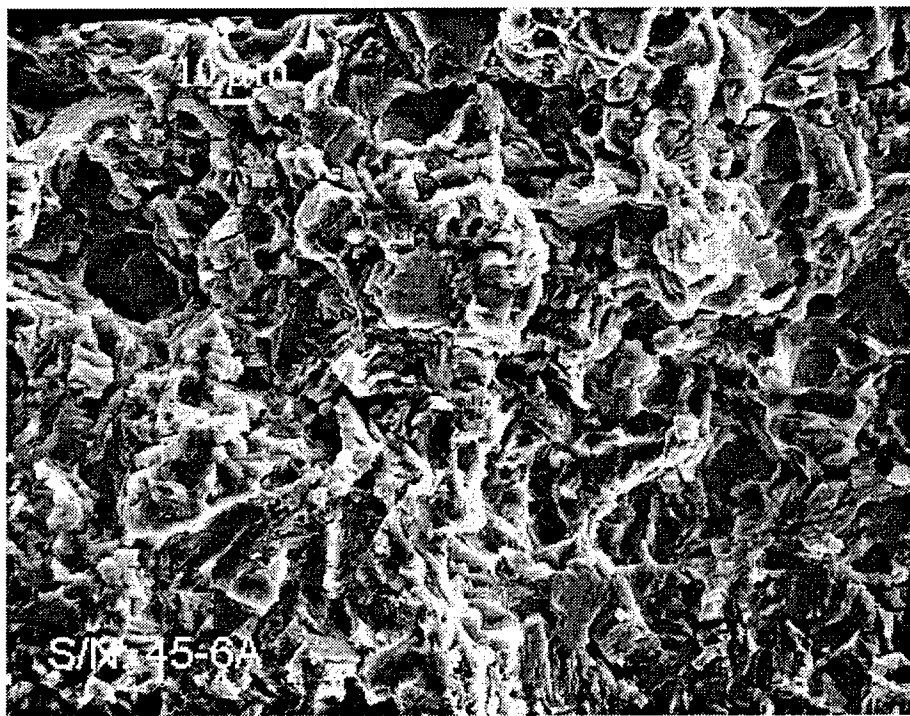


Figure 18: Fracture surface of fatigue specimen 45-6A in the Stage III (K_c) CG region showing transgranular quasi-cleavage with accompanying voids and secondary cracking.

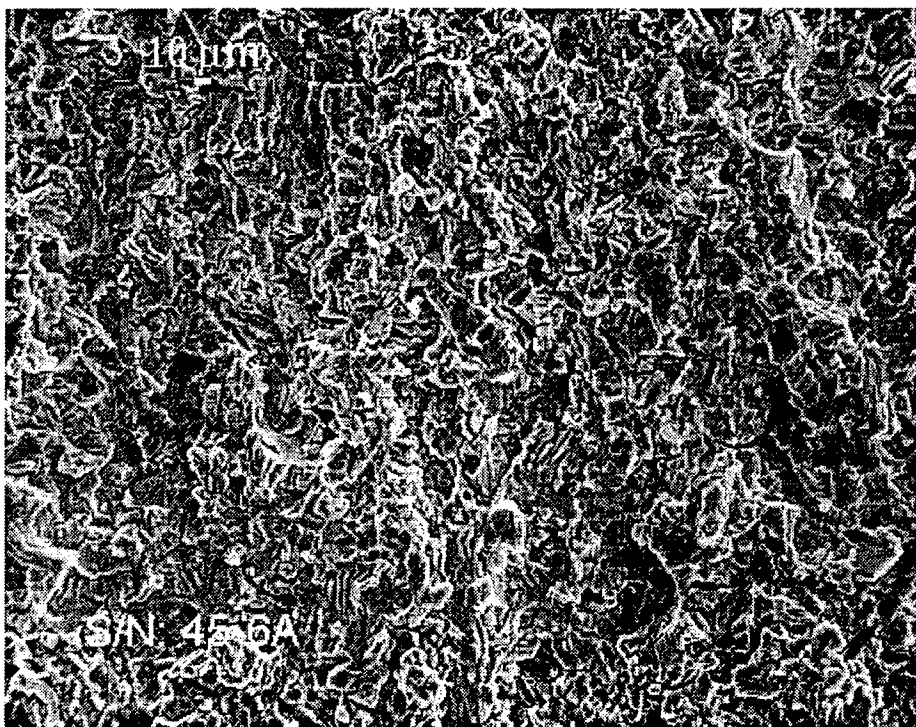


Figure 19: Fracture surface of fatigue specimen 45-6A in the Stage II (power-law CG) region. Transgranular quasi-cleavage with accompanying voids and significant secondary cracking.

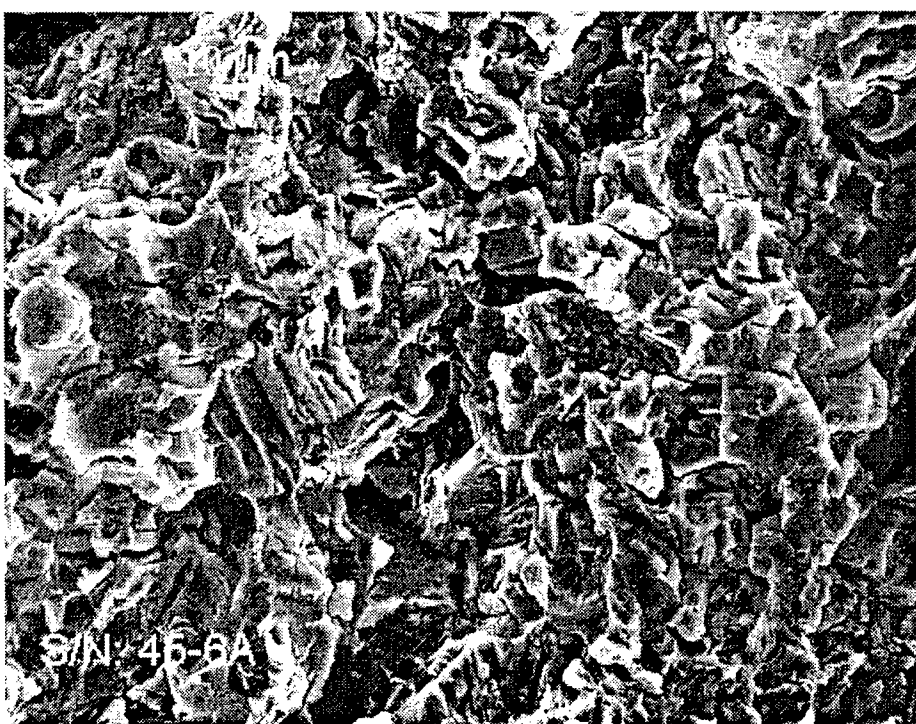


Figure 20: Same as Figure 19 but at higher magnification.

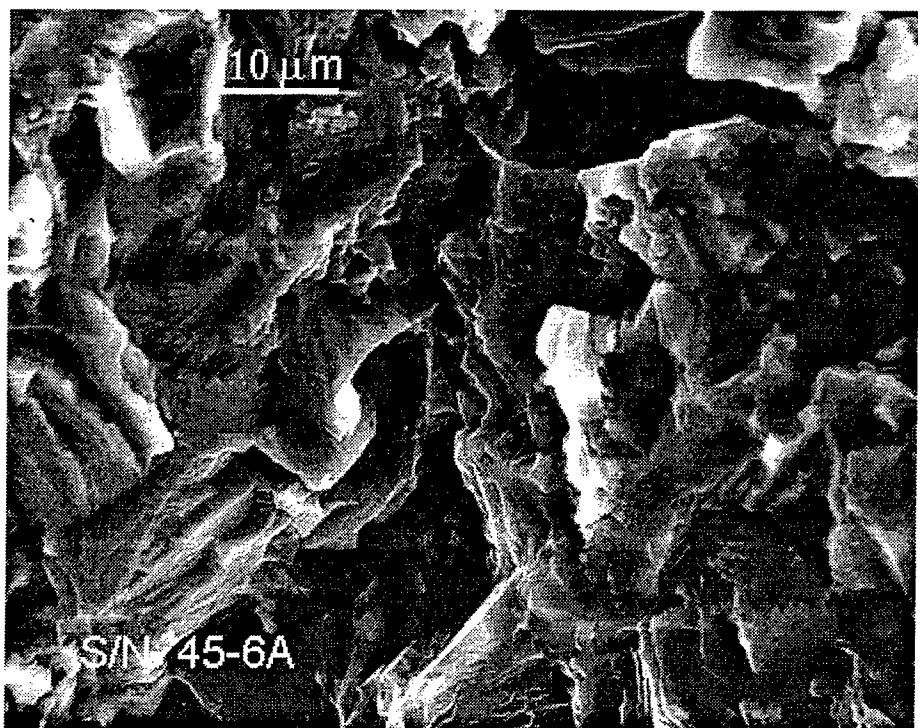


Figure 21: Same as Figures 19 and 20 but at higher magnification. Many fine cleavage steps are visible at this magnification.

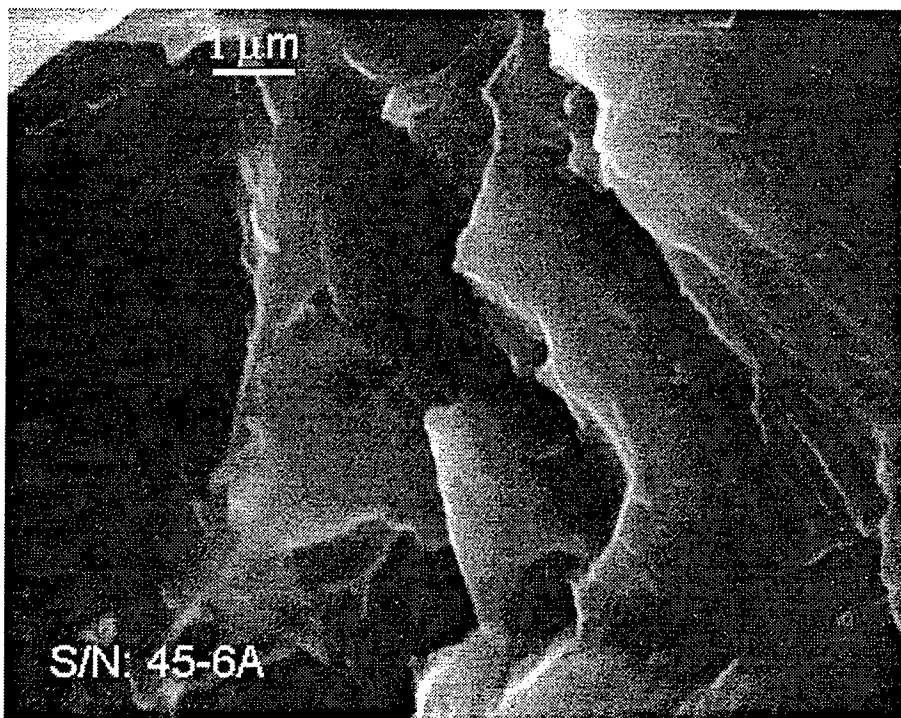


Figure 22: Same as Figures 19 through 21 but at higher magnification.

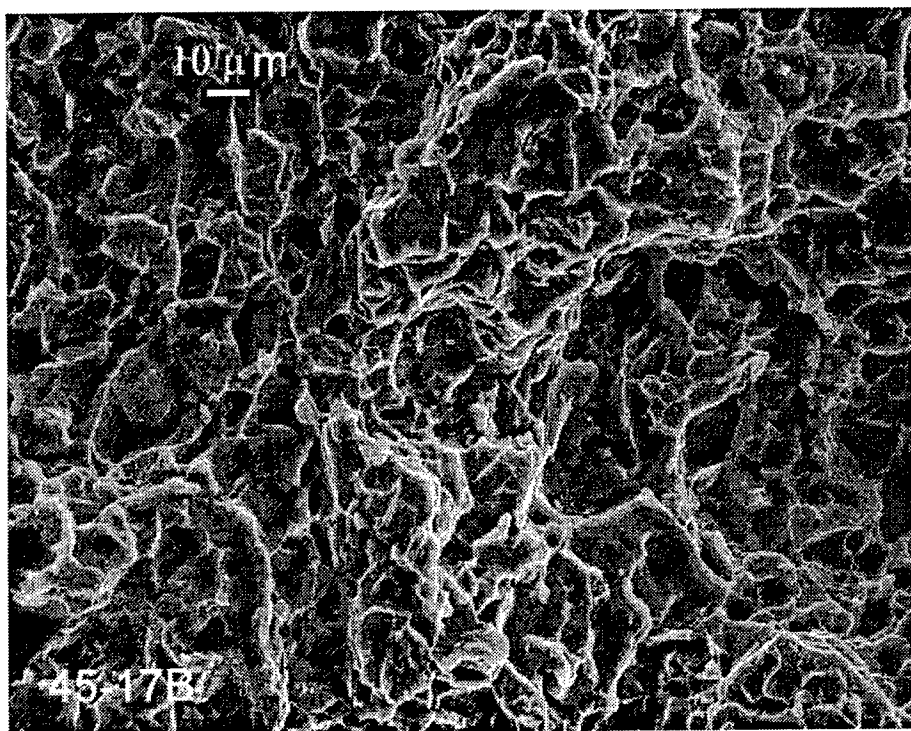


Figure 23: Fracture surface for the static K sustained-load cracking specimen 45-17B ($K_{max} \approx 63 \text{ MPa}\sqrt{m}$). The primary feature here is voids with some accompanying transgranular quasi-cleavage.

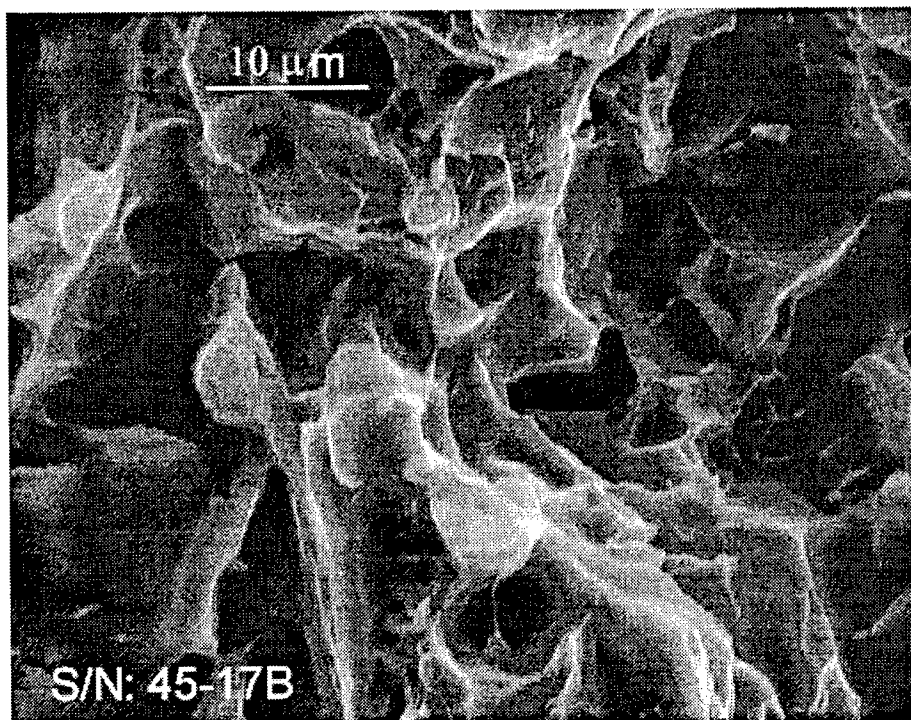


Figure 24: Same as Figure 23 but at higher magnification. Note the lack of fine cleavage steps in this photo as compared with those that develop during fatigue crack growth.

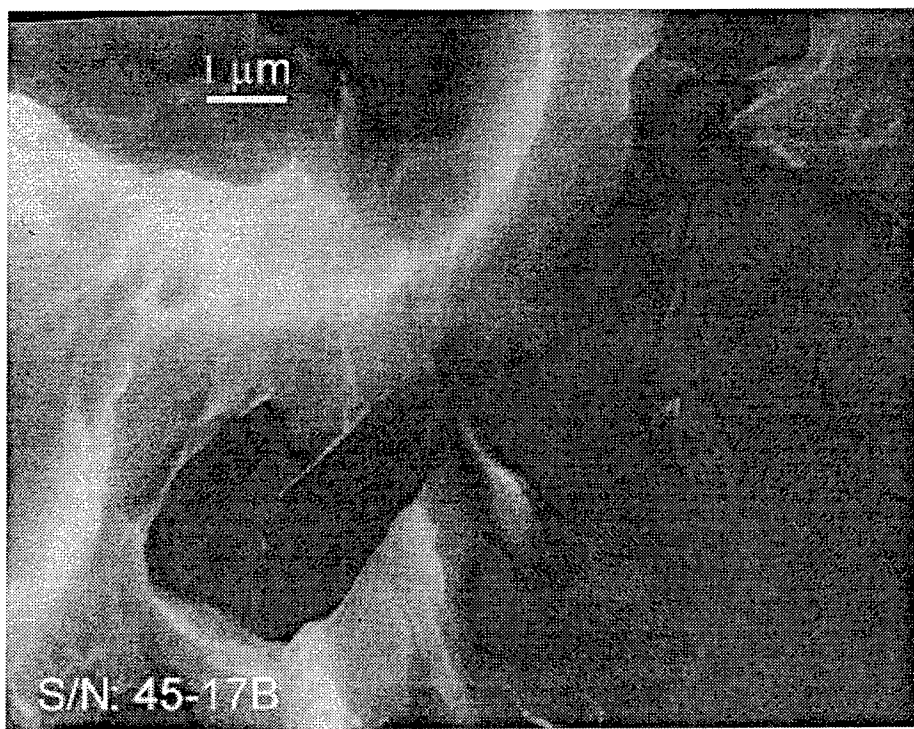


Figure 25: Same as Figures 23 and 24 but at higher magnification. Some cleavage steps are visible at this magnification but they are not as numerous nor as distinctive as those developed during fatigue crack growth.

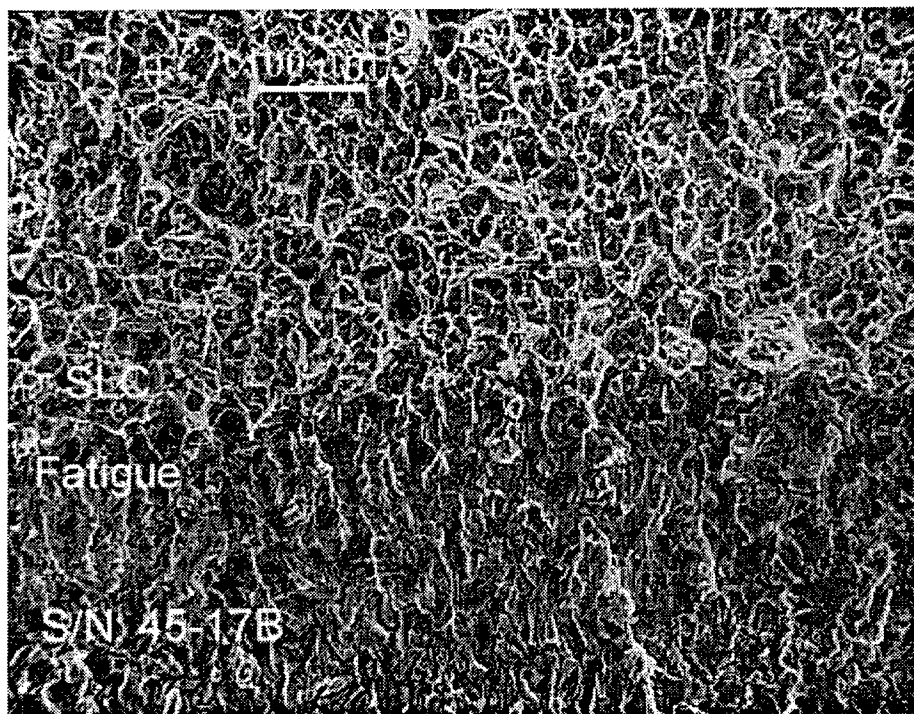


Figure 26: Transition region between regions of fatigue and SLC in specimen 45-17B. The transgranular quasi-cleavage and secondary cracking of fatigue contrasts nicely with the voids (ductile rupture features) of SLC.

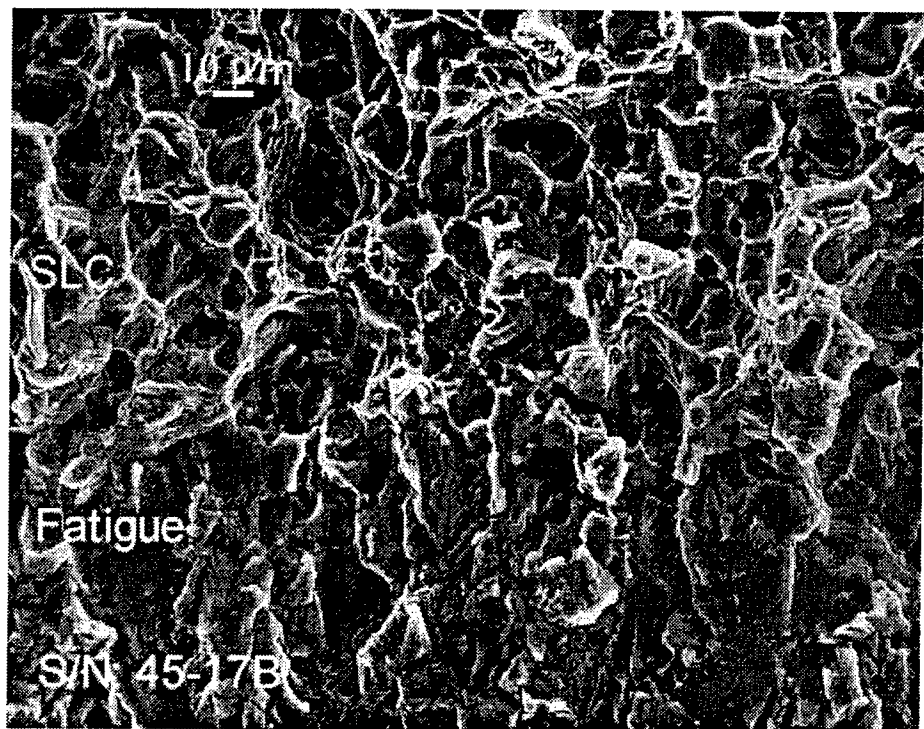


Figure 27: Same as Figure 26 but at higher magnification.

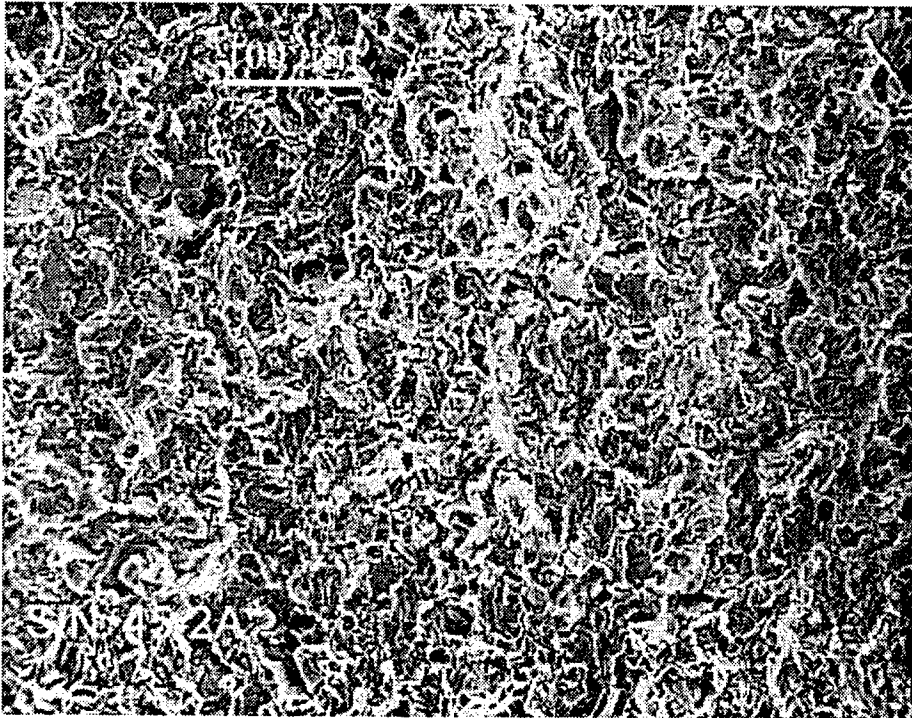


Figure 28: Fracture surface of ripple-loading SLC specimen 45-2A for $K_{max} = 60 \text{ MPa}\sqrt{m}$. Fractographic features common to both fatigue and SLC are evident in this photograph.

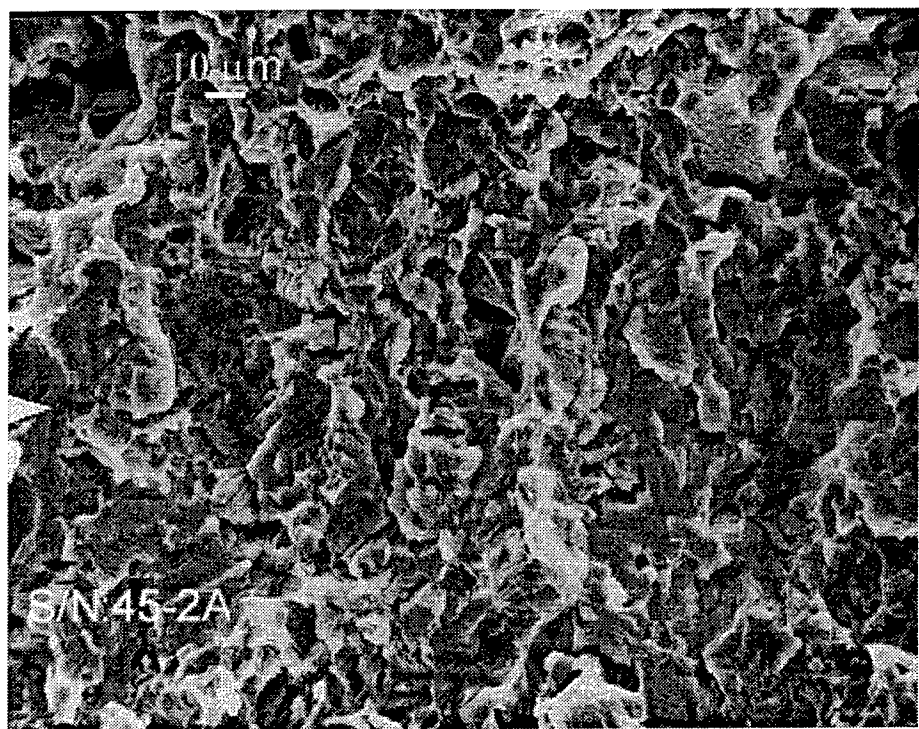


Figure 29: Same as Figure 28 but at higher magnification.

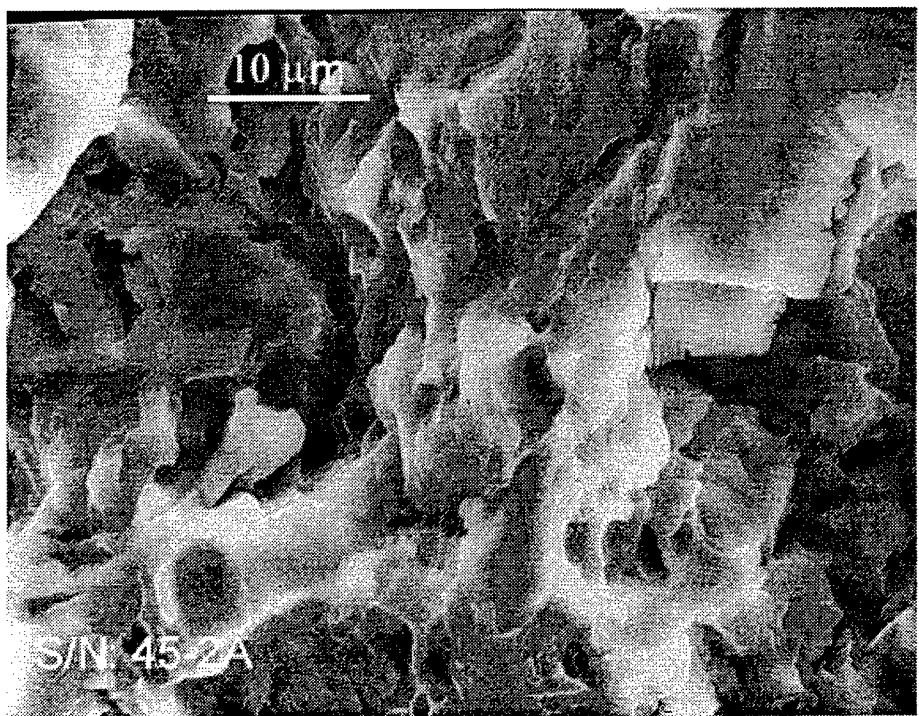


Figure 30: Same as Figures 28 and 29 but at higher magnification. Note the many fine cleavage steps and voids visible at this magnification.

References

1. Nicholas, T. and J. R. Zuiker, "On the Use of the Goodman Diagram for High Cycle Fatigue Design", *Int. J. Frac.*, Vol. 80, 1996, pp. 219-235.
2. Cowles, B. A., "High Cycle Fatigue in Aircraft Gas Turbines - An Industry Perspective", *Int. J. Frac.*, Vol. 80, 1996, pp. 147-163.
3. "High Cycle Fatigue (HCF) Science and Technology Program 1997 Annual Report", AFRL-PR-WP-TM-1998-2002, 1998.
4. Rosenberg, H. W., J. C. Chesnutt, and H. Margolin, "Fracture Properties of Titanium Alloys", in *Application of Fracture Mechanics for Selection of Metallic Structural Materials*, American Society for Metals, OH, 1982, pp. 213-252.
5. Moody, N. R., and J. E. Costa, "A Review of Microstructural Effects on Hydrogen-Induced Sustained Load Cracking in Structural Titanium Alloys", in *Microstructure/Property Relationships in Titanium Aluminides and Alloys*, TMS, 1991, pp. 587-604.
6. Meyn, D. A., "Effect of Hydrogen on Fracture and Inert-Environment Sustained Load Cracking Resistance of α - β Titanium Alloys", *Met. Trans. A*, Vol. 5, 1974, pp. 2405-2414.
7. Shih, D. S., I. M. Robertson, and H. K. Birnbaum, "Hydrogen Embrittlement of α Titanium: *In Situ* TEM Studies", *Acta Met.*, Vol. 36, 1988, pp. 111-124.
8. Birnbaum, H. K., "Mechanisms of Hydrogen-Related Fracture of Metals", in *Environment-Induced Cracking of Metals*, NACE-10, National Association of Corrosion Engineers, TX, 1990, pp. 21-29.
9. Neal, D. F., "Creep Fatigue Interactions in Titanium Alloys", in *6th World Conference on Titanium*, in France, 1988, pp. 175-180.
10. Reimann, W. H., "Room Temperature Creep in Ti-6Al-4V", *J. Materials*, JMLSA, Vol. 6, 1971, pp. 926-940.
11. Van Leeuwen, H. P., "The Application of Fracture Mechanics to Creep Crack Growth", *Engr. Frac. Mechs.*, Vol. 9, 1977, pp. 951-974.
12. Williams, D. N., "Effects of Hydrogen in Titanium Alloys on Subcritical Crack Growth under Sustained Load", *Matls. Sci. & Eng.*, Vol. 24, 1976, pp. 53-63.
13. Ruppen, J. A., C. L. Hoffman, V. M. Radhakrishnan, and A. J. McEvily, "The Effect of Environment and Temperature on the Fatigue Behavior of Titanium Alloys", in *Proc. 27th Sagamore Army Materials Research Conference*, Plenum, 1983, pp. 265-300.
14. Meyn, D., "Temperature Dependence of Sustained Load Cracking Caused by Residual Hydrogen in Ti-6Al-4V", in *Titanium Science and Technology*, G. Lutjering, U. Zwicker, and W. Bunk, Eds., Vol. 4, 1985, pp. 2565-2570.
15. Boyer, R. R., "Titanium and Titanium Alloys", in *ASM Metals Handbook*, 9th Ed., Vol. 9: Metallography and Microstructures, American Society for Metals, Metals Park, OH, 1985, pp. 458-475.

**SCALABLE PARALLEL SOLUTION OF THE 3D NAVIER-STOKES
EQUATIONS**

Karen A. Tomko
Assistant Professor
Department of Computer Science and Engineering

Final Report for:
Summer Research Extension Program

Wright State University
3640 Colonel Glen Highway
Dayton, OH 45435-0001

Sponsored by:
Air Force Office of Scientific Research
Bolling Air Force Base, Washington DC

and

Wright State University

December 1997

Scalable Parallel Solution of the 3D Navier-Stokes Equations

Karen A. Tomko

Assistant Professor

Department of Computer Science and Engineering
Wright State University

Abstract

Despite progress in parallel compiler technology, parallel aerospace applications are still primarily hand-crafted. This need for hand-crafting bars many computational scientist from utilizing the computational power of modern parallel systems. The objective of this project was to work in collaboration with the computational scientists in the CFD Research Branch of the Air Force Research Laboratory to develop tools to help automate parallelization of applications utilizing the grid parallel verions of the FDL3DI application. The grid parallel FDL3DI application, solves the three-dimensional Navier-Stokes equations for multiple Chimera (overset) grids by independantly executing the flow solver on each grid and exchanging interpolated boundary data in the overlapped regions each iteration.

Load imbalance is the main disadvantage of a grid based parallel solution of the Navier-Stokes equations. Current grid generation programs create multiple grids based on the geometric constraints of a particular flow problem, and do not usually generate grids of equivalent size. To address this problem we have designed a tool which will split multiple grids of varying size into an arbitrary number of equivalently sized subgrids, so that the computational load will be balanced accross processors.

A preliminary GridSplit utility has been developed and demonstrated which provides a convenient means of splitting a single rectangular grid into several subgrids. Using this tool, execution times for 2 to 32 processors where analyzed. Our example decompositions which partition in 3 dimensions exhibit greater scalability than 2 dimensional decompositions.

In addition, the grid parallel version of FDL3DI has been used to study several important flow problems. In this report we discuss two applications which are used to study vortex break down which can lead to tail buffet and an application to study the flowfields surrounding a synthetic jet. These applications have all been executed on the IBM SP2 where they are running almost as fast or faster than the Cray C90. The GridSplit tool will enable such applications to more easily take advantage of the SP2 and similar systems.

Scalable Parallel Solution of the 3D Navier-Stokes Equations

Karen A. Tomko

1 Introduction

Despite progress in parallel compiler technology, parallel aeroscience applications are still primarily hand-crafted. This need for hand-crafting bars many computational scientist from utilizing the computational power of modern parallel systems. The objective of this project was to work in collaboration with the computational scientists in the CFD Research Branch of the Air Force Research Laboratory to develop tools and techniques which will allow them to take advantage of the computational potential offered by the IBM SP2, Cray/SGI Origin 2000, and CRAY/SGI T3E systems which have recently become available at the Aeronautical Systems Center (ASC) Major Shared Resource Center (MSRC) at Wright Patterson Air Force base and the other Major Shared Resource Centers.

Many research and industrial groups have parallelized their CFD applications using a variety of techniques on a variety of parallel machines. Two distinct approaches have emerged.

1. Partitioning the input domain into multiple overlapped grids and assigning one grid to a processor.
2. Solving the entire input domain as a single set of equations and parallelizing the equation solver.

Each approach has advantages and drawbacks. Approach 1. has two main strengths. Firstly, it is conceptually very simple and requires relatively little modification to the source code. Secondly, since only the interpolation points due to the overlap between grids must be communicated between processors, the amount of communication is kept small. This approach has been used to parallelize the FDL3DI application developed by the CFD research branch of the Air Force Research Lab [17]. FDL3D solves the three-dimensional Navier-Stokes equations using the approximate-factorization algorithm of Beam and Warming in conjunction with a newton subiteration procedure to enhance the accuracy for rapid fluid motion.

Load imbalance is the main disadvantage of a grid based parallel solution of the Navier-Stokes equations. Current grid generation programs create multiple grids based on the geometric constraints of a particular flow problem, and are not designed to generate grids for parallel processing. Thus, the grid generation programs make no attempt to generate grids of equivalent size, such that each processor will have an equal amount of computational work. Nor do they attempt to generate more grids than the geometric complexity of the flow problem requires in order to increase parallelism.

To address this problem we have designed a tool which will split multiple grids of varying size into an arbitrary number of equivalently sized subgrids, such that subgrids can be created which require the same amount of computational work. A preliminary implementation of his automatic decomposition tool, called GridSplit, has been developed. Using the GridSpit tool, we have decomposed a single grid problem into 8-32 subgrids in order to evaluate the scalability of the parallel FDL3DI on an IBM SP2 parallel system.

FDL3DI has been used by many scientist to compute a variety of unsteady, vortical flows. The

application is currently being used to study the aerodynamics of a full F-22 aircraft. The grid parallel version of FDL3DI described in this paper has been used to study several important flow problems. For example flow situations in which vortex break down can lead to tail buffet [11], [5] and the flowfields surrounding a synthetic jet [12] have been studied. All of these studies require large grid systems and the performance of the simulations benefit from the computational power and large memory capacities available on parallel systems such as the IBM SP2.

The rest of this report provides a more in depth discussion of the GridSplit tool and the performance of the parallel version of FDL3DI. Related research is presented in Section 2. A description of the parallelization approach is given in Section 3, the design and current implementation of GridSplit is described in Section 4. Section 5 gives experimental performance measures for the parallel FDL3DI application and is followed in Section 6 by some example fluid flow applications which utilize the grid parallel version of FDL3DI.

2 Related Work

Many research and industrial groups have parallelized their Navier-Stokes equation solvers for parallel machines. Due to the simplicity of the grid parallel method, several of these groups have used an approach similar to that used in the parallel Chimera version of FDL3DI for their multiple grid applications [1, 3, 13, 19].

An alternative approach is to parallelize the flow solver, which uses an *alternating-direction-implicit* (ADI) direct solution method. A multi-partition method for ADI solvers has been used in POVERFLOW, a parallel version of the NASA Overflow code [4, 15, 14], and FDL3DI [7]. A uni-partition method is used in [13] by Ryan and Weeratunga. Additionally, Ryan and Weeratunga use a hybrid or hierarchical approach, exploiting parallelism at both the grid level and at the solver level. Each grid is assigned some number of processors proportional to its size[13].

For implicit applications, some form of compensation code may be required to maintain numerical accuracy when grids are broken into subgrids for parallelization. Meakin [10] and Lutton and Visbal [9] discuss the numerical accuracy of Chimera (or overset) grid solutions for unsteady flows. Both agree that using Chimera grid methods can compute flow fields with acceptable accuracy. However, the timestep size may have to be reduced or the number of Newton subiterations increased as the number of subgrids is increased.

Many grid partitioning algorithms have been developed for unstructured grids requiring non-overlapped domains. Two software tools providing such algorithms are Chaco [6] and Metis [8]. Blake adapts unstructured grid techniques to overset (overlapped) grids for solution of the Euler equations as described in [2].

3 Grid Parallel FDL3DI

As reported in [17], a simple approach has been taken for parallelizing FDL3DI. Each input grid is assigned to a separate processor. The flow equations for each grid are solved independently in parallel

and the interpolated boundary values are also updated in parallel. The boundary data is exchanged between processors then, on each processor, the Chimera boundary conditions and the physical boundary conditions are applied to the assigned grid.

The Single Program Multiple Data (SPMD) parallel programming style is used. The code running on each processor is identical and the processor identification number is used to determine which grid is assigned to each processor. The MPI message passing library is used for interprocessor communication. Point-to-point communication using send and receive calls are used to exchange the Chimera boundary data between processors.

The parallel algorithm is sketched out below.

Algorithm 1 (Parallel FDL3DI) *Calculate, in parallel, the three-dimensional compressible Navier-Stokes equations with the implicit Beam-Warming algorithm using the Chimera method for overlapped grids. This algorithm runs simultaneously on each processor. Grids are assigned to processors by a mapping between processor id numbers and grid numbers.*

1. Initialize message passing system
2. Read in the program parameters file and the restart file (the entire restart file is read in redundantly on each processor.)
3. Determine which boundary data elements must be exchanged between processors
4. Increment the time step
5. For the grid assigned to this processor
 - (a) Perform initialization
 - (b) Solve flow equation for current grid
 - (c) Calculate flow values for interpolated Chimera boundary points
 - (d) Send flow values for interpolated Chimera boundary points to each processor requiring the data
 - (e) Wait until all Chimera boundary data are received from other processors
 - (f) Update flow values for Chimera boundaries with data from donor grids
 - (g) Apply physical boundary conditions to non-Chimera boundaries.
6. Repeat Step 5 for each newton subiteration
7. Repeat Steps 4 thru 6 for each timestep
8. Send final flow results for each grid to processor 0 for output
9. Output results to a new restart file

The overall runtime of parallel FDL3DI is dominated by the solution of the flow equations on the processor with the largest grid. This solution time is linear in grid size as shown in Figure 1. The grid

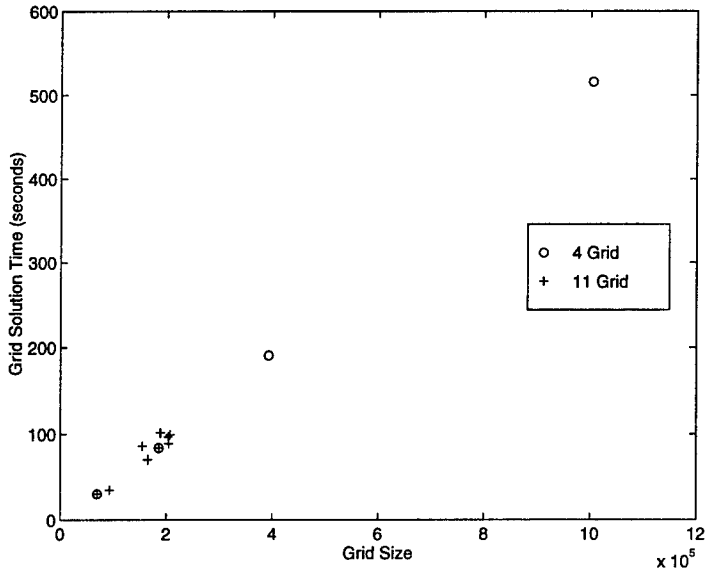


Figure 1: Time taken for solving flow equations on a single grid (NS3D subroutine) as a function of grid size.

size and solution time for the grids of two decompositions of a tail buffet simulation are diagrammed in the figure. The 4 Grid decomposition is based only on the geometric constraints of the problem, a delta wing and a flat plate, and contains one grid consisting of over 1 million grid points which comprises 60.7% of the total grid points. The 11 grid decomposition is a manual decomposition of the original 4 grid configuration which was implemented to increase parallelism and improve processor load balance. The largest grid of the 11 contains only 207 thousand grid points.

4 Automatic Grid Partitioning

The necessity for manual decomposition to improve processor load balance and increase the degree of parallelism is a severe limitation of the parallel FDL3DI application. To address this problem the author has designed a tool to automate the process of grid decomposition. The design and implementation were influenced by the FDL3DI application development environment.

When a computational scientist sets up a new flow problem, he or she goes through several steps.

1. Creation of the grid system for the simulation
2. Determination of interpolation stencils at overlapped boundaries. With FDL3DI, the PEGSUS software [16] which calculates stencils using trilinear interpolation is commonly employed.
3. Execution of the flow solver for some number of iterations.
4. Visualization of the output of the flow solver to aid in investigation of the flow features.

The last two steps are often repeated several times for the same grid configuration, thus the costs of grid generation and interpolation stencil generation are amortized. In addition, there are many variations of the FDL3DI flow solver, due to customizations inserted by individual scientists.

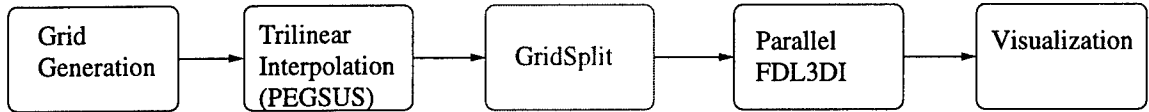


Figure 2: Application development process with incorporation of GridSplit

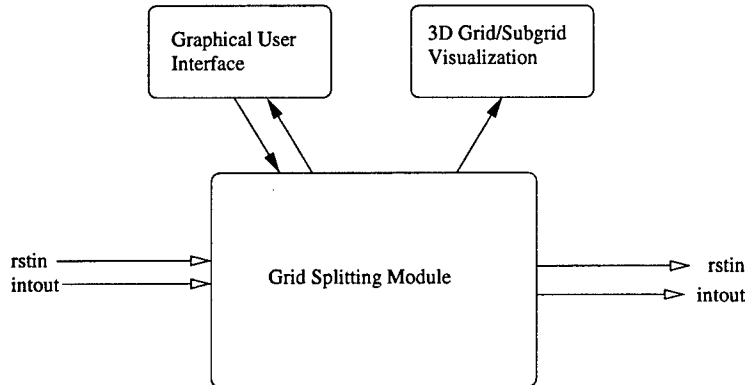


Figure 3: Highlevel Design of the GridSplit Application

The diagram in Figure 2 shows how the GridSplit application can be integrated into the FDL3DI development environment. GridSplit is an independent software tool which fits between PEGSUS and FDL3DI. The output of GridSplit is in the same format as the PEGSUS output thus FDL3DI runs exactly the same whether GridSplit is used or not, which makes it easy for the computational scientist to use GridSplit with his or her variation of the FDL3DI flow solver.

4.1 Design and Implementation

The GridSplit partitioning tool allows the user to cut a grid in as many locations in each dimension as desired. Planer cuts of 3-dimensional grids are supported. A diagram of the interface for GridSplit is given in Figure 3.

GridSplit functions as follows. A user provides the name of the PEGSUS interpolation data file (referred to as *intout* in Figure 3) and the name of a restart file containing the grid configuration and initial flow conditions (referred to as *rstin* in Figure 3). The user inputs the initial grid dimension and the number and location of cuts in each dimension of the grid. This input can be done via a graphical user interface but is done via a text file in the current implementation. GridSplit, calculates the starting and ending indices in each dimension for the subgrids, determines the overlap regions between subgrids and generates a listing of boundary and interpolation points for all of the new subgrid boundaries. It produces a new restart file *rstout* consisting of the x,y,z coordinates and flow variables for each subgrid and an *intout* file containing the subgrid boundary information which is compatible with the PEGSUS generated *intout* file. The new subgrids can be viewed using the FAST visualizations software, by converting the new *rstin* file into FAST format as is currently done for the restart file produced as output of the flow solver.

The current GridSplit implementation splits a single input grid into several subgrids, and is being extended to support multiple input grids. The algorithm is outlined below.

Algorithm 2 (GridSplit) *Split a single rectangular grid into several subgrids.*

1. *Read grid size and location for splitting from parameter file*
2. *Determine number of subgrids*
3. *For each subgrid*
 - *determine dimensions*
 - *store interpolation points into hash table*
4. *For each subgrid*
 - *determine boundary points for inter-subgrid boundary*
 - *for each boundary point find corresponding interpolation point in the hash table and identify donor subgrid*
5. *For each subgrid*
 - *create list of interpolation points that will be supplied to other grids.*
6. *Read original rstin file*
7. *Write the new rstin file*
8. *Write the new intout file*

As described above the user specifies a dimension and location at which the grid should be split. Figure 4 gives a 2-dimensional example with the grid split in the J dimension at index 10. The subgrids have an overlap of 5 with subgrid A extending from index 1 to index 12 of the original grid and subgrid B extending from index 8 to index 19 of the original grid. Consider subgrid A. It has two types of boundaries, the boundaries at I=1, I=15 and J=1 which are boundaries in the original grid, and the new boundary at J=12. The original boundaries can be handled by applying the physical boundary conditions used in the original single grid problem. The new boundary is handled as a chimera boundary with the values for columns J=11 and J=12 supplied from subgrid B. Likewise, subgrid A, supplies the values from its J=8 and J=9 columns for subgrid B's boundary points. This is similar to the way in which PEGSUS handles overlapped grids but is simpler since the subgrids produced by GridSplit will always contain overlapped points that are coincident, hence no interpolation of values is necessary.

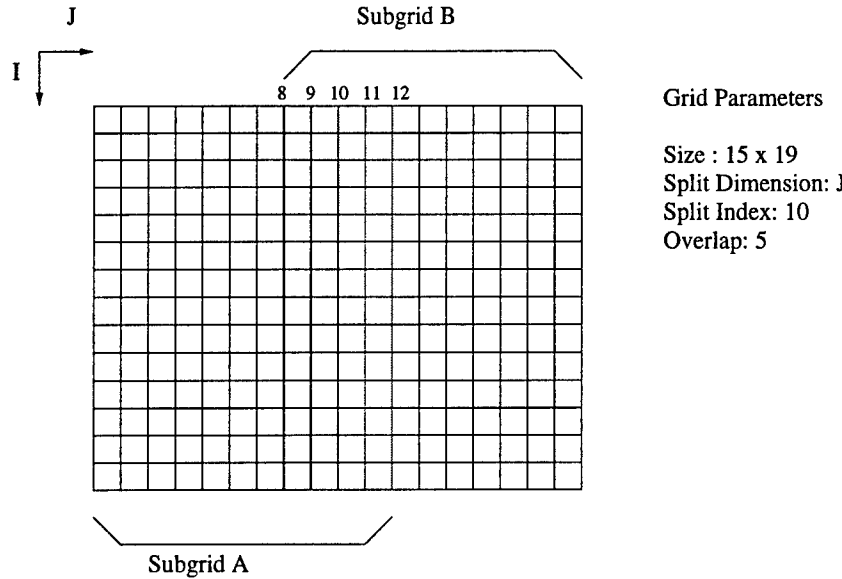


Figure 4: An example 2D grid split at $J=10$, with an overlap of 5

5 Parallel Performance

GridSplit was used to split a one million point grid with dimensions $100 \times 100 \times 100$ into 2, 4, 8, 16 and 32 subgrids. Two types of decomposition were performed 1) 2-Dimensional decompositions in which only the J and K dimensions are split and 2) 3-Dimensional decompositions in which I, J and K dimensions are split. The grid sizes and execution times for the various decompositions are given in Table 1 and Figure 5 respectively.

The 3-dimensional decomposition scale better as the number of processors is increased as can be seen in Figure 5. The reason the 3D decompositions perform better is because the size of the overlapped boundaries is smaller when partitioning in all 3 dimensions. As a result both the maximum grid size for a given number of processors is less and the size of the inter-subgrid boundaries are less resulting in fewer

Number of Grids	2D or 3D Decomposition	IDIM	JDIM	KDIM	Largest Subgrid	Boundary Points ¹
2	2D	100	53	100	530000	19208 (3.6%)
4	2D	100	53	53	280900	19992 (7.1%)
8	2D	100	29	53	153700	25284 (16.5%)
16	2D	100	29	29	84100	21168 (25.1%)
32	2D	100	17	29	49300	16464 (33.3%)
8	3D	53	53	53	148877	15608 (10.4%)
16	3D	53	53	29	81461	15916 (19.5%)
32	3D	53	29	29	44573	12482 (28.0%)

Table 1: Grid Dimensions for Automatically generated grids

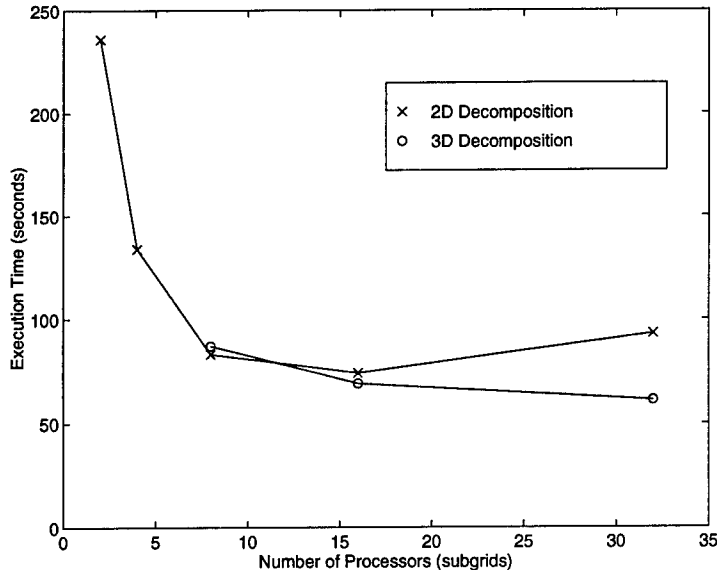


Figure 5: Execution time for a single rectangular grid, decomposed into a varying number of subgrids.

data to be exchanged between processors. For example, compare the 16 processor 2D decomposition with the 16 processor 3D decomposition in Table 1. In the 2D case the maximum grid size is 84100 points while the largest grid for the 3D case is 81461 points, 3% smaller. In addition upto 25% of the points for a 2D subgrid are boundary points and require inter-processor communication, while less than 20% of the points for a 3D subgrid are boundary points.

While the 3D results are encouraging, still little is gained in increasing the number of processors from 16 to 32. Some quick estimates for an 8 million point grid indicate that larger initial grids should scale better. Consider splitting an 8 million point grid with dimensions $200 \times 200 \times 200$ into 32 subgrids. The largest subgrid will have dimensions $103 \times 103 \times 53$ and contain 562,277 points. The subgrid boundary (2 planes for each face) will be at most 101,828 points which is 18% of the subgrid size, comparable to the boundary of the 16 process decomposition on the 1 million grid point example. Such large grids are expected for study of the flow problems described in the next section.

6 Example Flow Problems

Over the last six months, the CFD Research Branch of the Air Force Research Laboratory has started using the grid parallel FDL3DI application for the study of several interesting problems. Brief descriptions of three flow problems are given below. All three utilize or need to utilize a large number of grid points and thus require large amounts of both CPU time and memory.

Numerical Simulation of the Interaction Between a Leading-Edge Vortex and a Flexible Vertical Tail: A 17 grid parallel simulation for aeroelastic analysis of the interaction between a leading-edge vortex and a flexible vertical tail has been used to study vortex breakdown and tail buffet. The

Computer System	Number of Grids	Number of Processors	Execution Time (minutes)	Parallel Speedup
Cray C916	4	1	90	-
IBM SP2	4	1	888	1
IBM SP2	4	4	498	1.8
IBM SP2	11	11	105	8.4

Table 2: A Comparison of Execution Times for the Impingement of a Streamwise Vortex on a Plate

computations are for a delta wing model and a flexible vertical tail having characteristics similar to an F-15 fighter aircraft [11].

The original grid system based only on geometric constraints contained 436,841 grid points. After decomposing into 17 grids the total number of grid points is 543,201, with the largest grid comprising 44,604 points. The simulation has primarily been run on the IBM SP2, but has also been run on the CRAY C90. The simulation runs approximately 2.5 times faster when executed on 17 processors of the IBM SP2 than on the C90.

In addition to this 17 grid model a fine grid model employing 52 grids ranging in size from 68,040 to 95,779 points for a total of 4,547,813 grid points is currently under development. This simulation will be run entirely on the IBM SP2.

Numerical Simulation of the Impingement of a Streamwise Vortex on a Plate: The parallel implementation of the numerical simulation of the impingement of a streamwise vortex on a plate, was developed based on the vectorized version of the simulation which utilizes the sequential FDL3DI application on a Cray C916 system [5]. The simulation model consisted of a delta wing that generated a vortex which subsequently impinged on a thin plate placed downstream of the delta wing. A Chimera grid approach in which separate overlapping grids are used for the delta wing and plate has been used for these computations. Four grids, totaling to 1.65 million grid points, were initially employed for this simulation.

This initial 4 grid configuration, provides very poor load balancing for a parallel implementation. To improve the parallel efficiency, Raymond Gordnier, manually decomposed the 4 grid configuration into an 11 grid configuration. The delta wing grid was split into grids 7 grids and the O grid surrounding the flat plate was split into two grids in the 11 grid configuration. The other grids remained unchanged between the two configurations. While still not perfectly balanced the 11 grid configuration can potentially achieve a speedup of 8.0 over the serial 4 grid version when executed on 11 processors. A comparison of run times for the configurations described above are given in Table 2. For additional information on the parallel runs see [18].

Numerical Investigation of Synthetic Jet Flowfields: A preliminary investigation of the flowfields surrounding a synthetic jet was undertaken with a 2D model using a parallel flow solver based on the FDL3DI application. The synthetic jet application uses a 2nd order accurate time-marching scheme and an upwind algorithm for spatial discretization. The 3 original Chimera (overset) grids for the 2D

model contained 288 thousand, 79 thousand and 668 thousand grid points respectively and were manually subdivided into 14 grids. The model was executed on both a Cray/SGI C90 and an IBM SP2

A 3D simulation of a synthetic jet is under development. It is expected to employ 6 to 7 million grid points and be comprised of approximately 30 subgrids. Due to the simplicity of the geometry, rectangular grids can be used to model the jet actuator configuration. With the large number of required subgrids and a simple geometry, this application can easily take advantage of a tool such as GridSplit to aid in the parallelization.

7 Conclusion and Future Work

In this report we have demonstrated that the grid parallel FDL3DI application which solves the 3D Navier-Stokes Equations can be used to solve large fluid flow simulations on parallel systems such as the IBM SP2. Three example applications which use this code have been described and are running almost as fast or faster than on the Cray C90. Applications such as those just described could more easily take advantage of parallel systems with tools such as GridSplit to support automatic grid decomposition.

A preliminary GridSplit utility has been developed and demonstrated which provides a convenient means of splitting a single rectangular grid into several subgrids. Using this tool, execution times for 2 to 32 processors were analyzed. Our example decompositions which partition in 3 dimensions exhibit greater scalability than 2 dimensional decompositions. Additional scalability tests on a variety of grid sizes and a larger number of processors are required for a more complete view of the scalability of the application.

The current implementation of the GridSplit tool supports only rectangular grids. Support for O grids, C grids, H-H grids and possibly others needs to be incorporated to make it generally useful. It also must allow for multiple overset grids as input. Additionally a more convenient graphical user interface should be supplied which provides the ability to display subgrids and modify cut locations as necessary.

8 Acknowledgements

Thanks to Miguel Visbal and the members of the CFD research branch for their many discussions on fluid flow applications, overset grid methods and the HPC programming environment.

Computational resources for the work presented here were supported in part by a grant of HPC time from the DOD HPC Major Shared Resource Center, ASC, Wright-Patterson Air Force Base, Ohio. Additional computer resources were provided by the Ohio Super Computer Center, Columbus OH.

References

- [1] David Bailey, Tim Harris, William Saphir, Rob van der Wijngaart, Alex Woo, and Maurice Yarrow. The NAS parallel benchmarks 2.0. Technical Report NAS-95-020, NASA Ames Research Center, December 1995.
- [2] Douglas C. Blake. Application of unstructured grid domain decomposition techniques to overset grids. In *Eighth SIAM Conference on Parallel Processing for Scientific Computing*, March 1997.
- [3] Rob F. Van der Wijngaart. Efficient implementation of a 3-dimensional adi method on the iPSC/860. In *Proceedings of Supercomputing '93*, November 1993.
- [4] Rob F. Van der Wijngaart and Maurice Yarrow. RANS-MP: A portable parallel navier stokes solver. In *Computationl Aerosciences Workshop, NASA Ames Research Center*, August 1996.
- [5] Raymond E. Gordnier and Miguel R. Visbal. Numerical simulation of the impingement of a streamwise vortex on a plate. *AIAA Paper 97-1781*, June 1997.
- [6] Bruce Hendrickson and Robert Leland. The Chaco user's guide: Version 2.0. Technical Report SAND94-2692, Sandia National Laboratories, Albuquerque, NM, July 1995.
- [7] David Hudak. A study of a data-parallel implementation of an implicit solution of the 3D Navier-Stokes equations. Technical Report AFOSR Summer Faculty Research Program Final Report, Air Force Office of Scientific Research, 1997.
- [8] George Karypis and Vipin Kumar. METIS unstructured graph partitioning and sparse matrix ordering system, version 2.0. Technical report, Dept. Computer Science, University of Minnesota, August 1995.
- [9] Mark J. Lutton and Miguel R. Visbal. Time-accurate validation of the Chimera method for unsteady vortical flows. *AIAA Paper 96-2077*, June 1996.
- [10] Robert L. Meakin. On the spatial and temporal accuracy of overset grid methods for moving body problems. *AIAA Paper 94-1925*, June 1994.
- [11] Scott A. Morton, Donald P. Rizzetta, and Reid B. Melville. Numerical simulation of the interaction between a leading-edge vortex and a flexible vertical tail. *AIAA Paper (to Appear)*, January 1998.
- [12] Donald P. Rizzetta and Michael J. Stanek. Numerical investigation of synthetic jet flowfields, December 1997. Personal Communication.
- [13] J.S. Ryan and S.K. Weeratunga. Parallel computation of 3-D navier-stokes flowfields for supersonic vehicles. *AIAA Paper 93-0064*, January 1993.
- [14] Merritt H. Smith and Rob F. Van der Wijngaart. Granularity and the parallel efficiency of flow solution on distributed computer systems. *AIAA Paper 94-2260*, June 1994.
- [15] Merritt H. Smith, Rob F. Van der Wijngaart, and Maurice Yarrow. Improved multi-partition method for line-based iteration schemes. In *Computationl Aerosciences Workshop, NASA Ames Research Center*, March 1995.
- [16] N. Suhs and R. Tramel. *PEGSUS 4.0 User's Manual*. Arnold Engineering Development Center, Arnold AFB, TN, June 1991. AEDC-TR-91-8.
- [17] Karen A. Tomko. Grid level parallelization of an implicit solution of the 3D Navier-Stokes equations. Technical Report AFOSR Summer Faculty Research Program Final Report, Air Force Office of Scientific Research, 1996.

- [18] Karen A. Tomko. Grid level parallelization of an implicit solution of the 3D Navier-Stokes equations. Technical Report AFOSR Summer Faculty Research Program Final Report, Air Force Office of Scientific Research, 1997.
- [19] Jerry C. Yan, Dennis Jespersen, and Pieter Buning. Performance evaluation of OVERFLOW/PVM on a network of workstations. In *Computational Aerosciences Workshop, NASA Ames Research Center*, August 1996.

A COMPUTATIONAL METHOD FOR DETERMINING STEADY FLOW SEPARATION AND
STREAM TUBE CONTRACTION EFFECTS IN TURBOMACHINERY BLADE ROWS FOR
USE IN A FORCED RESPONSE PREDICTION SYSTEM

Andrew G. Szmerekovsky
Graduate Student

J. Mitch Wolff
Assistant Professor

Department of Mechanical and Materials Engineering

Wright State University
3640 Colonel Glenn Hwy.
Dayton, Ohio 45435-0001
Ph: (937) 775-5141
Fax: (937) 775-5009

Final Report for:
Summer Research Extension Program

Sponsored by:
Air Force Office of Scientific Research
Bolling Air Force Base, DC

March 1999

A COMPUTATIONAL METHOD FOR DETERMINING STEADY FLOW SEPARATION AND
STREAM TUBE CONTRACTION EFFECTS IN TURBOMACHINERY BLADE ROWS FOR
USE IN A FORCED RESPONSE PREDICTION SYSTEM

Andrew G. Szmerekovsky
Graduate Student

J. Mitch Wolff
Assistant Professor

Department of Mechanical and Materials Engineering
Wright State University

Abstract

This research project aerodynamically expands the Steady FLOW model (SFLOW) to include viscous and stream tube contraction effects. The viscous effects are incorporated for strong inviscid/viscous interactions. In particular, for off-design operating conditions strong viscous effects such as flow separation are important. The viscous effects are modeled using Prandtl's boundary layer equations solved by a finite difference method coupled with the inviscid model in both a direct and inverse manner. The enhanced steady aerodynamic model is then applied to a high-speed low aspect ratio rotor row for which experimental data is available. Analyses of other advanced design cascades are also conducted. Comparisons between experimental and computational results are made. The effects of viscosity and stream tube contraction is demonstrated. The steady potential inviscid/viscous interaction model is modified to include stream tube contraction effects. Though not demonstrated here, the enhanced analysis may be incorporated within an existing Forced REsponse Prediction System (FREPS) structure to investigate the significant effects of separated flow and stream tube contraction on the prediction of turbomachinery blade forced response.

Introduction

The prediction of the steady aerodynamic loading on two full-scale high-speed turbomachinery experimental configurations at the Air Force Research Lab (AFRL) Wright Laboratories Propulsion Directorate is given. The Steady FLOW (SFLOW) model was enhanced to include both viscous and streamtube contraction effects. The details of the mathematical formulation are given in the Master's thesis of Andrew Szmerekovosky [1]. In addition, several validation cases were analyzed to demonstrate the successful implementation of the model enhancements.

4.1 Advanced Damping for Low Aspect Ratio Fan (ADLARF) Rotor

4.1.1 ADLARF Experimental Configuration

ADLARF is a low aspect ratio fan rotor blade configuration described by Minkiewicz and Russler [2] and by Manwaring et al. [3]. The measurements for experiment were obtained in the Compressor Research Facility (CRF) of the Air Force Research Laboratory (AFRL) at Wright-Patterson AFB, Ohio.

The ADLARF configuration is a two-stage transonic compressor fan. The first stage consists of 16 low aspect ratio blades. The compressor was designed for high axial flow, which gives transonic conditions in the outer half of the first-stage rotor. Data was obtained at a low operating line (LOL) and nominal operating line (NOL), or design condition. Minkiewicz and Russler presented the NOL data in their paper. The purpose of this experimental rig was to advance the knowledge of the unsteady aerodynamics associated with a low-aspect ratio transonic fan where flow defects are generated by inlet distortions. Blade vibrations caused by the inlet distortions were measured using strain gauges located at the trailing edge root on the suction side, midspan on the trailing edge suction side, and midspan on the leading edge pressure side. Dynamic pressure transducers measured the unsteady pressure difference across the rotor blade at 85 per cent span. Figure 4.1 shows the ADLARF test rig.

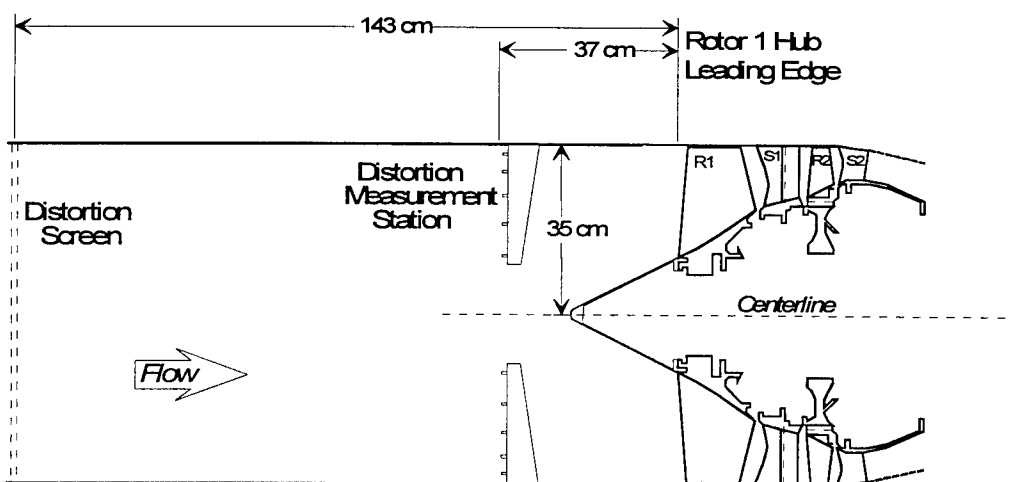


Figure 4.1 ADLARF Test Rig

4.1.2 ADLARF Flow Conditions

To simulate inlet distortions, screens of three (3/rev) and eight (8/rev) pressure distortions were used. Predicted resonance crossings for both 3/rev and 8/rev distortions were as follows: at 3/rev - first flex (1F) at 62% of design speed, and at 8/rev - second flex/first torsion (2F/1T) at 68% of design speed and a two stripe (2S) at 98% of design speed. Data from this experiment was collected at rotor speeds of 8100 RPM and 9100 RPM and an acceleration from 8100 to 9100 RPM for the 3/rev (1F) case. Figure 4.2 shows the Campbell diagram of the 1F-3/rev crossing. Note that resonance occurs near 8700 RPM.

The objective of this numerical analysis is to obtain aerodynamic steady flow field results for incorporation into a forced response prediction system. Since the experimental data available for the forced response of the ADLARF blades consists of a test run starting at 8100 RPM and then increasing up to 9100 RPM, computational SFLOW 1.7-IVI results were attempted for both the low (8100) and the high (9100) wheel speeds. See Appendix A for flow condition calculations and ADLARF SFLOW input parameters.

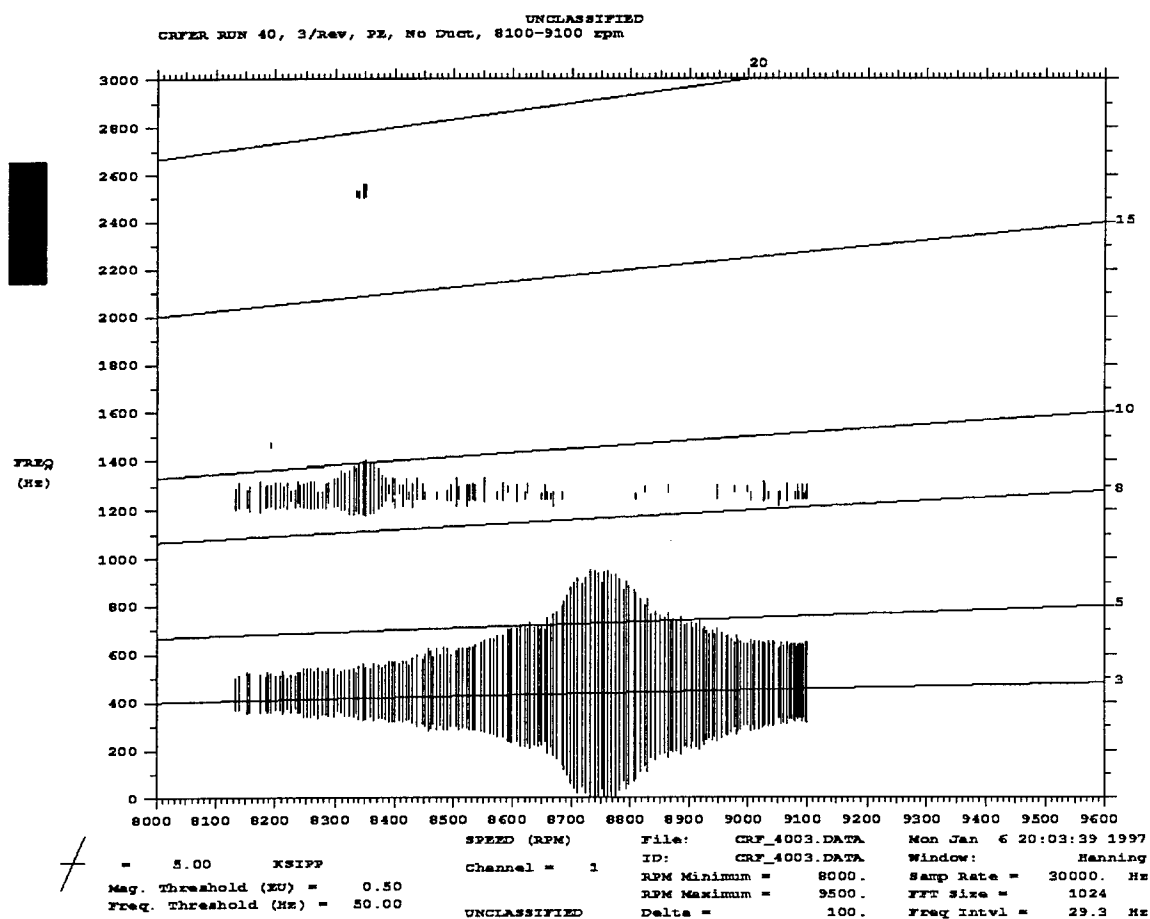


Figure 4.2 Campbell Diagram of 3/rev Crossing

Figures 4.3 through 4.9 show cross sections of the rotor blade at various spans. These geometries were obtained from the MSC/NASTRAN files used for structural analysis of the ADLARF blade. FREPS (see Appendix C) uses a strip theory approach to incorporate steady and unsteady

aerodynamic analyses (from SFLOW and LINFLO, respectively) with structural analysis from MSC/NASTRAN to perform a quasi-three dimensional aeroelastic analysis. Since the structural analysis was accomplished at these spans (Figs 4.3 through 4.9), the SFLOW and LINFLO analyses must also be accomplished at these spans. Therefore, the aerodynamic analysis will be consistent with the structural analysis. Since our objective is to predict the forced response of the ADLARF rotor blade to unsteady excitations, we used the cross sections provided from the structural analysis for our steady aerodynamic analysis. Our inlet Mach number was chosen by analyzing the flow conditions at the low (8100 RPM) and high (9100 RPM) speeds of the test run (see Appendix A). Numerical steady aerodynamic data from SFLOW will then be utilized by the unsteady aerodynamic analysis in LINFLO. Once this is accomplished, the results can be combined with the MSC/NASTRAN analysis and a FREPS aeroelastic analysis performed for the 3/rev case.

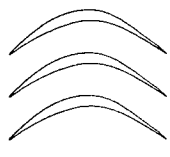


Figure 4.3 15% Span

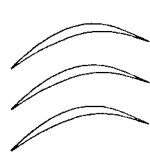


Figure 4.4 30% Span



Figure 4.5 45% Span



Figure 4.6 60% Span



Figure 4.7 75% Span



Figure 4.8 85% Span



Figure 4.9 100% Span

4.1.3 Computational Results

The SFLOW 1.7-IVI results are now shown. Verification of these results will come when the steady data is incorporated into the forced response prediction system (FREPS, see Appendix C) and compared with experimental stress data. These results will be incorporated with an unsteady

aerodynamic analysis (LINFLO) to computationally determine the forced response of the ADLARF rotor to a 3/rev (first flex) unsteady aerodynamic excitation in a later project.

We were able to obtain converged IVI results up to the 45% span, and inviscid results up to the 8100 RPM case for all spans. These results are presented below.

4.1.3.1 15% Span

15% span results for 8100 RPM are shown in Figures 4.10 through 4.13. Appendix A shows the calculations that led to the inputs for the SFLOW 1.7-IVI input file.

Starting with Figure 4.10, we note from the shear stress plot that no separation is predicted for the 15% span, although the flow comes close to separating around midchord on the pressure surface and at the trailing edge on the suction surface. Note there is also a corresponding increase in displacement thickness (Fig. 4.11) as the shear stress approaches zero. Mach number (Fig. 4.12) and surface pressure (Fig. 4.13) plots show that the IVI solution and inviscid solution are different everywhere except the 60-70% region of the pressure surface. On the airfoil surface prior to midchord, the IVI solution predicts lower speeds than the purely inviscid solution. On the latter half of the airfoil surfaces, the IVI prediction is a bit higher (by about 10% higher). With a relative chordal incidence angle of around 50° , if we account for camber, the angle of incidence is actually only 11° . Recall Figure 4.3, the lower surface is the pressure surface and the upper surface is suction. At a relative inlet Mach number of 0.5, the Re number is sufficiently high, 2.07×10^6 , that the flow remains attached to the surface.

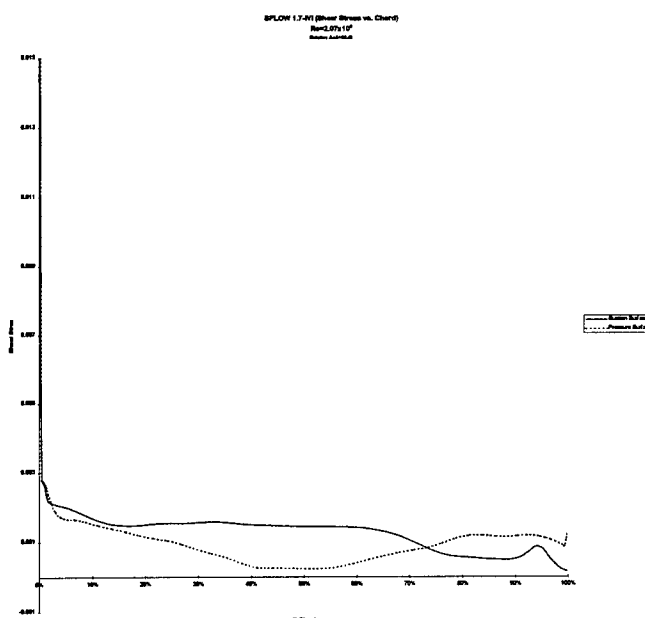


Figure 4.10 15% Span 8100 RPM Shear Stress Plot

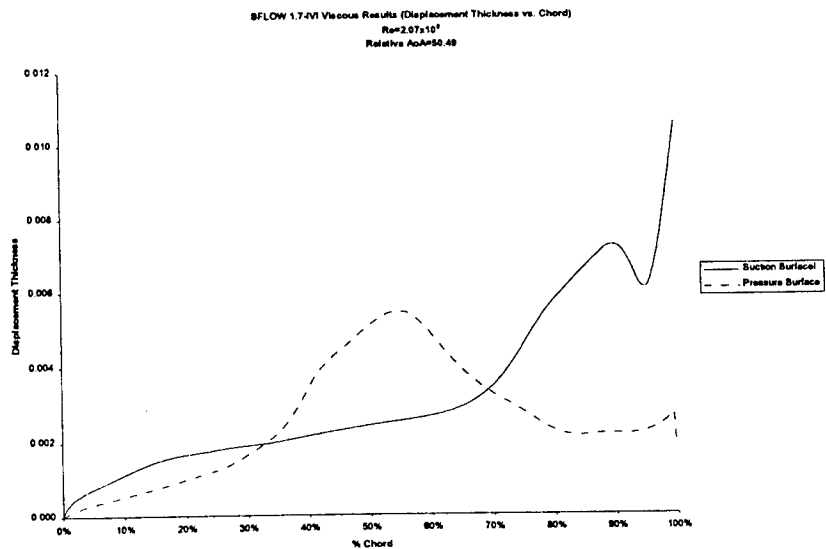


Figure 4.11 15% Span 8100 RPM Displacement Thickness Plot

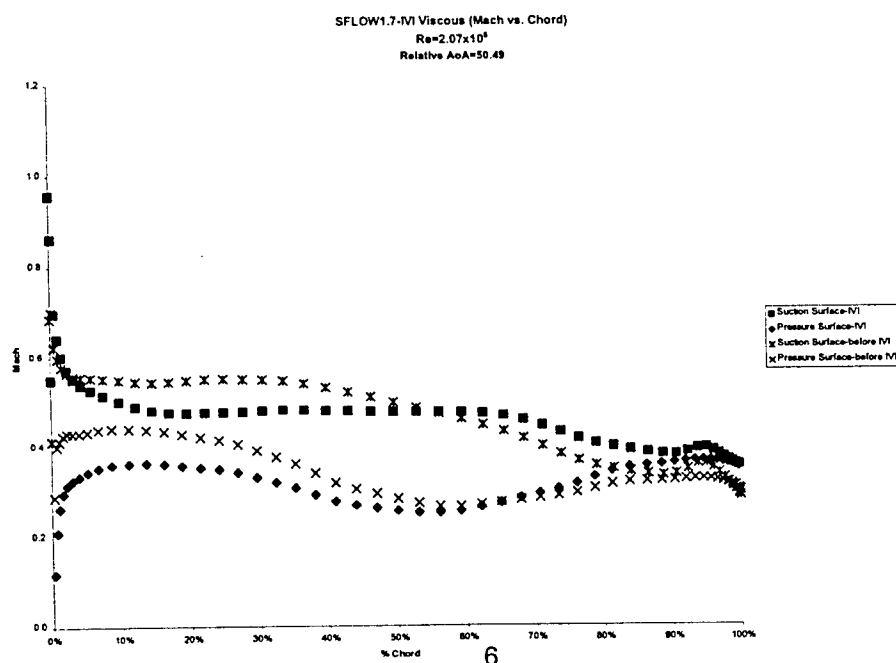


Figure 4.12 15% Span 8100 RPM Surface Mach Number Plot

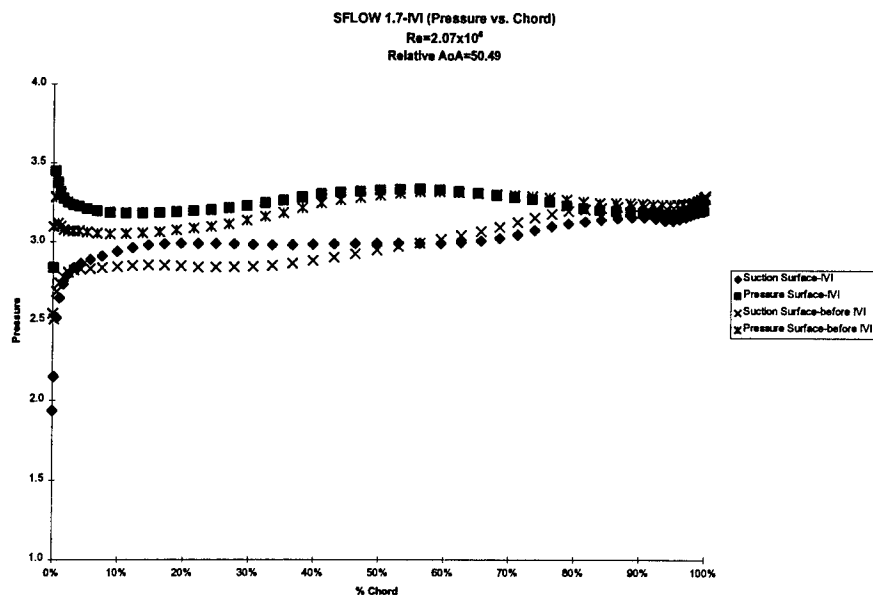


Figure 4.13 15% Span 8100 RPM Surface Pressure Plot

We can compare this solution to the results for 9100 RPM in Figures 4.14 through 4.17.

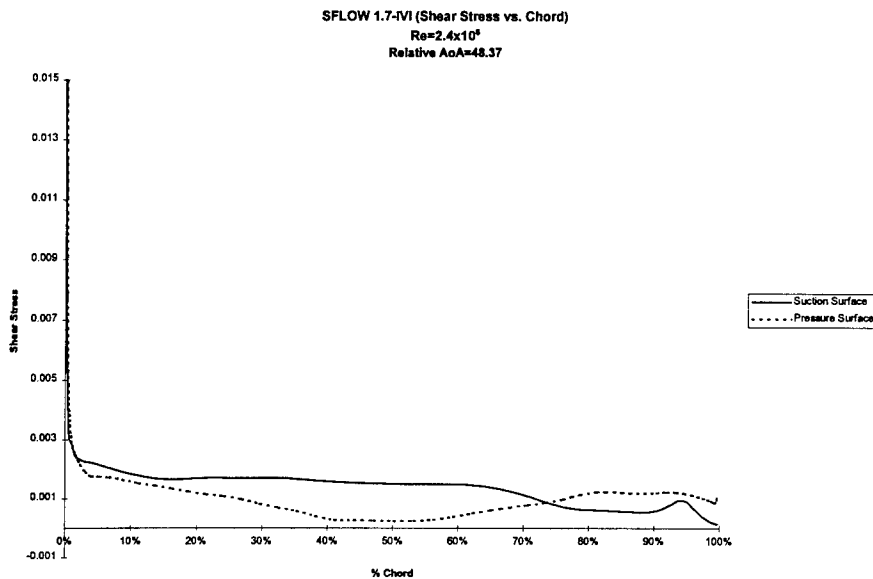


Figure 4.14 15% Span 9100 RPM Shear Stress Plot

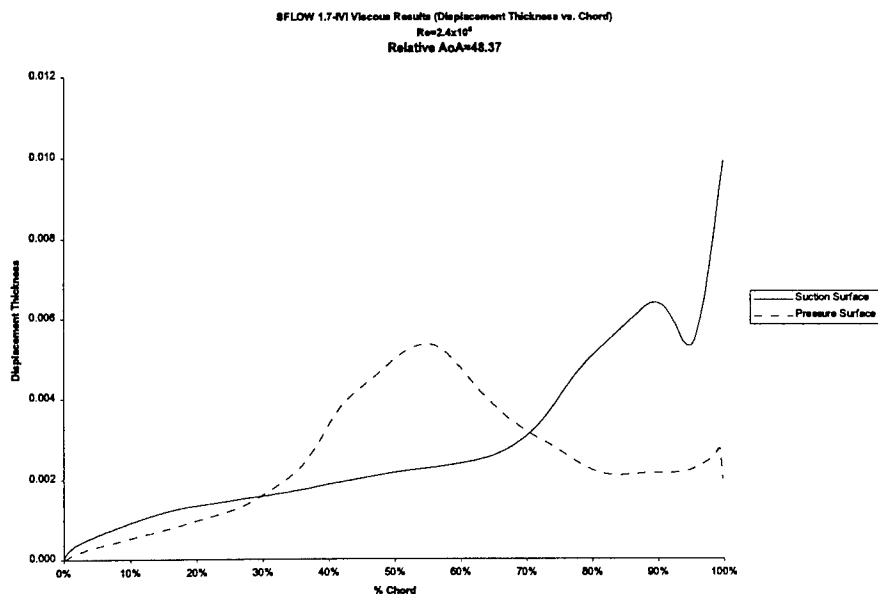


Figure 4.15 15% Span 9100 RPM Displacement Thickness Plot

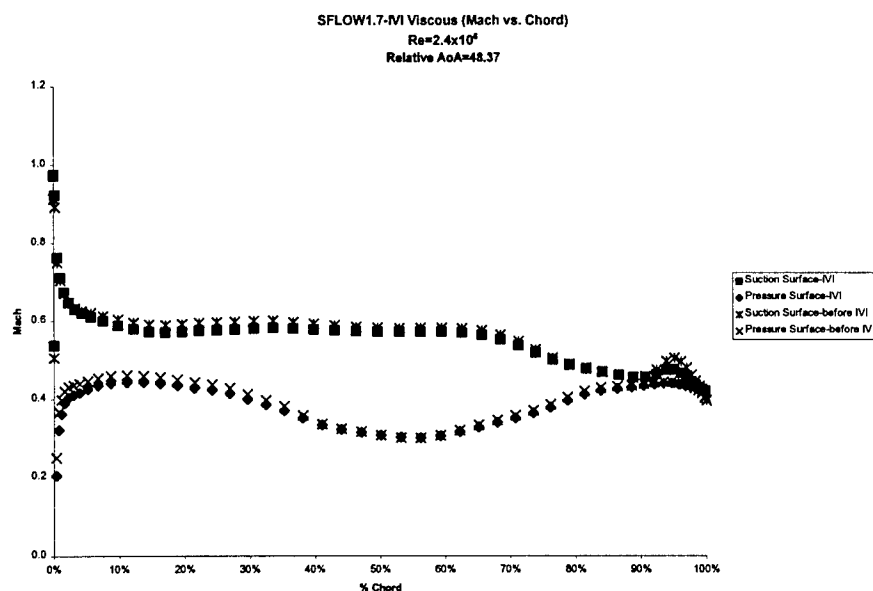


Figure 4.16 15% Span 9100 RPM Surface Mach Number Plot

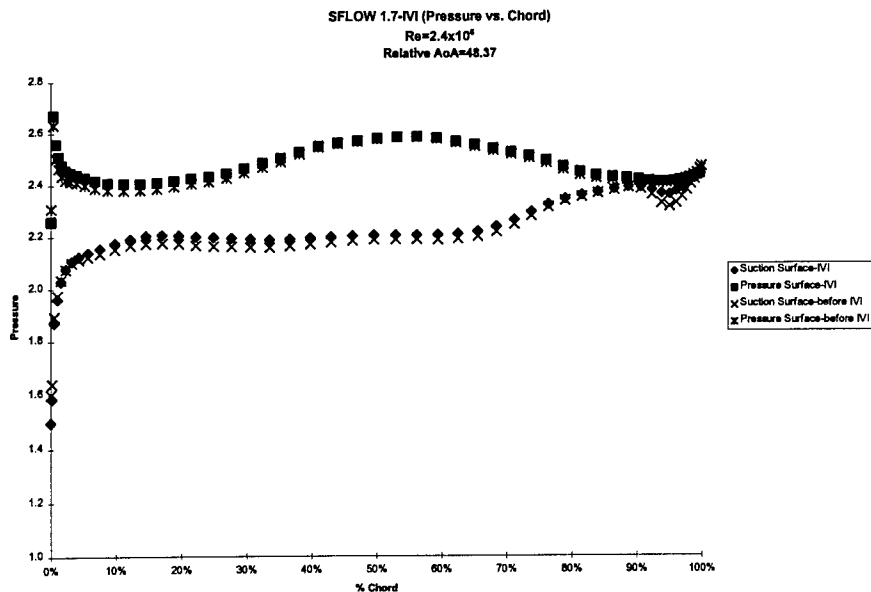


Figure 4.17 15% Span 9100 RPM Surface Pressure Plot

From the shear stress plot (Fig. 4.14), there is no separated flow predicted for the 15% span. The Re number is high enough (2.4×10^6), and the incidence angle including camber is low enough (9°) that the flow stays attached to the airfoil surface. The displacement thickness and shear stress plots for 8100 RPM and 9100 RPM are very similar. This is reasonable since the Reynolds number and incidence angle for both are relatively the same at each wheel speed. There is also a greater difference between the inviscid solution and the IVI solution for the 8100 RPM case. At 9100 RPM, the inviscid and IVI solutions are quite comparable to one another. This too, is reasonable, as we expect the flow at higher Re number and lower AOI to closely resemble inviscid flow. There are no appreciable differences between the inviscid and IVI results at 9100 RPM, except for the slightly higher surface pressure predicted on the suction surface at 95% chord by the IVI procedure.

4.1.3.2 30% Span

Figures 4.18 through 4.25 display the results for the 30% spanwise ADLARF cross-section at 8100 RPM and 9100 RPM.

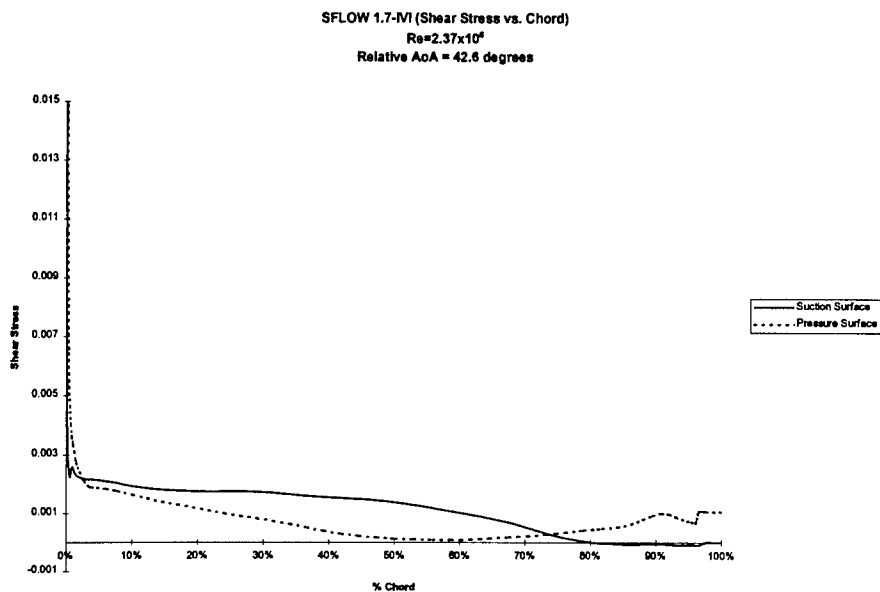


Figure 4.18 30% Span 8100 RPM Shear Stress Plot

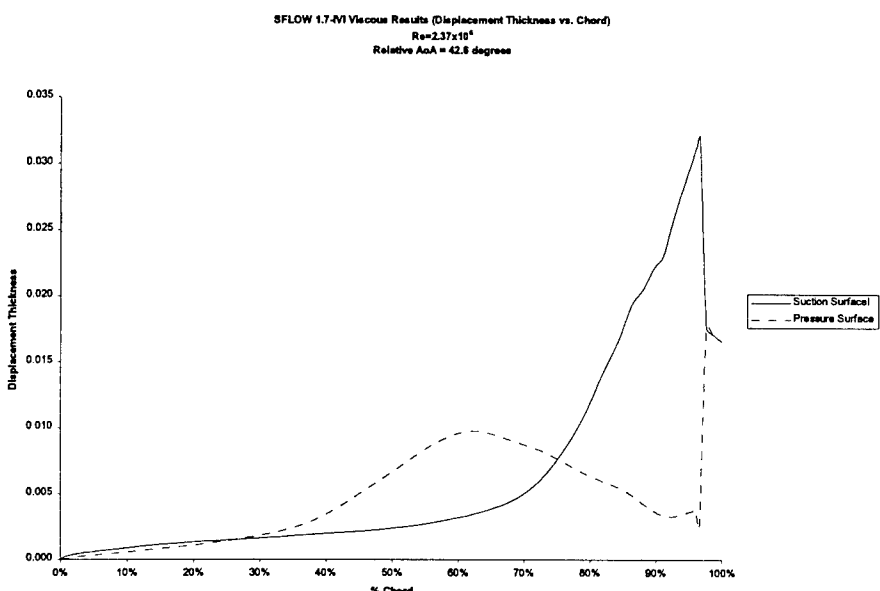


Figure 4.19 30% Span 8100 RPM Displacement Thickness Plot

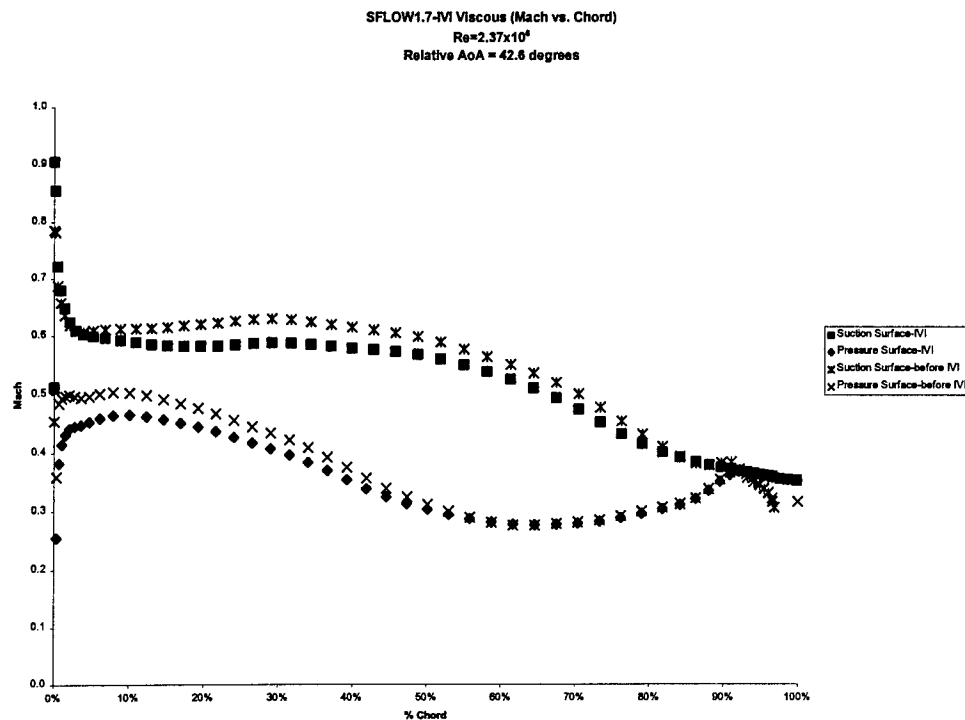


Figure 4.20 30% Span 8100 RPM Surface Mach Number Plot

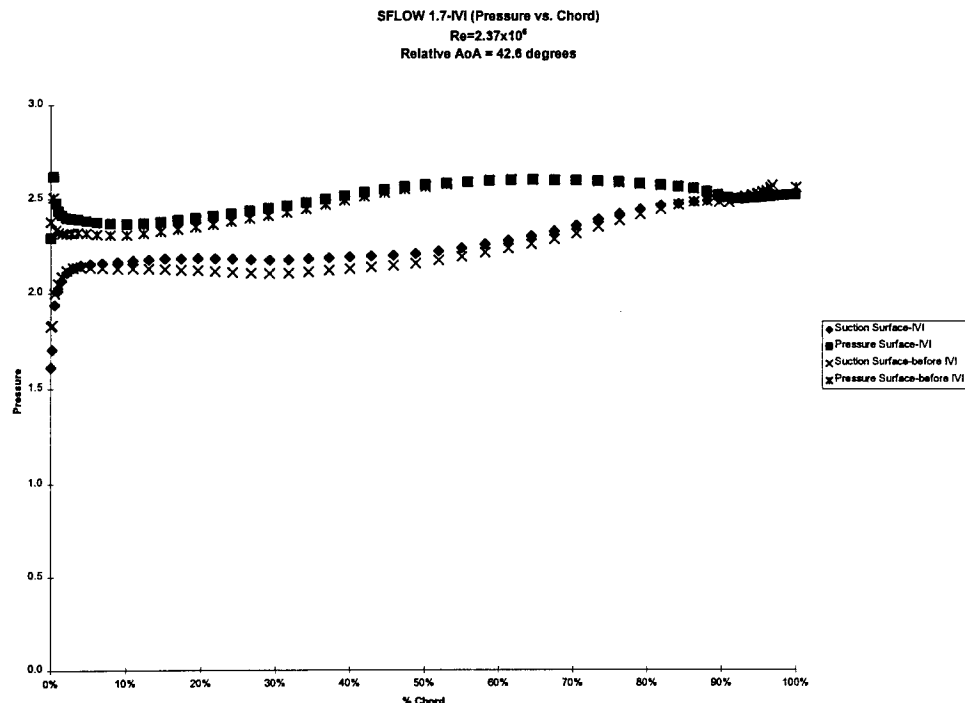


Figure 4.21 30% Span 8100 RPM Surface Pressure Plot

Separation occurs at 80% chord on the suction surface at 8100 RPM as shown in Fig. 4.18. This corresponds to the sharp rise in displacement thickness (Fig 4.19) that actually starts at 70% chord. The Mach number and pressure plots, Figs. 4.20 and 4.21 respectively, illustrate again how close the inviscid and IVI solutions are, except at the trailing edge. The trailing edge was modified in order to make it a sharp wedge for the Kutta condition. This change in geometry is reflected in the inviscid solution by an artifact that looks like a "hook." The IVI solution at the trailing edge, in contrast, smoothly approaches the wedge-shaped trailing edge. This is due to the separation that occurs at 80% chord and causes a wake, which is reflected by a smooth, straight line for the surface Mach number and pressure distribution. Note, the same type plots at 15% span mirror the inviscid "hook" at the trailing edge, but no flow separation is predicted. The high Reynolds number and low incidence angle (12.6°) at 30% span minimize the area of flow separation, but do not prevent it totally. The small area of flow separation on the suction surface near the trailing edge is caused by adverse pressure gradients that are a result of the slightly higher incidence angle for this span.

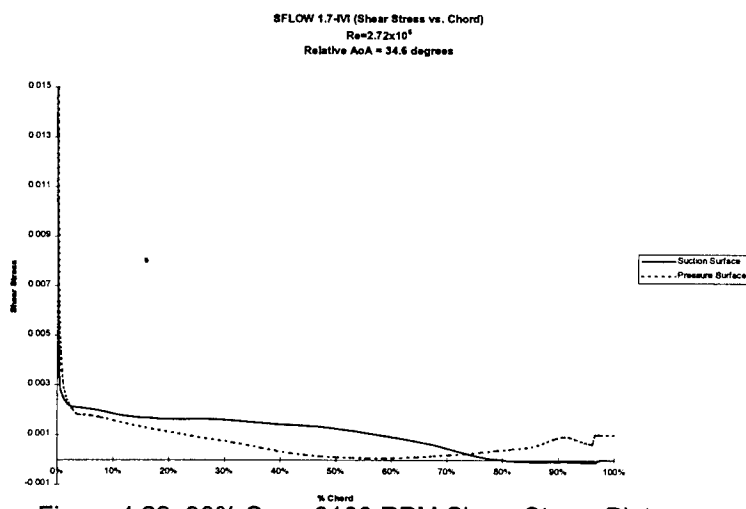


Figure 4.22 30% Span 9100 RPM Shear Stress Plot

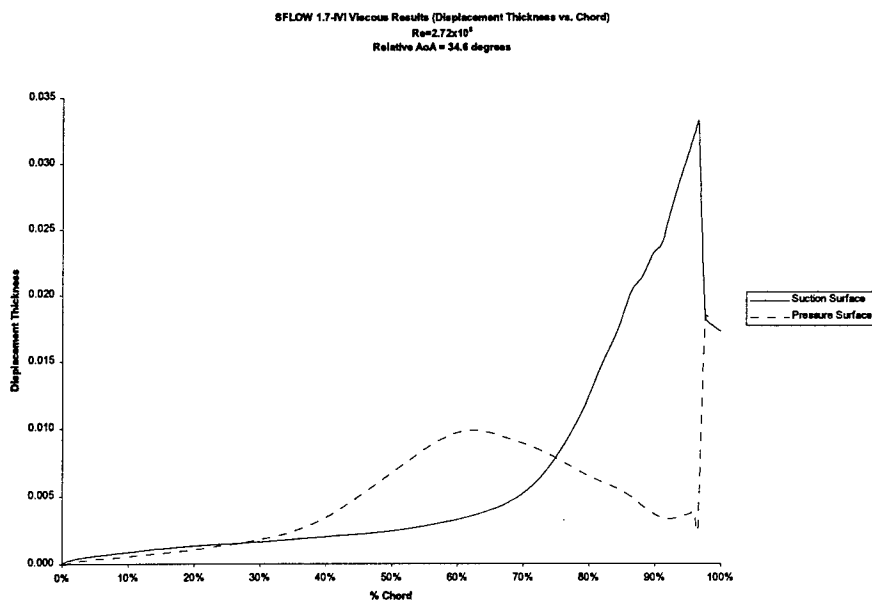


Figure 4.23 30% Span 9100 RPM Displacement Thickness Plot

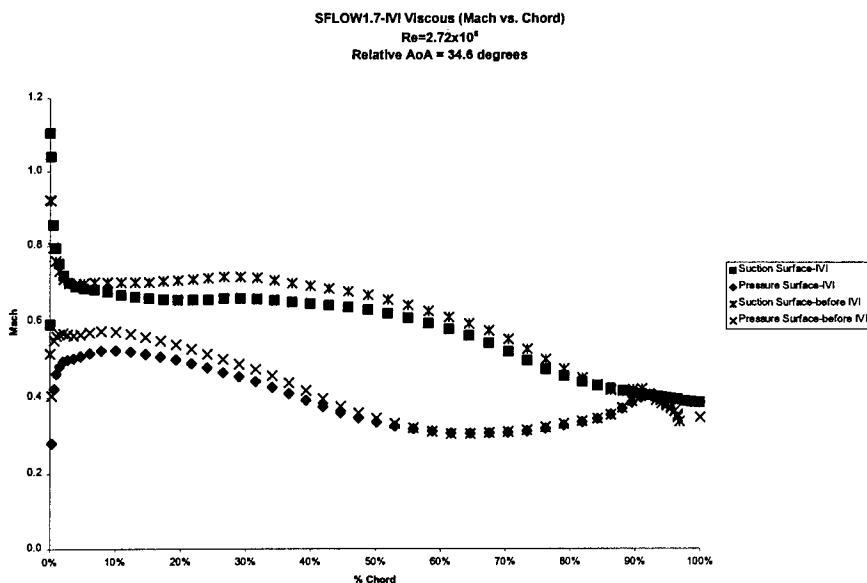


Figure 4.24 30% Span 9100 RPM Surface Mach Number Plot

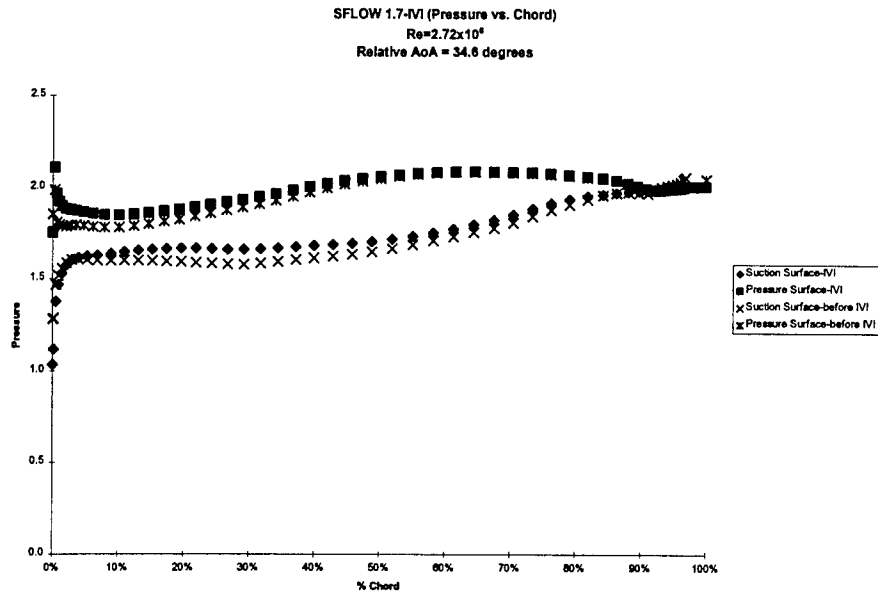


Figure 4.25 30% Span 9100 RPM Surface Pressure Plot

At 9100 RPM, we see very similar results as we did for 8100 RPM in Figs. 4.22 through 4.25. The shear stress plot shows separation at the same point on the airfoil surface. At 8100 RPM, however, there is a slight wiggle at the leading edge on the suction surface. The displacement thickness plot is very comparable to the 8100 RPM plot, but the boundary layer is slightly larger for 9100 RPM. Surface Mach (Fig. 4.24) and pressure (Fig. 4.25) plots show how the flow field slows down when viscous effects are taken into account. The wake near the trailing edge is also evident in these plots for the IVI solution. These are the main differences between inviscid and IVI solutions.

4.1.3.3 45% Span

Figures 4.26 through 4.29 show the 8100 RPM flow field at 45% span. We compare the results to the prior spans and higher wheel speed. The first thing we notice is that separation occurs at 75% chord (Figs. 4.26 and 4.30). This is in contrast to 30% span where separation occurs at 80% chord. Displacement thickness (Figs. 4.27 and 4.31) follows the shear stress trend just as it did in previous spans. There is also a trend on the pressure surface that is worthy of comment (see Figs. 4.28 and 4.32). The minimum point of shear stress on the pressure surface at all spans corresponds to a bubble-like increase in displacement thickness. When shear stress increases, with more favorable pressure gradients, there is a corresponding decrease in displacement thickness, and the threat of separation on the pressure side passes. As one moves up in span, this "bubble" appears further downstream on the pressure surface. At the higher wheel speed, 9100 RPM, the bubble at each span is located in the same area as at 8100 RPM.

At 8100 RPM we see pressure and Mach number results which are consistent with lower spans results. At 9100 RPM, there is a change in the pressure and Mach number plots for the inviscid solution

prior to IVI iterations (Figs. 4.32 and 4.33). For previous cases, the inviscid and viscous solutions are more evenly matched. For this case, however, the pressure difference between upper and lower surfaces of the airfoil at the leading edge is minimal when compared to the IVI solution.

There are two differences between the 8100 RPM case and the 9100 RPM case that might be the cause of this. The first is that the relative angle of inlet flow including camber is 10.3° at 9100 RPM and 12.1° at 8100 RPM. More importantly, the inlet Mach number is 0.74 at 9100 RPM and 0.65 at 8100 RPM. We may be running into transonic effects at the higher Mach number for the inviscid solution. Notice the rise in Mach number, Figure 4.33, around 30% chord on the suction surface for the inviscid solution. This too, is probably due to transonic effects causing overspeeding on the airfoil just prior to the flow expanding around the camber of the upper surface (refer to Figure 4.5).

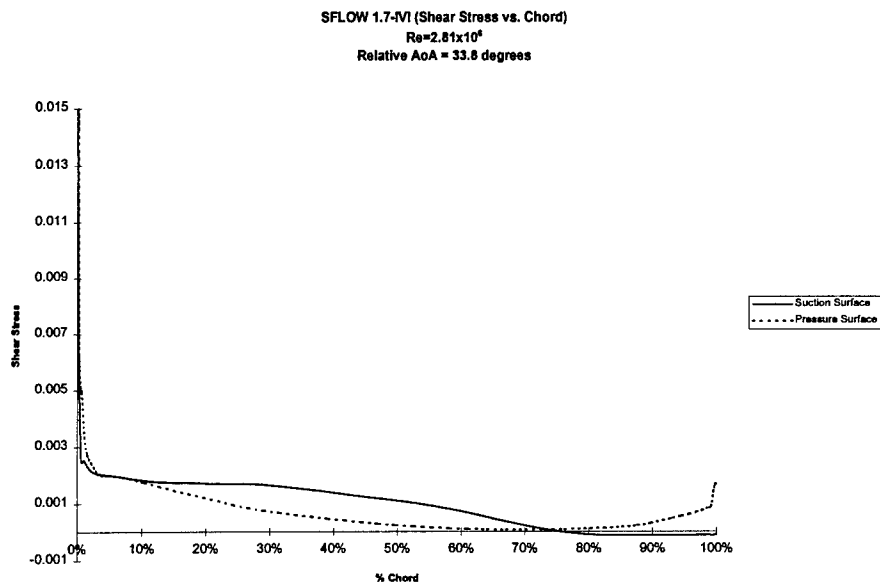


Figure 4.26 45% Span 8100 RPM Shear Stress Plot

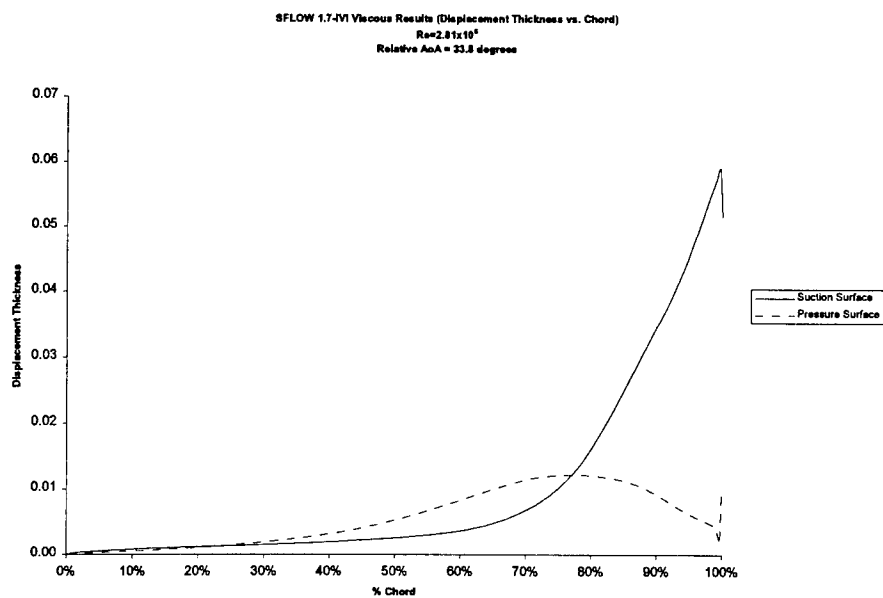


Figure 4.27 45% Span 8100 RPM Displacement Thickness Plot

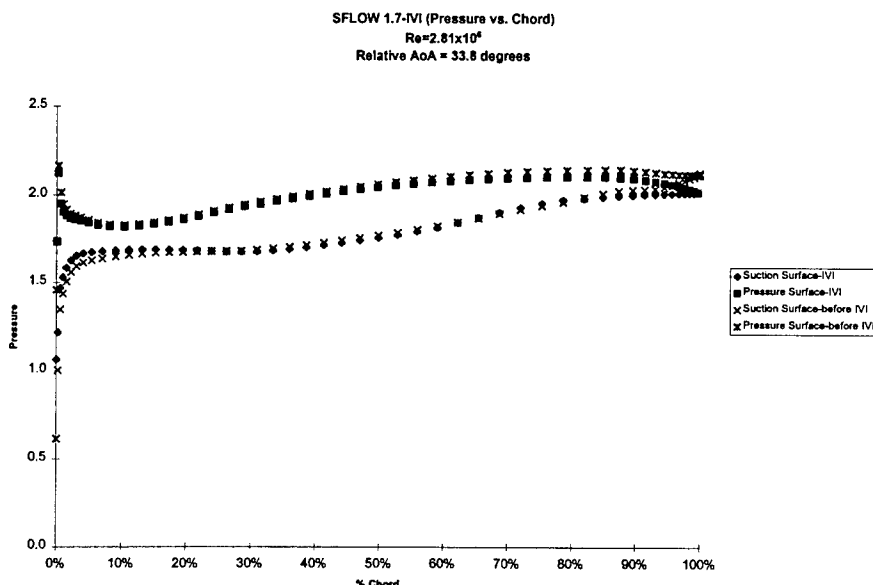


Figure 4.28 45% Span 8100 RPM Surface Pressure Plot

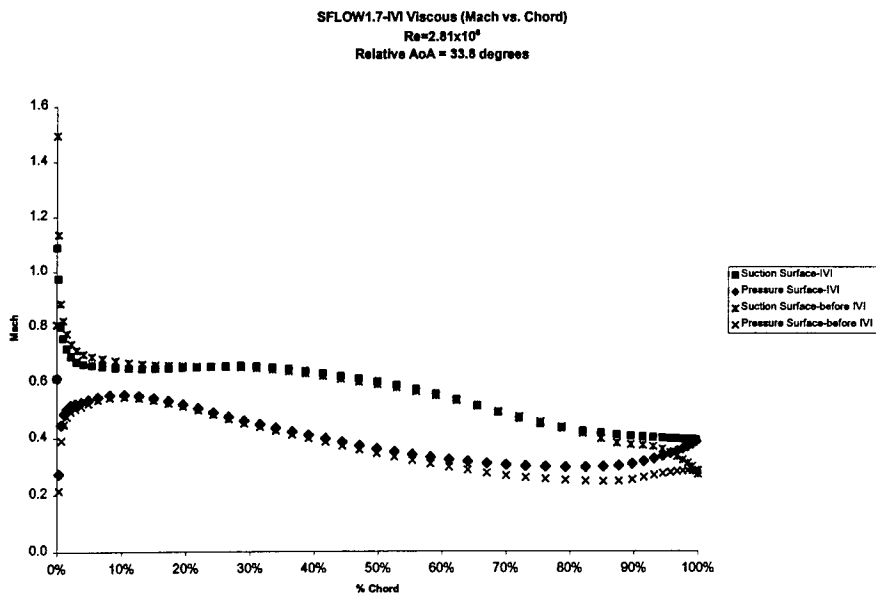


Figure 4.29 45% Span 8100 RPM Surface Mach Number Plot

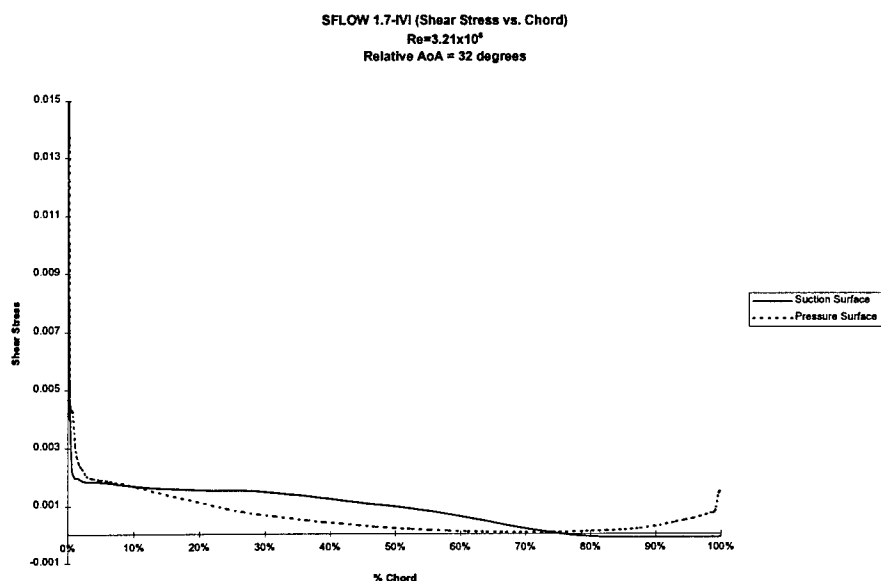


Figure 4.30 45% Span 9100 RPM Shear Stress Plot

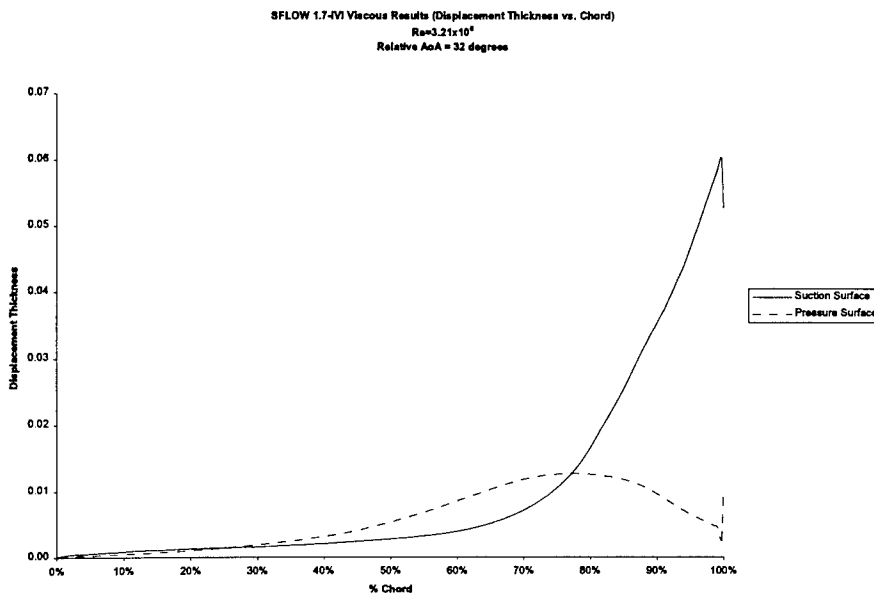


Figure 4.32 45% Span 9100 RPM Displacement Thickness Plot

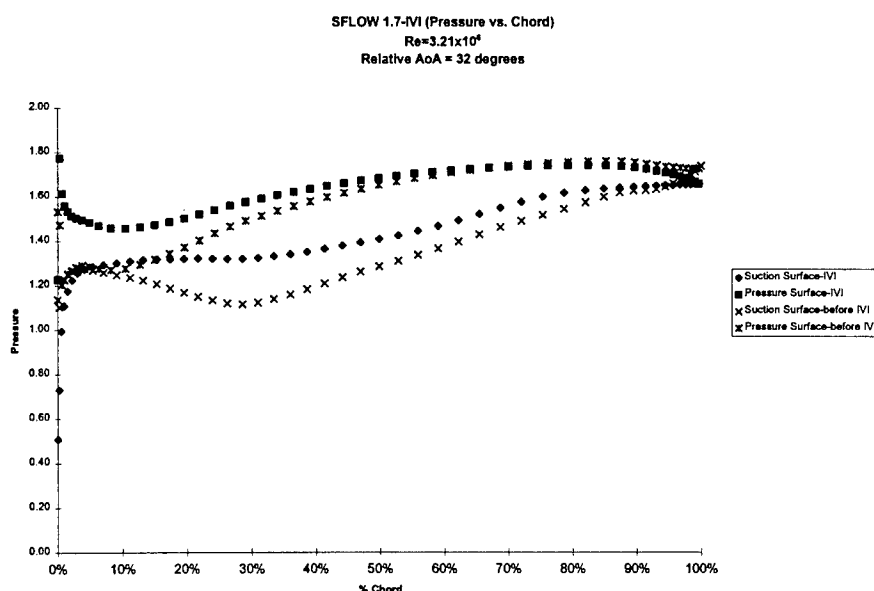


Figure 4.32 45% Span 9100 RPM Surface Pressure Plot

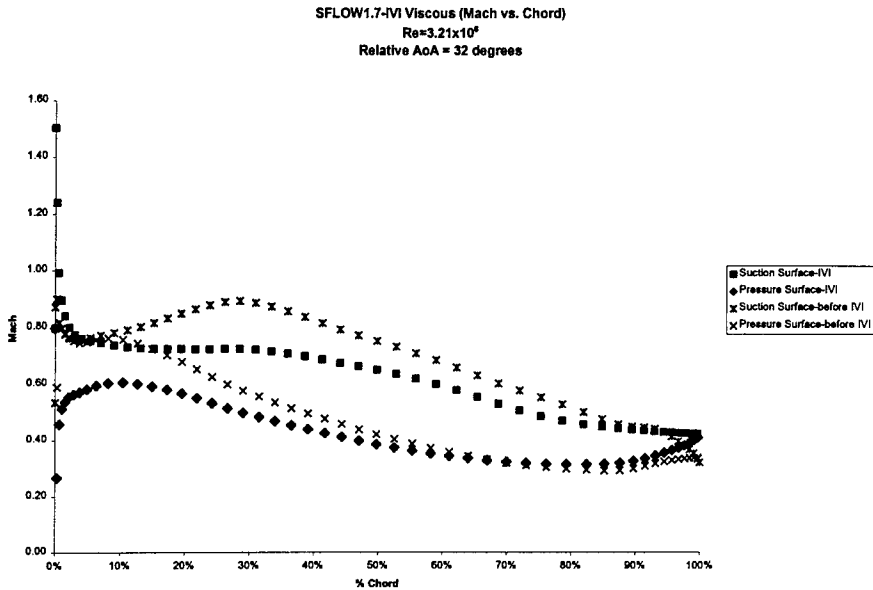


Figure 4.33 45% Span 9100 RPM Surface Mach Number Plot

4.1.3.4 60% Span

At 60% span, we were unable to obtain converged IVI solutions. Here, we present the inviscid results and make some observations about the steady inviscid flow field at this span when compared to lower spans.

First, the C_p (Fig. 4.34) and Mach number (Fig. 4.35) distributions for 8100 RPM will be analyzed. At the leading edge, we obtain the highest speeds, nearly 1.8 Mach on the suction side. The stagnation point, where the Mach number approaches zero, is located on the pressure side at the leading edge. Comparing the 8100 and 9100 RPM plots: the 9100 RPM peak speed (Fig. 4.37) at the leading edge is slightly lower than the 8100 RPM case. This high speed at the leading edge indicates a shock, since the Mach quickly slows down after it, and the pressure coefficient (Fig. 4.36) quickly rises.

By comparing these plots to the lower spans, we see that there is no shock at the leading edge for the lower spans. We can gradually see the flow approaching that condition as we compare 15% to 30% and 45% spans, but the shock doesn't appear until the 60% span inviscid solution.

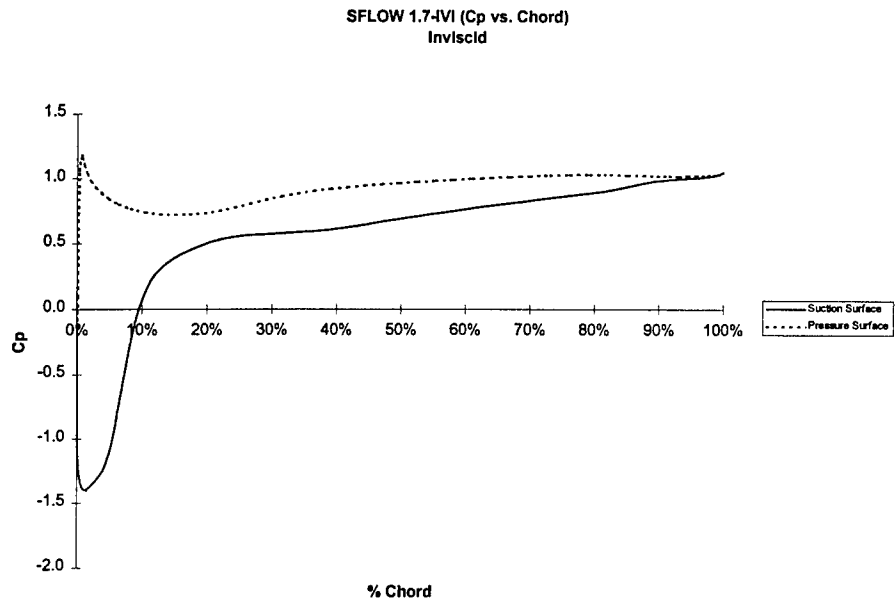


Figure 4.34 60% Span 8100 RPM Surface Cp Plot

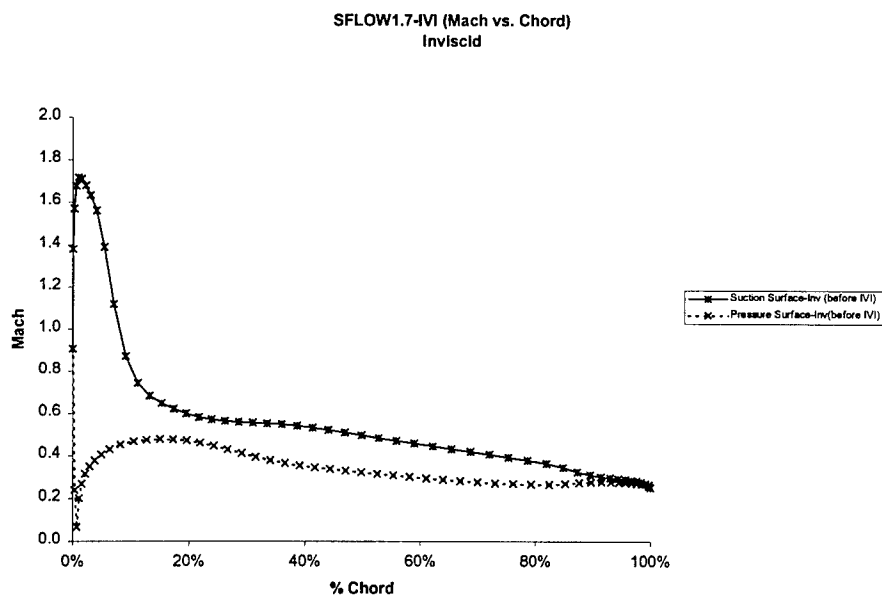


Figure 4.35 60% Span 8100 RPM Surface Mach Number Plot

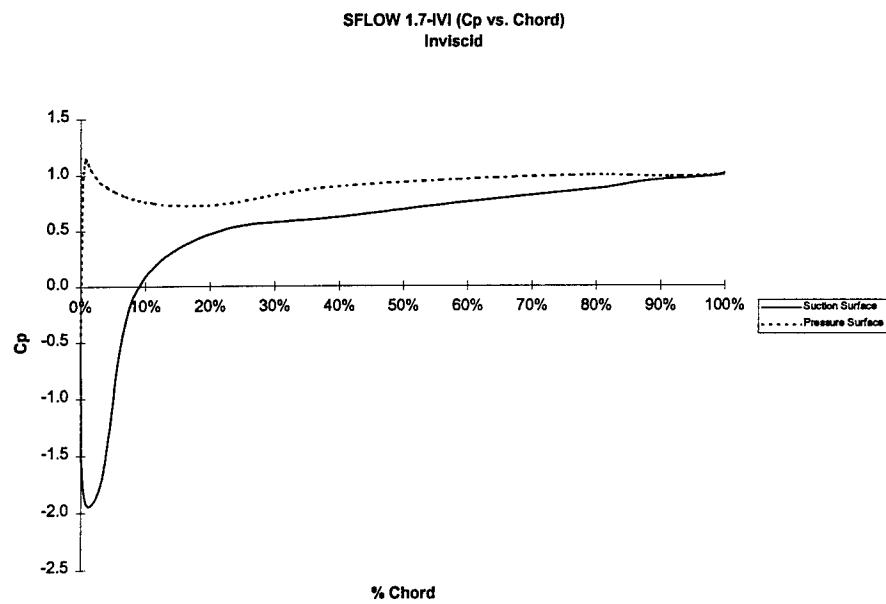


Figure 4.36 60% Span 9100 RPM Surface Cp Plot

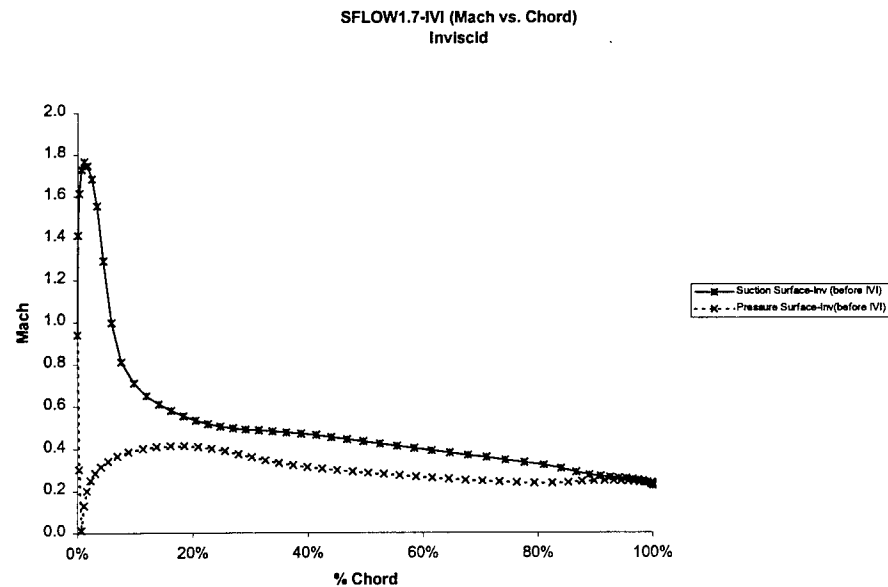


Figure 4.37 60% Span 9100 RPM Surface Mach Number Plot

4.1.3.5 75% Span

At the 75% span, we see similar behavior as observed at the 60% span. The shock gains some strength (Figs. 4.39 and 4.41), and the stagnation point remains in the same location. However, we note around 90% chord, there is a transition of the high pressure side from lower (pressure) to upper (suction) surface (Figs. 4.38 and 4.40). We search for an explanation in Fig. 4.7. There is a noticeable change in camber between the 60% and 75% spans. This decrease in camber would allow such a reversal of pressure near the trailing edge. Comparing the higher span cross sections to 75%, we see the trend in camber continues, so we would expect the current change near the trailing edge to also continue. There is no significant change in flow from 8100 to 9100 RPM at this span, except that at the higher wheel speed (Fig. 4.41), the surface Mach number slows down slightly further on downstream (2% versus 1% chord). Should this trend continue at higher speeds, we would expect the shock to travel downstream along the suction side of the airfoil as wheel speed increases.

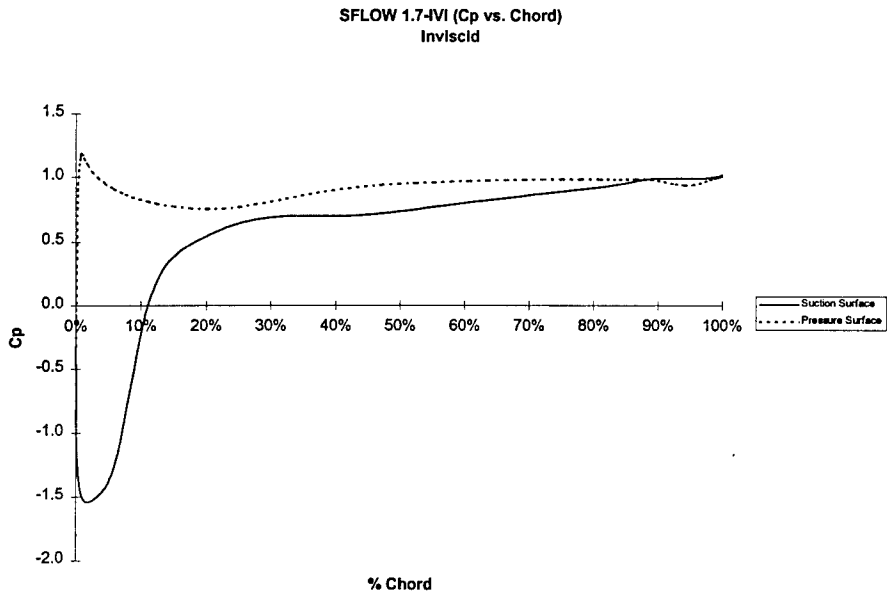


Figure 4.38 75% Span 8100 RPM Surface Cp Plot

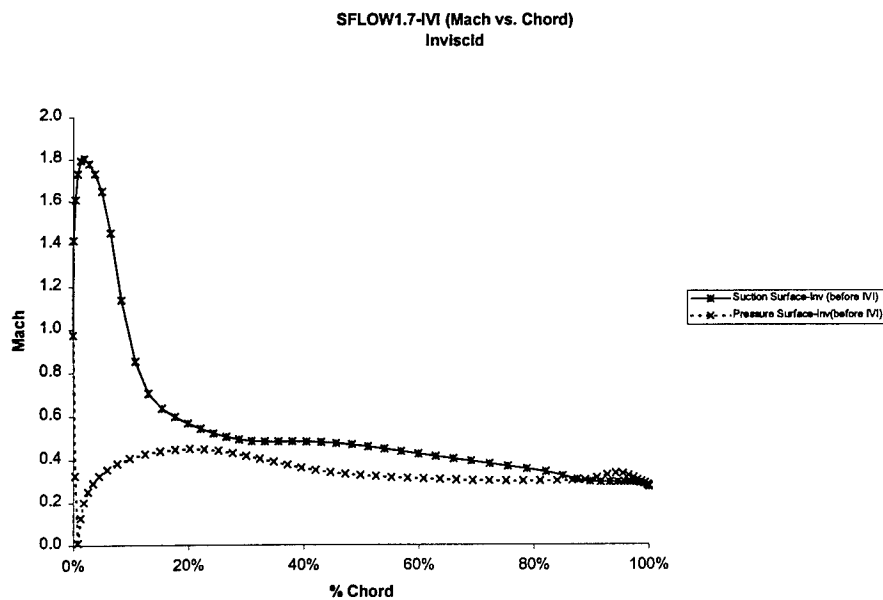


Figure 4.39 75% Span 8100 RPM Surface Mach Number Plot

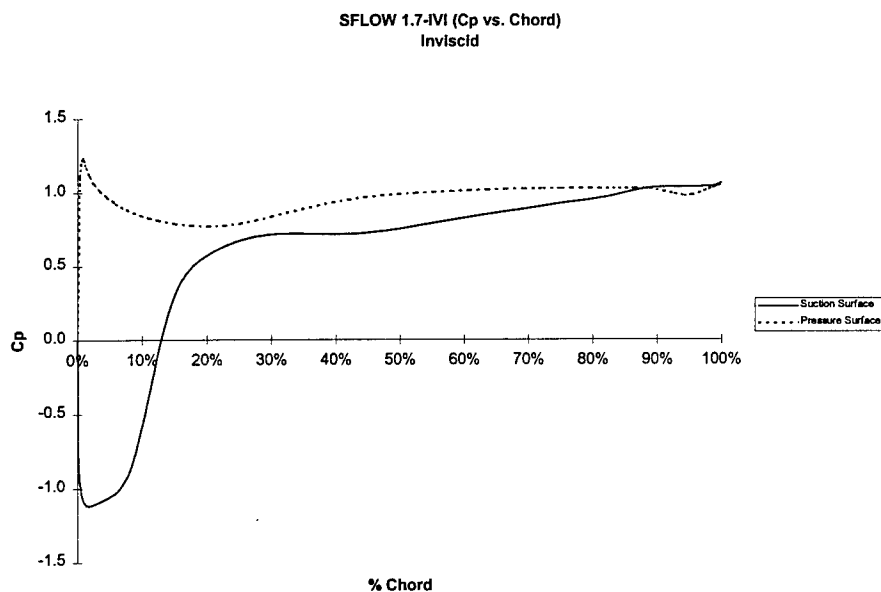


Figure 4.40 75% Span 9100 RPM Surface Cp Plot

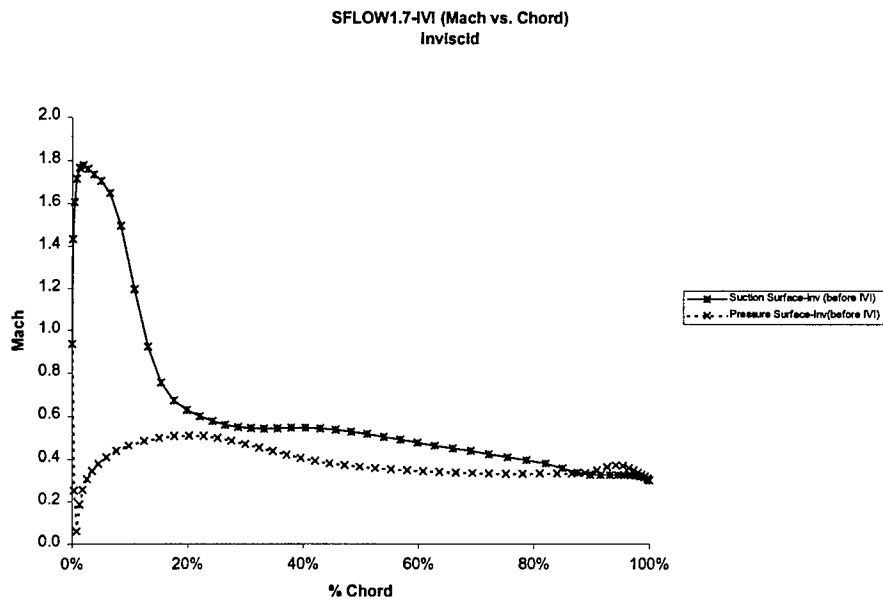


Figure 4.41 75% Span 9100 RPM Surface Mach Number Plot

4.1.3.6 85% Span

At 85% span, it is evident that the shock travels downstream on the airfoil's suction surface not just for increasing wheel speed, but also for increasing span. The change is not great, but it is still perceptible. As we go up in span and wheel speed, we would expect the shock to eventually move to mid chord. There is also an expansion wave on the lower surface of the airfoil that increases in strength with wheel speed. The flow on the pressure side increases abruptly from leading edge to 20% chord and then slows down gradually as the airfoil surface is followed by the flow (Figs. 4.43 and 4.45).

The reversal of high and low pressure sides also occurs further upstream as span is increased (Figs. 4.42 and 4.44). This may, however, also be an outcome of our adjustment to the trailing edge to make it a wedge for numerical analysis.

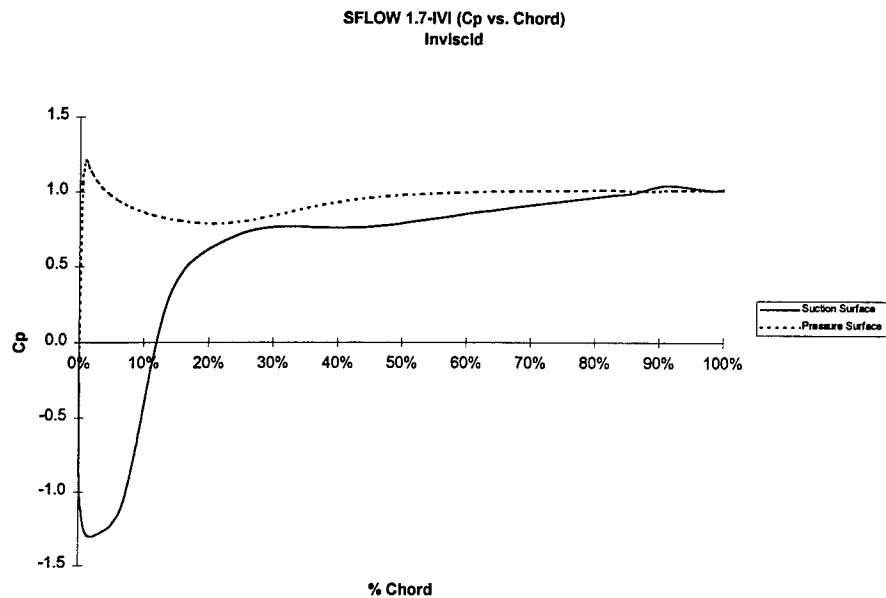


Figure 4.42 85% Span 8100 RPM Surface Cp Plot

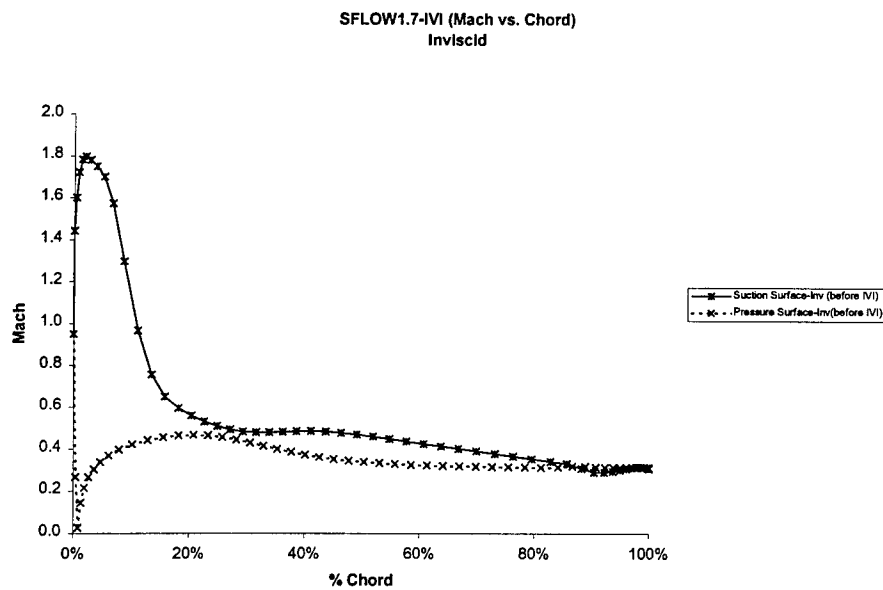


Figure 4.43 85% Span 8100 RPM Surface Mach Number Plot

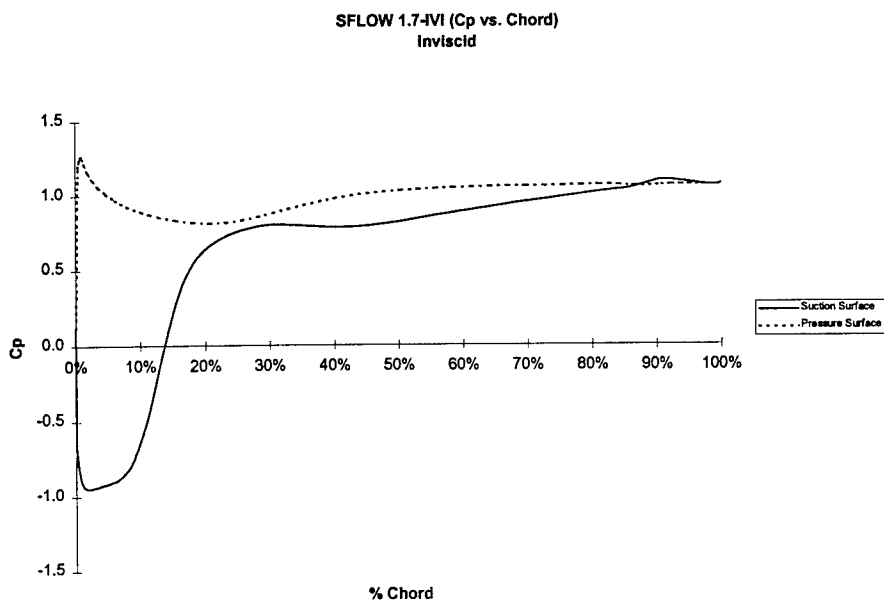


Figure 4.44 85% Span 9100 RPM Surface Cp Plot

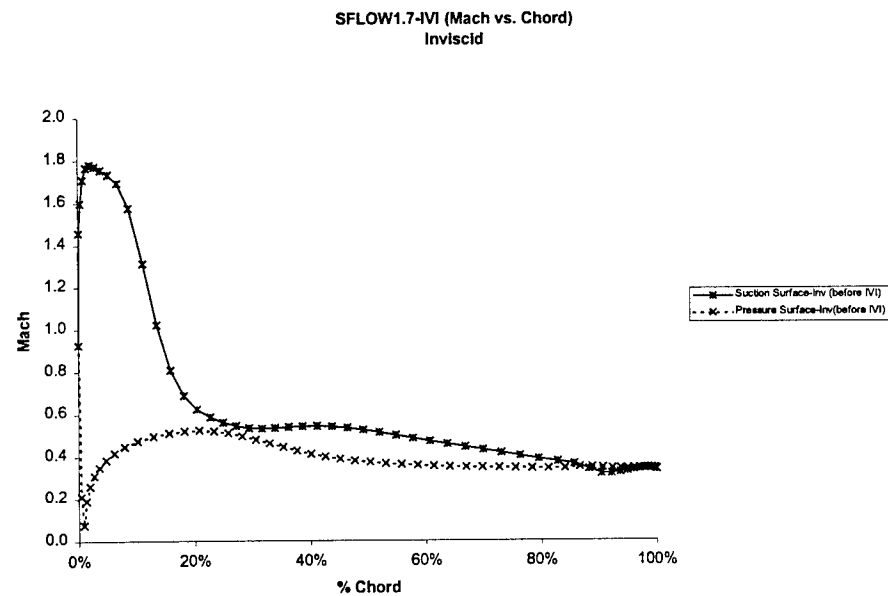


Figure 4.45 85% Span 9100 RPM Surface Mach Number Plot

4.1.3.7 100% Span

At 100% span, we were only able to obtain a converged solution for the 8100 RPM case. With this case, we are still able to observe that the trends in the solutions continue. The suction side shock moves further downstream on the airfoil and gains in strength. The expansion wave on the pressure side also increases and moves further downstream. This increase in discontinuities on pressure and suction sides is such that the Mach number (Fig. 4.47) for both surfaces actually becomes the same around 30% chord. The pressure change at the trailing edge (Fig. 4.46) does not move any further upstream, however.

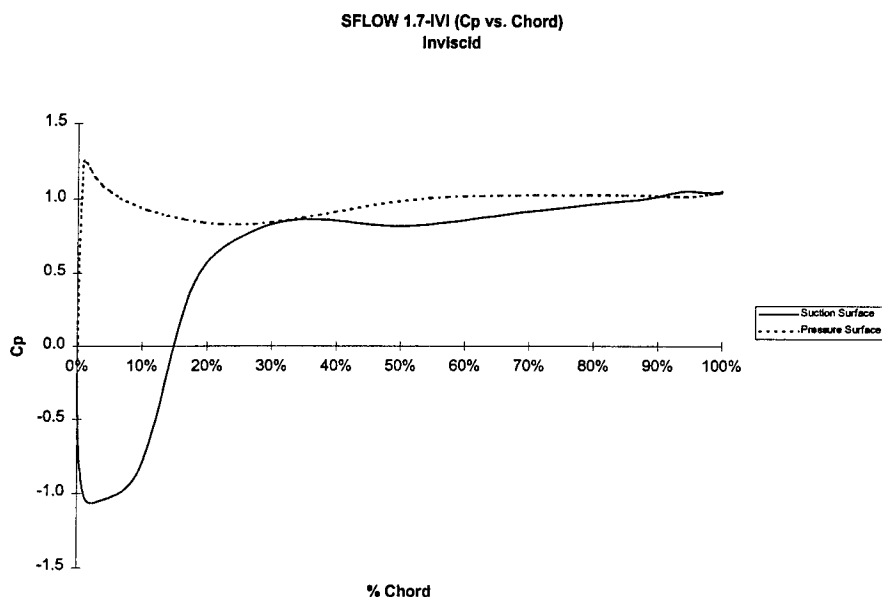


Figure 4.46 100% Span 8100 RPM Surface Cp Plot

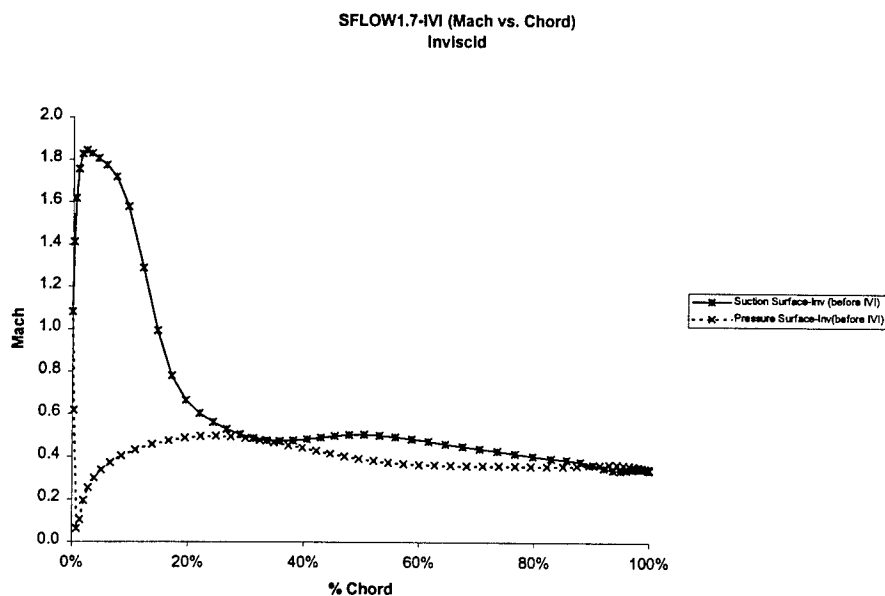


Figure 4.47 100% Span 8100 RPM Surface Mach Plot

The trends noted in this analysis agree with the steady results published by Manwaring, et al [3]. Although we could not obtain results for 85% span at the higher wheel speeds they published, extrapolation of the trends described above agree with the inviscid and viscous results they published.

Further study needs to be done before this geometry can be incorporated into a FREPS analysis. Viscous results must be obtained for spans at least up to 85% before the steady flow field is described sufficiently enough for use in the unsteady aerodynamic analysis (i.e., LINFL0) and flutter analysis (i.e., FREPS).

4.2 Stage Matching Investigation (SMI) Rotor

4.2.1 CARL-SMI Experimental Configuration

The Compressor Aero Research Lab (CARL) facility at Wright Patterson Air Force Base's Wright Laboratory is a full scale, high speed, highly loaded compression stage. The single stage compressor facility consists of an open or closed loop (currently open) tunnel system with an upstream venturi flow meter to measure the mass flow rate. The test compressor is driven by a 2,000 hp electric motor with a variable speed range of 6,000 to 21,500 rpm.

The current research compressor, Figure 4.48, was designed by CARL personnel and manufactured by Pratt & Whitney Aircraft Engines. The primary intent for this research compressor is for a Stage Matching Investigation (SMI), characterizing overall compressor performance. Therefore, a single stage core compressor consisting of a rotor and stator with 33 and 49 airfoil blades respectively is used. The outer diameter for both the rotor and stator is 19 inches. The SMI's core compressor design results in a transonic rotor. To study the effect of different upstream stages, an IGV assembly is placed upstream of the rotor section. The IGV's were designed by Pratt and Whitney with the purpose of creating a propagating wake consistent with a modern technology, highly loaded, low aspect ratio stage. The IGV's do not turn the flow as would a normal IGV assembly. It is possible to vary the axial spacing between the IGV's and the rotor. Three different spacings are possible 12%, 26%, and 56% of the rotor chord from the IGV trailing edge to the rotor leading edge. In addition, the number of IGV's in the upstream passage can be set to 12, 24 or 40 blades.

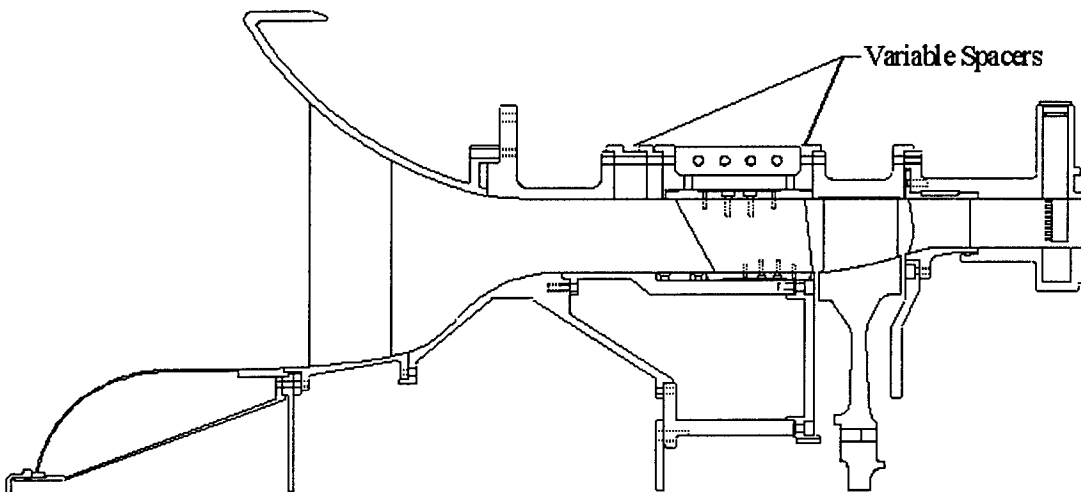


Figure 4.48 SMI Test Rig

As previously stated, the primary intent for the SMI rig is compressor performance research, but several forced response investigations have been completed in conjunction with the performance research. Upstream propagating pressure fluctuations on the IGV blade surface have been reported by Probasco, et al. [4] and Koch, et al. [5]. Also, Koch, et al. [6, 7] has investigated the 3-D vortical forcing

function experienced by the rotor generated by the IGV's. The vortical forcing function can be combined with the steady aerodynamic analysis from SFLOW to analyze the unsteady aerodynamics (LINFLO). Ultimately, resulting in a forced response prediction of the SMI rotor with the FREPS model. Future experiments at CARL on the SMI rig will result in stress measurements on the rotor. The stress measurements could then be compared to the FREPS predictions to assess the model's strengths and limitations.

4.2.2 SMI Flow Conditions

The SMI test case utilized for this investigation is 100% peak performance at design speed. A spreadsheet showing how input parameters were calculated is located in Appendix F. All rotor blade spans have transonic inlet Mach numbers at this operating condition. A viscous steady flow numerical analysis was performed by Dr. Randy Chriss, CARL, which shows a bow shock located at the leading edge of the 50% span results. The inviscid (SFLOW) analysis was unable to predict this bow shock although otherwise reasonable results were obtained. The capability of the full potential steady flow equations used in SFLOW to predict a bow shock is quite limited. Figures 4.49 through 4.53 show the spans of the SMI rotor blade that were analyzed using SFLOW.



Figure 4.49 10% Span



Figure 4.50 30% Span



Figure 4.51 50% Span



Figure 4.52 70% Span



Figure 4.53 90% Span

4.2.3 Computational Results

Computational results are shown below. Verification of these results will come when the steady data is incorporated into the forced response prediction system (FREPS, see Appendix C) and compared with experimental stress data. The steady results will be incorporated with an unsteady aerodynamic analysis (LINFLOW) to computationally determine the forced response of the SMI rotor to various unsteady vortical aerodynamic excitations.

We were unable to obtain converged IVI results at this time, however inviscid results were obtained up to the 90% span. An inlet Mach number of 0.99 was used in every case because of convergence problems SFLOW had when dealing with an inlet Mach number of unity or higher. Also, most spans obtained better results when the flow incidence angle was increased by one over the calculated value shown in Appendix F. These results are presented below. In Appendix G are tables of the SFLOW inputs used to obtain the following solutions.

4.2.3.1 10% Span

Results for the 10% span of the SMI rotor cascade are shown in Figures 4.54 and 4.55. The steady coefficient of pressure is plotted in Fig. 4.54 and the surface Mach number distribution is plotted in Fig. 4.55. The flow behaves relatively well at 10% span, except for the peak Mach number around 30% chord. There is no real indication of a shock yet, since the flow decelerates gradually as the trailing edge is approached. At the leading edge, however, there is no great pressure differential between upper and lower surfaces. The solution shows a basically smooth flow, except for spurious indications at less than 5% of the chord which is not unusual for a steady full potential flow code such as SFLOW. SFLOW is notoriously inaccurate right at the leading edge (less than 5% chord) where overspeeding can occur.

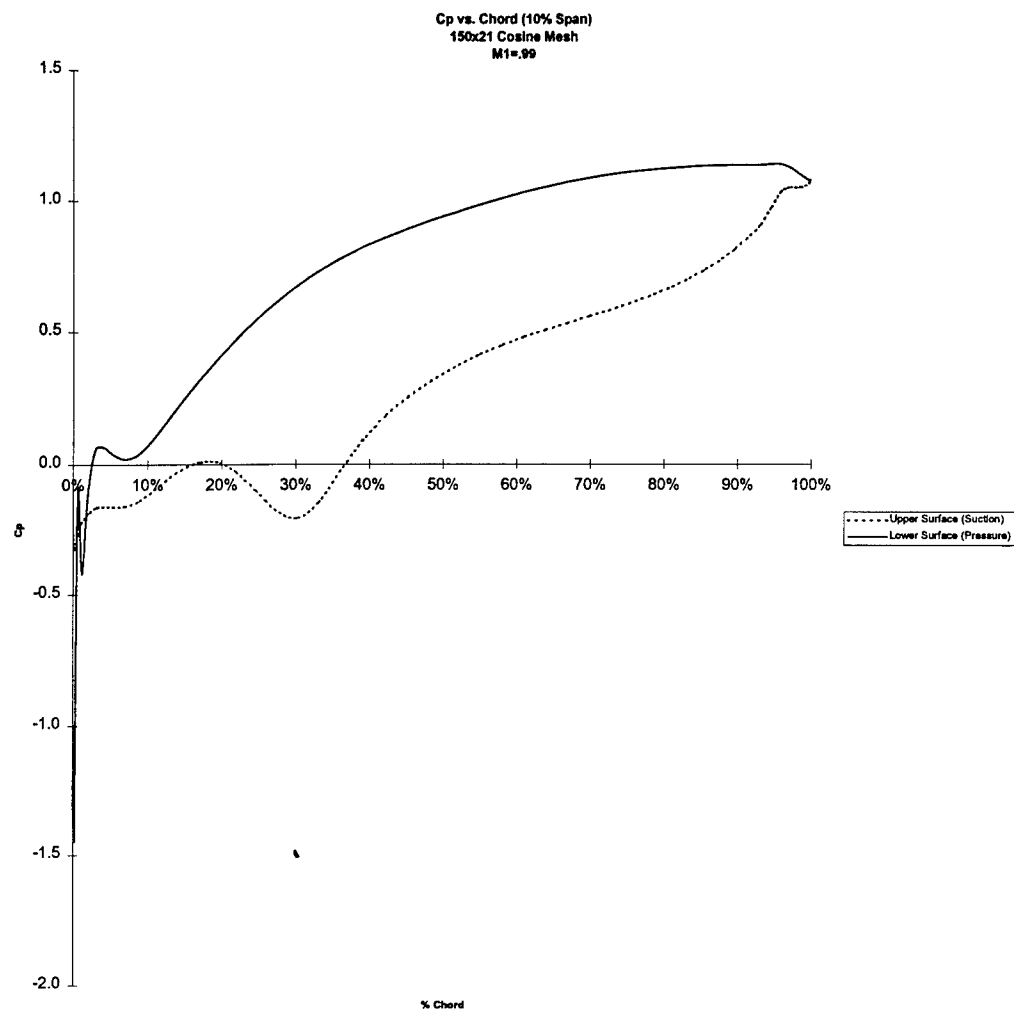


Figure 4.54 10% Span Surface Cp Plot

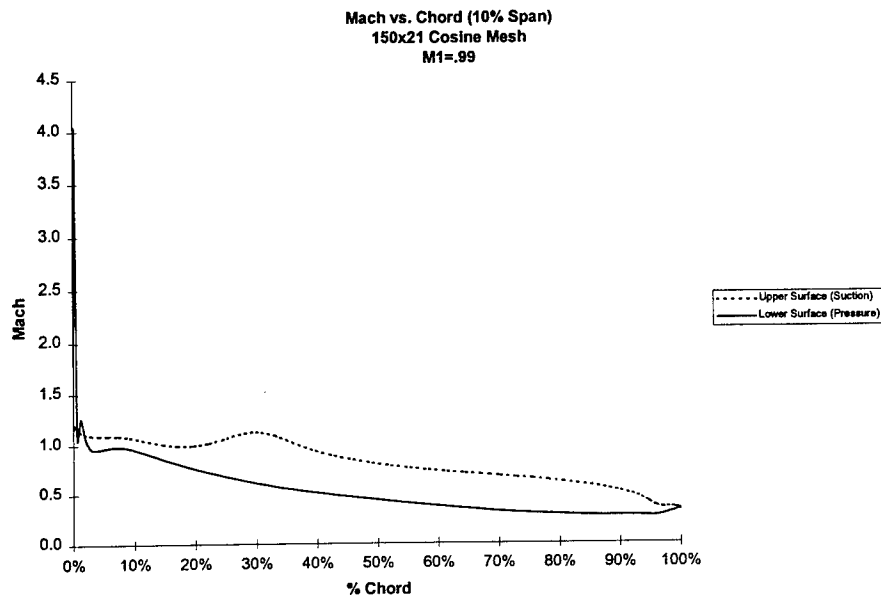


Figure 4.55 10% Span Surface Mach Number Plot

4.2.3.2 30% Span

The results for 30% span are plotted in Figures 4.56 and 4.57. The coefficient of pressure plot (Fig. 4.56) and Mach number (Fig 4.57) both show a strong shock on the suction surface. From 10% to 20% chord on the suction surface, there is no smearing of the shock that would normally come with viscous effects. The shock is quite sharp and pronounced. The decrease in steady flow speed and increase in coefficient of pressure is more pronounced after 10% chord. Flow behavior at the leading edge indicates some overspeeding at the leading edge on the upper surface, however, the flow behavior isn't as erratic as it is at the 10% span leading edge. Also note that on the lower surface, there is an indication of expansion that peaks around 10% chord, but this may also be due to the presence of higher flow speeds around the upper surface of the airfoil just beneath the one under study in the cascade. We see a flow solution that is much smoother than the 10% span solution above.

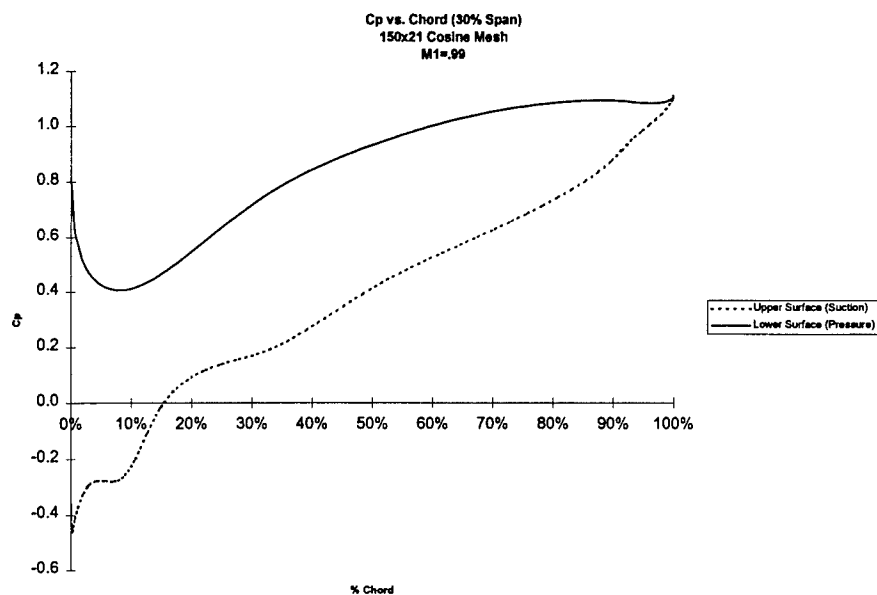


Figure 4.56 30% Span Surface Cp Plot

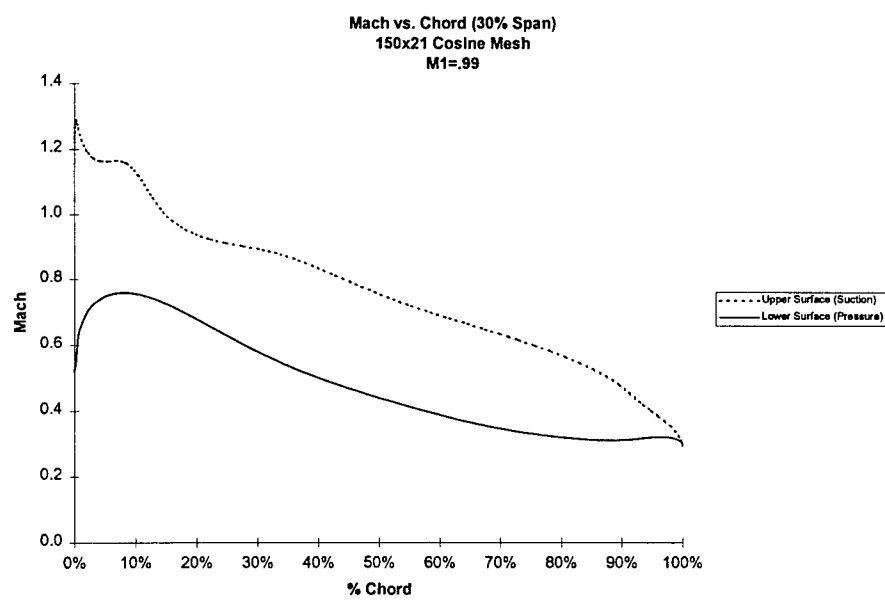


Figure 4.57 30% Span Surface Mach Number Plot

4.2.3.3 50% Span

Figure 4.58 shows the coefficient of pressure plot and Figure 4.59 shows the Mach number distribution for the 50% span cascade. At the leading edge, the Mach number is actually lower on the upper surface and higher on the lower surface than at 30% span. This time, the peak Mach number and corresponding low pressure coefficient are located around 15% chord, but we don't see the pronounced bubble of higher speed we did at 10% span and the Mach number is actually lower on the upper surface. The presence of a shock is seen as the flow compresses around both upper and lower surfaces after 10% chord. Peak Mach number on the lower surface is still located around 10% chord. Again, the leading edge solution shows a stagnation point on the lower surface and a strong shock at the upper surface at the leading edge, but the viscous three dimensional analysis by Dr. Randy Chriss, CARL, shows a bow shock which the full potential inviscid SFLOW code does not accurately predict.

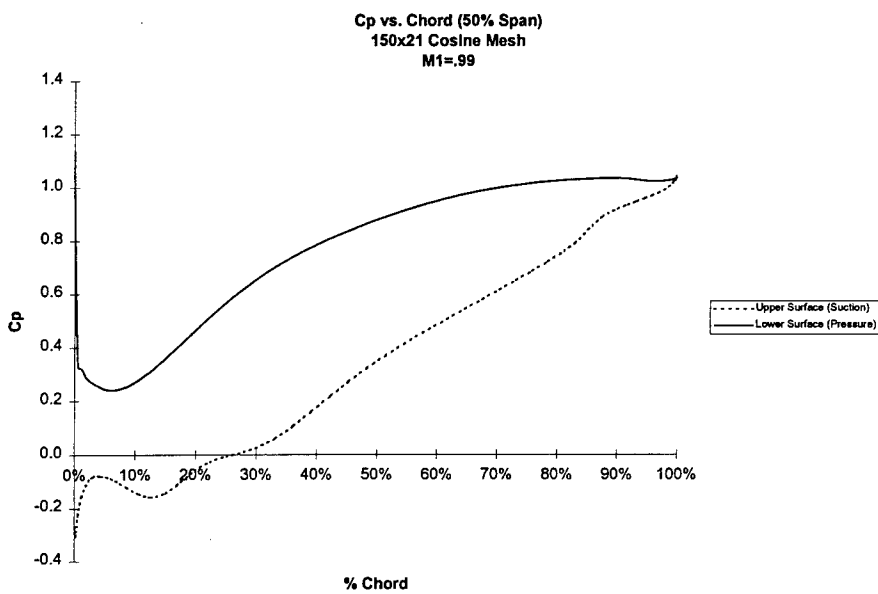


Figure 4.58 50% Span Surface Cp Plot

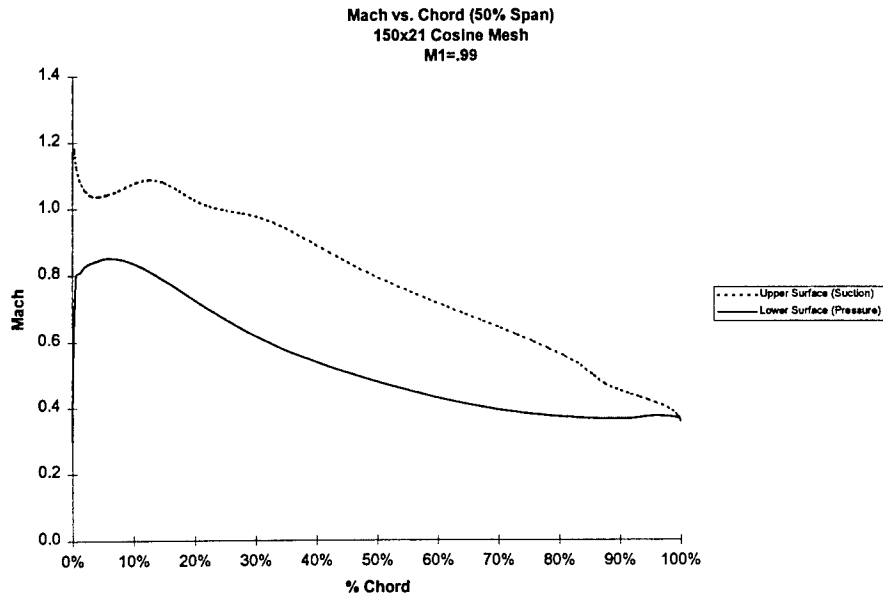


Figure 4.59 50% Span Surface Mach Number Plot

4.2.3.4 70% Span

Results shown in Figures 4.60 and 4.61 for the 70% span cascade are very similar to the results at 50% span. This is reasonable, since the figures of the cascades (Figures 4.51 and 4.52) indicate they are similar in geometry. Also, because of problems with supersonic inlet conditions, the same inlet Mach number was used for both cases. The main difference in solutions is near the trailing edge. Note that there is less camber in the 70% span cross section than the 50% span. This is probably the cause of the discrepancy at the trailing edge when compared against the 50% span. In both the coefficient of pressure (Fig. 4.60) and Mach number (Fig 4.61) plots, the flow at the trailing edge lower surface takes a small but sharp jump in subsonic Mach number prior to meeting the upper surface flow at the sharp trailing edge point to follow the Kutta condition. Artifacts such as this have been attributed to forcing the trailing edge to a sharp point in order to meet the Kutta condition. Also, the chord was extended by almost 10% so that a good mesh could be generated by SFLOW. Both of these factors, coupled with the small change in camber from 50% to 70% span, contribute to the spurious results near the trailing edge.

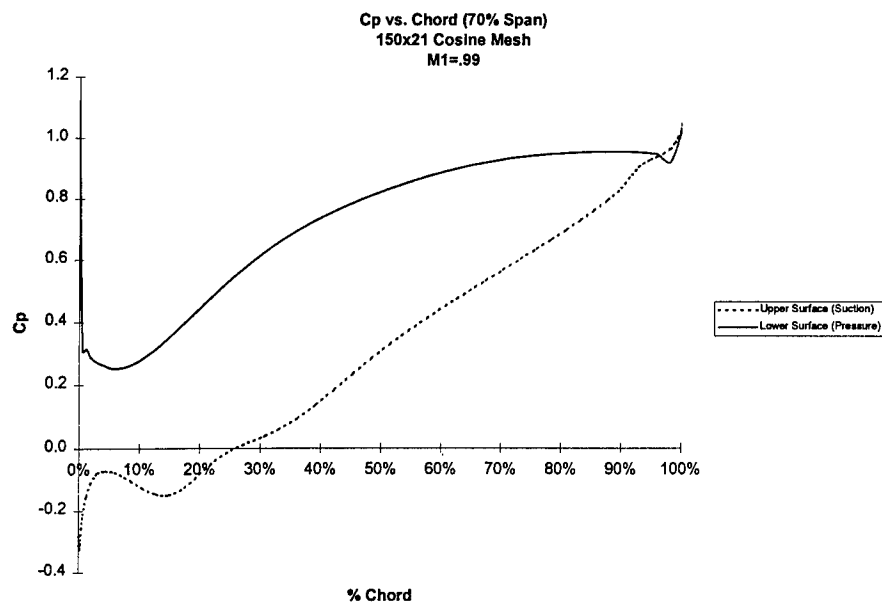


Figure 4.60 70% Span Surface Cp Plot

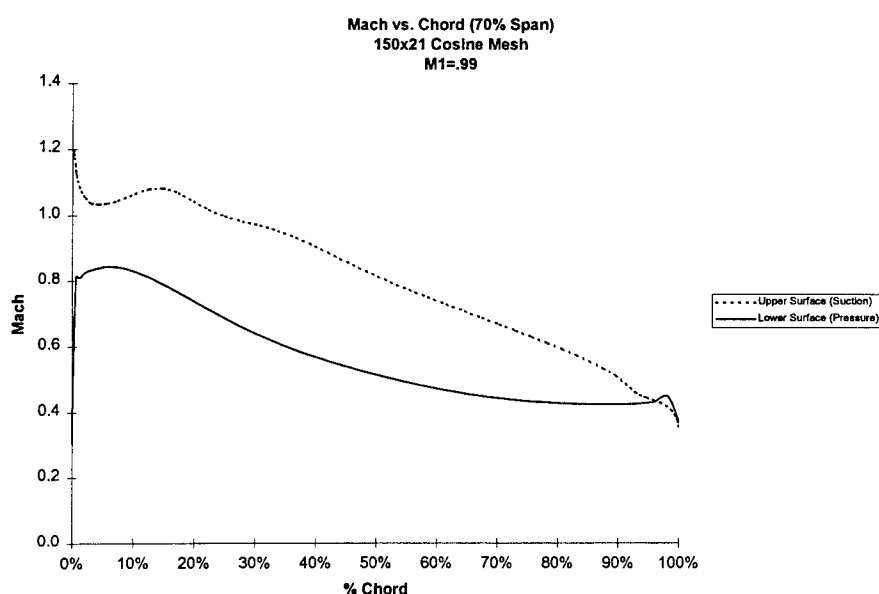


Figure 4.61 70% Span Surface Mach Number Plot

4.2.3.5 90% Span

The coefficient of pressure is plotted against chord in Figure 4.62 and the Mach number distribution is shown in Figure 4.63. We again see similar results between this cascade and both 50% and 70%. Probably due to the same inlet Mach number being used for cascades of similar geometry with only small changes in incidence angle. Had we been able to use the actual inlet Mach numbers calculated, there is still only a change of 0.1 between 50% span and 90% span. The change in incidence angle is only about 5 degrees between the same spans. Therefore, we would expect the results to be similar despite the same inlet Mach number being used for each cascade. The noticeable difference is again at the trailing edge. This time, the solution comes to a nicer close at the trailing edge without the small but sharp expansion on the lower surface. The change in geometry at the trailing edge to meet Kutta condition and to allow for a better mesh does not always produce problems in the solution at the trailing edge. Since the cascade geometries are very similar between 70% and 90% span, the change in incidence angle was probably just enough to cause the trailing edge solution to change.

Overall, when a comparison is made of the cascades from 10% to 90% span, we see a definite shock form at 30% span where it appears the strongest, but is located further upstream on the upper surface than higher spans. At 50%, a weaker shock is located a little further downstream (15% chord versus 10% chord). After that, the shock maintains the relatively same strength and position, and the flow doesn't change drastically. The flow on the lower surface increases to a higher value at the trailing edge as the span increases.

Had supersonic inlet Mach numbers been used, we would expect the solution to show stronger shocks that are located further downstream on the upper surface chord. When we view the 3-D viscous solution from Dr. Chriss at 50% span, we see that SFLOW does not predict the bow shock located at the leading edge for that span and the shock on the upper surface is sharper for the SFLOW results. In this SFLOW analysis, there are no viscous effects that would dampen the solution out at all.

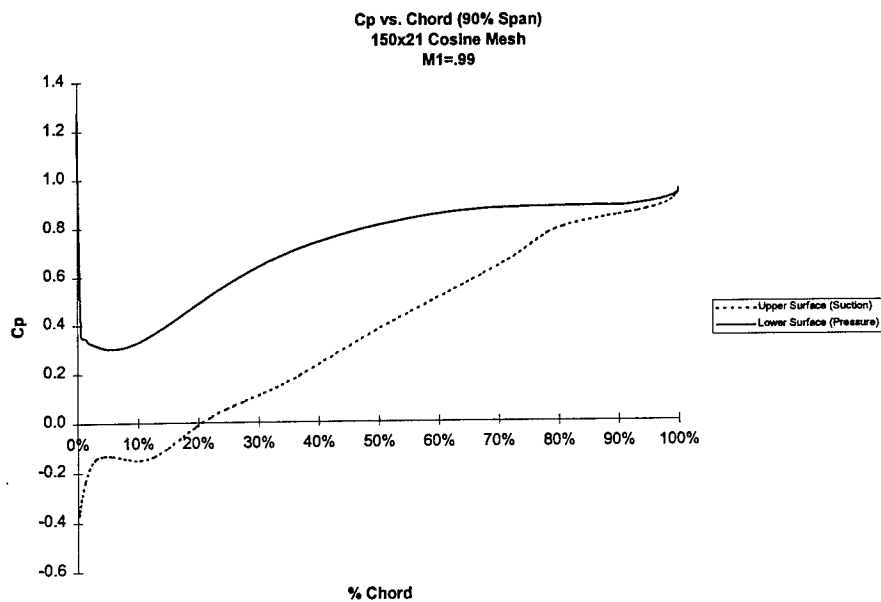


Figure 4.62 90% Span Surface Cp Plot

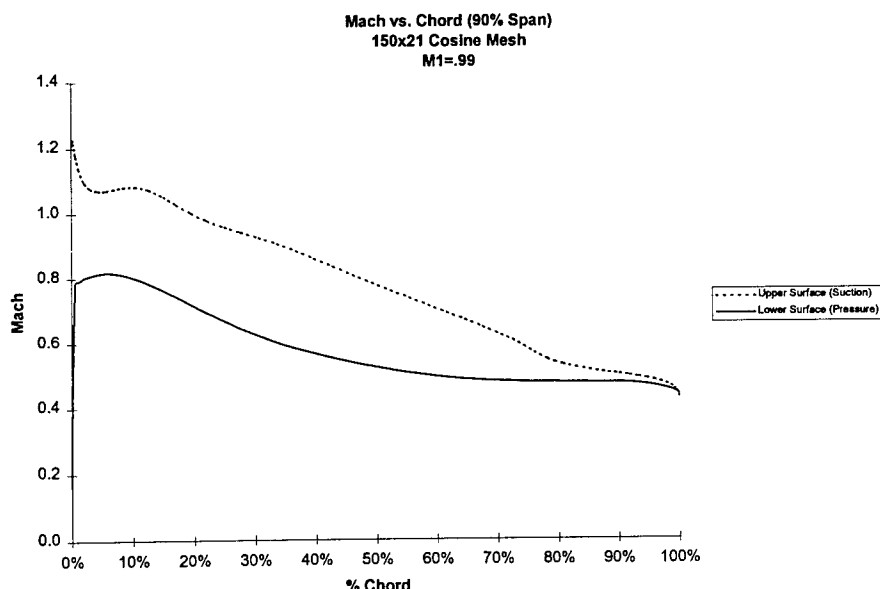


Figure 4.63 90% Span Surface Mach Number Plot

**EXPERIMENTS ON CONSOLIDATION OF ALUMINUM POWDERS
USING SIMPLE SHEAR**

**K. Ted Hartwig and Humberto Zapata
Department of Mechanical Engineering
Texas A&M University
College Station, Texas 77843-3123**

FINAL REPORT

For

**Summer Faculty Research Program
Research and Development Laboratories
5800 Uplander Way
Culver City, California 90230-6608**

Sponsored By:

**Air Force Office of Scientific Research
Bolling Air Force Base, D.C.
and
Research and Development Laboratory**

September 1998

Experiments on Consolidation of Aluminum Powders Using Simple Shear

**K. Ted Hartwig
Associate Professor
Department of Mechanical Engineering
Texas A&M University**

Abstract

The effect of equal channel angular extrusion on the consolidation of -325 mesh 6061 Al powder was studied. The variables examined include evacuation versus non-evacuation, extrusion can geometry, number of extrusion passes, extrusion route and extrusion temperature. Post extruded material was characterized by ductility, hardness, metallography and tensile testing before and after heat treatment and compared to commercially wrought 6061 aluminum. The most important findings are that nearly full consolidation can be achieved after one extrusion pass and that the tensile strength of the consolidated powder (following a post extrusion heat treatment) is equivalent to that of wrought material.

Table of Contents

I.	Introduction	1
II.	Discussion of the Problem	1
III.	Methodology	1
IV.	Results	3
V.	Conclusions	4
VI.	References	5
VII.	Figures	6

Experiments on Consolidation of Aluminum Powders Using Simple Shear

K. Ted Hartwig

I. Introduction

Powder metallurgy (P/M) offers one of our most powerful tools for fabricating advanced high performance materials [1]. In addition, the field is currently growing faster than other metalworking technologies as more P/M applications have become economically viable. The need for unique properties and materials which are difficult to process by alternative methods have also driven this growth. Continued growth will depend strongly on, 1) consolidation of high performance materials to full density, 2) fabrication of difficult to deform materials with uniform micro-structures, 3) economical consolidation of specialty alloys with mixed phases and, 4) synthesis of bulk non-equilibrium materials such as amorphous, microcrystalline or metastable alloys [2].

II. Discussion of the Problem

Full density processing is motivated by improvements in strength, ductility and toughness that typically accompany elimination of pore volume in P/M products. In fact, the performance levels of fully dense P/M material can exceed those of wrought product. Full density and the level of properties in the P/M product are achieved by the right combination of consolidation stress, time at temperature and particle size. Higher temperatures encourage consolidation but may degrade final properties due to grain growth. Higher stresses during processing are favorable, providing a larger driving force for powder consolidation. Smaller particles respond better to sintering and densification. Large shear stresses disrupt surface films on the particles and facilitate bonding. Improved mechanical properties can be achieved for compacted materials by processing at lower temperatures, given adequate particle bonding has occurred [3, 4].

Because the rate and degree of P/M product densification are aided by stress, diffusion (higher temperature, smaller particles/grains and longer processing times) and shear strain, equal channel angular extrusion (ECAE) under the correct conditions should be very effective at powder consolidation.

III. Methodology

Equal channel angular extrusion is a relatively new materials processing method which employs simple shear to uniformly strain bulk material [5-7]. Multiple ECAE passes gives very high effective strains and can be applied to elongate grains and separated phases in composite materials [8]. The surface area of a material volume element subjected to simple shear by ECAE is related to the shear strain as shown by Equation 1:

$$S = \frac{2 + [(2N \cot \phi)^2 + 1]^{1/2}}{3} \quad (1)$$

where ϕ is one-half the die angle (see Figure 1) and N is the number of extrusion passes. Multiple ECAE passes through an extrusion die at a 90° angle and with the billet oriented so that grains elongate in the same direction with each extrusion give a substantial increase in material element surface area as shown in Table 1 below:

Table 1: The Surface Area of a Cubic Element Subjected to Multiple ECAE Passes Through a 90° Die

Pass No.	Equivalent Strain (in/in)	Material Element Surface Area Ratio
0	0	1.00
1	1.15	1.41
2	2.31	2.04
4	4.62	3.35
8	9.24	6.01

The above discussion explains why ECAE is potentially an effective method for consolidating powders. This basic concept was tested in a series of preliminary experiments at Texas A&M University, in collaboration with Ames Laboratory, on Cu (30 v/o) and 304 stainless steel (30 v/o) plus Nd-Fe-B (70 v/o) mixed powder composites. The mixed powders were compacted to approximately 70% theoretical density, placed in pure copper or 304 stainless steel containers, out gassed and evacuated and extruded at cryogenic temperature (77 K), room temperature or 300°C. Consolidation to ~97% theoretical density and magnetic particle fracture were successfully achieved. The results of these experiments are very encouraging for the development of advanced composite magnetic materials with improved corrosion, mechanical, and thermal properties.

The main objective of the research undertaken on this contract was to identify the best method(s) of applying equal channel angular extrusion to powder consolidation. The approach taken has been to thoroughly study one material (aluminum alloy 6061) that is already fabricated commercially by conventional P/M methods. The powdered metal is placed in an extrusion can for ECAE processing. The effects of billet/can geometry (up to one-inch square by five-inches long), powder compaction density, number of ECAE passes, billet orientation (route) during extrusion, and extrusion temperature were investigated. Density, micro-structural and mechanical property characterization results on ECAE processed materials are compared with commercially prepared wrought material. The intent of this evaluation of ECAE for powder consolidation was to uncover the basic parameters (extrusion temperature, route, and number of passes) needed to effectively apply the method

to the consolidation of many different (including advanced mixed metal and metal/ceramic) powdered materials.

Work on this project was broken into two phases. During Phase I, the compaction effectiveness of ECAE was studied with unevacuated powder contained in pure copper thick-walled cans. The variables examined included level of pre-compaction, and the effect of can geometry. During Phase II the effects of ECAE route, number of passes, and extrusion temperature were evaluated on evacuated powder. The billet geometry used in Phase II was similar to Phase I; evacuation and e-beam sealing of the cans was done by personnel at the Ames-DOE Laboratory.

IV. Results

A. Phase I

Three levels of powder pre-compaction were examined: 1) un-compacted, 2) compacted into thick discs and, 3) compacted directly in the billet can. The un-compacted powder had a density of 1.61 g/cm^3 or about 60% of the theoretical density. The pre-compacted discs and material directly compacted into billet cans had a density of 2.08 g/cm^3 or about 80% theoretical. The compaction taking place during ECAE caused an increase in the powder density to $2.45\text{--}2.57 \text{ g/cm}^3$ or to 90-95% theoretical density. These latter measurements were taken from ECAE billets partially extruded. Samples for the measurement were extracted from the region of the billet that was compacted by the press load but had not received simple shear (i.e., this material did not go through the die corner shear zone). Fully extruded powder (single-pass ECAE) has a density of $2.66\text{--}2.71 \text{ g/cm}^3$ or from 99-100% theoretical density. The density of wrought 6061 Al was measured to be 2.70 g/cm^3 which agrees with the literature. Density results from experiments where the method of pre-compaction and the geometry of the extrusion cans were varied, are illustrated in Figure 1.

From Figure 1 it is evident that can geometry and level of pre-compaction (at least over the ranges of the parameters examined in this study) have little effect on the final level of compaction achieved by one-pass ECAE. The compaction level due to ECAE compression and reached prior to shear appears to be slightly higher for thinner-walled cans.

B. Phase II

The variation in compact density as a function of extrusion temperature for single-pass extrusions is shown in Figure 2. Density is seen to rise from about 2.69 g/cm^3 for room temperature extrusions to 2.70 g/cm^3 for extrusions at 300°C . For comparison, the density of wrought aluminum 6061 is 2.70 g/cm^3 . The uncertainty in the density measurements is on the order of 0.5% or less than 0.02 g/cm^3 .

Figure 3 shows that two-passes at room temperature via route A or C gives the same density which is slightly above the density of one-pass material and slightly below the density of wrought 6061. For all cans, the density of single-pass or multi-pass powdered 6061 Al is above 99.5% of the theoretical density.

Figures 4 and 5 illustrate the effect of ECAE on tensile strength and ductility for material with or without a heat treatment after extrusion. Figure 4a gives results for as-extruded single-pass material while 4b is for the corresponding solution heat treated, quenched, and aged material. It is impressive that as-extruded single-pass material has tensile properties that are above 50% of those for wrought material and that following heat treatment, the tensile strength of the extruded powder is equivalent to (or slightly above) that of wrought material. Heat treatment does, however, lower ductility as shown in Figure 4b. It should be noted that the tensile test data are for specimens cut in the direction of the billet long-axis and that transverse mechanical properties were not evaluated.

Figures 5a and 5b illustrate the effect of pass number and route on tensile properties. As-extruded strength is seen to rise and ductility to fall as the number of passes increases. Heat treatment causes all specimens to have a tensile strength equivalent to wrought material, but lowers ductility to around 5% for route C processing. Tensile data on heat-treated multi-pass route A material was not successfully collected.

Figures 6 and 7 show SEM images of the fracture surfaces for wrought and 4C material extruded at 150°C. Ductile fracture characteristics are apparent in the as-received and heat-treated wrought material (Figure 6). The unheat-treated 4C material fracture surface (Figure 7a) shows evidence of particle boundary cleavage. The fracture surface in this case does not appear with many of the torn ridges evident in ductile fracture. The heat treated 4C material fracture surface (Figure 7b) shows evidence of diffusion effects and less cleavage than the unheat-treated material, but does not exhibit much ductile fracture appearance. One notable difference between the heat-treated 4C and wrought material (fracture surfaces) is feature size: the 4C material appears to have a smaller average fracture dimple size. This characteristic may be evidence of grain refinement from the ECAE processing.

V. Conclusions

The first phase of work on unevacuated 6061 Al powder yielded important results which were utilized in Phase II. In summary the findings of Phase I included:

1. It was confirmed that simple shear applied via ECAE is highly effective in consolidating 6061 Al powder. A single extrusion at room temperature yields a product with above 99.5% of the theoretical density.
2. The level of pre-compaction does not significantly affect the level of consolidation by ECAE. Un-compacted powder consolidates as well as pre-compacted powder.
3. In studies of the effects of can geometry, no major differences were seen in going

from thin (0.125") to thick (0.25") walls or from short (1/4") end plugs to long (1.5") end plugs. However, a slight decrease in level-of-compaction was seen with the thicker wall cans. It is realized that the level-of-compaction achieved is directly related to the hydro-static pressure conditions existing during extrusion and that this study did not fully explore how this pressure is influenced by can geometry. Subsequent experiments with very thin-walled containers indicate that walls and/or end zones that are too thin will inhibit compaction efficiency.

During Phase II the effects of multi-pass extrusion, ECAE route, and extrusion temperature were investigated using evacuated 6061 Al powder. All of the material in this phase was initially un-compacted. The main conclusions are as follows:

1. Most of the consolidation resulting from ECAE occurs during the first extrusion pass. Slight improvements are seen as the number of passes increases to four.
2. The effect of extrusion temperature is minor for the range 23°C to 300°C.
3. The tensile strength of four-pass as-extruded powder reaches that of wrought material. Ductility of route A material increases as the number of passes increases to four while that of route C material decreases.
4. The tensile strength of single, two or four-pass route C material after heat treatment is the same as wrought material. Ductility of route C material after heat treatment is much less than that of wrought material.
5. There is evidence that route A yields better mechanical properties than route C.

VI. References

1. R.M. German, Powder Metallurgy Science, 2nd Edition, Metal Powder Industries Federation, Princeton, NJ (1994).
2. Ibid, p. 22.
3. T.R. Bieler, R.S. Mishra, and A.K. Mukherjee, "High-Strain-Rate Superplasticity in Aluminum-Matrix Composites," *Journal of Metals*, pp. 52-57, (February 1996).
4. R.Z. Valiev, A.V. Kornikov, and R.R. Mulyukov, "Structure and Properties of Ultrafine-Grained Materials Produced by Severe Plastic Deformation," *Mat. Sci. and Engr. A*, A168, pp. 141-148 (1993).
5. V.M. Segal, "Mechanical Processing by Simple Shear," *Mat. Sci. Engr. A*, A197-2, pp. 157-164 (1995).
6. Nikolai K. Tsenev, Ruslan Z. Valiev, Yan Ma, and Terence G. Langdon, "An Investigation of Ductility and Microstructural Evolution in an Al-3%-Mg Alloy With Submicron Grain Size," *J. Mat. Res.*, Vol. 8, No. 11, pp. 2810-2818, (1993).
7. R.Z. Valiev, E.V. Kozlov, Yu F. Ivanov, J. Lian, A.A. Nazarov, and B. Baudelet, "Deformation Behavior of Ultra-Fine-Grained Copper," *Acta Metall. Mater.*, Vol. 42, No. 7, pp. 2467-2475 (1994).
8. V.M. Segal, K.T. Hartwig, and R.E. Goforth, "In Situ Composites Processed by Simple Shear," *Mat. Sci. Engr. A*, in press.

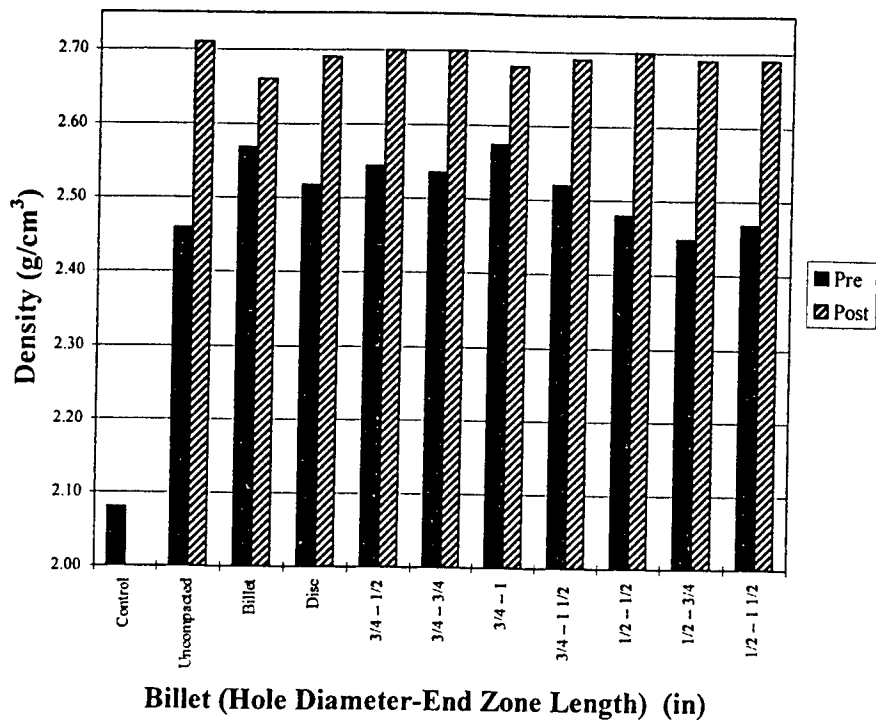


Figure 1: Density of pre-and post-ECAE processed 6061 Aluminum for various can geometries.

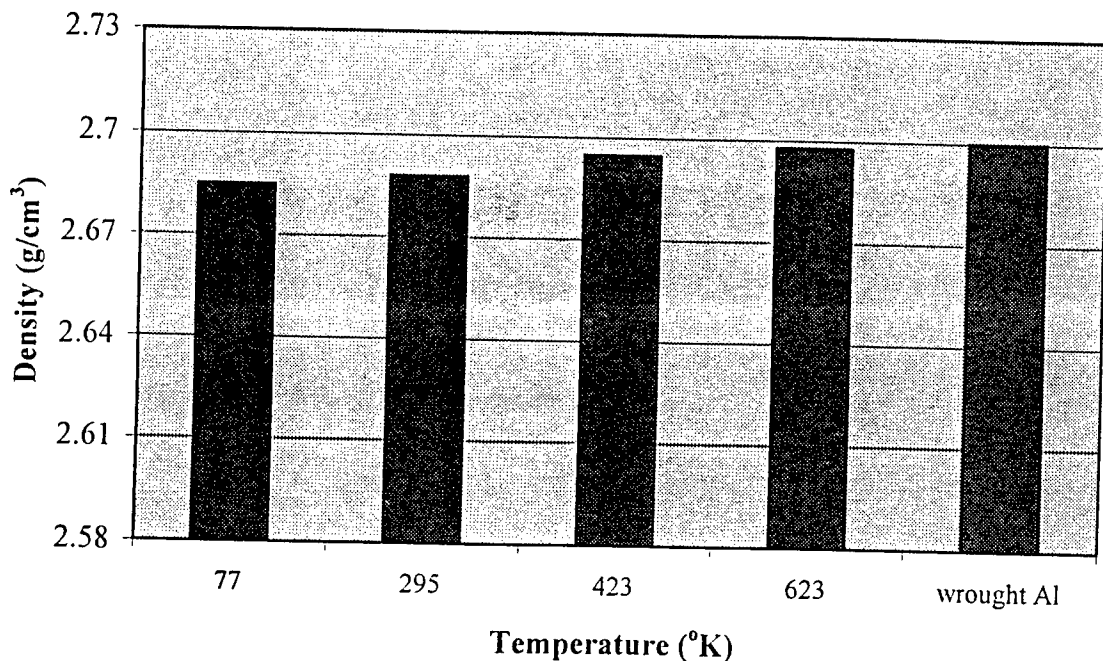


Figure 2. Density versus extrusion temperature for single-pass ECAE.

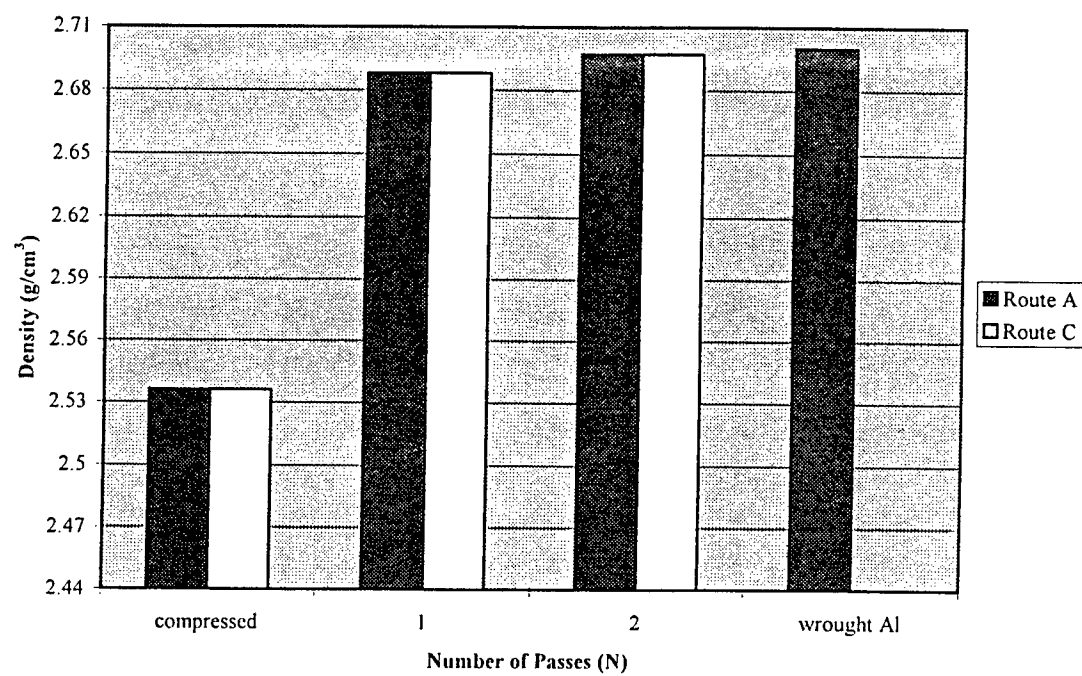


Figure 3. Density versus number of extrusions for room temperature route A and C ECAE.

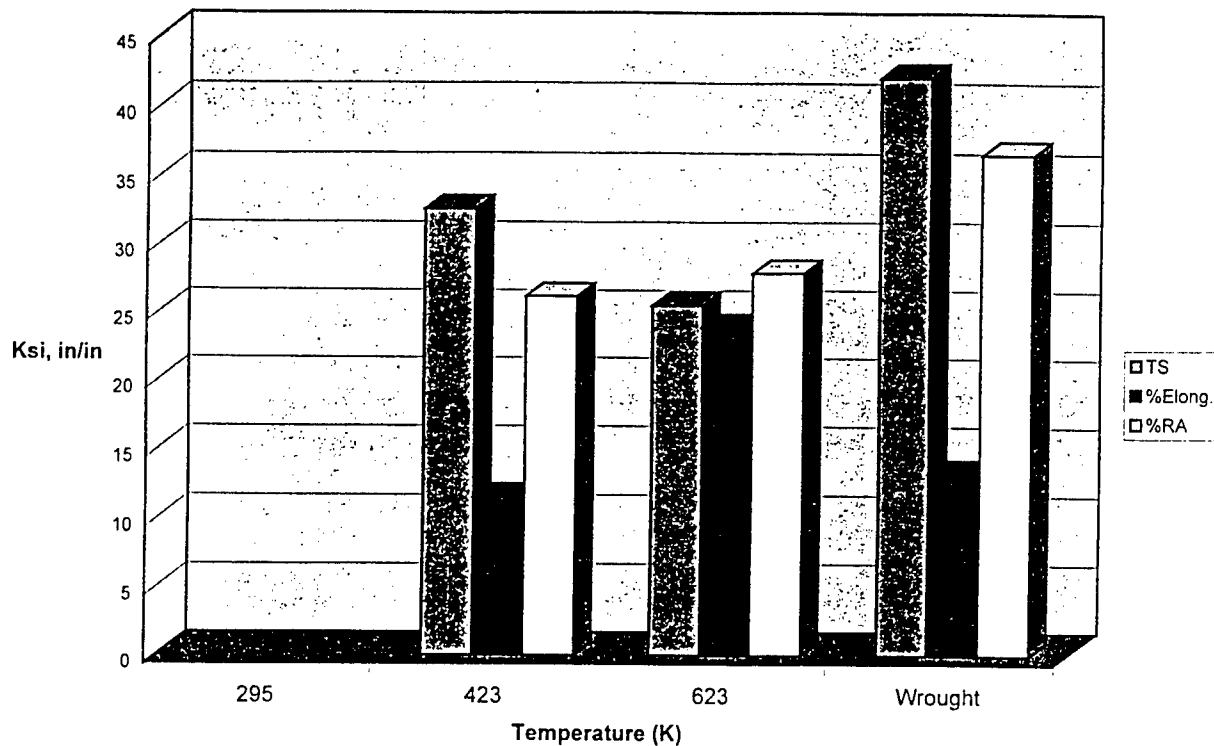


Figure 4a. Tensile strength, percent elongation and percent area reduction for as-extruded single-pass ECAE material.

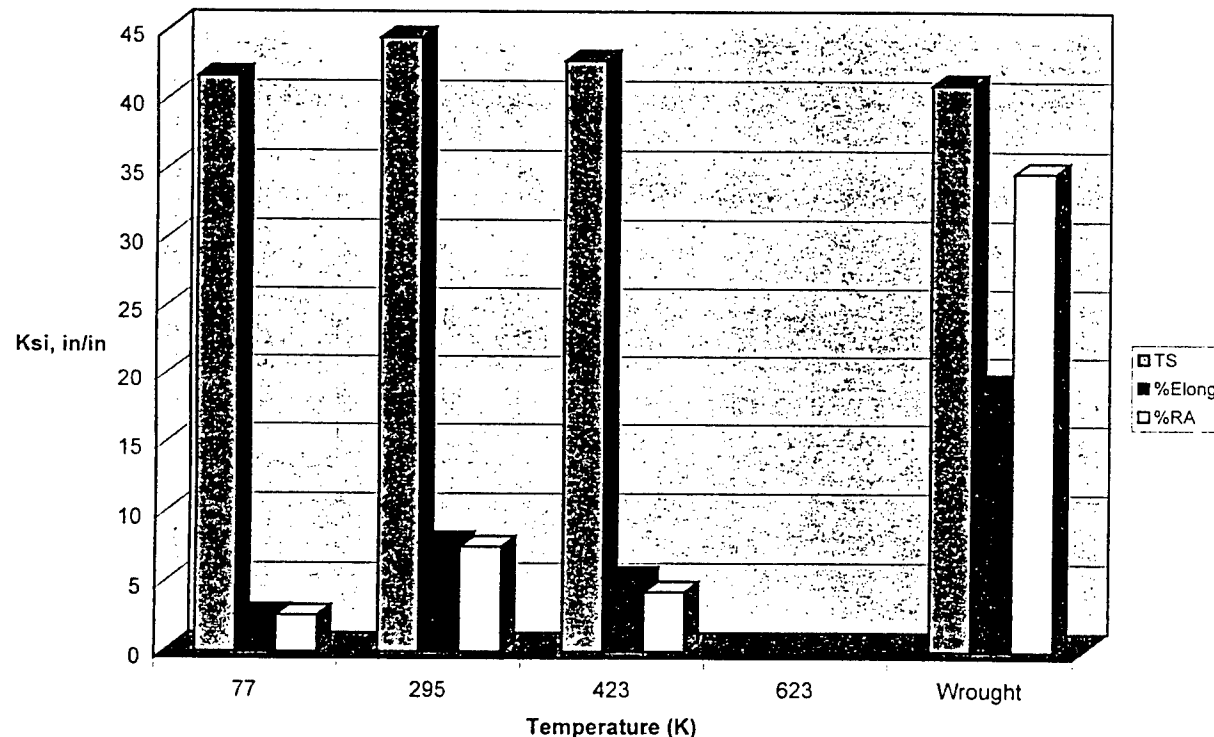


Figure 4b. Tensile strength, percent elongation and percent area reduction for heat-treated single-pass ECAE material.

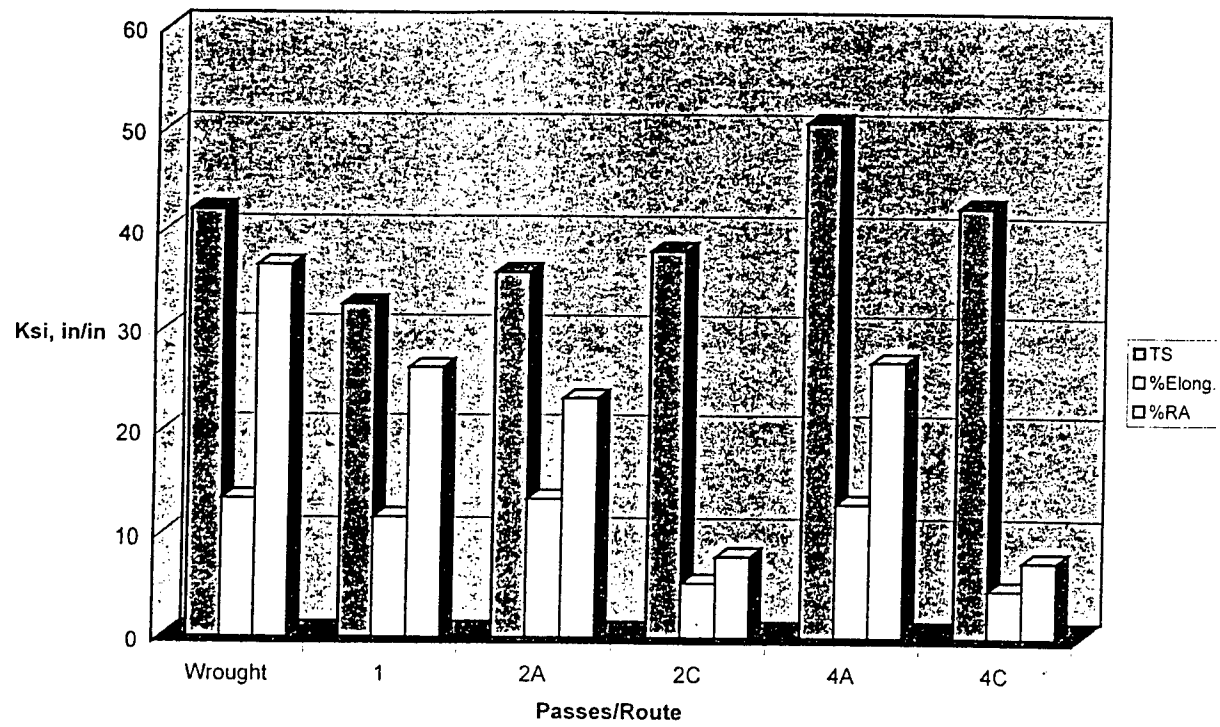


Figure 5a. Tensile properties for as-extruded multi-pass ECAE material.

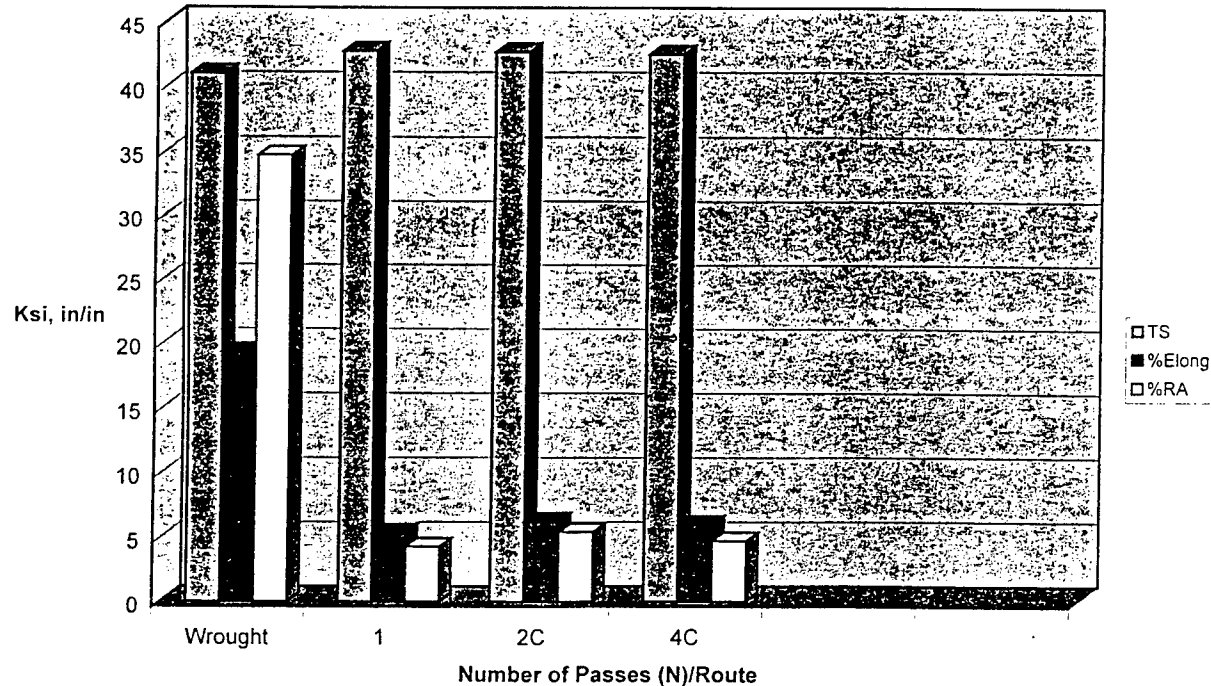
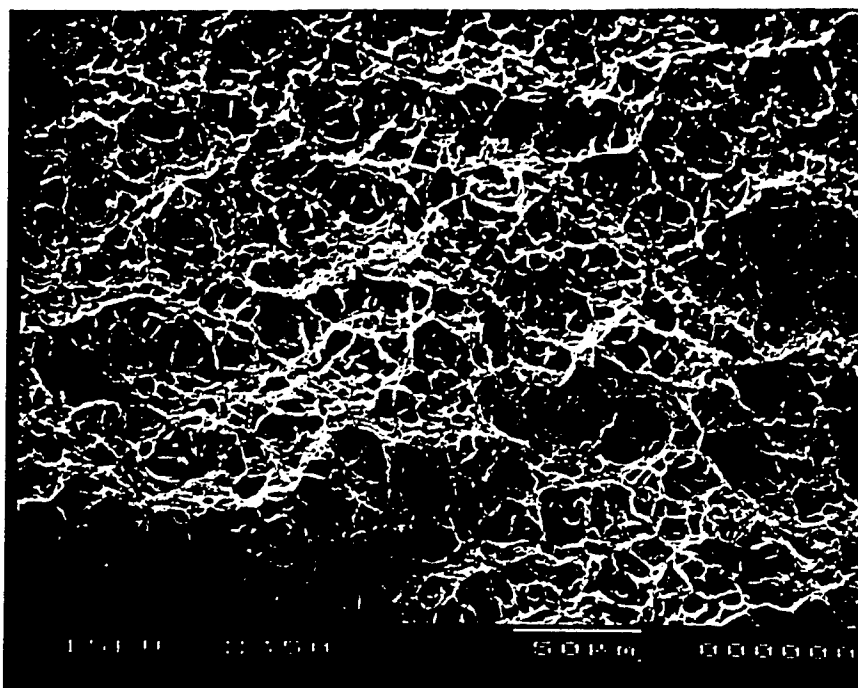
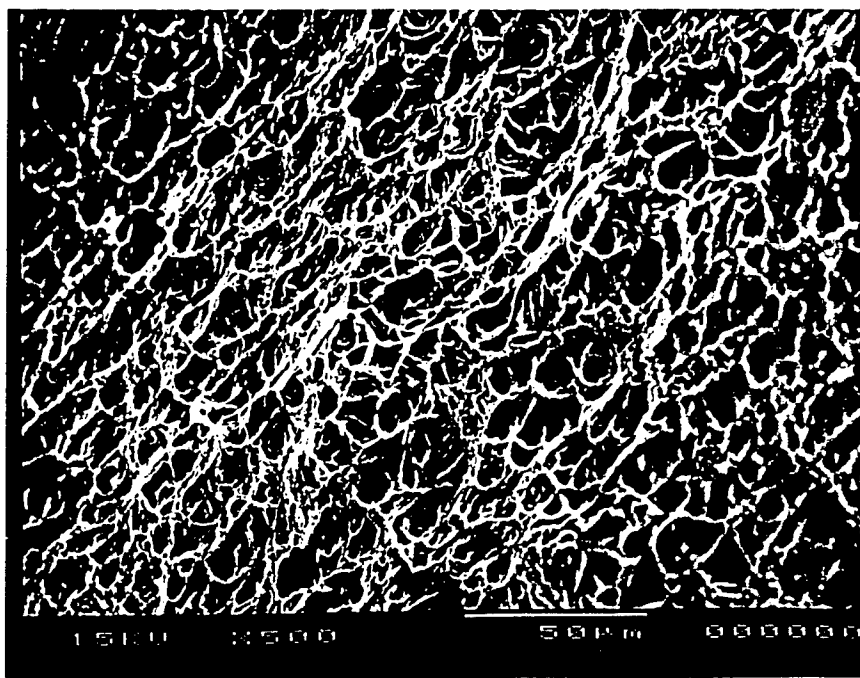


Figure 5b. Tensile properties for heat-treated multi-pass ECAE material.

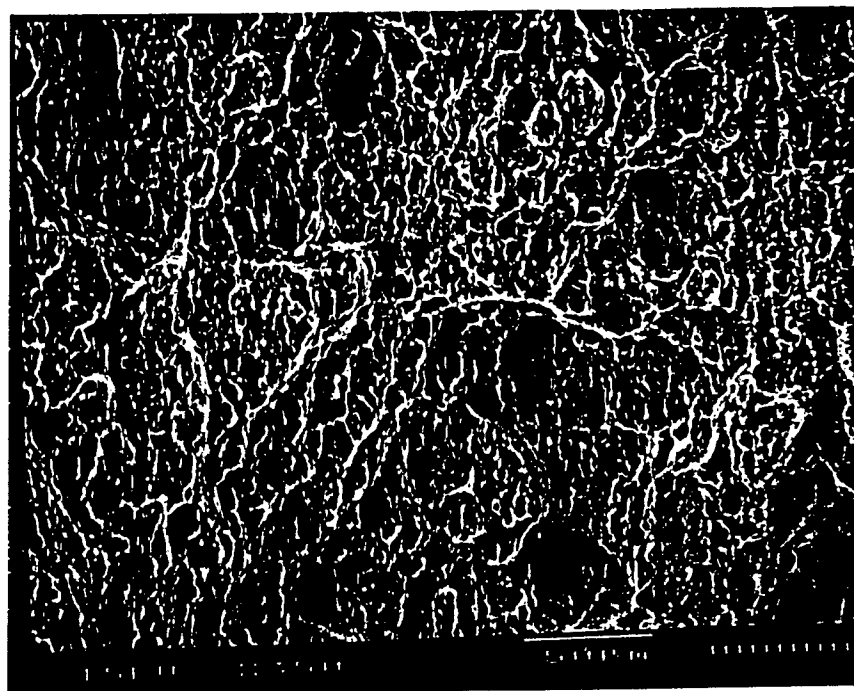


(a)

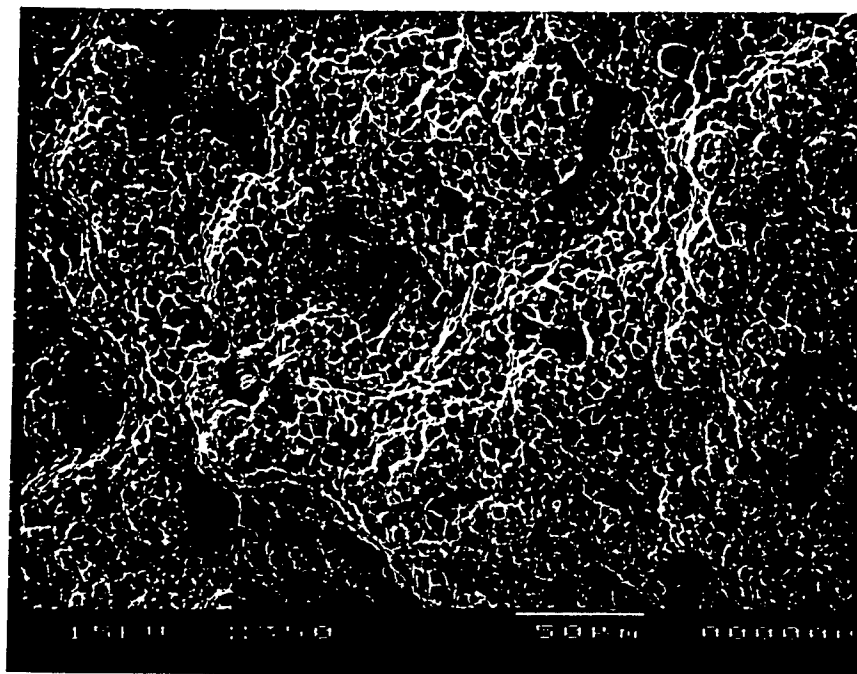


(b)

Figure 6. Fracture surfaces of a) as-received wrought 6061 Al and b) heat-treated 6061 Al.



(a)



(b)

Figure 7. Fracture surfaces of a) 4C as-extruded 6061 Al powder and b) 4C heat-treated 6061 Al powder.

ERROR COMPENSATION IN MUELLER MATRICES:
ACCOUNTING FOR IMPERFECT POLARIZERS

Diana M. Hayes
Department of Mathematics

University of North Texas
Denton, TX 76203

Final Report for:
1996 Summer Research Extension Program

Sponsored by:

Air Force Office of Scientific Research
Bolling AFB, DC

and

University of North Texas

June 1998

ERROR COMPENSATION IN MUELLER MATRICES:
ACCOUNTING FOR IMPERFECT POLARIZERS

Diana M. Hayes
University of North Texas

Abstract

The dual rotating retarder polarimeter generates a periodic sequence of signal measurements from an optical sample. The Mueller matrix of the sample is a function of the associated Fourier coefficients. Seven systematic errors in the dual rotating retarder polarimeter were considered in the analysis: two retardance errors, three alignment errors, and two diattenuation errors. Sample Mueller matrix equations were calculated that compensate for these seven systematic errors.

ERROR COMPENSATION IN MUELLER MATRICES:
ACCOUNTING FOR IMPERFECT POLARIZERS

Diana M. Hayes

Introduction

Azzam (1978) proposed the design of a dual rotating retarder polarimeter and Goldstein (1992) describes the construction in detail. Rotating the retarders at fixed angles θ and 5θ , respectively, generates a periodic sequence of signal measurements. This sequence corresponds to a unique Fourier series,

$$I(\theta) = a_0 + \sum_{n=1}^{12} (a_n \cos(2n\theta) + b_n \sin(2n\theta)).$$

The sample Mueller matrix elements are each a function of the Fourier coefficients, a_i and b_i , and of θ , the rotation angle of the first retarder. Work by Goldstein and Chipman (1990) and Chenault, Pezzaniti, and Chipman (1992) gave error compensation equations that corrected for retardance error in both retarders and for three possible alignment errors within the components of the polarimeter. The results contained in this paper extend these previous equations to include compensation for imperfect polarizers, namely polarizers with diattenuation less than one.

Matrices for Symbolic Computation of the Fourier Coefficients

The following is a brief description of the matrices and vectors involved in the symbolic calculations. The dual rotating retarder polarimeter described in the introduction is

represented by the composition of Mueller matrices

$$P_2 \cdot R_2 \cdot M \cdot R_1 \cdot P_1 .$$

In traditional manner the composition reads from right to left. The system begins with the first polarizer, followed by the first retarder, the sample Mueller matrix M , the second retarder, and finally the second polarizer. The goal is to write the sample Mueller matrix as a function of the retarders and polarizers.

Each retarder is a function of the three variables:

$$\text{retardance} = \delta,$$

$$\text{angle of rotation} = \theta, \quad \text{and}$$

$$\text{alignment error} = \epsilon.$$

An alignment error of ϵ results in the net rotation to be $\theta + \epsilon$ instead of θ . To shorten the expression we substitute $\psi = 2\theta + 2\epsilon$. The resulting retarder matrix has the form

$$R(\theta, \epsilon, \delta) = R(\psi, \delta)$$

$$= \begin{bmatrix} 1 & 0 & 0 & 0 \\ 0 & \cos^2(\psi)(1 - \cos(\delta)) + \cos(\delta) & \sin(\psi)\cos(\psi)(1 - \cos(\delta)) & -\sin(\psi)\sin(\delta) \\ 0 & \sin(\psi)\cos(\psi)(1 - \cos(\delta)) & \sin^2(\psi)(1 - \cos(\delta)) + \cos(\delta) & \cos(\psi)\sin(\delta) \\ 0 & \sin(\psi)\sin(\delta) & -\cos(\psi)\sin(\delta) & \cos(\delta) \end{bmatrix},$$

Each polarizer is a function of two variables:

$$\text{diattenuation} = \rho \quad \text{and} \quad \text{alignment error} = \epsilon.$$

The resulting polarizer matrix has the form

$$P(\rho, \epsilon) = \frac{1}{2} \begin{bmatrix} 1 & \rho \cos(2\epsilon) & \rho \sin(2\epsilon) & 0 \\ \rho \cos(2\epsilon) & \sqrt{1-\rho^2} \sin^2(2\epsilon) + \cos^2(2\epsilon) & (1 - \sqrt{1-\rho^2}) \cos(2\epsilon) \sin(2\epsilon) & 0 \\ \rho \sin(2\epsilon) & (1 - \sqrt{1-\rho^2}) \cos(2\epsilon) \sin(2\epsilon) & \sqrt{1-\rho^2} \cos^2(2\epsilon) + \sin^2(2\epsilon) & 0 \\ 0 & 0 & 0 & \sqrt{1-\rho^2} \end{bmatrix}.$$

The symbolic calculations were based on the following composition:

$$\begin{bmatrix} I \\ x \\ y \\ z \end{bmatrix} = P(\rho_2, \epsilon_5) \cdot R(5\theta, \delta_2, \epsilon_4) \cdot M \cdot R(\theta, \delta_1, \epsilon_3) \cdot P(\rho_1, 0) \cdot \begin{bmatrix} 1 \\ 0 \\ 0 \\ 0 \end{bmatrix},$$

where the sample Mueller matrix

$$M = \begin{bmatrix} m_{11} & m_{12} & m_{13} & m_{14} \\ m_{21} & m_{22} & m_{23} & m_{24} \\ m_{31} & m_{32} & m_{33} & m_{34} \\ m_{41} & m_{42} & m_{43} & m_{44} \end{bmatrix}.$$

The signal measurements correspond to measuring only the first element, I , of the resulting four element Stokes vector. The application of a multitude of trigonometric identities produced the following formulas for the Fourier coefficients. The α_i 's are linear combinations of the ϵ_i 's and the β_i 's are functions of the δ_i 's. Equations for these space-saving variables are listed after the Fourier coefficients.

$$\begin{aligned} a_0 &= \frac{1}{2}\rho_1\beta_3m_{12} + \frac{1}{4}\rho_1\rho_2\beta_3\beta_4 \cos(2\epsilon_5)m_{22} + \frac{1}{4}\rho_1\rho_2\beta_3\beta_4 \sin(2\epsilon_5)m_{32} \\ &\quad + \frac{1}{2}\rho_2\beta_4 \cos(2\epsilon_5)m_{21} + \frac{1}{2}\rho_2\beta_4 \sin(2\epsilon_5)m_{31} + m_{11} \end{aligned}$$

$$\begin{aligned} a_1 &= \rho_1 \sin(\delta_1) \sin(2\epsilon_3)m_{14} + \frac{1}{2}\rho_1\rho_2\beta_4 \sin(\delta_1) \sin(2\epsilon_3) \cos(2\epsilon_5)m_{24} \\ &\quad + \frac{1}{2}\rho_1\rho_2\beta_4 \sin(\delta_1) \sin(2\epsilon_3) \sin(2\epsilon_5)m_{34} \end{aligned}$$

$$\begin{aligned}
a_2 &= \frac{1}{4}\rho_1\rho_2\beta_1\beta_4 \sin(4\epsilon_3) \cos(2\epsilon_5)m_{23} + \frac{1}{4}\rho_1\rho_2\beta_1\beta_4 \sin(4\epsilon_3) \sin(2\epsilon_5)m_{33} \\
&\quad + \frac{1}{2}\rho_1\beta_1 \sin(4\epsilon_3)m_{13} + \frac{1}{4}\rho_1\rho_2\beta_1\beta_4 \cos(4\epsilon_3) \cos(2\epsilon_5)m_{22} \\
&\quad + \frac{1}{4}\rho_1\rho_2\beta_1\beta_4 \cos(4\epsilon_3) \sin(2\epsilon_5)m_{32} + \frac{1}{2}\rho_1\beta_1 \cos(4\epsilon_3)m_{12} \\
a_3 &= -\frac{1}{4}\rho_1\rho_2\beta_1 \sin(\delta_2) [\cos(\alpha_3)m_{43} + \sin(\alpha_3)m_{42}] \\
a_4 &= -\frac{1}{2}\rho_1\rho_2 \sin(\delta_1) \sin(\delta_2) \cos(\alpha_1)m_{44} \\
a_5 &= \frac{1}{2}\rho_2 \sin(\delta_2) \sin(\alpha_5) [\rho_1\beta_3m_{42} + 2m_{41}] \\
a_6 &= \frac{1}{2}\rho_1\rho_2 \sin(\delta_1) \sin(\delta_2) \cos(\alpha_2)m_{44} \\
a_7 &= \frac{1}{4}\rho_1\rho_2\beta_1 \sin(\delta_2) [\cos(\alpha_4)m_{43} - \sin(\alpha_4)m_{42}] \\
a_8 &= \frac{1}{8}\rho_1\rho_2\beta_1\beta_2 [(m_{22} + m_{33}) \cos(\alpha_9) + (m_{32} - m_{23}) \sin(\alpha_9)] \\
a_9 &= \frac{1}{4}\rho_1\rho_2\beta_2 \sin(\delta_1) [\cos(\alpha_6)m_{34} + \sin(\alpha_6)m_{24}] \\
a_{10} &= \frac{1}{4}\rho_1\rho_2\beta_2\beta_3 \cos(\alpha_{11})m_{22} + \frac{1}{2}\rho_2\beta_2 \cos(\alpha_{11})m_{21} \\
&\quad + \frac{1}{4}\rho_1\rho_2\beta_2\beta_3 \sin(\alpha_{11})m_{32} + \frac{1}{2}\rho_2\beta_2 \sin(\alpha_{11})m_{31} \\
a_{11} &= -\frac{1}{4}\rho_1\rho_2\beta_2 \sin(\delta_1) [\sin(\alpha_7)m_{24} + \cos(\alpha_7)m_{34}] \\
a_{12} &= \frac{1}{8}\rho_1\rho_2\beta_1\beta_2 [\sin(\alpha_{10})(m_{23} + m_{32}) + \cos(\alpha_{10})(m_{22} - m_{33})]
\end{aligned}$$

$$b_1 = \rho_1 \sin(\delta_1) \cos(2\epsilon_3) m_{14} + \frac{1}{2} \rho_1 \rho_2 \beta_4 \sin(\delta_1) \cos(2\epsilon_3) \cos(2\epsilon_5) m_{24}$$

$$+ \frac{1}{2} \rho_1 \rho_2 \beta_4 \sin(\delta_1) \cos(2\epsilon_3) \sin(2\epsilon_5) m_{34}$$

$$b_2 = \frac{1}{4} \rho_1 \rho_2 \beta_1 \beta_4 \cos(4\epsilon_3) \cos(2\epsilon_5) m_{23} + \frac{1}{4} \rho_1 \rho_2 \beta_1 \beta_4 \cos(4\epsilon_3) \sin(2\epsilon_5) m_{33}$$

$$+ \frac{1}{2} \rho_1 \beta_1 \cos(4\epsilon_3) m_{13} - \frac{1}{4} \rho_1 \rho_2 \beta_1 \beta_4 \sin(4\epsilon_3) \cos(2\epsilon_5) m_{22}$$

$$- \frac{1}{4} \rho_1 \rho_2 \beta_1 \beta_4 \sin(4\epsilon_3) \sin(2\epsilon_5) m_{32} - \frac{1}{2} \rho_1 \beta_1 \sin(4\epsilon_3) m_{12}$$

$$b_3 = \frac{1}{4} \rho_1 \rho_2 \beta_1 \sin(\delta_2) [\sin(\alpha_3) m_{43} - \cos(\alpha_3) m_{42}]$$

$$b_4 = \frac{1}{2} \rho_1 \rho_2 \sin(\delta_1) \sin(\delta_2) \sin(\alpha_1) m_{44}$$

$$b_5 = -\frac{1}{2} \rho_2 \sin(\delta_2) \cos(\alpha_5) [\rho_1 \beta_3 m_{42} + 2m_{41}]$$

$$b_6 = -\frac{1}{2} \rho_1 \rho_2 \sin(\delta_1) \sin(\delta_2) \sin(\alpha_2) m_{44}$$

$$b_7 = -\frac{1}{4} \rho_1 \rho_2 \beta_1 \sin(\delta_2) [\sin(\alpha_4) m_{43} + \cos(\alpha_4) m_{42}]$$

$$b_8 = -\frac{1}{8} \rho_1 \rho_2 \beta_1 \beta_2 [(m_{22} + m_{33}) \sin(\alpha_9) + (m_{23} - m_{32}) \cos(\alpha_9)]$$

$$b_9 = \frac{1}{4} \rho_1 \rho_2 \beta_2 \sin(\delta_1) [\sin(\alpha_6) m_{34} - \cos(\alpha_6) m_{24}]$$

$$b_{10} = \frac{1}{4} \rho_1 \rho_2 \beta_2 \beta_3 \cos(\alpha_{11}) m_{32} + \frac{1}{2} \rho_2 \beta_2 \cos(\alpha_{11}) m_{31}$$

$$- \frac{1}{4} \rho_1 \rho_2 \beta_2 \beta_3 \sin(\alpha_{11}) m_{22} - \frac{1}{2} \rho_2 \beta_2 \sin(\alpha_{11}) m_{21}$$

$$b_{11} = \frac{1}{4} \rho_1 \rho_2 \beta_2 \sin(\delta_1) [\cos(\alpha_7) m_{24} - \sin(\alpha_7) m_{34}]$$

$$b_{12} = \frac{1}{8}\rho_1\rho_2\beta_1\beta_2 [\cos(\alpha_{10})(m_{23} + m_{32}) + \sin(\alpha_{10})(m_{33} - m_{22})]$$

$$\begin{aligned}
\beta_1 &= 1 - \delta_1 & \beta_3 &= 1 + \delta_1 \\
\beta_2 &= 1 - \delta_2 & \beta_4 &= 1 + \delta_2 \\
\alpha_1 &= 2\epsilon_4 - 2\epsilon_3 - 2\epsilon_5 & \alpha_7 &= 2\epsilon_5 - 4\epsilon_4 - 2\epsilon_3 \\
\alpha_2 &= 2\epsilon_4 + 2\epsilon_3 - 2\epsilon_5 & \alpha_8 &= -2\epsilon_5 + 4\epsilon_4 - 2\epsilon_3 \\
\alpha_3 &= 2\epsilon_4 - 4\epsilon_3 - 2\epsilon_5 & \alpha_9 &= -2\epsilon_5 + 4\epsilon_4 - 4\epsilon_3 \\
\alpha_4 &= 2\epsilon_4 + 4\epsilon_3 - 2\epsilon_5 & \alpha_{10} &= -2\epsilon_5 + 4\epsilon_4 + 4\epsilon_3 \\
\alpha_5 &= 2\epsilon_5 - 4\epsilon_4 & \alpha_{11} &= 4\epsilon_4 - 2\epsilon_5 \\
\alpha_6 &= -4\epsilon_4 + 2\epsilon_3 + 2\epsilon_5
\end{aligned}$$

Calibration: Solving for the Systematic Errors

The general experimental procedure begins with calibration of the equipment. Calibration consists of running through the sequence of measurements with no sample in the polarimeter. Mathematically, this corresponds to substituting the identity matrix for the sample Mueller matrix. This substitution allows the experimenter to determine the values of the system errors. The formulas for the system errors are listed below.

$$\begin{aligned}
\epsilon_3 &= \frac{1}{4} \arctan\left(\frac{b_8}{a_8}\right) - \frac{1}{4} \arctan\left(\frac{b_{10}}{a_{10}}\right) \\
\epsilon_4 &= \frac{1}{2} \arctan\left(\frac{b_2}{a_2}\right) - \frac{1}{2} \arctan\left(\frac{b_6}{a_6}\right) + \frac{1}{4} \arctan\left(\frac{b_8}{a_8}\right) - \frac{1}{4} \arctan\left(\frac{b_{10}}{a_{10}}\right) \\
\epsilon_5 &= \frac{1}{2} \arctan\left(\frac{b_2}{a_2}\right) + \frac{1}{2} \arctan\left(\frac{b_8}{a_8}\right) - \frac{1}{2} \arctan\left(\frac{b_{10}}{a_{10}}\right)
\end{aligned}$$

$$\begin{aligned}\delta_1 &= \arccos \left(\frac{a_{10} \cos(\alpha_9) - a_8 \cos(\alpha_{11})}{a_{10} \cos(\alpha_9) + a_8 \cos(\alpha_{11})} \right) \\ \delta_2 &= \arccos \left(\frac{a_2 \cos(\alpha_9) - a_8 \cos(4\epsilon_3 - 2\epsilon_5)}{a_2 \cos(\alpha_9) + a_8 \cos(4\epsilon_3 - 2\epsilon_5)} \right) \\ \rho_1 \rho_2 &= \frac{4(a_0 - 1)}{\beta_3 \beta_4 \cos(2\epsilon_5)} \quad \text{or alternately} \quad \rho_1 \rho_2 = \frac{2a_6}{\sin(\delta_1) \sin(\delta_2) \cos(\alpha_2)}\end{aligned}$$

It is useful to note that the equations for the δ_i 's and ϵ_i 's are unchanged from the equations determined by Chenault, Pezzaniti, and Chipman (1992). Unfortunately, the calibration equations only allow for the product of the two diattenuation values to be calculated. This leaves several avenues for dealing with the problem of determining the individual values.

1. If the diattenuation of both polarizers is known at the outset, then those values can be substituted for ρ_1 and ρ_2 .
2. If statistical specifications for each of the two polarizers are known, then error can be attributed to each polarizer in proportion to the variance of its accuracy. A special case of this scenario occurs when only one of the polarizers needs to be considered imperfect. Then all of the diattenuation error can be attributed to the other polarizer.
3. If both of the polarizers may be imperfect and no additional information is known, then a final alternative assumes $\rho_1 = \rho_2 = \sqrt{\rho_1 \rho_2}$.

In general, the retarders and polarizers are factory generated optical components, so their inherent imperfections cannot be altered. However, the alignment of the components can be adjusted to make the values of the ϵ_i 's as close to zero as possible.

Error Compensation Equations for the
Sample Mueller Matrix

As a result of the calibration procedure, the error terms ϵ_1 , ϵ_2 , ϵ_3 , δ_1 , δ_2 , ρ_1 , and ρ_2 are all known quantities. Once the calibration procedure is complete, the sample to be analyzed is placed in the polarimeter. The sequence of signal measurements is taken and the corresponding Fourier series is computed. In particular, the Fourier coefficients the a_i 's and the b_i 's are now known values.

The previous section contained equations that gave the Fourier coefficients as functions of the polarimeter's components. By solving these equations for the sample Mueller matrix elements, the m_{ij} 's become functions of the Fourier coefficients and of the error terms. These values known from calibration are then substituted into the following equations to give the sample Mueller matrix.

$$m_{44} = \frac{4}{\rho_1 \rho_2 \sin(\delta_1) \sin(\delta_2)} \left(\frac{a_6}{\cos(\alpha_2)} - \frac{a_4}{\cos(\alpha_1)} \right)$$

$$m_{43} = 8 \left(\frac{b_3 \sin(\alpha_3) - a_3 \cos(\alpha_3) + a_7 \cos(\alpha_4) - b_7 \sin(\alpha_4)}{\rho_1 \rho_2 \beta_1 \sin(\delta_2)} \right)$$

$$m_{42} = (-8) \left(\frac{a_3 \sin(\alpha_3) + b_3 \cos(\alpha_3) + b_7 \cos(\alpha_4) + a_7 \sin(\alpha_4)}{\rho_1 \rho_2 \beta_1 \sin(\delta_2)} \right)$$

$$m_{41} = \frac{(-4)b_5}{\rho_2 \sin(\delta_2) \cos(\alpha_5)} - \frac{\rho_1 \beta_3 m_{42}}{2}$$

$$m_{24} = 8 \left(\frac{a_9 \sin(\alpha_6) - b_9 \cos(\alpha_6) - a_{11} \sin(\alpha_7) + b_{11} \cos(\alpha_7)}{\rho_1 \rho_2 \beta_2 \sin(\delta_1)} \right)$$

$$m_{34} = 8 \frac{a_9 \cos(\alpha_6) + b_9 \sin(\alpha_6) - a_{11} \cos(\alpha_7) - b_{11} \sin(\alpha_7)}{\rho_1 \rho_2 \beta_2 \sin(\delta_1)}$$

$$m_{14} = \frac{4b_1}{\rho_1 \sin(\delta_1) \cos(2\epsilon_3)} - \frac{\rho_2 \beta_4}{2} (m_{24} \cos(2\epsilon_5) + m_{34} \sin(2\epsilon_5))$$

$$m_{22} = 16 \left(\frac{a_8 \cos(\alpha_9) + a_{12} \cos(\alpha_{10}) - b_8 \sin(\alpha_9) - b_{12} \sin(\alpha_{10})}{\rho_1 \rho_2 \beta_1 \beta_2} \right)$$

$$m_{33} = 16 \left(\frac{a_8 \cos(\alpha_9) - b_8 \sin(\alpha_9) - a_{12} \cos(\alpha_{10}) + b_{12} \sin(\alpha_{10})}{\rho_1 \rho_2 \beta_1 \beta_2} \right)$$

$$m_{23} = 16 \left(-\frac{a_8 \sin(\alpha_9) - b_8 \cos(\alpha_9) + a_{12} \sin(\alpha_{10}) + b_{12} \cos(\alpha_{10})}{\rho_1 \rho_2 \beta_1 \beta_2} \right)$$

$$m_{32} = 16 \left(\frac{a_8 \sin(\alpha_9) + b_8 \cos(\alpha_9) + a_{12} \sin(\alpha_{10}) + b_{12} \cos(\alpha_{10})}{\rho_1 \rho_2 \beta_1 \beta_2} \right)$$

$$m_{12} = 8 \left(\frac{a_2 \cos(4\epsilon_3)}{\rho_1 \beta_1} - \frac{b_2 \sin(4\epsilon_3)}{\rho_1 \beta_1} \right) - \frac{\rho_2 \beta_4}{2} (\cos(2\epsilon_5)m_{22} + \sin(2\epsilon_5)m_{32})$$

$$m_{13} = 8 \left(\frac{a_2 \sin(4\epsilon_3)}{\rho_1 \beta_1} + \frac{b_2 \cos(4\epsilon_3)}{\rho_1 \beta_1} \right) - \frac{\rho_2 \beta_4}{2} (\cos(2\epsilon_5)m_{23} + \sin(2\epsilon_5)m_{33})$$

$$m_{21} = 8 \left(\frac{a_{10} \cos(\alpha_{11}) - b_{10} \sin(\alpha_{11})}{\rho_2 \beta_2} \right) - \frac{\rho_1 \beta_3 m_{22}}{2}$$

$$m_{31} = 8 \left(\frac{a_{10} \sin(\alpha_{11}) + b_{10} \cos(\alpha_{11})}{\rho_2 \beta_2} \right) - \frac{\rho_1 \beta_3 m_{32}}{2}$$

$$\begin{aligned} m_{11} = & 4a_0 - \left(\frac{1}{2} \rho_1 \beta_3 m_{12} + \frac{1}{2} \rho_2 \beta_4 \cos(2\epsilon_5) m_{21} + \frac{1}{2} \rho_2 \beta_4 \sin(2\epsilon_5) m_{31} \right. \\ & \left. + \frac{1}{4} \rho_1 \rho_2 \beta_3 \beta_4 \cos(2\epsilon_5) m_{22} + \frac{1}{4} \rho_1 \rho_2 \beta_3 \beta_4 \sin(2\epsilon_5) m_{32} \right) \end{aligned}$$

Conclusions

The diattenuation error compensation was only partially successful since the normal calibration procedure does not admit solving for the two diattenuation variables, ρ_1 and ρ_2 , separately. Nevertheless, since the product of these two errors can be ascertained through calibration, three possible alternatives to this stumbling block were enumerated.

1. Measure diattenuation separately.
2. Attribute the error to each polarizer in proportion to its statistical accuracy.
3. Spread the error equally between the two polarizers by taking the square root of the product.

Finally, the error compensation equations agreed with previous results by Goldstein and Chipman (1990) and by Chenault, Pezzaniti, and Chipman (1992), and these new equations were verified numerically with mathematical software.

References

1. R. M. A. Azzam, *Photopolarimetric measurement of the Mueller matrix by Fourier analysis of a single detected signal*, Opt. Lett. **2**, 148-150 (1978).
2. David B. Chenault, Joseph L. Pezzaniti, and Russell A. Chipman, *Mueller matrix algorithms*, Proc. SPIE Vol. 1746, 231-246, (1992).
3. Dennis H. Goldstein and Russell A. Chipman, *Error analysis of a Mueller matrix polarimeter*, J. Opt. Soc. Am. , **7**(4), 693-700 (1990).
4. Dennis H. Goldstein, *Mueller matrix dual-rotating retarder polarimeter*, Applied Optics, **31**(31), 6676-6683, (1992).